DISSERTATION

REALIZING THERMOMETRIC CONTROL OF COBALT-59 SPIN-BASED PROBES VIA LIGAND DESIGN

Submitted by

Tyler M. Ozvat

Department of Chemistry

In partial fulfillment of the requirements

for the degree of Doctor of Philosophy

Colorado State University

Fort Collins, Colorado

Spring 2022

Doctoral Committee:

Advisor: Joseph M. Zadrozny

Anthony K. Rappé
Andy McNally
Kathryn A. Ross

ABSTRACT

REALIZING THERMOMETRIC CONTROL OF COBALT-59 SPIN-BASED PROBES VIA LIGAND DESIGN

Cobalt-59 is an exemplary nucleus for the design of NMR thermometers through its highly responsive nuclear spin properties such as its temperature-driven chemical shift ($\Delta\delta/\Delta T$) and relaxation dynamics ($\Delta T_1/\Delta T$ and $\Delta T_2/\Delta T$). Investigated through a series of low-spin d^6 Co^{3+} octahedrally coordination complexes, the temperature dependences of the ^{59}Co nuclear spin properties are readily affected by molecular features such as coordination geometry, ligand identity, and local environmental factors. However, precise control of these thermometric properties (i.e., $\Delta\delta/\Delta T$, $\Delta T_1/\Delta T$, and $\Delta T_2/\Delta T$) via ligand design is absent. While it is known that molecular identity, defined by the coordinating ligand, ultimately dictates the thermometric properties of the ^{59}Co-containing complex, it is neither known how it is governed nor how it may be improved. Thus, the goal of this dissertation aims to explore fundamental design principles that inform on the synthetic control of thermometric properties of ^{59}Co via molecular features. Presented herein is the first comprehensive collection of experimental and computational investigations on the temperature-dependence of ^{59}Co in a series of structurally similar coordination complexes with progressively encapsulating ligands. Through a suite of spectroscopic and theoretical techniques, a critical lens has been applied to establish a variety of key structural implications. These key points include the enhancement of thermometric properties via multidentate ligand encapsulation, temperature-driven structure, symmetry, and lastly, mass-induced changes to ligand-specific vibrational modes. The identified design principles pave way for future studies of either new ligand systems, coordination geometries, or other NMR-active transition metal nuclei.

ACKNOWLEDGEMENTS

I must start my acknowledgments by saying that I am truly blessed to have been simply fortunate enough to attend graduate school, such that I have been given a remarkable opportunity to pursue my passion for learning about the natural world through the lens of chemistry. To this end, I have many individuals to thank for this fruition. Ultimately, it would be my staunchest supporters that fostered the basic ingredients – *passion, opportunity, hard work,* and *talent* – for the successes I have had in my personal and professional growth through graduate school. Regarding this five-year journey, it would be remiss not to acknowledge briefly, at the very least, the factors that led me to chemistry.

I attended my undergraduate institution, Fort Lewis College, without any preconceived notion to pursue chemistry. However, it wasn't long before, and to my delight, that I had discovered a profound joy for learning about the fundamentals of atoms and molecules in my freshman level chemistry course. From the start of this entry level course, my interests in chemistry were invariably fostered through the mentoring excellence of each and every one of my chemistry course instructors throughout college. This is truly no understatement. I was astonished by these individuals whose talents were driven by their own great enthusiasm for learning and teaching chemistry. As a senior undergraduate, I felt compelled to follow in their footsteps which was to pursue chemistry to graduate school as they had. To these influential role models, many of which might not have ever realized it, I thank you for the *passion* you demonstrated.

On this note, I must acknowledge the two most influential mentors of my undergraduate career, Prof. Kenny Miller and Prof. Aimee Morris, to whom strongly supported me as a rising student in chemistry. My very first introduction to chemistry research was through natural product synthesis under Prof. Kenny Miller who welcomed me into his lab and taught me the fundamentals of synthesis and spectroscopy. He supported my continued involvement in research through two undergraduate summer research programs at Fort Lewis College and Colorado State University. In search of additional research experience, I was welcomed into another research lab by Prof. Aimee Morris who taught me the essentials of inorganic synthesis. Both of my undergraduate mentors exuded extreme knowledgeability in their fields and taught

me how to be proficient and capable in a chemistry research laboratory. Their early investments in me as a research student ultimately opened the door for me to attend graduate school. To both of my undergraduate mentors, Profs. Kenny Miller and Aimee Morris, I thank you for the *talent* you have shown and cultivated in me.

Upon attending graduate school as a first-year student, I met Prof. Joe Zadrozny who was himself a new inorganic chemistry professor. My first interaction with Joe was at the recruitment department poster session where I can recall nothing he was actually saying about "*quantum*", "*qubits*", and "*spin*" things. I only remember thinking to myself, "*This sounds difficult. And I am not interested in physical chemistry!*". Fortunately, I would rethink the idea of learning about these difficult concepts when I rotated in his lab and realized how "dope" his research ideas were. Looking back, I know I made the right decision to join his group as I learned that his mentorship is defined by stoking enthusiasm for research in others and is met with undying encouragement. He impressed upon his ability to typified high-quality chemistry presentations and effortlessly communicate complex topics. As a result, I received guidance and encouragement throughout the entirety of my graduate research, including through many obstacles. Among many words of inspiration spoken to me by Joe, the most impactful were, "*The path of least resistance is least rewarding*". To my graduate advisor, Prof. Joseph Zadrozny, who ultimately accepted me as one of his first graduate students and would provide me an incredible *opportunity* to work in his lab, to pursue graduate-level research, and to grow as an individual.

Lastly, and most dearly, I wish to thank my parents Matt and Rebecca who have always been the most important role-models long before graduate school. Early on I thought that I would follow in their footsteps and enlist in the military, but I was told, "*We served your time in the military, so do something better*". And to me, graduate school would be the start of "*something better*". To this end, I am grateful to both of my parents as they have been my ultimately source of love, strength, and encouragement. Their support has ultimately made it possible for me to achieve my academic goals. Within me, they fostered the skill to find the fun in anything and everything, even in the most challenging circumstances. They have taken every step of this journey with me and have never stopped pushing me to be my best in graduate

school, in life, and beyond. To my parents, Matt and Rebecca, I am endlessly grateful for the *hard work* mentality you have instilled in me.

Acknowledgements by Dissertation Chapter

Chapter 2 contains work reproduced from the journal article *Influence of Ligand Encapsulation on Cobalt-59 Chemical-Shift Thermometry* by Tyler M. Ozvat, Manuel E. Peña, and Joseph M. Zadrozny (*Chemical Science* **2019**, *10*, 6727–6734). Co-author Manny E. Peña contributed equally to this article through the synthesis of many compounds, room temperature UV-vis, as well as the variable temperature, variable solvent, and inversion-recovery T_1 ^{59}Co-NMR studies.

The work in this chapter was performed with the support of Colorado State University (CSU) and the NIH (R21-EB027293). All NMR data were collected from the Materials and Molecular Analysis (MMA) at CSU, which was supported by a NIH-SIG award (1S10OD021814-01) and the CSU-CORES Program. Raman spectroscopy data were collected at the Raman Microspectroscopy Laboratory, Department of Geological Sciences, University of Colorado Boulder.

Chapter 3 contains work reproduced from the journal article *EXAFS Investigation of Temperature-Driven Structure in Cobalt-59 Molecular NMR Thermometers* by Tyler M. Ozvat, George E. Sterbinsky, Anthony J. Campanella, Anthony K. Rappé, and Joseph M. Zadrozny (*Dalton Transactions* **2020**, *49*, 16380–16385). George E. Sterbinsky assisted in the experimental setup, and interpretation of all X-ray absorbance spectroscopy data at the Advanced Photon Source (9-BM) at Argonne National Laboratory. Anthony J. Campanella assisted in the sample preparation and collection of X-ray absorption spectroscopy data. Prof. Anthony K. Rappé provided computational resources and assisted in the interpretation of computational data.

The work detailed in this chapter was performed with the support of Colorado State University (CSU) and the NIH (R21-EB027293). Collection of X-ray absorbance spectroscopy data was performed at beamline 9-BM of the Advanced Photon Source (APS), a U.S. Department of Energy (DOE) Office of Science User Facility operated for the DOE Office of Science by Argonne National Laboratory under

contract No. DE-AC02-06CH11357. Computational resources are enabled by the Catalysis Collaboratory for Light-activated Earth Abundant Reagents (C-CLEAR), which is supported by the National Science Foundation (NSF) and the Environmental Protection Agency through the Networks for Sustainable Molecular Design and Synthesis (CHE-1339674) at CSU.

Chapter 4 contains work reproduced from the journal article *Ligand Control of ^{59}Co Nuclear Spin Relaxation Thermometry* by Tyler M. Ozvat, Spencer H. Johnson, Anthony K. Rappé, and Joseph M. Zadrozny (*Magnetochemistry* **2020**, *6*, 58). Spencer. H. Johnson assisted in select experimental data collection and conducted the calculation of correlation times. Prof. Anthony K. Rappé provided computational resources and assisted in the interpretation of computational data.

The work done in this chapter was performed with the support of Colorado State University (CSU) and the NIH (R21-EB027293). NMR experiments were performed on an instrument at the CSU Analytical Resources Core, which is supported by an NIH-SIG award (1S10OD021814-01) and the CSU-CORES Program. Computational resources are enabled by the Catalysis Collaboratory for Light-activated Earth Abundant Reagents (C-CLEAR), which is supported by the National Science Foundation (NSF) and the Environmental Protection Agency through the Networks for Sustainable Molecular Design and Synthesis (CHE-1339674) at Colorado State University, Fort Collins. Spencer H. Johnson acknowledges the Colorado Chapter of the ARCS Foundation for their continued support.

Chapter 5 contains work reproduced from the journal article *Isotopomeric Elucidation of the Mechanism of Temperature Sensitivity in ^{59}Co-NMR Molecular Thermometers* by Tyler M. Ozvat, Anthony K. Rappé, and Joseph M. Zadrozny (*Inorganic Chemistry* **2022**, *61*, 778–785). Prof. Anthony K. Rappé provided computational resources and assisted in the interpretation of computational data.

The work detailed in this chapter performed with the support of Colorado State University (CSU) and the National Institutes of Health (R21-EB027293). We wish to thank the Materials and Molecular Analysis (MMA) at CSU where all NMR experiments and standard molecular characterization were performed, which was supported by an NIH-SIG award (1S10OD021814-01) and the CSU-CORES Program. Computational resources are enabled by the Catalysis Collaboratory for Light-activated Earth

Abundant Reagent (C-CLEAR), which is supported by the National Science Foundation (NSF) and the Environmental Protection Agency through the Networks for Sustainable Molecular Design and Synthesis (CHE-1339674) at CSU.

DEDICATION

My parents Matt and Rebecca

TABLE OF CONTENTS

CHAPTER 1 – Introduction

1.1. Forward

For many chemists, the topics of nuclear magnetic resonance (NMR) spectroscopy are first encountered within their undergraduate organic chemistry courses. Ideally, it is in respective organic chemistry labs that these chemists become structural elucidation practitioners of small molecules through this spectroscopic technique. As a result, NMR spectroscopy is often framed within the context of the ^{1}H isotope of hydrogen, and this is for good reason. The ^{1}H nucleus possesses arguably the most favorable nuclear magnetic properties, while also having a 99.98% natural abundance, making it readily detectable by NMR. Without the contextual basis of the ^{1}H nucleus, the concepts and theories of NMR would certainly be challenging. However, it should be noted early on that nearly every element of the periodic table possesses at least one stable isotope with characteristic nuclear magnetic properties, and thus NMR is a spectroscopic technique that may be applied to study molecular structure of nearly any chemical system.

To understand NMR through the lens of only the ^{1}H nucleus would be to remain at "square-one" of the periodic table. For those seeking to move beyond "square-one", this chapter acts as an advanced introduction of NMR in the context of first-row transition metal nuclei. Relative to ^{1}H and other dipolar ($I = {}^{1}/_{2}$) nuclear spin systems, quadrupolar ($I > {}^{1}/_{2}$) nuclear spin systems, which describe nearly all first-row transition metals, are generally less commonly discussed in introductory course work. While basic principles of NMR still apply, additional consideration must be made for quadrupolar nuclei. In an effort to understand these consequences, great emphasis will be place on the NMR-active ^{59}Co nucleus which ultimately serves as the focal point of NMR thermometry in this dissertation. The information given in this chapter assumes that the reader is familiar with the NMR of ^{1}H. The following section begins with a brief context of nuclear spin where many comparisons are made between the well-known ^{1}H and transition metal nuclei, and later sections shift towards temperature-dependent nuclear spin properties of ^{59}Co.

1.2. Review of NMR with Transition Metal Nuclei

1.2.1. Context and Scope

The use and application of nuclear magnetic resonance (NMR) spectroscopy is limited only by the number of NMR-active nuclei on the periodic table.[1] Fortunately, nearly every element of the periodic table possesses at least one stable isotope with a nuclear magnetic moment (μ), thus almost all elements may be considered magnetic and therefore detectable by NMR. This magnetic-based spectroscopic technique readily investigates the individual hydrogen atoms in small organic molecules by probing μ of the ^{1}H isotope, for example. If the same organic molecule contains carbon, NMR may similarly probe each and every carbon atom by detecting the magnetism of the ^{13}C isotope. Many other magnetic isotopes of various elements are also encountered including nitrogen (^{15}N), oxygen (^{17}O), fluorine (^{19}F), silicon (^{29}Si), phosphorous (^{31}P), chlorine (^{35}Cl), and bromine (^{79}Br). Importantly, each of the nuclei possess characteristic magnetic properties. A key feature of this nuclear magnetism is its ability to report on its local molecular structure, such as the identity, number, and relative positions of the neighboring atoms, as well as the nature of the bonds holding them together. Thus, NMR spectroscopy is a premier structural investigation technique providing critical insight to the local environment of atoms that form complex molecules.

To a synthetic inorganic chemist, NMR finds its use by probing the structure of ligands for metal-centered coordination complexes, yet less attention is generally given to the metal-center itself. Generally, this is due to a range of complicating factors introduced by the metal-center and makes metal-targeted NMR challenging. The extent of these challenges is divided according to *1)* the nuclear magnetic properties of the metal nucleus, and *2)* the molecular properties (i.e., physical and chemical) of the coordination complex. First and foremost, a nucleus must be sufficiently NMR-active, and this is governed by a variety of compounding factors such as nuclear spin properties and natural abundance. Yet, while a particular metal may possess an NMR-active nucleus, the molecular properties of the complex may render NMR unsuitable. Metal-ion oxidation state and coordination geometry may produce a paramagnetic species by the presence of one or more unpaired electrons. The presence of an open-shell species complicates the NMR measurements as the unpaired electron possesses its own magnetic moment and interferes with the *nuclear*

magnetic moment at the nucleus. The relative strength of the electronic magnetic moment contextualizes this obstacle, as it exceeds that of the ^{1}H nucleus by 660 times.[2] Despite these challenges, there are several cases in which the nuclear magnetic properties are sufficient, *and* the molecular properties of the coordination complex provide few to no barriers to informing on a transition-metal nucleus. One of the most readily measured transition metal nuclei by NMR is cobalt-59 when it forms Co^{3+} octahedrally coordinated complexes. Reasons for this will be introduced in later parts of this introduction and demonstrated in later chapters.

1.2.2. Nuclear Spin

The origins of nuclear magnetic moment μ in a given nucleus arise from an uneven number of protons and/or neutrons within the nucleus. Regarding ^{1}H and many other smaller NMR-active nuclei (e.g., ^{13}C, ^{15}N, ^{17}O, ^{19}F, ^{29}Si, ^{31}P, etc.), it is the presence of either a singly unpaired number of neutrons or protons that leads to the nucleus bearing a nuclear spin value of $I = {}^{1}/_{2}$. For each additional unpaired neutron or proton, the value of I increases by ${}^{1}/_{2}$ and is often the case for transition metals. Importantly, μ is required for a nucleus to be observed by NMR spectroscopy and a nucleus bearing a magnetic moment may simply be considered NMR-active. The magnitudes of μ are unique to each NMR-active nucleus where, for example, ^{1}H possesses $\mu = 2.79\ \mu_N$ and ^{59}Co possesses $\mu = 4.62\ \mu_N$.[3] The nuclear spin quantum number (I) plays an important role in determining the value of μ. It is proportional to I through the gyromagnetic ratio (γ) of a given nucleus (i.e., $\mu = \gamma I$). Thus, a nucleus may only interact with an applied magnetic field (see next section) when $I > 0$, while a nucleus with $I = 0$ does not exhibit a nuclear magnetic moment. Regarding the transition metals, each element of the first row possesses at least one NMR-active nucleus. Values of nuclear spin range from $I = {}^{1}/_{2}$ (^{57}Fe) to $I = {}^{7}/_{2}$ (^{45}Sc, ^{49}Ti, ^{51}V, and ^{59}Co) (*Figure 1.1*). Of the transition metals, only ^{57}Fe possesses a ${}^{1}/_{2}$-spin system akin to ^{1}H, while all other isotopes of the series bear larger nuclear spin values. While nuclear spin of $I > 0$ illustrates that a nucleus is NMR-active, other factors determine whether it is easily observed or measured by NMR.[4] These factors include the intrinsic value of γ where larger values make a nucleus readily detectible since it determines both μ and frequency (ν).

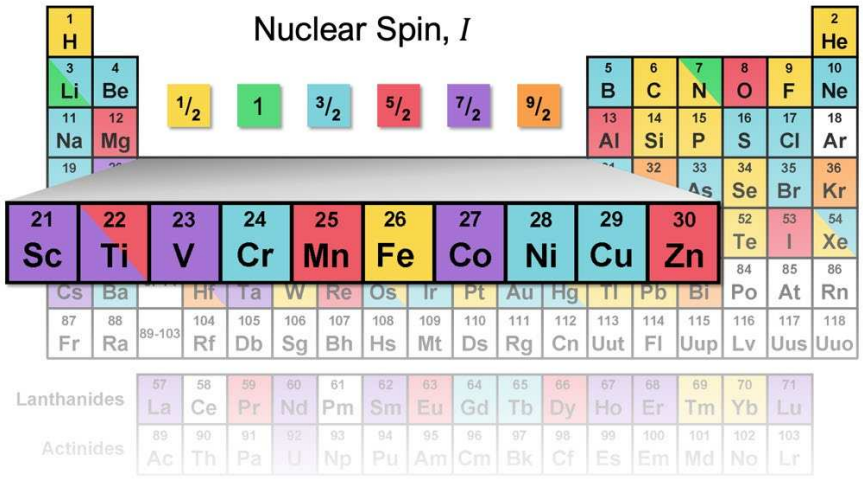

Figure 1.1. Nuclear spin values (I) of the various elements on the periodic table. The series of first-row transition metals are emphasized to show their NMR-active nuclei.

Lastly, and perhaps of most practical necessity, is the natural abundance of a given NMR-active isotope. Large natural abundances lend a nucleus greater detectability and reduces the need for long NMR experiments. A list of properties for the first-row transition metals is compared to ^{1}H below (Table.1.1). Categorically, nuclei that possess $I = {}^{1}/_{2}$ are defined as dipolar while nuclei with $I > {}^{1}/_{2}$ are quadrupolar. The two terms refer to the distribution of charge about the center of the nucleus where the distribution of a dipolar nucleus occurs spherically, and that of a quadrupolar nucleus can occur non-spherically.[5] Physical interpretations of quadrupolar nuclei quickly shift beyond the scope of applied chemistry and will not be reviewed here, however, many literature reviews on their application in NMR can be found elsewhere.[6–8]

Table 1.1. Tabulated values of nuclear magnetic spin properties for comparison between ^{1}H and transition metal nuclei. Negative values of γ signify its direction against its nuclear spin.

Nucleus	Nuclear Spin I	Gyromagnetic Ratio γ (10^7 T^{-1}s^{-1})	Frequency at 11.74 T ν (MHz)	Natrual Abundance %	Nucleus	Nuclear Spin I	Gyromagnetic Ratio γ (10^7 T^{-1}s^{-1})	Frequency at 11.74 T ν (MHz)	Natrual Abundance %
^{1}H	$^{1}/_{2}$	26.75	500.00	99.89					
^{45}Sc	$^{7}/_{2}$	6.50	121.47	100.0	^{57}Fe	$^{1}/_{2}$	0.87	16.16	2.12
^{47}Ti	$^{5}/_{2}$	–1.51	28.18	7.44	^{59}Co	$^{7}/_{2}$	6.32	118.07	100.0
^{49}Ti	$^{7}/_{2}$	–1.51	28.19	5.41	^{61}Ni	$^{3}/_{2}$	–2.39	44.68	1.14
^{51}V	$^{7}/_{2}$	7.05	131.44	99.75	^{63}Cu	$^{3}/_{2}$	7.10	132.53	69.15
^{53}Cr	$^{3}/_{2}$	–1.51	28.26	9.50	^{65}Cu	$^{3}/_{2}$	7.60	141.97	30.85
^{55}Mn	$^{5}/_{2}$	6.61	123.32	100.0	^{67}Zn	$^{5}/_{2}$	1.68	31.27	4.10

1.2.3. Nuclear Magnetic Interactions

The exact number of allowed spin states of μ are determined by the angular momentum quantum number (m) of the nuclear spin such that for a $^1/_2$-spin system, $I = {}^1/_2$ and $m_I = \pm{}^1/_2$. Here, the two allowed orientations of μ are $+{}^1/_2$ (spin-up) and $-{}^1/_2$ (spin-down) and describes the case for any dipolar nucleus. The interaction of a quadrupolar nucleus in a magnetic field is similar but with additional spin states. Compared to ^{1}H ($m_I = \pm{}^1/_2$) with *two* spin states (i.e., $\pm{}^1/_2$) in a magnetic field, the spin system of ^{59}Co ($m_I = \pm{}^7/_2$) possesses a total of *eight* spin states with four pairs of spin-up and spin-down states (i.e., $\pm{}^7/_2$, $\pm{}^5/_2$, $\pm{}^3/_2$, and $\pm{}^1/_2$). The number of individual spin states can be determined according to the value I of any NMR-active nucleus, where the number of states is determined by $2I + 1$. The differences in the interactions of dipolar and quadrupolar nuclei are best contextualized when an external magnetic field is applied to the NMR-active nucleus.

As the term implies, the nuclear magnetic moment μ of a nucleus is magnetic and may "interact" with other magnetic fields. In the absence of an applied magnetic field (B_0), spin states are degenerate and there is no preference for μ to adopt a spin orientation. It is only when an NMR-active nucleus is arranged inside B_0 that certain orientations (i.e., spin states) of μ are allowed where the sign resembles the direction of alignment with (+) or against (–) the direction of B_0 – this is what is meant by "interact" (i.e., the Zeeman interaction) (*Figure 1.2*).

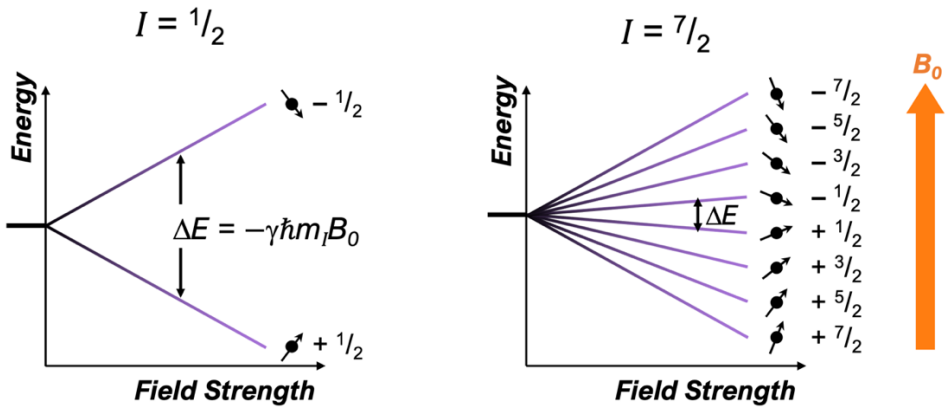

Figure 1.2. Magnetic interactions of $I = {}^1/_2$ (left) and $I = {}^7/_2$ (right) spin systems with their respective nuclear spin states m_I in a magnetic field B_0 showing the field-dependence of ΔE between two states. Spins orientations (arrows) are shown relative to the direction with (+) or against (–) B_0.

It should be noted that the strength of this interaction increases linearly such that an increasing field strength increases the energy separation between neighboring m_I spin states. The field-dependent energy difference (ΔE) between two given nuclear spin states is very low in energy, relative to other spectroscopies and typically utilized radiofrequencies ranging between 60–600 MHz. The exact value of ΔE for specific transition is determined by the difference in energy (E) between two states, where E of a given state of m_I is proportional to the strength of the applied field B_0 through its nuclear gyromagnetic ratio γ and constant value $\hbar$ (i.e., $E = -\gamma\hbar m_I B_0$). Comparison of ΔE shows the differences in energy of the $\Delta m_I = \pm 1$ NMR transition between ^{1}H and other transition metals. In an applied field of 11.74 T, the energy of the NMR transition of ^{1}H is 0.0167 cm^{-1} (500 MHz) while the highest energy transition of the first-row metals is for ^{65}Cu at 0.0047 cm^{-1} (141.97 MHz). The stark differences in energies of the NMR transition reflect the different gyromagnetic ratios of each nucleus. As an added point of context, the energies of these nuclear magnetic transitions pale in comparison to other spectroscopic transitions such as in UV/vis spectrophotometry. The electronic transitions of some cobalt complexes commonly occur within a range of 32,000 and 16,000 cm^{-1}, respectively.[9]

It should be noted that the resonance frequencies listed above (*see Table 1.2.1*) are the precise energy difference of a central NMR transition for the respective molecular standard at 0 ppm. For example, the 500 MHz resonance frequency, which corresponds to a 0.0167 cm^{-1} $\Delta m_I = \pm 1$ NMR transition, is specific for the protons of tetramethylsilane (the 0-ppm standard for ^{1}H-NMR), and not all ^{1}H nuclei exhibit the exact same transition energy. In fact, when the same nucleus is placed in different structural and chemical environments, the transition energies are slightly increased or decreased by only a fraction of the total transition energy between two neighboring spin states. For the ^{1}H nucleus at 11.74 T, typical chemically induced changes in the 0.0167 cm^{-1} NMR transition are meager, occurring over a 2×10^{-7} cm^{-1} energy range. These variations are small and more often understood in terms of frequency (Hz) where the resonance frequency of the ^{1}H transition occurs at 500 MHz at 11.74 T, and the chemically induced changes of the nucleus reflect a 6,000 Hz shift from the 500 MHz. Compared to the ^{59}Co nucleus in the same magnetic field (118.67 MHz), much larger changes in the energy of the central transition can occur by over

1.53 MHz, roughly 307 times more than change in ^{1}H. Ultimately, this is a primary strategy for inferring molecular structure via NMR, where minute or vast differences in resonance frequencies are caused by the chemical environment of the nucleus – referred to as "*chemical shift*" (δ). And while NMR is a technique that probes the atomic nucleus, the range over which the transition energies change is a governed by the behavior of the accompanying electrons, described in the following section.

1.2.4. Nuclear Shielding and Chemical Shift Range

Recalling that the magnetic interaction of μ is proportional to the strength of B_0, the presence of either core or valence electrons can change the strength of the external field at the electron-bearing nucleus. Since electrons possess their own magnetic moments, they too experience interactions with the applied field and produce local magnetic fields. As a result, the total magnetic field at a nucleus is a sum of B_0 and the local magnetic fields produces by the electromagnetic interactions. While these modifications to the magnetic field are miniscule, they are significant enough to produce changes in how effectively the surrounding electrons shield the nucleus from B_0 – thus *nuclear shielding* (σ). For the purpose of this dissertation, two types of shielding will be considered when impacting the nucleus: diamagnetic (σ_d) and paramagnetic (σ_p) shielding, which respectively reduce and enhance B_0 (i.e., $B_{local} = B_0(1 - (\sigma_d + \sigma_p))$ where σ_p is a negative term).[10] Either reducing σ_d or increasing σ_p yields a more deshielded nucleus, thus *increasing* B_{local}. Conversely, either increasing σ_d or decreasing σ_p yields a more shielded nucleus, thus *decreasing* B_{local}. These local modifications to B_0 are ultimately reflected by the chemical shifts in a collected NMR spectrum.

The paramagnetic term is an essential consideration in metal-based NMR, and it is what sets it apart from the namely diamagnetic mechanisms of chemical shift in ^{1}H NMR. In the simplest physical terms, the impact of the diamagnetic term is set by the distance of the electrons to the nucleus where electrons that are withdrawn from the nucleus provide it less shielding. This effect is demonstrated by ^{1}H NMR when considering the impact of electron withdrawing substituents bound to a ^{1}H nucleus. For example, the ^{1}H nucleus become more deshielded from CH_2Cl_2, (5.97 ppm) to $CHCl_3$ (7.26 ppm) with the addition of the

electron withdrawing chloro group. On the other hand, the paramagnetic term is most simplistically concerned with the electronic excitation energy (ΔE) between molecular orbitals of a molecule, where the magnitude of σ_p is inversely proportional to ΔE of the transition between the ground and excited state. In order for a nucleus to exhibit high paramagnetic shielding, the nucleus must generally participate in bonding that yields the lowest energy difference between the frontier molecular orbitals. The relationship between electronic structure and chemical shielding is well-described among octahedrally coordinated Co^{3+} complexes and is detailed later on.

Those familiar with ^1H NMR know that the typical range of chemical shifts of small organic molecules occurs over a 12-ppm window. However, NMR-active transition metal nuclei exhibit chemical shift ranges many orders of magnitudes beyond the ^1H nucleus (*Figure 1.3*).[11]

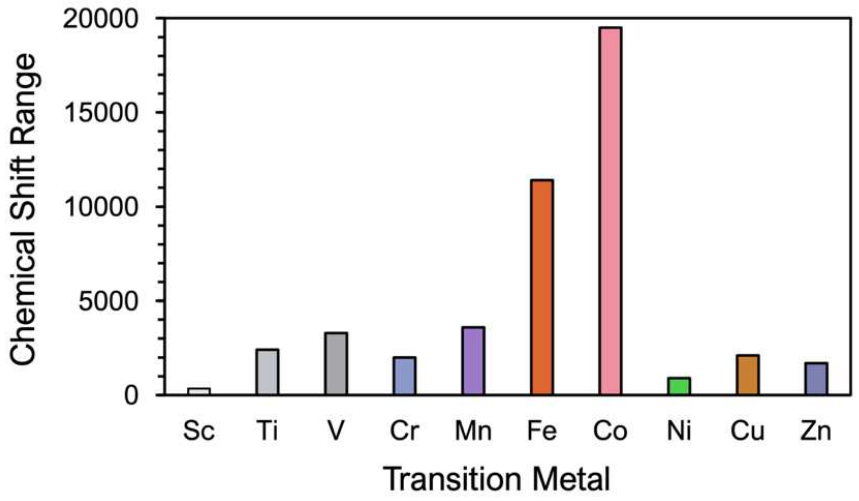

Figure 1.3. Known chemical shift ranges of the first-row transition metals ranging from less than 1,000 ppm to roughly 20,000 ppm.

The various chemical shift ranges of the metal series are as small as 350-ppm and 900-ppm wide for Sc and Ni, respectively. Conversely, the largest chemical shift ranges occur at near 11,5000-ppm and 20,000-ppm wide for Fe and Co, respectively.[11,12] For now, it should be understood that considerations of both diamagnetic and paramagnetic terms ultimately summarize the total chemical shift range of a given NMR-active nucleus. The shift range of ^1H is purely a feature of the diamagnetic shielding through changes in the electron-withdrawing or donating properties of molecular substituents. NMR-active nucleui with larger

shift ranges arise due to paramagnetic shielding. Thus a large chemical shift range is attributed to a high degree of paramagnetic shielding and explains why transitions metals have some of the largest chemical shift ranges on the period table.

1.3. Chemical Shift of Cobalt-59

1.3.1. A Brief Historical Context

Our modern understanding of chemical shift (δ) in nuclear magnetic resonance spectroscopy can be tied back to some of the first ^{59}Co-NMR studies from the 1950's.[9,13] As it is now known, the term *"chemical shift"* generally describes the variation in resonance frequency of a given nucleus due to differing chemical environments. However, this understanding would not take shape until large differences in *expected* resonance frequencies were observed by W. D. Knight for many nuclei.[14] For instance, one of the first reports of chemical shift was by ^{14}N NMR and showed an approximate 300 ppm difference in resonance frequency between NH_4^+ and NO_3^- salts.[15] Here it was remarked, and first addressed, that the large shift in resonance frequency of the ^{14}N nucleus may dependent upon its molecular structure. Soon after, large differences in the resonance frequencies of first-row transition metal nuclei were also reported including the ^{59}Co nucleus by Proctor & Yu.[13] It was this landmark study that reported the largest chemical shift for a single nucleus at 13,000 ppm between $Co(acac)_3$ and $K_3[Co(CN)_6]$. Here, it was also discovered that the ^{59}Co chemical shift was remarkably sensitive to temperature unlike the temperature-driven chemical shifts of other known nuclei.

Relationships between molecular structure and chemical shift were quickly established for the ^{59}Co nucleus. In a publication by Freeman et al.,[9] a series of low-spin Co^{3+} octahedrally coordinated complexes were studied to investigate the dependence of ^{59}Co-NMR chemical shift on their electronic absorption energies. Later, Griffith and Orgel[16] would explain the relationship between electronic transition energies and paramagnetic shielding through application of Ramsey's theory of chemical shifts. As a result, it is now understood that low-energy electronic transitions are intimately tied to paramagnetic shielding in low-spin Co^{3+} complexes via Ramsey's equation (see *Section 1.3.2*). Hence, cobalt-59 holds a unique place in the

history of NMR and is responsible for developing our modern understanding of chemical shift in transition-metal nuclei.

1.3.2. The Relation Between Chemical Shift and Electronic Structure

One of the most remarkable features of the ^{59}Co nucleus is the total span of its chemical shift range over 20,000 ppm.[17] This includes chemical shifts of complexes at various oxidation states and coordination geometries. However, the most commonly reported ^{59}Co-NMR data are for octahedrally coordinated complexes of low-spin d^6 systems. These octahedral complexes include $[Co(CN)_6]^{3-}$, $[Co(en)_3]^{3+}$, $[Co(NO_2)_6]^{3-}$, $Co(acac)_3$, and $[Co(ox)_3]^{3-}$ with various donor atom and ligands, for example. Among these complexes, the value of $\delta(^{59}Co)$ is quite different for each Co^{3+} species. The variation in chemical shift is related to the energy difference between the octahedrally split *3d* orbitals such that a 100 cm^{-1} change in ligand field roughly corresponds to an 80-ppm shift (*Figure 1.4*).

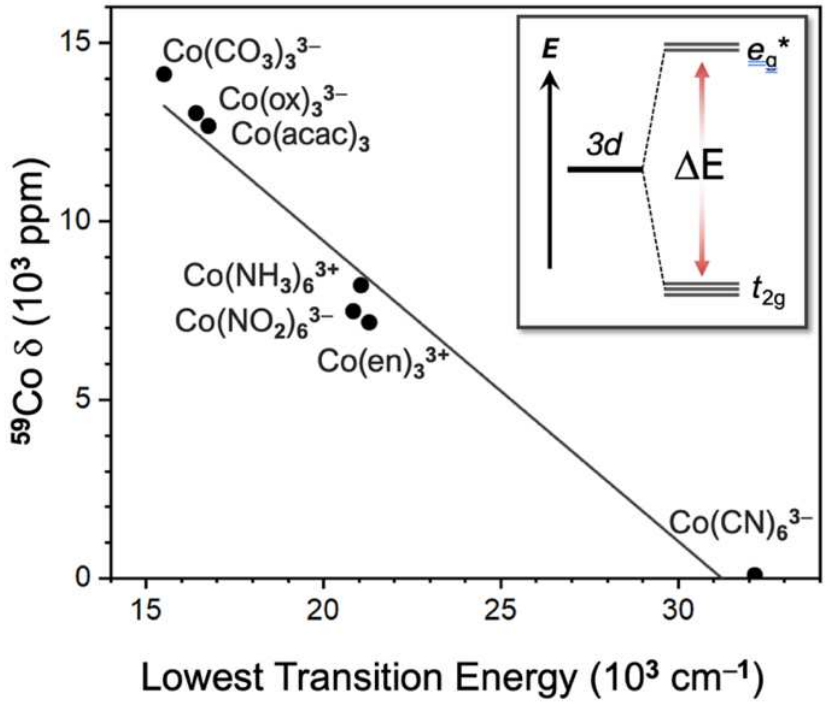

Figure 1.4. ^{59}Co chemical shift δ, as a function of lowest transition energy ΔE for various low-spin $3d^6$ octahedral complexes. The inset shows ΔE of the *d*-orbital splitting between t_{2g} and e_g* orbital sets.

It is shown that complexes with strong ligand field strengths exhibit smaller $\delta(^{59}\text{Co})$ values and the opposite is true for weak ligand field complexes. The chemical shift reference standard $K_3[Co(CN)_6]$ (0 ppm) is an example of the ^{59}Co nucleus in a strong ligand field where the lowest energy excitation is ~32,000 cm^{-1}.[9,18] In contrast, the weak ligand field complex $Co(acac)_3$ (13,000 ppm) shows its lowest-energy excitation at ~16,000 cm^{-1}. The inverse dependence of $\delta(^{59}\text{Co})$ on ligand field is demonstrated for other structurally similar cobalt complexes. Between these two complexes, the ^{59}Co nucleus in weak ligand field complexes is extremely deshielded compared to strong ligand fields. Evaluation of ligand field strength Δ_o, can be deduced from electronic excitation energies where transitions between the t_{2g} and e_g* sets is separated by some energy difference, ΔE. Thus, ΔE is related to Δ_o, and changes in molecular structure and ligand identity affect ΔE. The differences in $\delta(^{59}\text{Co})$ for various complexes can be explained through Ramsey's shielding equation which provides theoretical interpretation of chemical shift in terms of σ_d and σ_p according to the ground-state molecular wave function:

$$\sigma = \frac{e^2}{2mc^2}\left\langle\psi_0\left|\frac{x^2+y^2}{r^3}\right|\psi_0\right\rangle - \left(\frac{e^2}{2mc^2}\right)^2 \sum_n \left\{\frac{\langle\psi_0|\hat{L}|\psi_n\rangle\left\langle\psi_n\left|\frac{2\hat{L}}{r^3}\right|\psi_0\right\rangle}{E_n - E_0} + \frac{\left\langle\psi_0\left|\frac{2\hat{L}}{r^3}\right|\psi_n\right\rangle\langle\psi_n|\hat{L}|\psi_0\rangle}{E_n - E_0}\right\}$$

σ_d *(diamagnetic term)* σ_p *(paramagnetic term)*

The full illustration of Ramsey's equation is provided to contextualize the two shielding terms and the complete evaluation can be found in several textbooks or reviews on chemical shift. Its significance in this dissertation is *1)* the paramagnetic term shows a dependence of both the ground (Ψ_0) *and* excited (Ψ_n) state wavefunctions where the sum of the energy difference ($\Delta E = E_n - E_0$) of all electronic excited states are considered, and *2)* the diamagnetic term is strictly dependent on (Ψ_0), and independent of ΔE. While Ramsey's equation is concerned with the average value of ΔE, the paramagnetic term is readily simplified knowing *only* the energy of the lowest excited state in place of the average electronic transition energy.[17] Hence, the source of large deshielding in weak ligand field complexes comes from a greater paramagnetic contribution; the extent of which is reflected by low values of ΔE. The paramagnetic term of Ramsey's

equation defines the order of dependence such that ΔE drives σ_p, which then determines $\delta(^{59}\text{Co})$. The proportionality of this relationship is emphasized below:

$$\sigma_p \propto \frac{1}{\Delta E}$$

Since ΔE is not a factor in the diamagnetic term, its contribution to $\delta(^{59}\text{Co})$ is negligible, regardless of ligand field strength. It has been approximated that roughly 84% of the diamagnetic shielding of the ^{59}Co nucleus stems from the first and second shell of core electrons.[19] Thus, large variation in $\delta(^{59}\text{Co})$ is due to is driven by electronic excitations of the valence electrons of the frontier orbitals.[2,18,19]

1.3.3. Synthetic Control of Nuclear Spin

The application of the spectrochemical series to a Co^{3+} ion exemplifies the simplest means of synthetic control of $\delta(^{59}\text{Co})$, where strong and weak field ligands produce lesser and greater deshielding via the paramagnetic term, respectively. To this affect, octahedrally coordinated donor atoms decrease the shielding of the metal-ion nucleus from C < N < O. Even for the same set of donor atoms, changes in the ligand identity and structure produce large changes in $\delta(^{59}\text{Co})$. The expected consequences of chelation, for example, are nicely illustrated for $Co–N_6$ octahedral geometries in which the denticity of N-donor atoms increase from mono, bi, and hexadentate ligands. Respectively, from $[Co(NH_3)_6]^{3+}$, $[Co(en)_3]^{3+}$, and $[Co(diNOsar)]^{3+}$, the $\delta(^{59}\text{Co})$ decrease from 8171, 7154, and 6894 ppm.[20] Intriguingly, the difference in $\delta(^{59}\text{Co})$ between the mono and hexadentate complexes reaches nearly 1300 ppm for the same donor-atoms. Relative to the chemical shift ranges of other paramagnetic-shifted nuclei, this is still a considerable effect on the ^{59}Co nucleus and exemplifies its potential for highly controllable nuclear spin properties. Ultimately, these properties can be utilized to understand the subtle impacts of physical and chemical environmental factors through molecular structure.

By designing the molecular shell that shuttles and induces changes to this nuclear sensor, it is possible to address a vast range of sensing applications by tailoring the coordinated atoms, ligands, and functional groups. In this case, molecular design strategies include virtually any aspect of synthetic control

in the ligand. To name of few of these controllable parameters are donor atom variety, ligand bonding, ligand denticity or chelation, ligand rigidity, functionalization, solubility, charge, counterion, etc. Each aspect of synesthetic control is a route to testing the response of the ^{59}Co nucleus to its ligand environment. While the response to the ligand is informative via $\delta(^{59}\text{Co})$, it is ultimately a goal to understand how the *change* in $\delta(^{59}\text{Co})$ is mediated through the *change* in molecular structure to some external or environmental factor. In order to detect temperature, for example, the ^{59}Co nucleus must be receptive to a thermally driven alterations of the molecule, and it is by consequence of a dynamic structure that the metal nucleus may inform on its environment beyond the ligand shell. These dynamics may include changes to the primary coordination geometry or molecular symmetry, both known to have large consequences to the nuclear spin properties of ^{59}Co.

1.4. NMR Thermometry

1.4.1. Motivation for Nuclear Spin-Based Probes

The use of magnetic resonance imaging (MRI) for biomedical diagnosis is one of the most powerful applications of nuclear magnetic resonance. The principles of NMR lend themselves as a platform for non-invasive and non-ionizing imaging techniques for the detection of inner-anatomical diseases and ailments throughout the body. Despite these capabilities, an abundance of local environmental and chemical factors is not informed by current MRI methods such as, for example, internal or local temperatures, biologically relevant ranges of acidity, and identity or differentiation of free radicals. The detection of these properties outside biologically relevant ranges generally occurs within a rather small window, and detection of these small changes requires highly sensitive designable molecular spin-based probes. The nuclear spin properties of the ^{59}Co nucleus are highly sensitive to local chemical environments and hold high potential to be designed into molecular sensors for many chemical sensing potential applications. Designing said ^{59}Co-based nuclear spin sensors would chart novel chemical sensing agents while also encouraging nuclear spin detection through other nuclear spin systems that would otherwise remain outside the capabilities of current MRI-based diagnostic tools.

It is asserted here that the ^{59}Co nucleus is the ultimate node of response and detection to minute changes in local environment. The sensitivity of the nucleus to structure is defined by its inherent nuclear magnetic properties and defines the extent to which the nucleus may act as a useful NMR thermometer. The ^{59}Co nucleus is one of the most favorable nuclear platforms ($I = {}^{7}/_{2}$, $\mu = 4.62\ \mu_N$, 100% abundance) for designing highly sensitive spin-based molecular probes for implantation as a magnetic resonance-based temperature sensing agent. The most notable nuclear magnetic properties are its large nuclear spin value of $I = {}^{7}/_{2}$ playing a role in determining the strength of its nuclear magnetic moment $\mu = 4.62\ \mu_N$, and this, in turn, influences its interaction with an applied magnetic field. Another factor that makes the study of this nucleus favorable is its gyromagnetic ratio (γ) which directly impacts it detectability by NMR. While this value is small relative to other nuclei, (i.e., ^{1}H) it is large enough to allow the study of this nucleus around radiofrequencies of 118–119 MHz. The nucleus is also made readily detectable due to its 100% natural abundance. In tandem with its physical and chemical tunability via synthetic control, these nuclear properties deem the ^{59}Co nucleus a platform for enabling highly sensitive nuclear spin-based probes.

Demonstrated by its large chemical shift range (20,000 ppm), the exceptional relationship between molecular geometry and electronic structure may be detected by ^{59}Co NMR. Thus, temperature-driven variations in the structure of a single cobalt complex are readily elucidated by $\delta(^{59}\text{Co})$ and may be implemented as a mechanism for chemical shift imaging. However, realization of the proposed applications is currently lacking and the extent to which changes in $\delta(^{59}\text{Co})$ occur are unknown for a given molecular system until studied by variable-temperature ^{59}Co NMR. More specifically, the exact molecular design parameters of low-spin octahedral Co^{3+} complexes which yield high thermometry is unknown. This dearth of knowledge bestows motivation to develop fundamental and synthetic design principles that achieve highly temperature-responsive molecular systems.

1.4.2. Thermometry in Cobalt-59 Complexes

The ^{59}Co nucleus has two methods of thermometry at its immediate disposal which are temperature-driven changes in its chemical shift and relaxation dynamics. Firstly, chemical shift thermometry is a

mechanism which operates by observing the *change* in chemical shift ($\Delta\delta$) of the target nucleus in a given molecule at different temperatures. The range over which the chemical shift changes provides a metric to quantitatively evaluating the sensitivity of an NMR molecular thermometer. The temperature coefficient may be expressed linearly by simply considering $\Delta\delta$ with respects to the change in temperature (ΔT), thus a coefficient of temperature sensitivity is represented by $\Delta\delta/\Delta T$ in units of ppm/°C. The second method of NMR thermometry is via spin relaxation, which includes spin-lattice T_1 and spin-spin T_2 relaxation times. Both forms of spin dynamics are time-dependent properties of the nuclear magnetic moment and changes in relaxation times (ΔT_1 or ΔT_2) inform on interactions with the local environment of the nucleus. Similar to the linear $\Delta\delta/\Delta T$ expression for chemical shift thermometry, ΔT_1 or ΔT_2 can be expressed by a change in temperature for thermally driven relaxation coefficients defined by $\Delta T_1/\Delta T$ or $\Delta T_2/\Delta T$ in units of s/°C. When applied to the study of a cobalt complex, both forms of thermometry may be evaluated via similar ^{59}Co-NMR experiments, where the *position* and *width* are the primary features of an NMR peak that illustrate the changes in chemical shift and relaxation times, respectively.

Between the two features of nuclear magnetism that may act as platforms of thermometry, cobalt complexes provide a clear illustration of the unique temperature-dependent properties that can arise from the same NMR-active nucleus composed in different molecules. For the few complexes which the temperature-dependence of $\delta(^{59}\text{Co})$ is known, values of $\Delta\delta/\Delta T$ range between 1.50 and 3.15 ppm/°C, corresponding to the strong-field $K_3[Co(CN)_6]$ and weak-field $Co(acac)_3$ coordination complexes. In these systems, the result of increased temperature on chemical shift pushes $\delta(^{59}\text{Co})$ downfield to higher frequencies. In similar complexes, the shape of the linewidth also becomes more sharpened with the increase in temperature, reflecting longer T_1 times for the ^{59}Co nucleus. Even simple comparisons of T_1 at 25 °C for $K_3[Co(CN)_6]$ (T_1 = 120 ms) and $Co(acac)_3$ (T_1 = 1.78 ms) show that this spin property varies drastically with its molecular structure at the same temperature. These two complexes were the subject of Levy et al. who insinuated the use of ^{59}Co as a highly sensitive NMR thermometer.[21] Their work is an important demonstration of how crucial molecular structure is to temperature-dependent nuclear spin properties. Hence, the molecular structure of the low-spin octahedral cobalt system holds immense potential

for designing highly sensitive NMR thermometric probes. Yet, the rationalization of designable molecular features has yet to be defined.

1.4.3. Temperature-dependent Chemical Shift

The use of ^{59}Co-containing complexes as NMR chemical-shift thermometers was first suggested by comparing the temperature sensitivities in $\delta(^{59}\text{Co})$ for $K_3[Co(CN)_6]$ and $Co(acac)_3$.[21] Variable temperature ^{59}Co NMR was employed to determine that values of $\Delta\delta/\Delta T$ were quite different, where $\Delta\delta/\Delta T$ for $Co(acac)_3$ (3.15 ppm/°C) is more than twice as large as $K_3[Co(CN)_6]$ (1.50 ppm/°C). Since this report, the fundamental question remains: *what molecular features control ^{59}Co $\Delta\delta/\Delta T$ in these low-spin octahedral complexes?* Regarding the study of the ^{51}V chemical shift, it has been surmised by Jameson et al. that $\Delta\delta/\Delta T$ stems from the changes in the primary coordination sphere, namely changes in the metal-ligand bond lengths of the NMR-active nucleus.[22,23] Thus, the structural mechanism for thermometry in these systems is expected to operate by the slight changes in the primary coordination sphere of the molecule such as the Co–L bonds (*Figure 1.5*).

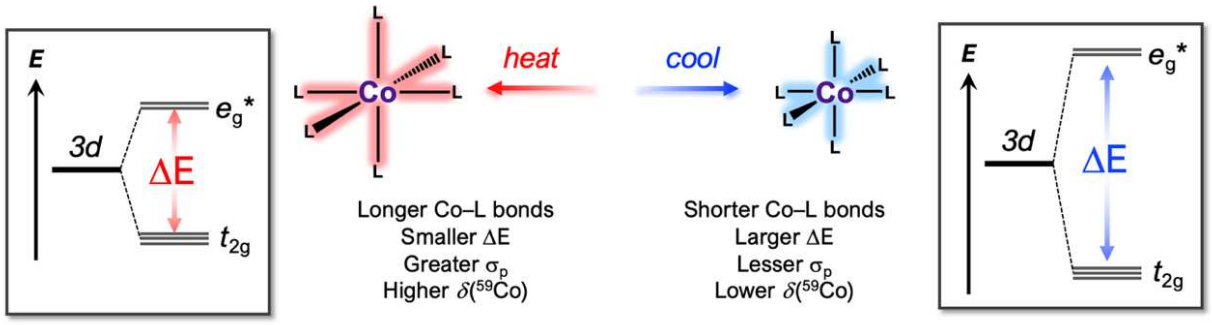

Figure 1.5. Representation of the structural mechanism that impacts temperature sensitivity in $\delta(^{59}\text{Co})$. The temperature-driven structure, drives change in electronic structure, impacts the nuclear paramagnetic shielding, and finally leads to a change in $\delta(^{59}\text{Co})$.

The interpretation of this physical mechanism lies in the driving force for changes in chemical shift, and the primary factor that defines it in cobalt complexes, i.e., the variation in the paramagnetic shielding σ_p. Any changes occurring by the expansion of Co–L_6 bond lengths have a direct consequence on the ligand field strength (Δ_o) which is the primary factor for determining σ_p, which are inversely related to one another.

Thermally driven expansion of the Co–L_6 coordination sphere leads to weaker Δ_o, lowering ΔE between octahedrally split *3d* orbitals, and contributing larger paramagnetic shielding to the total shielding term ($\sigma = \sigma_d + \sigma_p$). Recall that the paramagnetic term is negative and dominates the shielding term such that larger paramagnetic contributions yield a more deshielded nucleus.

Conversely, contraction of the Co–L_6 primary coordination sphere leads to stronger Δ_o, increasing ΔE, and reducing the paramagnetic contributions to the ^{59}Co nucleus, yielding a more shielded nucleus. In summary, these series of properties explain the linkage between molecular structure, electronic structure, nuclear shielding, and finally nuclear resonance. It also accounts for the increase in $\delta(^{59}\text{Co})$ with increasing temperature for every low-spin Co^{3+} complex measured to date. However, the extent to which $\delta(^{59}\text{Co})$ increases with temperature (i.e., positive values of $\Delta\delta/\Delta T$) becomes more complex for multidentate chelated structures. The aforementioned mechanism is simplistic and does not justify $\Delta\delta/\Delta T$ in more complex molecules. While an established relationship between $\delta(^{59}\text{Co})$ v. Δ_o is useful for interpreting the effects of molecular structure on the ^{59}Co nucleus, it does not account for trends in $\Delta\delta/\Delta T$ v. Δ_o. This point is not illustrated for $K_3[Co(CN)_6]$ and $Co(acac)_3$, where at first glance, one may interpret the vast differences in Δ_o between the two complexes (approximately 16,000 and 32,000 cm^{-1}, respectively) as a means for designing $\Delta\delta/\Delta T$ such that a highly temperature sensitive complex requires a weal ligand field. While the correlation between these two cases may be compelling, the value of Δ_o itself if not a decisive design parameter, however, it is more appropriately the *change* in Δ_o (i.e., change in ΔE) that would impart trends in $\Delta\delta/\Delta T$. This realization is made by revisiting the electronic excitation origin of $\delta(^{59}\text{Co})$. Knowing the inverse dependence of σ_p on ΔE, it can be posited that ultimately the variation in σ_p is governed by the variation in ΔE for a given complex, and it is a thermally driven variation in ΔE that yields a complex the largest $\Delta\delta/\Delta T$.

In this light, variation in bond lengths of the primary coordination sphere that arise from vibrational modes are large contributors to $\Delta\delta/\Delta T$. Vibrational modes are ultimately a governing factor of thermal dependence for a molecular structure that influences the variation in ΔE. Again, regarding low-spin d^6 octahedrally coordinated systems, it is through this ΔE energy gap of the t_{2g} and e_g* sets that the thermal

dependence of vibrational modes may govern $\Delta\delta/\Delta T$. Importantly, not all vibrations are expected to contribute to the variation in ΔE equally, and thus, the type and energy of a given vibrational mode may impact $\Delta\delta/\Delta T$ differently. Firstly, symmetric vibrations that facilitate stretching along the metal-ligand bonds are critical for influencing ΔE, the analog to ligand field strength. Secondly, low-energy vibrational modes are highly populated relative to high-energy modes, thus dictating how vibrations contribute to molecular structure. A vibrational mechanism of $\Delta\delta/\Delta T$ for ^{59}Co complexes is given in Chapter 5. It should be reemphasized that consideration of ΔE is namely important for determining $\delta(^{59}\text{Co})$ but not precisely the temperature sensitivity $\delta(^{59}\text{Co})$, where the change in ΔE is a more important consideration, and a feature unique to the ligand or given molecular structure.

1.4.4. Nuclear Spin Dynamics

By virtue of its quadrupolar nucleus, ^{59}Co ($I = {}^{7}/_{2}$) is predisposed to be an extraordinary probe of molecular structure through symmetry. Quadrupolar nuclei possess an intrinsic property known as the electric quadrupole moment (Q) not exemplified by ^{1}H or any $^{1}/_{2}$-spin system. In addition to μ, the electric quadrupole moment provides a unique probe of local structure from its surrounding environment as it interacts with the local electric field gradient (EFG). It is the EFG that can change according to molecular structure and symmetry. For example, highly symmetric environments produce small field gradients while asymmetric environments produce large ones. Considering symmetry is particularly important to the study of transition-metal ions by NMR as the interaction of Q and the EFG reflects slight alterations such as the coordination geometry about a quadrupolar metal center.[24,25] Physical interpretations of quadrupolar nuclei quickly shift beyond the scope of applied chemistry and will not be reviewed here, however, many literature reviews on their application in NMR are provide here.[5–7]

The largest implication of a quadrupolar nucleus is its impact on the relaxation dynamics of the nuclear spin. These dynamics include the spin-lattice (T_1) and spin-spin (T_2) relaxation which are time-dependent properties of magnetization of the nuclear spin in a certain direction to B_0. For example, nuclear

spin can be magnetized in alignment with B_0 using radiofrequency-based pulse sequences.[10,26] The basic application of a T_1 experiment is detailed below (*Figure 1.6*).

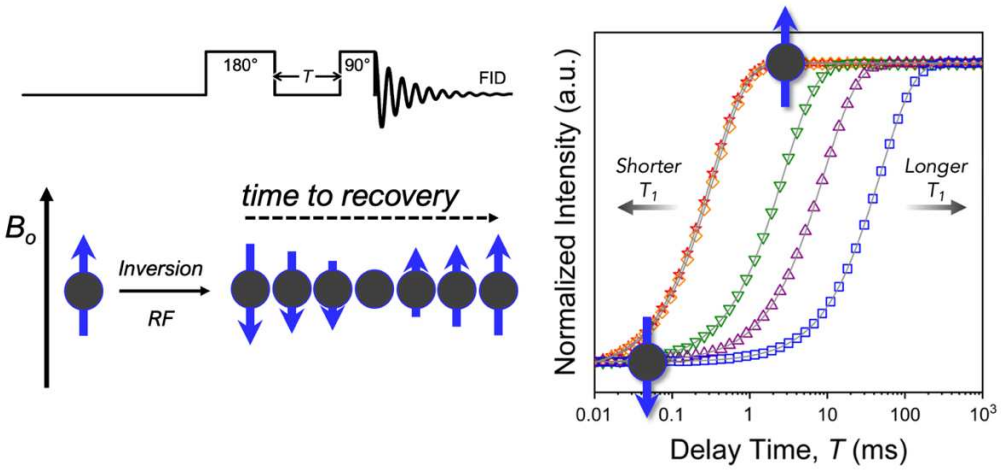

Figure 1.6. *Top Left:* Inversion-recovery NMR pulse sequence experiment. *Left:* Basics of nuclear spin behavior in an applied magnetic field (B_0) where inversion (alignment against the field) via radiofrequencies is achieve at the 180° pulse of the sequence. Relaxation describes the time for the nuclear spin magnetization to recover by realigning with B_0. *Right:* Example T_1 data that show relaxation curves of a nucleus.

Importantly, these time-dependent properties in quadrupolar nuclei are highly diagnostic of the molecular structure as they are dictated by the symmetry of a given structure. As has been shown in many ^{59}Co complexes, values of T_1 are primarily attributed to the interaction between Q and EFG, termed the "electric quadrupolar coupling interaction" or more simply "quadrupolar relaxation". Larger quadrupolar relaxation in a molecule is fostered by greater asymmetry and produces short T_1 and T_2. Conversely, this coupling is diminished in highly symmetric complexes such as $K_3[Co(CN)_6]$ (T_1 = 103.0 ms) and $[Co(NH_3)_6]Cl_3$ (T_1 = 48.5 ms) in which these monodentate systems adopt ideal octahedral symmetries relative to less-symmetric multidentate analogues (i.e., T_1 = 91 ms for $[Co(en)_3]Cl_3$).[20,27] Regarding the temperature dependence of molecular structure, alterations in structure have a direct impact on the spin dynamics through changes in the quadrupolar coupling. As temperature drives a structure towards greater or lesser symmetric distortion, changes in the quadrupolar coupling are expected to increase and decrease, respectively. This feature of the nucleus can be used as another form of thermometry (other than chemical

shift) but is complexified by also considering the temperature-dependence of its correlations time in solution. Examples of thermally dependent spin properties are detailed in Chapter 4.

1.5. Dissertation Organization

The contents of this dissertation are based on the author's own published works during his doctoral research, which span four first-author journal articles. Each chapter details a single journal article, thus providing its own set of experiments, results, and discussions which are organized akin to journal-article style formatting. While each chapter may be thought of as a stand-alone parcel of knowledge, each contributes to the same prevailing question – how, *and ultimately why*, does molecular structure affect the temperature-dependent nuclear magnetic properties of ^{59}Co? And this is the motivating question addressed throughout this dissertation.

The four journal articles that form the basis of this dissertation are found in Chapters 2–5, and are listed here, respectively:

1. Ozvat, T.M.; Peña, M.E.; Zadrozny, J.M. Influence of Ligand Encapsulation on Cobalt-59 Chemical-Shift Thermometry. *Chem. Sci.* **2019**, *10*, 6727–6734. (DOI: 10.1039/C9SC01689A)
2. Ozvat, T.M.; Sterbinsky, G.E.; Campanella, A.J.; Rappé, A.K.; Zadrozny, J.M. EXAFS Investigation of Temperature-Driven Structure in Cobalt-59 Molecular NMR Thermometers. *Dalton Trans.* **2020**, *49*, 16380–16385. (DOI: 10.1039/D0DT01391A)
3. Ozvat, T.M.; Johnson, S.H.; Rappé, A.K.; Zadrozny, J.M. Ligand Control of ^{59}Co Nuclear Spin Relaxation Thermometry. *Magnetochemistry* **2020**, *6*, 58. (DOI: 10.3390/magnetochemistry6040058)
4. Ozvat, T.M.; Rappé, A.K.; Zadrozny, J.M. Isotopomeric Elucidation of the Mechanism of Temperature Sensitivity in ^{59}Co-NMR Molecular Thermometers. *Inorg. Chem.* **2021**, *61*, 778–785. (DOI: 10.1021/acs.inorgchem.1c03326)

1.5.1. Chapter Summaries

This first chapter serves to introduce the necessary concepts, context, and motivation for the experimental groundwork in the following chapters. Each chapter is a collection of experimental and computational methods that demonstrate the intricate and multifaceted relationship between molecular structure and nuclear magnetic properties of the ^{59}Co nucleus. Furthermore, each chapter embarks on a unique investigation of controllable and improved temperature sensitive spin-based probes. By this point, a launching point has been provided for the overarching search for structure-property relationships in highly temperature-sensitive ^{59}Co-based nuclear spin probes. For convenience, summaries of Chapters 2–5 are provided below.

Chapter 2 details the temperature-dependent chemical shift (δ) of the ^{59}Co nucleus in six cobalt coordination compounds, four of which previously had unreported temperature-dependent ^{59}Co chemical shift data. The design of this study was to investigate structurally similar complexes with slightly different coordination environments about the Co^{3+} metal ion and understand the relation of the nuclear magnetic properties of the ^{59}Co nucleus to their ligand-defining molecular structures. In this manner, reconciling molecular structure with nuclear spin would demonstrate a practical approach to achieving synthetic tunability of nuclear resonance thermometry. Thus, a series of five $Co–N_6$ octahedrally-coordinated complexes, increasing from mono, bi, tri, to hexadentate ligation, exemplified a trend in metal-ion encapsulation through inter-connective ligand structures, where the monodentate v. hexadentate ligands were the least and most encapsulated, respectively. The sixth compound in this study was of $K_3[Co(CN)_6]$, the ^{59}Co-NMR chemical shift standard (0 ppm). The effects of this encapsulation on the ^{59}Co nuclear magnetic thermometry were the focus of spectroscopic investigation, including Raman, spin-lattice relaxation T_1, and variable temperature UV/vis measurements.

Chapter 3 takes a step further in the investigation of the structure-property relationship of the ^{59}Co nucleus by direct evaluation of temperature-dependent molecular structure. Quantitation of thermometric structural properties including temperature-driven metal-ligand bond distances, in relation to their temperature-driven chemical shifts, was the key insight of this study. This investigation was primarily made

via variable temperature extended X-ray absorbance fine-structure (EXAFS) spectroscopy to examine the same series of Co^{3+} complexes from Chapter 2. Experimentally determined Co–N_6 bond distances were then utilized computationally to predict the range of deviations from octahedral to trigonal prismatic Co–N_6 geometry in each structure implying the strongly influenced nature of ^{59}Co nuclear magnetism from minute changes in coordination environment.

Chapter 4 highlights another feature of the ^{59}Co nuclear magnetism that may be harnessed for the design of highly temperature-sensitive spin-based probes, i.e., spin-relaxation dynamics. Owing to the large spin value of ^{59}Co ($I = {}^{7}/_{2}$), this study takes advantage of its exceptionally sensitive quadrupolar moment to coordination symmetry to evaluate temperature-dependent spin-lattice, T_1 and spin-spin, T_2 relaxation times. In suit, this chapter studies the spin-dynamics of the same five compounds from Chapters 2, where spin relaxation is namely driven by the coupling quadrupolar in the ^{59}Co nucleus. Quantitation of the quadrupolar coupling was determined from experimentally guided predictions of molecular structures (from Chapter 3). This study is among few to demonstrate the evaluation of quadrupolar coupling constants from solution-phase structure determinations and informs on new design parameters for temperature-dependent spin relaxation-based probes.

Chapter 5 makes an in-depth experimental and computational investigation of how slight changes in structure (by incrementally increasing mass) about the ^{59}Co nucleus have an impact on the thermal nuclear spin. The directly bound N-donor atoms bear exchangeable protons which were swapped with deuterons, and subsequently studied via variable temperature ^{59}Co NMR. It was found that differences in the temperature dependence of the ^{59}Co chemical shift were uniquely dependent on structure. Computational data sought to investigate the vibrational consequences of deuteration, since the change in mass has a direct consequence on the energies and populations of molecular vibrational states. These evaluations thoroughly demonstrated that the conflicting experimental trends in temperature dependent chemical shifts were dependent on the opposing changes in populations of Raman-specific vibrational states.

References

(1) Harris, R. K.; Mann, B. E. NMR and the Periodic Table; Academic Press, 1978.

(2) Drago, R. S. Physical Methods for Chemists, 2nd ed.; Saunders College Publishing, 1992.

(3) Stone, N. J. Table of Nuclear Magnetic Dipole and Electric Quadrupole Moments. *At. Data Nucl. Data Tables* **2005**, *90* (1), 75–176.

(4) Kaupp, M.; Bühl, M. Nuclear Magnetic Resonance (NMR) Parameters of Transition Metal Complexes: Methods and Applications. In Encyclopedia of Inorganic Chemistry; John Wiley & Sons, Ltd, 2009.

(5) Drago, R. S. "Quadrupole Moments" Physical Methods for Chemists; Saunders College Publishing, 1992.

(6) Smith, J. A. S. Nuclear Quadrupole Resonance Spectroscopy. General Principles. *J. Chem. Educ.* **1971**, *48* (1), 39.

(7) Pyykkö, P. Spectroscopic Nuclear Quadrupole Moments. *Mol. Phys.* **2001**, *99* (19), 1617–1629.

(8) Ozerov, R. P.; Vorobyev, A. A. 8 - Physical Principles of Resonance Methods in Chemistry. In Physics for Chemists; Ozerov, R. P., Vorobyev, A. A., Eds.; Elsevier: Amsterdam, 2007; pp 497–529.

(9) Freeman, R.; Murray, G. R.; Richards, R. E. Cobalt Nuclear Resonance Spectra. *Proc. R. Soc. London. Ser. A* **1957**, *242* (1231), 455–466.

(10) Hore, P. J. Nuclear Magnetic Resonance; Oxford University Press, 1995.

(11) Mason, Joan. Patterns of Nuclear Magnetic Shielding of Transition-Metal Nuclei. *Chem. Rev.* **1987**, *87* (6), 1299–1312.

(12) Kidd, R. G. Nuclear Shielding of the Transition Metals. In Annual Reports on NMR Spectroscopy; Webb, G. A., Ed.; Academic Press, 1980; Vol. 10, pp 1–79.

(13) Proctor, W. G.; Yu, F. C. On the Nuclear Magnetic Moments of Several Stable Isotopes. *Phys. Rev.* **1951**, *81* (1), 20–30.

(14) Knight, W. D. Nuclear Magnetic Resonance Shift in Metals. *Phys. Rev.* **1949**, *76* (8), 1259–1260.

(15) Proctor, W. G.; Yu, F. C. The Dependence of a Nuclear Magnetic Resonance Frequency upon Chemical Compound. *Phys. Rev.* **1950**, *77* (5), 717–717.

(16) Griffith, J. S.; Orgel, L. E. The Residual Paramagnetism and Nuclear Magnetic Resonance Spectra of Cobaltic Complexes. *Trans. Faraday Soc.* **1957**, *53*, 601.

(17) Kidd, R. G. Transition Metal NMR Spectroscopy. In The Multinuclear Approach to NMR Spectroscopy; Lambert, J. B., Riddell, F. G., Eds.; NATO ASI Series; Springer Netherlands: Dordrecht, 1983; pp 445–456.

(18) Benedek, G. B.; Englman, R.; Armstrong, J. A. Temperature and Pressure Dependence of the Co^{59} Nuclear Resonance Chemical Shift. *J. Chem. Phys.* **1963**, *39* (12), 3349–3363.

(19) Bramley, R.; Brorson, M.; Sargeson, A. M.; Schaeffer, C. E. Cobalt-59 NMR Chemical Shifts of Cobalt(III) Complexes; Correlations with Parameters Calculated from Ligand-Field Spectra. *J. Am. Chem. Soc.* **1985**, *107* (9), 2780–2787.

(20) Ozvat, T. M.; Peña, M. E.; Zadrozny, J. M. Influence of Ligand Encapsulation on Cobalt-59 Chemical-Shift Thermometry. *Chem. Sci.* **2019**, *10* (27), 6727–6734.

(21) Levy, G. C.; Terry Bailey, J.; Wright, D. A. A Sensitive NMR Thermometer for Multinuclei FT NMR. *J. Magn. Reson.* **1980**, *37* (2), 353–356.

(22) Jameson, C. J. Vibrational Analysis and Mean Bond Displacements in $M(XY)_6$ Complexes. *J. Am. Chem. Soc.* **1987**, *109* (9), 2586–2588.

(23) Jameson, C. J.; Rehder, D.; Hoch, M. Isotope and Temperature Dependence of Transition-Metal Shielding in Complexes of the Type $M(XY)_6$. *J. Am. Chem. Soc.* **1987**, *109* (9), 2589–2594.

(24) Kirby, C. W.; Puranda, C. M.; Power, W. P. Cobalt-59 Nuclear Magnetic Relaxation Studies of Aqueous Octahedral Cobalt(III) Complexes. *J. Phys. Chem.* **1996**, *100* (35), 14618–14624.

(25) Doddrell, D. M.; Bendall, M. R.; Healy, P. C.; Smith, G.; Kennard, C. H. L.; Raston, C. L.; White, A. H. ^{59}Co and ^{13}C Nuclear Spin Relaxation Studies in Solutions of Symmetric, Bidentate Cobalt(III) Complexes. On the Mechanism of ^{59}Co Spin Relaxation. Crystal Structure Determination of Tris(tropolonato)cobalt(III). *Aust. J. Chem.* **1979**, *32* (6), 1219–1230.

(26) Levitt, M. H. Spin Dynamics: Basics of Nuclear Magnetic Resonance, 2nd ed.; Wiley.

(27) Ozvat, T. M.; Johnson, S. H.; Rappé, A. K.; Zadrozny, J. M. Ligand Control of ^{59}Co Nuclear Spin Relaxation Thermometry. *Magnetochemistry* **2020**, *6* (4), 58.

CHAPTER 2 – Influence of Ligand Encapsulation on Cobalt-59 Chemical-Shift Thermometry

2.1. Overview

Thermometry via magnetic resonance imaging (MRI) would provide a powerful noninvasive window into physiological temperature management. Cobalt-59 nuclear spins demonstrate exceptional temperature dependence of their NMR chemical shift, yet the insight to control this dependence via molecular design is lacking. We present the first systematic evidence that encapsulation of this spin system amplifies the temperature sensitivity. We tested the temperature dependence of the ^{59}Co chemical shift, $\Delta\delta/\Delta T$ (ppm/°C), in a series of five Co^{3+} complexes as a function of increasing encapsulation within the first coordination sphere. This study spans from $[Co(NH_3)_6]Cl_3$, with no interligand connectivity, to a fully encapsulated dinitrosarcophagine (diNOsar) complex, $[Co(diNOsar)]Cl_3$. We discovered $\Delta\delta/\Delta T$ values that span from 1.44(2) ppm/°C in $[Co(NH_3)_6]Cl_3$ to 2.04(2) ppm/°C in $[Co(diNOsar)]Cl_3$, the latter among the highest for a molecular complex. The data herein suggest that designing ^{59}Co-NMR thermometers toward high chemical stability can be coincident with high $\Delta\delta/\Delta T$. To better understand this phenomenon, variable-temperature UV-vis, ^{59}Co-NMR relaxation, Raman spectroscopic, and variable-solvent investigations were performed. Data from these measurements highlight an unexpected impact of encapsulation – an increasingly dynamic and flexible inner coordination sphere. These results comprise the first systematic studies to reveal insight into the molecular factors that govern $\Delta\delta/\Delta T$ and provide the first evidence of ^{59}Co nuclear-spin control via vibrational means.

2.2. Introduction

The structural flexibilities of metal complexes are key design principles for applications in the areas of reactivity,[1,2] medicine,[3] photophysical properties,[4] and magnetic information storage.[5] Flexibility engenders stimuli-dependent changes in the coordination geometry of a metal, hence, impacting *d*-orbital energies and any properties stemming from electronic structure.[6] Thus, the control of flexibility is

potentially a powerful way for targeting applications for metal complexes. One such application is biomedical thermometry by magnetic resonance imaging (MRI),[7,8] where the temperature-dependent structure of a flexible complex induces temperature-dependent spin-Hamiltonian parameters or relaxation times. If this variation could be harnessed to develop an imaging technique, such application would circumvent many of the challenges associated with invasive thermometry, e.g., the point-like nature of the measurement.

One promising system for such thermometry by magnetic resonance is the cobalt-59 nucleus in low-spin Co^{3+} complexes. This NMR-active nucleus is 100% natural abundance, $I = {}^{7}/_{2}$, and a receptivity of ca. 30% that of ^{1}H. Furthermore, the ^{59}Co nucleus displays a wide reported chemical shift (δ) window (20,000 ppm) due to a paramagnetic contribution to $\delta(^{59}Co)$ which is directly tied to the electronic structure, i.e., ligand field strength Δ_o.[9–11] For complexes that contain ^{59}Co nuclei, changes in solution structure, such as lengthening metal-ligand bonds, can impact Δ_o, imparting changes in $\delta(^{59}Co)$, and providing a mechanism for thermometry. In principle, $\delta(^{59}Co)$ could be used to spatially map temperature through a technique known as chemical shift imaging.[12–14] Initial studies reveal sensitivities ($\Delta\delta/\Delta T$) on the order of 1–3 ppm/°C,[15–20] order-of-magnitude upgrades to the possibilities for conventional ^{1}H-NMR thermometry.[21,22] Hence, these species may be useful to develop as new probes for chemical-shift imaging of temperature.[12] However, fundamental insight about the factors to govern that sensitivity is lacking (this chapter details one factor – encapsulation – as depicted in *Figure 2.1*).

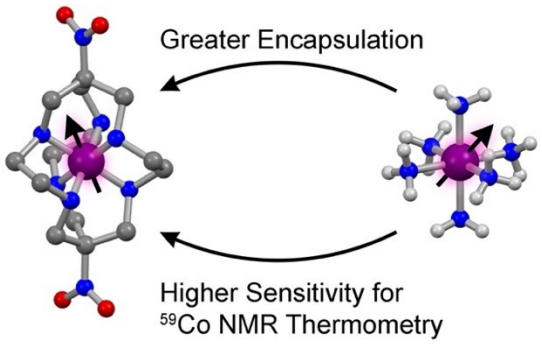

Figure 2.1. The tested design parameter in this chapter, from least-encapsulated $[Co(NH_3)_6]^{3+}$ (right) to most-encapsulated $[Co(diNOsar)]^{3+}$ (left) structures, of low-spin d^6-octahedral Co^{3+} complexes. Anions and hydrogens omitted for clarity where necessary. Purple, blue, red, grey, and light grey spheres correspond to cobalt, nitrogen, oxygen, carbon, and hydrogen atoms, respectively.

As a result, design principles for enhancing $\Delta\delta/\Delta T$ values are absent, and the true potential of cobalt-59 NMR thermometers for MRI remains unrealized.

This chapter details the first systematic exploration of molecular factors that govern $\Delta\delta/\Delta T$ in a family of ^{59}Co-NMR thermometers. As a first step, we sought to explore the role of ligand encapsulation on the temperature sensitivity of the ligand field and ^{59}Co-NMR properties. Encapsulation is known to afford enhanced stability for metal complexes via the chelate and related macrocyclic effects.[23] Such stability is an important property for any imaging agent, as release of the metal can both induce toxicity and deactivate the magnetic species being used as a sensor. At the same time, a rigid, encapsulated ion can be readily envisioned to lack the flexibility needed for thermometry via structural change. Hence, encapsulation, while affording significant chemical stability, might simultaneously subdue the ability to sense temperature via ^{59}Co NMR.

To test this hypothesis, we investigated $\Delta\delta/\Delta T$ for a series of encapsulated ^{59}Co nuclei of the low-spin Co^{3+} complexes $[Co(NH_3)_6]Cl_3$ (**1**),[24] $[Co(en)_3]Cl_3$ (**2**, en = ethylenediamine),[25] $[Co(tn)_3]Cl_3$ (**3**, tn = trimethylenediamine),[26] $[Co(tame)_2]Cl_3$ (**4**, tame = triaminomethylethane),[27] $[Co(diNOsar)]Cl_3$ (**5**, = dinitrosarcophagine),[28] and $K_3[Co(CN)_6]$, the ^{59}Co-NMR standard. This series of complexes was selected to enable an investigation of molecular and electronic structure on $\Delta\delta/\Delta T$ (*Figure 2.2*).

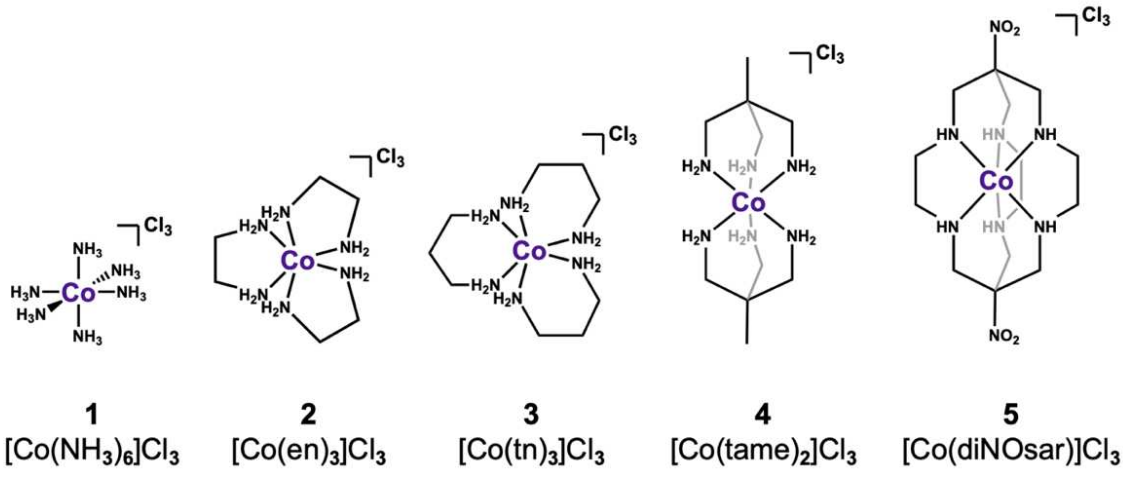

Figure 2.2. The series of Co^{3+} complexes with progressively encapsulated ligand systems from **1–5**. All studied complexes possess chloride anions. Anions and hydrogens bound to carbons are omitted for clarity.

First, we hypothesized that the increasing connectivity between the nitrogen donor atoms in **1–5** would engender an increasingly rigid coordination environment and, hence, suppress $\Delta\delta/\Delta T$. Thus, we expected that sensitivity to temperature would be compromised in favor of chemical stability. Indeed, the fully-encapsulating sarcophagine scaffold[23,28,29] will only surrender its NMR-active Co^{3+} ion under harsh conditions – heating in concentrated cyanide solution or acidic media.[30,31] The second investigation enabled by this set of complexes is the test of whether $\Delta\delta/\Delta T$ correlates directly with Δ_o. The ^{59}Co chemical shift is proportional to $1/\Delta_o$,[10] hence, these studies are the first to reveal three key facts about $\Delta\delta/\Delta T$. Firstly, in contrast to our expectations, encapsulation enhances $\Delta\delta/\Delta T$. That is – the "rigid" ligand frameworks in **5** and **4** induce a stronger temperature dependence in $\delta(^{59}Co)$ (and Δ_o) than the less-encapsulated species **1–3**. Indeed, variable-temperature UV-vis and ^{59}Co spin-lattice relaxation (T_1) studies indicate that encapsulation counterintuitively supports higher temperature dependence in the coordination geometry. Second, our studies show that Δ_o alone does not correlate to the magnitude of $\Delta\delta/\Delta T$. Finally, Raman spectroscopy studies suggest molecular vibrational lifetimes, posited to be elongated by high interconnectivity among donor atoms, are important factors governing $\Delta\delta/\Delta T$. Together, the data highlight a new implication that ligand encapsulation may be used as a strategy for achievable spin-based MR thermometers.

2.3. Experimental Section

2.3.1. General Considerations

Compounds were synthesized as previously reported unless otherwise specified. Compounds **1** and $K_3[Co(CN)_6]$ were purchased from commercial vendors and recrystallized prior to measurement. 1,1,1-tris(aminomethyl)ethane trihydrochloride (tame·3HCl) was synthesized from a previously reported procedure.[32] All other precursors and chemicals were purchased from commercial vendors and used as received. General UV-vis spectra were collected on aqueous solutions of **1–5** and $K_3[Co(CN)_6]$ with an Agilent 8453 UV-vis spectrophotometer. IR spectra were collected on solid powders with a Bruker TENSOR II FTIR spectrometer. Combustion analyses were performed by Robertson Microlit Laboratories.

2.3.2. Preparation of Compounds

Synthesis of $[Co(en)_3]Cl_3 \cdot 3H_2O$ (**2**$\cdot 3H_2O$). This complex was synthesized following a previously published procedure.[33] A crystalline, yellow-orange solid was obtained (7.071 g, 40.5% yield) after air drying. IR (cm^{-1}, ATR): 438 (vs), 471 (m), 580 (w/s), 706 (s/vw), 780 (s), 898 (s/vw), 1057 (s), 1124 (s/w), 1156 (s), 1254 (s/vw), 1280 (s/vw), 1326 (s/w), 1364 (s/w), 1439 (m), 1463 (s), 1561 (s), 1583 (m), 3096 (s), 3204 (m), 3484 (m). UV-vis (H_2O): λ_{max} (nm) (ε_M ($M^{-1}cm^{-1}$)): 338 (81) and 465 (83). Anal. Calcd. (Found) for $C_6H_{24}Cl_3CoN_6 \cdot 3H_2O$: 18.03 (17.59) %C, 7.57 (7.55) %H, and 21.02 (20.95) %N.

Synthesis of $[Co(tn)_3]Cl_3 \cdot 3.5H_2O$ (**3**$\cdot 3.5H_2O$). This complex was synthesized using a modified literature procedure.[26] Here, $CoCl_2 \cdot 6H_2O$ (6.0 g, 0.025 mol) and 8.5 mL of 85% trimethylenediamine were dissolved in 20.0 mL of water. To this solution, 2.10 mL of conc. HCl were added slowly followed by 0.5 g of activated charcoal. The solution was aerated with stirring for 18 hr, then filtered and the collected solid was washed with 3 × 7 mL of H_2O. To the filtrate and washings were added 95 mL of MeOH and 50 mL of Et_2O. The precipitate crashed out of solution and was filtered to yield a crystalline, salmon-colored solid (9.80 g, 28.0%). Collected spectra match reported data.[27] IR (cm^{-1}, ATR): 420 (s), 448 (w/s), 488 (w/s), 515 (w/s), 520 (s), 690 (m/w), 720 (s/vw), 733 (s/vw), 886 (s/w), 931 (s), 1039 (vs), 1088 (s/vw), 1138 (m/vw), 1185 (s), 1208 (s/w), 1234 (s), 1274 (m/w), 1310 (s/vw), 1362 (m/w), 1413 (m/w), 1456 (s/vw), 1478 (w/s), 1571 (m), 2888 (w/s), 2962 (m), 3090 (s), 3151 (m), 3392 (m/w). UV-vis (H_2O): λ_{max} (nm) (ε_M ($M^{-1}cm^{-1}$)): 350 (76) and 485 (74). Anal. Calcd. (Found) for $C_9H_{30}Cl_3CoN_6 \cdot 3.5H_2O$: 23.98 (24.11) %C, 8.27 (8.06) %H, and 18.64 (18.59) %N.

Synthesis of $[Co(tame)_2]Cl_3 \cdot 1.5H_2O$ (**4**$\cdot 1.5H_2O$). The trihydrate was synthesized using a modified literature procedure.[27] tame·3HCl (0.645 g, 2.85 mmol) was dissolved in 5 mL of water and mixed with Ag_2O (1.33 g, 5.74 mmol). The mixture was covered in aluminum foil and stirred for 2 hr. The resulting mixture was filtered to obtain a colorless solution, which was then added to a mixture of $CoCl_2 \cdot 6H_2O$ (0.239 g, 1.00 mmol) and activated charcoal (0.043 g). After 1 min, 0.5 mL of conc. HCl was added, and the solution was stirred for two hours under gentle aeration. The resulting orange-brown solution was then

filtered through a pad of celite into dilute HCl (2.5 mL, 1 M). This solution was concentrated, filtered, and placed in an ice bath, forming bright orange, hexagonal crystals. The crystals were filtered and washed with ~15 mL of acetone and ethanol to obtain a bright orange, crystalline solid (0.355 g, 46.2%). IR (cm^{-1}, ATR): 424 (vs), 571 (vw/s), 745 (m/vw), 815 (m/vw), 888 (m/vw), 908 (s/w), 1009 (s), 1068 (s/vw), 1128 (s/vw), 1153 (s/w), 1227 (m), 1310 (m/vw), 1349 (s/vw), 1373 (m/vw), 1401 (s/vw), 1460 (s/w), 1500 (m/vw), 1545 (m/vw), 1594 (m), 1600 (m), 2884 (s/w), 2947 (m), 3027 (s), 3150 (m), 3499 (m). UV-vis (H_2O): λ_{max} (nm) (ε_M ($M^{-1}cm^{-1}$)): 338 (67) and 468 (78). Anal. Calcd. (Found) for $C_{10}H_{30}Cl_3CoN_6 \cdot 1.5H_2O$: 28.15 (28.31) %C, 7.79 (7.45) %H, and 19.64 (19.62) %N.

Synthesis of $[Co(diNOsar)]Cl_3 \cdot 2H_2O$ (**5**$\cdot 2H_2O$). This complex was synthesized following a previously published procedure.[30] The resultant orange, powdery compound (4.30 g, 55.0%) revealed spectra that match reported data.[28] IR (cm^{-1}, ATR): 438 (s/w), 467 (s), 503 (m), 597 (vs/w), 621 (s/vw), 787 (vs/w), 812 (vs), 840 (s/w), 873 (s/w), 952 (s/w), 974 (m/vw), 1019 (s/w), 1060 (m), 1077 (m), 1131 (m/vw), 1171 (s/vw), 1198 (s/vw), 1236 (s/vw), 1271 (s/vw), 1342 (s), 1382 (s/vw), 1429 (s/vw), 1453 (m), 1555 (vs), 1602 (m/w), 1655 (m/vw), 2375 (m/vw), 2947 (m), 3004 (m/w), 3032 (m), 3409 (m/w), 3466 (m/w). UV-vis (H_2O): λ_{max} (nm) (ε_M ($M^{-1}cm^{-1}$)): 342 (204) and 475 (161). Anal. Calcd. (Found) for $C_{14}H_{30}Cl_3CoN_8O_4 \cdot 2H_2O$: 29.21 (29.32) %C, 5.95 (5.70) %H, and 19.46 (19.36) %N.

2.3.3. Variable Temperature ^{59}Co-NMR Measurements

NMR spectra were obtained at Colorado State University (CSU) on a Varian Unity INOVA 500. All variable temperature NMR measurements for $K_3[Co(CN)_6]$ and compounds **1**–**4** were collected in 100 mM solutions of H_2O, with the exception of **5**, which was measured in a 33.3 mM solution. Experiments performed as a function of concentration reveal no difference in $\Delta\delta/\Delta T$ for **1**–**5** in this concentration range. For variable solvent studies, the NMR measurements were acquired for compound **2** in ~20 mM solutions of DMSO and d_6-DMSO, ~15 mM solution of DMF, and ~10 mM solution of HMPA. These concentrations were selected on the basis of highest level of solubility for **2** in these solvents. For all measurements, standards of methanol and ethylene glycol were used to monitor and accurately determine the temperature

inside of the magnet. Samples were permitted to equilibrate for 15 minutes inside the 5 mm broadband probe between each temperature.

Spin-lattice relaxation times were collected via inversion recovery measurements. Samples of **1**–**5** were prepared at 0.33 mM concentration in H_2O. Samples were prepared on the bench and not deoxygenated, as such treatment has been shown to not have substantial effect on spin-lattice relaxation for the ^{59}Co nucleus.[34] Moreover, many other studies also omit the step,[17,19,20,35] making for better comparative analyses. Pulse lengths for the π and π/2 pulses were 22.5 and 11.25 μs, respectively, with a recycle delay generally $5 \times T_1$ for the given system. For all compounds at all temperatures, inversion recovery curves were each successfully fit using a monoexponential function.

2.3.4. Variable Temperature UV-vis Measurements

Compounds **1**–**5** were prepared as samples in water to concentrations of 9.5 mM (**1**), 6.7 mM (**2**), 5.9 mM (**3**), 6.5 mM (**4**), and 4.5 mM (**5**). Absorbance measurements were made with a DH-2000-BAL Ocean Optics UV/vis NIR spectrometer equipped with T300-RT-UV/VIS Transmission dip probe of 1-inch path length. Temperature control of each sample was performed with a heated oil-bath monitored via thermocouple. Sample temperatures were monitored separately and allowed to equilibrate to the surrounding oil-bath. Upon equilibration, absorbance spectra for each sample were collected in intervals of 5 °C between 25–60 °C. For a given sample, the individual absorbance spectra were normalized and fit with a consistent baseline correction and Gaussian distribution to determine changes in peak maxima over temperature. Two absorption energies corresponding to $^1A_{1g} \rightarrow {}^1T_{1g}$ and $^1A_{1g} \rightarrow {}^1T_{2g}$ were present in each sample measurement. Absorption energies (E) were used to determine E/B (B = Racah parameter) on a d^6 Tanabe-Sugano diagram for all Co^{3+} compounds. Using the lower energy transition $^1A_{1g} \rightarrow {}^1T_{1g}$, values of B were determined for each compound at each temperature interval, then used to calculate Δ_o, respectively (*Table A1.1*)

2.3.5. Raman Spectroscopic Measurements

Raman spectra of compounds **1–5** were collected at the CU Microspectroscopy Lab. Spectra were obtained using a Horiba LabRAM HR Evolution Spectrometer equipped with a 785 nm NIR laser (Nd:YAG). Each of the dried compounds were measured as powder samples individually loaded onto glass slides. All spectra were collected between 100–650 cm^{-1} by the same spectral resolution utilizing 1,800 gr/mm grating and 24 mW laser power. Spectral deconvolution was performed in the Horiba LabSpec6 program on baseline-corrected spectra. Peaks were modeled with the pseudo-Voigt function (1), where A is peak amplitude, ω is peak width, x_0 is peak center, and g is the Gaussian linear mixing coefficient. Note that the character of the peak can be an indication of the mechanism of broadening: Gaussian for inhomogeneous broadening and Lorentzian for homogeneous broadening.[36] On the basis of the g values obtained from spectral deconvolution via Eq. 1 (*Table A1.4*), there is a distribution of different peak types in the observed spectra. These all point to the necessity of subsequent, deeper investigations to understand linewidth as a function of ligand identity.

$$V = A\left(g \cdot \exp\left(\frac{(x-x_0)^2}{(\omega/2\sqrt{\ln(2)})^2}\right) + (1-g)\cdot \frac{1}{1+(x-x_0)^2/(\omega/2)^2}\right) \quad \text{(Eq. 1)}$$

2.4. Results and Discussion

Understanding the temperature sensitivity of the chemical shift requires first establishing the electronic structure of the Co^{3+} ions in **1–5**. UV-vis electronic absorption spectra of compounds **1–5** and $K_3[Co(CN)_6]$ in H_2O reproduce reported results for the individual complexes, wherein the lowest energy peak the $^1A_{1g}\rightarrow{}^1T_{1g}$ transition and the higher energy peak indicates the $^1A_{1g}\rightarrow{}^1T_{2g}$ transition.[10,28] The energies of these two peaks and a Tanabe-Sugano diagram permit quantitation of Δ_o, which increases from **3** (22,376 cm^{-1}) to **5** (22,754 cm^{-1}) and **1** (23,018 cm^{-1}) to **4** (23,276 cm^{-1}) to **2** (23,321 cm^{-1}). These values are consistent with literature values for **1–5** and stand in contrast to the strong ligand field of $K_3[Co(CN)_6]$ that engenders a Δ_o of 38,000 cm^{-1}.[37] Cobalt-59 resonant frequencies were observed for **1–5** over the

range of 6,800 to 8,400 ppm (referenced to $K_3[Co(CN)_6]$). According to the ^{59}Co chemical shifts, the magnitude of Δ_o increases in the order **3** < **1** < **4** < **2** < **5** < $K_3[Co(CN)_6]$ (*Figure 2.3*).

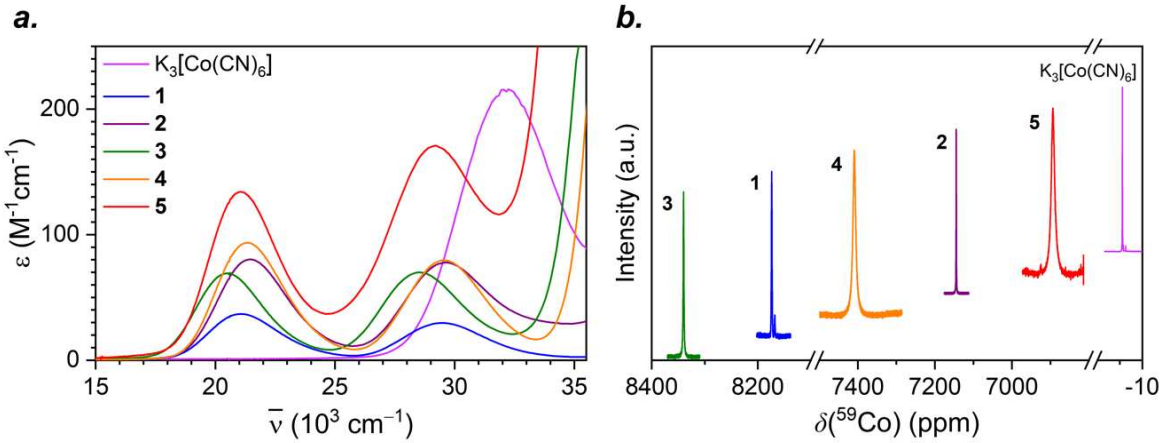

Figure 2.3. Characterization of Co^{3+} electronic structure in **1–5** by UV-vis and ^{59}Co NMR. ***a.*** Electronic absorption spectra for **1–5** and $K_3[Co(CN)_6]$ in H_2O at room temperature. The lower-energy peak is the $^1A_{1g}$ to $^1T_{1g}$ transition while the higher-wavenumber peak is $^1A_{1g}$ to $^1T_{2g}$. ***b.*** ^{59}Co-NMR (118.67 MHz) spectra for **1–5** and $K_3[Co(CN)_6]$ in H_2O at room temperature.

This order is at odds with the trend obtained from electronic absorption spectroscopy measurements. However, reported correlations between UV-vis peak position and $\delta(^{59}Co)$ are only approximate, not quantitative.[9,10] Nevertheless, these measurements provide (*i*) two points of reference to test for a correlation between $\Delta\delta/\Delta T$ and Δ_o, and (*ii*) the location of the ^{59}Co-NMR resonances for variable-temperature analyses.

Variable-temperature ^{59}Co-NMR spectra were collected for **1–5** and $K_3[Co(CN)_6]$ in H_2O from 10–60 °C to explore the temperature dependence of $\delta(^{59}Co)$. With increasing temperature, peaks for **1–5** and $K_3[Co(CN)_6]$ shift downfield to higher $\delta(^{59}Co)$. This temperature-dependent shift of peaks is consistent with varying coordination geometry in solution.[18,38] As temperature is increased, energy is introduced into the vibrational modes of the cobalt complex, expanding M–L bond distances and engendering generally weaker Δ_o.[18,39]

Precise determination of the sensitivity of the ^{59}Co-NMR resonance to temperature was achieved via linear regression of the temperature-dependent data (*Table A1.2, and Figure A1.8*). Analyses revealed

$\Delta\delta/\Delta T$ values for $K_3[Co(CN)_6]$ and **1–5**, respectively, of 1.44(1), 1.44(2), 1.38(1), 1.30(2), 1.71(1), and 2.04(2) ppm/°C (*Figure 2.4*).

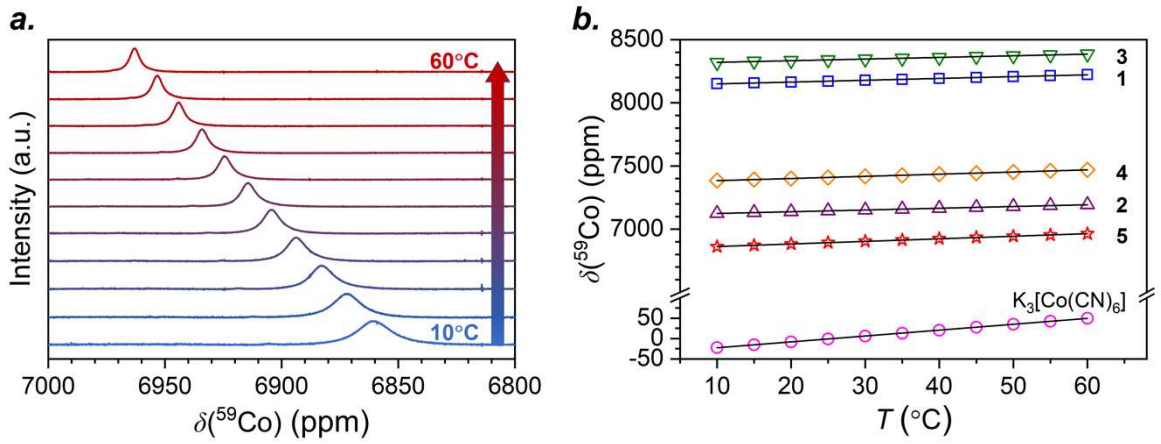

Figure 2.4. a. Variable temperature chemical shift (^{59}Co, 118 MHz) of **5** in H_2O (33 mM) from 10–60 °C. ***b.*** The change in $\delta(^{59}Co)$ as a function of temperature for $K_3[Co(CN)_6]$ and **1–5**. The slopes of the linear regression fits (*black traces*) indicate the values of reported $\Delta\delta/\Delta T$ (ppm/°C) for each compound.

These values are within the ranges of sensitivity reported for the few ^{59}Co-NMR thermometers,[15–18,20] but it's worth noting that, to the best of our knowledge, the $\Delta\delta/\Delta T$ of **5** is eclipsed only by $Co(acac)_3$, a molecule that is completely unsuitable for aqueous (e.g., physiological) conditions.[16,20] Most importantly (and surprisingly), these data indicate that the highest sensitivity to changes in temperature is held by the completely encaged complex **5**.

The values of $\Delta\delta/\Delta T$ follow an opposing trend to the initial hypothesis, in that **5**, with the highest degree of encapsulation, displays the strongest $\Delta\delta/\Delta T$. Complex **4**, with the second highest degree of encapsulation, displays the second highest sensitivity of our studied complexes. Yet, a comprehensive trend for all complexes on the basis of encapsulation is not indicated by these data. For example, in **1** and $K_3[Co(CN)_6]$, the ligand donor atoms are not connected in any manner. Yet, these species demonstrate higher $\Delta\delta/\Delta T$ than both **2** and **3**, which contain bidentate chelates. Furthermore, the collected data show that electronic structure considerations alone (specifically, Δ_o) do not govern sensitivity. Here, neither the trend in Δ_o extracted from UV-vis (**3** < **5** < **1** < **4** < **2** < $K_3[Co(CN)_6]$) nor that from the 25 °C ^{59}Co NMR (**3** < **1** < **4** < **2** < **5** < $K_3[Co(CN)_6]$) reproduce the trend in $\Delta\delta/\Delta T$ (*Table A1.3 and Figure A1.9*).

The foregoing results highlight the need for deeper studies to derive fundamental insight. An important implication of the foregoing results is the concept that the encaged complex counterintuitively demonstrates the highest fluxionality in the inner-coordination structure. Four key experiments were applied to further test this rationale.

If the molecular structure of $[Co(diNOsar)]Cl_3$ is truly more temperature-dependent than **1–4**, then Δ_o for **5** should show the greatest temperature dependence. Variable-temperature UV-vis of **1–5** show slight shifts to lower energy with increasing temperature. Analyses of these data reveal a change in Δ_o as a function of temperature, $\Delta\Delta_o/\Delta T$ (*Figure 2.5*).

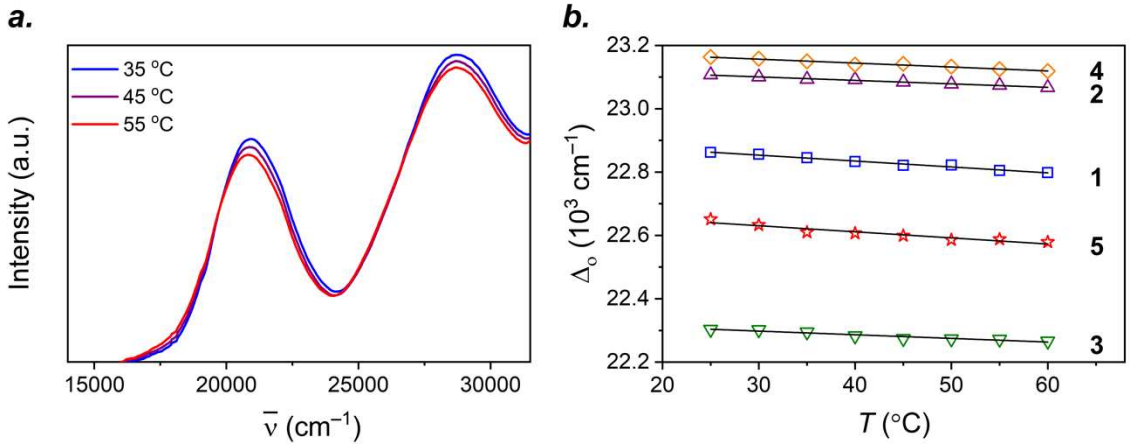

Figure 2.5. a. Variable temperature UV-vis of **5** in H_2O (4.5 mM) showing red-shifted peaks with increasing temperature. ***b.*** Temperature dependence of Δ_o for **1–5**. The slopes of the linear regression fits (*black traces*) indicate the values of $\Delta\Delta_o/\Delta T$ (cm^{-1}/°C) for each compound.

Over **1–5**, $\Delta\Delta_o/\Delta T$ assumes values of –2.78(4), –1.36(17), –2.91(5), –3.70(17), and –5.65(32) cm^{-1}/°C for **1–5** respectively. These spectral changes are consistent with studies probing temperature-dependent UV-vis spectra for metal complexes wherein spin-state changes are absent[40,41] (e.g., by spin-crossover[42] or valence tautomerization[43]). These data trend in a manner (particularly for **2–5**) that seems opposed to an association between encapsulation and increased rigidity of the coordination environment. Indeed, **5** exhibits the largest change in temperature, followed by **4**, then **3** and **1**, and finally **2**. Hence, these data point to a more dynamic inner coordination sphere.

If the inner coordination sphere is less rigid upon encapsulation, then cobalt-59 spin-lattice relaxation times, T_1, should reflect that point. Indeed, the $I = {}^7/_2$ cobalt-59 nucleus is quadrupolar, and, hence, its spin-lattice relaxation rate ($1/T_1$) is dominated by fluctuations in the local electric field gradient.[44] Hence, the anticipated higher fluxionality in the Co–N_6 environment of **4** and **5**, compared to the more symmetric **1–3**, should corresponding to shorter ^{59}Co T_1. Analysis of the inversion recovery times of the ^{59}Co-NMR peak reveals T_1 for each compound. Importantly, trends in T_1 times followed the trend in encapsulation, wherein **1** displayed the longest T_1 (48.47(5) ms), followed by **2** (9.09(2) ms) and **3** (2.73(1) ms). In contrast, the species of highest encapsulation, **4** and **5**, had the shortest T_1 values (346(1) and 323(1) μs, respectively) (*Figure 2.6*).

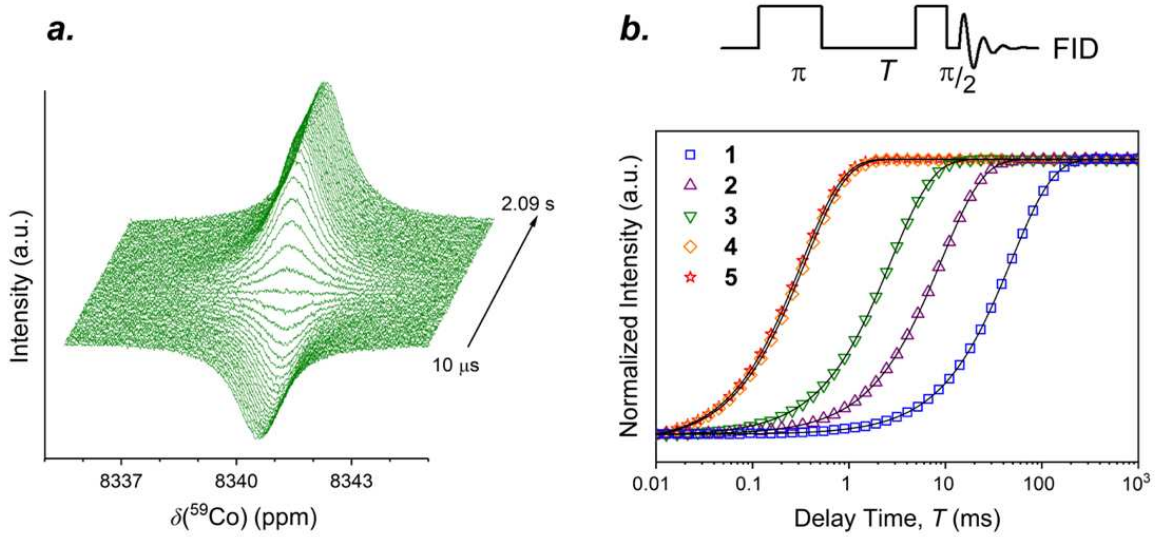

Figure 2.6. a. Inversion recovery of ^{59}Co-NMR (118.67 MHz) peak for **3** in water (33 mM) at 25 °C. ***b.*** The pulse sequence used for ^{59}Co T_1 inversion recovery of **1–5** over varied delay times T (s) following a π-pulse (22 μs). Monoexponential fits (*black traces*) of relaxation data were made to evaluate T_1 for each compound.

For **1** and **2**, these values match previously reported results.[35,44,45] Quadrupolar relaxation is also enhanced in systems with higher ^{59}Co quadrupolar coupling of the ^{59}Co nucleus, which is smaller for high-symmetry complexes.[9] The compound **1** is clearly higher symmetry (O_h) than **2–5** (D_3). This symmetry difference is likely an important contributor to the T_1 of **1** versus **2–5**, but quadrupolar couplings in this latter set of compounds are similar (when known).[34,35] Moreover, solution-phase rotational rates for the series extrema,

1 and **5**, are similar,[34] suggesting rotational correlation is not the driving difference in T_1 across the series. Together, these points suggest that considerations beyond symmetry/rotation define T_1 for these compounds. In light of the other data in this chapter, we propose that the T_1 trend evidences a more dynamic coordination environment upon encapsulation, though deeper investigations are needed to test this hypothesis.

Vibrational spectra in the 100-650 cm^{-1} window, wherein metal-ligand vibrations typically occur, ought to vary with rigidity as well.[46] To test this concept, microcrystalline powders of **1–5** were analyzed via Raman spectroscopy. As the probed molecules increase in structural complexity, so do the Raman spectra, with compound **1** exhibiting 8, **2** displaying 12, and **5** producing 21 bands below 650 cm^{-1} (*Figure 2.7*).

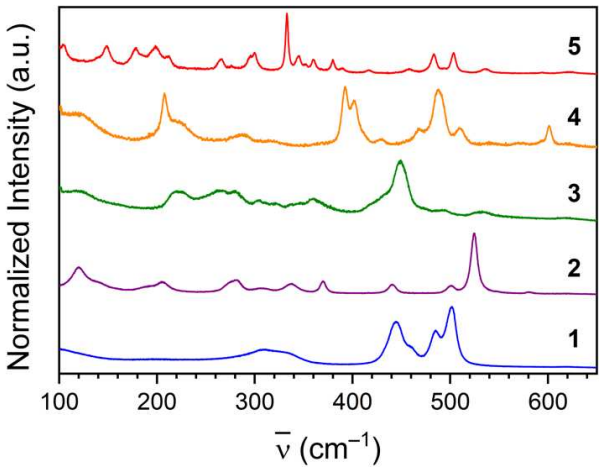

Figure 2.7. Raman spectroscopy data of **1–5** collected as pure powder samples. In each spectrum, the linewidths of individual peaks are determined from fits (by full width at half-max, FWHM) to determine the lifetime of each vibrational state (see *Section 2.3.5*, Chapter 2 for details). The lifetimes of all vibrations in the 100–600 cm^{-1} energy range are averaged to encompass the Co–N vibrational modes in each complex.

Previous reports identify symmetric Co–N bond stretches at 500 and 486 cm^{-1} for **1**, and 526, 444, and 476 cm^{-1} for **2**.[47,48] For **3–5**, in contrast, no Raman spectra are reported to the best of our knowledge. Closer inspection of the Raman spectra reveals a general sharpening of transitions with increasing encapsulation. This sharpening is most noticeable when comparing the spectra of lesser encapsulated compounds **1–3** with the completely encapsulated species **5**. Linewidth analyses of the observed vibrations for **1–5** permitted

relative quantitation of the general degree of sharpness of these spectra (*Table A1.4 and Figures A1.13–A1.17*). The averages of the peak linewidths for the spectra are ordered from **5** < **2** < **4** < **1** < **3**, where the fully encapsulated species, **5**, exhibits the smallest average peak width.

On the basis of the variable-temperature NMR and UV-vis data, the highest flexibility is observed for **5**. However, the lifetime of the NMR experiment is much longer than that of vibrational spectroscopy.[49] Hence, one may therefore expect the greater structural variability from the NMR and UV-vis analyses to result in greater inhomogeneous broadening of the vibrational peaks for **5**. The observations from the Raman spectra are in contrast to this expectation, as **5** demonstrates the sharpest peaks. One alternative mechanism that governs peak linewidths is homogeneous broadening, which causes sharper peaks for excitations that have longer lifetimes.[50] This mechanism is acknowledged as dominant in studies of $M(CO)_n$ at room temperature in solution.[36,51] If operative and dominant in powders of **1–5**, this admittedly simplistic model of broadening would suggest that the lifetimes of the vibrations of the coordination sphere are being enhanced by encapsulation. Translation of the average linewidths of **1–5** into average vibrational, spectroscopic lifetimes (via the relationship FWHM = $1/\pi\tau$) yields lifetimes of 0.4(2), 0.6(3), 0.4(2), 0.8(4), and 1.3(4) ps for **1–5**, respectively.

The foregoing linewidth interpretation should be treated with caution owing to three specific factors. First, differences in microcrystalline environment can have an important impact on Raman linewidths.[52,53] We note, however, that a preliminary powder diffraction analysis of the same samples measured by Raman spectroscopy did not reveal a stark trend of crystallinity correlating to the observed lifetimes (*Figure A1.18*). Second, modes of differing symmetries can yield different linewidths,[36] as is likely evidenced here in the spread of linewidths in the deconvoluted peaks. Third, true elucidation of the vibration lifetimes requires time-resolved methods, which would also help differentiate inhomogeneous versus homogeneous broadening mechanisms.[51] These data clearly motivate further solution-phase, time-resolved vibrational studies, a critical component of planned follow up work. Nevertheless, the obtained lifetimes are in the general picosecond range expected for metal complexes.[36,51]

If encapsulation affects $\Delta\delta/\Delta T$ via vibrations, that insight would provide a new design principle for vibrational control of molecular spin. Variable-solvent studies of **2** were performed as a test of this concept. In particular, as the polar N–H bonds of the coordinated nitrogen atoms in **1–5** likely interact with the aqueous environment, this interaction should mediate the vibrations and structure of the $[Co(en)_3]^{3+}$ moiety, potentially imparting large differences to $\Delta\delta/\Delta T$. Indeed, such hydrogen bonding interactions are demonstrated to enable modulation of M–N and M–O bonds in other molecular systems.[54,55] Here, this concept is being tested for temperature-dependent magnetic effects.

Initial studies focused on one member of the series, **2**, dissolved in four additional solvents: dimethylformamide (DMF), hexamethylphosphoramide (HMPA),[¤] dimethylsulfoxide (DMSO) and d_6-dimethylsulfoxide (d_6-DMSO). These solvents were selected to test the dependence of $\Delta\delta/\Delta T$ on polarity. Some solvent/deuteration impacts on $\delta(^{59}Co)$ are reported,[56] such as for the ClO_4^- salt of **2** and stems from modulation of the N-atom ligand field via hydrogen bonding between the solvent and N–H protons.[57] However, the solvent-dependent effects on thermometry are not yet understood. ^{59}Co-NMR spectra collected at 25 °C reveal a peak position that shifts over a range of 200 ppm as a function of solvent identity (*Figure 2.8*).

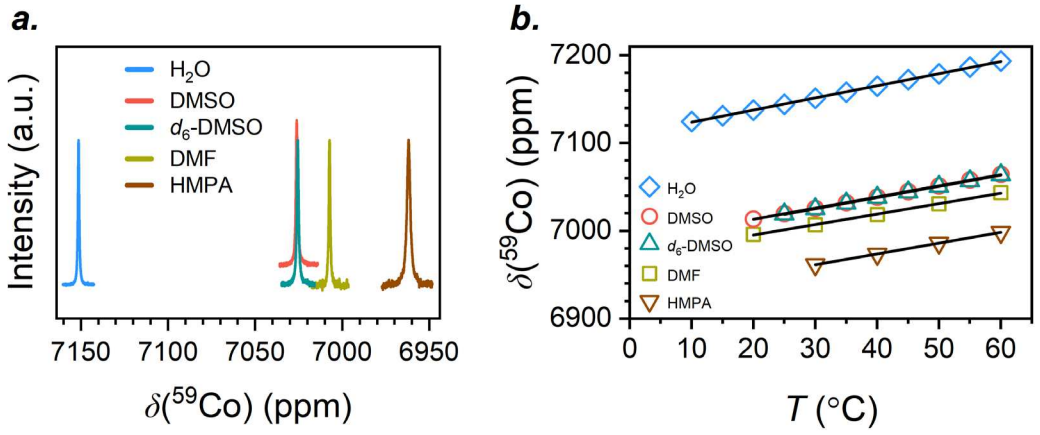

Figure 2.8. a. Chemical shift studies (^{59}Co, 118.67 MHz) of **2** in various solvents (30 mM) at 25 °C. ***b.*** The change in $\delta(^{59}Co)$ as a function of temperature for **2** in each solvent. The slopes of the linear regression fits (*black traces*) indicate the values of reported $\Delta\delta/\Delta T$ (ppm/°C) of **2** in each solvent.

Furthermore, only a tiny shift in $\delta(^{59}Co)$ is observed between DMSO and d_6-DMSO, also in line with expected results.[56] Variable temperature analyses tested the impact of these differing solvent cages on

$\Delta\delta/\Delta T$ (*Table A1.5 and Figures A1.19–A1.22*). Here, analysis of the variable-temperature ^{59}Co-NMR peak positions as a function of solvent demonstrate a noticeable impact of solvent identity on $\Delta\delta/\Delta T$. As in H_2O, all ^{59}Co-NMR chemical shifts move downfield with increasing temperature. Linear regression of these temperature-dependent data reveal $\Delta\delta/\Delta T$ values of 1.19(2), 1.23(1), 1.27(1), and 1.28(1) ppm/°C, respectively, for DMF, HMPA, DMSO, and d_6-DMSO. These values are all lower than in H_2O ($\Delta\delta/\Delta T$ = 1.38(1) ppm/°C) and indicate nearly no role for solvent deuteration on $\Delta\delta/\Delta T$ in the present compound.

Comparison of the solvent-dependent $\Delta\delta/\Delta T$ results for **2** against measures of solvent-solute interaction potentially provide deeper insight into the role of the solvent cage (*Figure 2.9*).

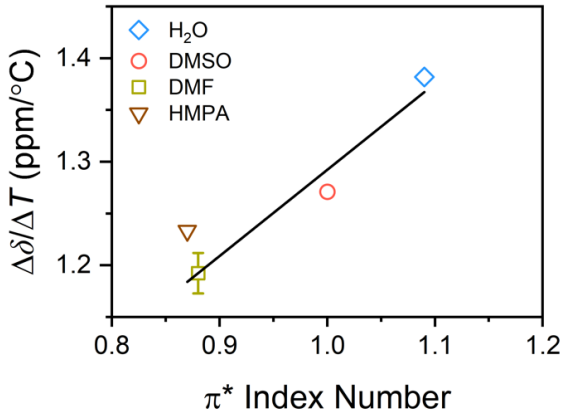

Figure 2.9. The impact of solvent polarity π* on $\Delta\delta/\Delta T$ of **2** in H_2O, DMSO, HMPA, and DMF. Error bars are within width of symbols except for DMF. The linear regression (*black trace*) has R^2 = 0.9.

In particular, the trend in $\Delta\delta/\Delta T$ was contrasted against, *i*) the solvent acceptor and donor numbers,[58,59] *ii*) the π* solvent polarity scale,[60,61] and, *iii)* the β and α hydrogen-bonding donor/acceptor scales (*Figure A1.23*).[61,62] There may be an approximate correlation between $\Delta\delta/\Delta T$ and acceptor number, whereas there is clearly none for donor number and little, if any, with β. Analysis with α values is complicated as α is 0 for all solvents here except H_2O.[60] However, the π* scale clearly reveals a correlation.

The foregoing data point toward a coordination environment that is counterintuitively more flexible and dynamic with increasing encapsulation. Electron transfer studies of sarcophagine-like ligands provided the first assertions of rigidity in encapsulated Co^{3+} complexes based on a conformationally inflexible environment.[63–67] We propose that this conformation-based description of rigidity is insufficient for

understanding the trend of $\Delta\delta/\Delta T$. Instead, we tentatively posit an alternative, spin-relevant interpretation in this context. Here, the enhanced connectivity in **4** and **5** ensures a higher rigidity in the coordination environment, except in this case the rigidity permits vibrations of the encapsulated coordination environment to persist longer. Such longer lifetimes ultimately sustain a change in the coordination sphere by lengthening the equilibrium Co–N bond distances. Hence, there is a temperature dependence of Δ_o and $\delta(^{59}\text{Co})$ in **4** and **5** that is larger than **1**–**3**. This tentative interpretation of the data is also consistent with the solvent dependence of $\Delta\delta/\Delta T$ in **2**, as the solvent cage is known for impacting vibration lifetimes in coordination complexes.[36,68,69] The fundamental argument we propose here is an analogue to the justification of long phonon lifetimes in materials like diamond,[70,71] except here related to the molecular vibrations of a complex in solution. These studies clearly motivate future investigations to evaluate the validity of this picture of vibration-controlled spin properties.

Furthermore, the solvent-dependent data hint at a rich area of inquiry into the role of the second coordination sphere and counterions. When considering the $[Co(en)_3]^{3+}$ unit, interactions with the solvent are most easily intuited via the N–H protons accepting electron density from solvent molecule lone pairs. However, the data do not enable us to conclusively say this interaction is the one guiding $\Delta\delta/\Delta T$. The association of a higher $\Delta\delta/\Delta T$ with a higher π^* index of solvent polarity[60] would mesh with the intuited picture of the $[Co(en)_3]^{3+}$ to solvent interaction. Such a picture would also be consistent with the match between a lower β value and a higher $\Delta\delta/\Delta T$, as a low β occurs when a solute will only weakly accept a proton.[62] Thus, these data suggest that the N–H interactions are key to understanding $\Delta\delta/\Delta T$. However, the interpretation isn't without some uncertainty. To the extent that there is any correlation of $\Delta\delta/\Delta T$ with solvent properties, it is with their acceptor number, not donor number, meaning that $[Co(en)_3]^{3+}$ acts as a donor. This argument only makes sense if one also considers the lone pairs of a bound Cl^- counterion. Earlier studies of $[Co(en)_3]^{3+}$ and $[Co(diNOsar)]^{3+}$ demonstrate a close association between these species and their Cl^- counterions that persists in solution.[34,67,72] Noted reservations about generalizing the acceptor/donor number scale lend caution to the second explanation of the solvent-dependent data.[73]

Nevertheless, the conflict between these two interpretations underlines the necessity of further investigations into the role of the counterion and solvent cage on $\Delta\delta/\Delta T$.

2.5. Conclusion

The foregoing results are the first evidence of synergy between ligand encapsulation and enhanced temperature-dependent magnetic changes in metal-ion nuclear spins. Such knowledge is of broad impact, as exploiting molecular rigidity to control magnetism is an emerging trend in designing molecules for other spin-based technologies, e.g., molecular quantum bit development.[74–76] Importantly, the presented arguments potentially tie vibration lifetimes to nuclear magnetism – necessitating future time-resolved measurements to test the validity of this analysis. Finally, our studies reveal that beyond the ligand, manipulations of the counterion and solvent cage are the next stage for understanding the mechanisms that control $\Delta\delta/\Delta T$. Beyond the targeted applications in thermometry, the concepts herein could be extended to understanding the impacts of molecular rigidity on other spin-based applications, for example, designing electron paramagnetic resonance imaging probes,[77] rigid systems for dynamic nuclear polarization[78–80] (particularly with metal ions),[81,82] or molecular quantum sensors.[83,84]

References

(1) Bestgen, S.; Rees, N. H.; Goicoechea, J. M. Flexible and Versatile Pincer-Type PGeP and PSnP Ligand Frameworks. *Organometallics* **2018**, *37*, 4147–4155.

(2) Coates, G. W.; Waymouth, R. M. Oscillating Stereocontrol: A Strategy for the Synthesis of Thermoplastic Elastomeric Polypropylene. *Science* **1995**, *267*, 217–219.

(3) Riccardi, L.; Genna, V.; De Vivo, M. Metal–Ligand Interactions in Drug Design. *Nat. Rev. Chem.* **2018**, *2*, 100–112.

(4) Mara, M. W.; Fransted, K. A.; Chen, L. X. Interplays of Excited State Structures and Dynamics in Copper(I) Diimine Complexes: Implications and Perspectives. *Coord. Chem. Rev.* **2015**, *282–283*, 2–18.

(5) Mannini, M.; Pineider, F.; Danieli, C.; Totti, F.; Sorace, L.; Sainctavit, P.; Arrio, M.-A.; Otero, E.; Joly, L.; Cezar, J. C.; Cornia, A.; Sessoli, R. Quantum Tunnelling of the Magnetization in a Monolayer of Oriented Single-Molecule Magnets. *Nature* **2010**, *468*, 417–421.

(6) Figgis, B. N.; Hitchman, M. A. *Ligand Field Theory and Its Applications*; Wiley-VCH: New York, 1999.

(7) Rieke, V.; Pauly, K. B. MR Thermometry. *J. Magn. Reson. Imaging* **2008**, *27* (2), 376–390.

(8) Townsend, D.; Cheng, Z.; Georg, D.; Drexler, W.; Moser, E. Grand Challenges in Biomedical Physics. *Front. Phys.* **2013**, *1*, 1–6.

(9) Chan, J. C. C.; Au-Yeung, S. C. F. Cobalt-59 NMR Spectroscopy. In *Annual Reports on NMR Spectroscopy*; Academic Press, 2000; Vol. 41, pp 1–54.

(10) Bramley, R.; Brorson, M.; Sargeson, A. M.; Schaeffer, C. E. Cobalt-59 NMR Chemical Shifts of Cobalt(III) Complexes; Correlations with Parameters Calculated from Ligand-Field Spectra. *J. Am. Chem. Soc.* **1985**, *107* (9), 2780–2787.

(11) Yamasaki, A. Cobalt-59 Nuclear Magnetic Resonance Spectroscopy in Coordination Chemistry. *J. Coord. Chem.* **1991**, *24* (3), 211–260.

(12) Brateman, L. Chemical Shift Imaging: A Review. *Am. J. Roentgenol.* **1986**, *146* (5), 971–980.

(13) Haase, A.; Frahm, J.; Hanicke, W.; Matthaei, D. ^{1}H NMR Chemical Shift Selective (CHESS) Imaging. *Phys. Med. Biol.* **1985**, *30* (4), 341–344.

(14) Brown, T. R.; Kincaid, B. M.; Ugurbil, K. NMR Chemical Shift Imaging in Three Dimensions. *Proc. Natl. Acad. Sci.* **1982**, *79* (11), 3523–3526.

(15) Webb, A. G.; Wong, M.; Niesman, M.; Kolbeck, K. J.; Wilmess, L. J.; Magin, R. L.; Suslick, K. S. In-Vivo NMR Thermometry with Liposomes Containing ^{59}Co Complexes. *Int. J. Hyperthermia* **1995**, *11* (6), 821–827.

(16) Levy, G. C.; Terry Bailey, J.; Wright, D. A. A Sensitive NMR Thermometer for Multinuclei FT NMR. *J. Magn. Reson.* **1980**, *37* (2), 353–356.

(17) Gillies, D. G.; Sutcliffe, L. H.; Williams, A. J. Variable-Temperature High-Pressure Investigation of the Cobalt-59 NMR Spectroscopy of Aqueous $K_3[Co(CN)_6]$. *Magn. Reson. Chem.* **2002**, *40* (1), 57–64.

(18) Benedek, G. B.; Englman, R.; Armstrong, J. A. Temperature and Pressure Dependence of the Co^{59} Nuclear Resonance Chemical Shift. *J. Chem. Phys.* **1963**, *39* (12), 3349–3363.

(19) Kanakubo, M.; Ikeuchi, H.; Sato, G. P. Concentration Dependence of Cobalt-59 Longitudinal Relaxation Times of Tris(acetylacetonato)cobalt(III) in Acetonitrile. *J. Magn. Reson., Ser. A* **1995**, *112* (1), 13–16.

(20) Kanakubo, M.; Uda, T.; Ikeuchi, H.; Satô, G. P. Solvent and Temperature Dependence of ^{59}Co NMR Chemical Shifts of Tris(acetylacetonato)cobalt(III) and Tris(dipivaloylmethanato)cobalt(III). *J. Solution Chem.* **1998**, *27* (7), 645–653.

(21) De Poorter, J.; Wagter, C. D.; Deene, Y. D.; Thomsen, C.; Ståhlberg, F.; Achten, E. Noninvasive MRI Thermometry with the Proton Resonance Frequency (PRF) Method: In Vivo Results in Human Muscle. *Magn. Reson. Med.* **1995**, *33* (1), 74–81.

(22) Carter, D. L.; MacFall, J. R.; Clegg, S. T.; Wan, X.; Prescott, D. M.; Charles, H. C.; Samulski, T. V. Magnetic Resonance Thermometry During Hyperthermia for Human High-Grade Sarcoma. *Int. J. Radiat. Oncol.* **1998**, *40* (4), 815–822.

(23) Voloshin, Y. Z.; Belaya, I. G.; Krämer, R. H. *The Encapsulation Phenomenon*; Springer International Publishing: Cham, Switzerland, 2016.

(24) Bjerrum, J.; McReynolds, J. P.; Oppegard, A. L.; Parry, R. W. Hexamminecobalt(III) Salts. *Inorg. Synth.* **1946**, *II*, 216–221.

(25) Work, J. B.; McReynolds, J. P. Tris(ethylenediamine)cobalt(III) Chloride. *Inorg. Synth.* **1946**, *II*, 221–222.

(26) Bailar, J. C.; Work, J. B. Some Coördination Compounds of Cobalt Containing Trimethylenediamine and Neopentanediamine. *J. Am. Chem. Soc.* **1946**, *68* (2), 232–235.

(27) Geue, R. J.; Snow, M. R. Structure, Conformational Analysis and Optical Activity of a Bis(tridentate)cobalt(III) Complex. $(+)_{589}$-ΔλλBis[1,1,1-Tris(aminomethyl)ethane]cobalt(III) Chloride $(+)_{589}$-(*R*,*R*)-Tartrate Hydrate. *Inorg. Chem.* **1977**, *16* (2), 231–241.

(28) Geue, R. J.; Hambley, T. W.; Harrowfield, J. M.; Sargeson, A. M.; Snow, M. R. Metal Ion Encapsulation: Cobalt Cages Derived from Polyamines, Formaldehyde, and Nitromethane. *J. Am. Chem. Soc.* **1984**, *106* (19), 5478–5488.

(29) Gahan, L. R.; Harrowfield, J. M. Sepulchrate: Four Decades On. *Polyhedron* **2015**, *94*, 1–51.

(30) Cai, H.; Fissekis, J.; Conti, P. S. Synthesis of a Novel Bifunctional Chelator AmBaSar Based on Sarcophagine for Peptide Conjugation and ^{64}Cu Radiolabelling. *Dalton Trans.* **2009**, 5395–5400.

(31) Bottomley, G.; Clark, I.; Creaser, I.; Engelhardt, L.; Geue, R.; Hagen, K.; Harrowfield, J.; Lawrance, G.; Lay, P.; Sargeson, A.; See, A.; Skelton, B.; White, A.; Wilner, F. The Synthesis and Structure of Encapsulating Ligands: Properties of Bicyclic Hexamines. *Aust. J. Chem.* **1994**, *47* (1), 143–179.

(32) Qin, C.-J.; James, L.; Chartres, J. D.; Alcock, L. J.; Davis, K. J.; Willis, A. C.; Sargeson, A. M.; Bernhardt, P. V.; Ralph, S. F. An Unusually Flexible Expanded Hexaamine Cage and Its CuII Complexes: Variable Coordination Modes and Incomplete Encapsulation. *Inorg. Chem.* **2011**, *50* (18), 9131–9140.

(33) Krause, R.; Megargel, E. Student Synthesis of Tris(ethylenediamine)cobalt(III) Chloride. *J. Chem. Educ.* **1976**, *53* (10), 667.

(34) Masuda, Y.; Yamatera, H. ^{59}Co Nuclear Magnetic Resonance Study of the Interactions of the Tris(ethylenediamine)cobalt(III) Cation with Various Anions in Aqueous Solution. *J. Phys. Chem.* **1988**, *92* (7), 2067–2071.

(35) Kirby, C. W.; Puranda, C. M.; Power, W. P. Cobalt-59 Nuclear Magnetic Relaxation Studies of Aqueous Octahedral Cobalt(III) Complexes. *J. Phys. Chem.* **1996**, *100* (35), 14618–14624.

(36) Turner, J. J. Infrared Vibrational Band Shapes in Excited States. *Coord. Chem. Rev.* **2002**, *230* (1), 213–224.

(37) Alexander, J. J.; Gray, H. B. Electronic Structures of Hexacyanometalate Complexes. *J. Am. Chem. Soc.* **1968**, *90* (16), 4260–4271.

(38) Jameson, C. J.; Rehder, D.; Hoch, M. Isotope and Temperature Dependence of Transition-Metal Shielding in Complexes of the Type $M(XY)_6$. *J. Am. Chem. Soc.* **1987**, *109* (9), 2589–2594.

(39) Englman, R. Some Temperature Dependent Effects on the Optical Absorption Line Shape of Paramagnetic Ions. *Mol. Phys.* **1960**, *3* (1), 23–34.

(40) Koplitz, L. V.; Kim, K.; McClure, D. S. Temperature Dependence of 10*Dq* for Aqueous Hexaaquomanganese(II). *Inorg. Chem.* **1994**, *33* (4), 702–704.

(41) Holmes, O. G.; McClure, D. S. Optical Spectra of Hydrated Ions of the Transition Metals. *J. Chem. Phys.* **1957**, *26* (6), 1686–1694.

(42) Gütlich, P.; Garcia, Y.; Goodwin, H. A. Spin Crossover Phenomena in Fe(II) Complexes. *Chem. Soc. Rev.* **2000**, *29* (6), 419–427.

(43) Tezgerevska, T.; Alley, K. G.; Boskovic, C. Valence Tautomerism in Metal Complexes: Stimulated and Reversible Intramolecular Electron Transfer between Metal Centers and Organic Ligands. *Coord. Chem. Rev.* **2014**, *268*, 23–40.

(44) Ader, R.; Loewenstein, A. Nuclear Magnetic Relaxation Studies in Solutions of Symmetric Cobalt(III) Complexes. *J. Magn. Reson.* **1971**, *5* (2), 248–261.

(45) Au-Yeung, S. C. F.; Buist, R. J.; Eaton, D. R. Spin-Lattice Relaxation in Co Complexes of Low Symmetry. *J. Magn. Reson. (1969-1992)* **1983**, *55* (1), 24–38.

(46) Kazuo Nakamoto. *Infrared and Raman Spectra of Inorganic and Coordination Compounds,* 6th ed.; Wiley-VCH, 2009.

(47) Chen, Y.; Christensen, D. H.; Sørensen, G. O.; Nielsen, O. F.; Pedersen, E. The Skeletal Vibrational Spectra and Metal–Ligand Force Constants of Cobalt(III) Ammine Complexes. *J. Mol. Struct.* **1993**, *299*, 61–72.

(48) Stein, P.; Miskowski, V.; Woodruff, W. H.; Griffin, J. P.; Werner, K. G.; Gaber, B. P.; Spiro, T. G. Raman Antiresonance: De-enhancement of Raman Intensity by Forbidden Electronic Transitions. *J. Chem. Phys.* **1976**, *64* (5), 2159–2167.

(49) Drago, R. S. *Physical Methods for Chemists*, 2nd ed.; Saunders College Publishing, 1992.

(50) McHale, J. L. *Molecular Spectroscopy*, 2nd ed.; CRC Press: Boca Raton, 2017.

(51) Tokmakoff, A.; Fayer, M. D. Infrared Photon Echo Experiments: Exploring Vibrational Dynamics in Liquids and Glasses. *Acc. Chem. Res.* **1995**, *28* (11), 437–445.

(52) Inada, H.; Ohnishi, K.; Nomura, S.; Higuchi, A.; Nakano, H.; Shirota, Y. Photo- and Electro-Active Amorphous Molecular Materials: Morphology, Structures, and Hole Transport Properties of Tri(biphenyl-4-yl)amine. *J. Mater. Chem.* **1994**, *4* (2), 171–177.

(53) Petzelt, J.; Kamba, S.; Gregora, I. Infrared and Raman Spectroscopy of ILL-Ordered Crystals. *Phase Transitions* **1997**, *63* (1–4), 107–145.

(54) Borovik, A. S. Bioinspired Hydrogen Bond Motifs in Ligand Design: The Role of Noncovalent Interactions in Metal Ion Mediated Activation of Dioxygen. *Acc. Chem. Res.* **2005**, *38* (1), 54–61.

(55) Lucas, R. L.; Powell, D. R.; Borovik, A. S. Preparation of Iron Amido Complexes via Putative Fe(IV) Imido Intermediates. *J. Am. Chem. Soc.* **2005**, *127* (33), 11596–11597.

(56) Grahn, H.; Edlund, U.; Holak, T. A. A ^{59}Co NMR Chemical Shift and Relaxation Study of Preferential Solvation toward Tris(acetylacetonato)cobalt(III). *Magn. Reson. Chem.* **1987**, *25* (6), 497–502.

(57) Gonzalez, G.; Mayer, U.; Gutmann, V. Solvent Effects on the Structure of $Co(en)_3^{3+}$. *Inorg. Nucl. Chem. Lett.* **1979**, *15* (3), 155–159.

(58) Fawcett, W. R. Acidity and Basicity Scales for Polar Solvents. *J. Phys. Chem.* **1993**, *97* (37), 9540–9546.

(59) Mayer, U.; Gutmann, V.; Gerger, W. The Acceptor Number – A Quantitative Empirical Parameter for the Electrophilic Properties of Solvents. *Monast. Chem.* **1975**, *106* (6), 1235–1257.

(60) Kamlet, M. J.; Abboud, J. L.; Taft, R. W. The Solvatochromic Comparison Method. 6. The π* Scale of Solvent Polarities. *J. Am. Chem. Soc.* **1977**, *99* (18), 6027–6038.

(61) Kamlet, M. J.; Abboud, J. L. M.; Abraham, M. H.; Taft, R. W. Linear Solvation Energy Relationships. 23. A Comprehensive Collection of the Solvatochromic Parameters, π*, α, and β, and Some Methods for Simplifying the Generalized Solvatochromic Equation. *J. Org. Chem.* **1983**, *48* (17), 2877–2887.

(62) Taft, R. W.; Shuely, W. J.; Doherty, R. M.; Kamlet, M. J. Linear Solvation Energy Relationships. 39. A Multiple Substituent Parameter Equation for β Values (Hydrogen-Bond Acceptor Basicities) of XYZP=O Compounds. *J. Org. Chem.* **1988**, *53* (8), 1737–1741.

(63) Geue, R. J.; McCarthy, M. G.; Sargeson, A. M. Synthesis, Chiroptical Properties, and Electron Self-Exchange Reactivity of a Rigid Pentacyclic Metal Ion Cage System with D_3 Symmetry. *J. Am. Chem. Soc.* **1984**, *106* (26), 8282–8291.

(64) Bernhardt, P. V.; Bygott, A. M. T.; Geue, R. J.; Hendry, A. J.; Korybut-Daszkiewicz, B. R.; Lay, P. A.; Pladziewicz, J. R.; Sargeson, A. M.; Willis, A. C. Stabilization of Cobalt Cage Conformers in the Solid State and Solution. *Inorg. Chem.* **1994**, *33* (20), 4553–4561.

(65) Sargeson, A. M.; Lay, P. A. Dependence of the Properties of Cobalt(III) Cage Complex as a Function of the Derivatization of Amine Substituents. *Aust. J. Chem.* **2009**, *62* (10), 1280–1290.

(66) Algarra, A. G. Computational Insights into the Isomerism of Hexacoordinate Metal–Sarcophagine Complexes: The Relationship between Structure and Stability. *Eur. J. Inorg. Chem.* **2015**, *2015* (3), 503–511.

(67) Ling, I.; Sobolev, A. N.; Hashim, R.; Harrowfield, J. M. Stereochemistry of Cage Amine Complexes – Probing the Ligand Conformational Flexibility with Hydrogen Bonds. *Cryst. Eng. Comm.* **2014**, *16* (48), 11058–11063.

(68) Sando, G. M.; Zhong, Q.; Owrutsky, J. C. Vibrational and Rotational Dynamics of Cyanoferrates in Solution. *J. Chem. Phys.* **2004**, *121* (5), 2158–2168.

(69) King, J. T.; Ross, M. R.; Kubarych, K. J. Water-Assisted Vibrational Relaxation of a Metal Carbonyl Complex Studied with Ultrafast 2D-IR. *J. Phys. Chem. B* **2012**, *116* (12), 3754–3759.

(70) Bergman, L.; Nemanich, R. J. Raman Spectroscopy for Characterization of Hard, Wide-Bandgap Semiconductors: Diamond, GaN, GaAlN, AlN, BN. *Annu. Rev. Mater. Sci.* **1996**, *26* (1), 551–579.

(71) Lee, K. C.; Sussman, B. J.; Nunn, J.; Lorenz, V. O.; Reim, K.; Jaksch, D.; Walmsley, I. A.; Spizzirri, P.; Prawer, S. Comparing Phonon Dephasing Lifetimes in Diamond Using Transient Coherent Ultrafast Phonon Spectroscopy. *Diam. Relat. Mater.* **2010**, *19* (10), 1289–1295.

(72) Iida, M.; Nakamori, T.; Mizuno, Y.; Masuda, Y. Ion-Pairing Effects on the ^{59}Co Electric Field Gradients in the NMR Relaxations of Tripositive Cobalt(III) Complex Ions. *J. Mol. Liq.* **1995**, *65–66*, 269–272.

(73) Laurence, C.; Gal, J.-F. *Lewis Basicity and Affinity Scales*; Wiley, 2010.

(74) Atzori, M.; Tesi, L.; Benci, S.; Lunghi, A.; Righini, R.; Taschin, A.; Torre, R.; Sorace, L.; Sessoli, R. Spin Dynamics and Low Energy Vibrations: Insights from Vanadyl-Based Potential Molecular Qubits. *J. Am. Chem. Soc.* **2017**, *139* (12), 4338–4341.

(75) Atzori, M.; Benci, S.; Morra, E.; Tesi, L.; Chiesa, M.; Torre, R.; Sorace, L.; Sessoli, R. Structural Effects on the Spin Dynamics of Potential Molecular Qubits. *Inorg. Chem.* **2018**, *57* (2), 731–740.

(76) Escalera-Moreno, L.; Baldoví, J. J.; Gaita-Ariño, A.; Coronado, E. Spin States, Vibrations and Spin Relaxation in Molecular Nanomagnets and Spin Qubits: A Critical Perspective. *Chem. Sci.* **2018**, *9* (13), 3265–3275.

(77) Berliner, L. J. *In Vivo EPR (ESR)*, 1st ed.; Springer, 2003; Vol. 18.

(78) Kiesewetter, M. K.; Corzilius, B.; Smith, A. A.; Griffin, R. G.; Swager, T. M. Dynamic Nuclear Polarization with a Water-Soluble Rigid Biradical. *J. Am. Chem. Soc.* **2012**, *134* (10), 4537–4540.

(79) Zagdoun, A.; Casano, G.; Ouari, O.; Lapadula, G.; Rossini, A. J.; Lelli, M.; Baffert, M.; Gajan, D.; Veyre, L.; Maas, W. E.; Rosay, M.; Weber, R. T.; Thieuleux, C.; Coperet, C.; Lesage, A.; Tordo, P.; Emsley, L. A Slowly Relaxing Rigid Biradical for Efficient Dynamic Nuclear Polarization Surface-Enhanced NMR Spectroscopy: Expeditious Characterization of Functional Group Manipulation in Hybrid Materials. *J. Am. Chem. Soc.* **2012**, *134* (4), 2284–2291.

(80) Dane, E. L.; Corzilius, B.; Rizzato, E.; Stocker, P.; Maly, T.; Smith, A. A.; Griffin, R. G.; Ouari, O.; Tordo, P.; Swager, T. M. Rigid Orthogonal Bis-TEMPO Biradicals with Improved Solubility for Dynamic Nuclear Polarization. *J. Org. Chem.* **2012**, *77* (4), 1789–1797.

(81) Corzilius, B.; Smith, A. A.; Barnes, A. B.; Luchinat, C.; Bertini, I.; Griffin, R. G. High-Field Dynamic Nuclear Polarization with High-Spin Transition Metal Ions. *J. Am. Chem. Soc.* **2011**, *133* (15), 5648–5651.

(82) Corzilius, B.; Michaelis, V. K.; Penzel, S. A.; Ravera, E.; Smith, A. A.; Luchinat, C.; Griffin, R. G. Dynamic Nuclear Polarization of ^{1}H, ^{13}C, and ^{59}Co in a Tris(ethylenediamine)cobalt(III) Crystalline Lattice Doped with Cr(III). *J. Am. Chem. Soc.* **2014**, *136* (33), 11716–11727.

(83) Balasubramanian, G.; Lazariev, A.; Arumugam, S. R.; Duan, D. Nitrogen-Vacancy Color Center in Diamond–Emerging Nanoscale Applications in Bioimaging and Biosensing. *Curr. Opin. Chem. Biol.* **2014**, *20*, 69–77.

(84) Schirhagl, R.; Chang, K.; Loretz, M.; Degen, C. L. Nitrogen-Vacancy Centers in Diamond: Nanoscale Sensors for Physics and Biology. *Annu. Rev. Phys. Chem.* **2014**, *65* (1), 83–105.

CHAPTER 3 – Temperature-Driven Molecular Structure in Cobalt-59 NMR Thermometers

3.1. Overview

Cobalt-59 nuclei are known for extremely thermally sensitive chemical shifts (δ), which in the long term could yield novel magnetic resonance thermometers for bioimaging applications. In this chapter, we apply extended X-ray absorption fine-structure spectroscopy (EXAFS) for the first time to probe the exact variations in physical structure that produce the exceptional thermal sensitivity of the ^{59}Co-NMR chemical shift. We apply the technique to five Co^{3+} complexes: $[Co(NH_3)_6]Cl_3$ (**1**), $[Co(en)_3]Cl_3$ (**2**) (en = ethylenediamine), $[Co(tn)_3]Cl_3$ (**3**) (tn = trimethylenediamine), $[Co(tame)_2]Cl_3$ (**4**) (tame = 1,1,1-tris(aminomethyl)ethane), and [Co(diNOsar)]Cl_3 (**5**) (diNOsar = dinitrosarcophagine). The solution-phase EXAFS data reveal increasing Co–N bond distances for these aqueous complexes over a ~50 °C temperature window, expanding by $\Delta r_{(Co–N)}$ = 0.0256(6) Å, 0.0020(5) Å, 0.0084(5) Å, 0.0006(5) Å, and 0.0075(6) Å for **1–5**, respectively. Computational analyses of the structural changes reveal that increased connectivity between the donor atoms encourages complex structural variations. These results imply that rich temperature-dependent structural variations define the ^{59}Co-NMR thermometry in macrocyclic complexes.

3.2. Introduction

Magnetic resonance imaging (MRI) thermometry would enable minimally invasive thermal therapies to treat benign and malignant disease.[1–5] In order to develop applicable molecular probes for this technology, it is essential to understand how to program variable-temperature MR properties via molecular structure design. ^{59}Co is a promising nucleus for developing this technology as it has a stronger temperature-dependent chemical shift ($\Delta\delta/\Delta T$) than any other nucleus in a closed-shell molecule and an enormous (~18,000 ppm) chemical shift window.[6–8] These advantages are coupled with numerous others for the ^{59}Co isotope, including a relatively high nuclear magnetic moment ($I = {}^7/_2$, $\mu = 4.62\ \mu_N$), 100% natural abundance,

and high receptivity (0.278 relative to ^{1}H).[8] Hence, the nucleus is worth of considerable further investigation.

The present record for temperature sensitivity of the ^{59}Co chemical shift $\Delta\delta/\Delta T$ is 3.15 ppm/°C for $Co(acac)_3$.[9] Toward eventual *in vivo* utility, it is necessary to develop design principles for higher $\Delta\delta/\Delta T$ values. Furthermore, owing to the toxicity of free cobalt ions in the body,[10] and the desire for an MR probe to maintain functionality, design strategies should ideally harness macrocyclic ligands that yield extremely stable complexes. With these points in mind, we recently reported that $\Delta\delta/\Delta T$ for the ^{59}Co nucleus is enhanced for macrocyclic chelates as opposed to mono- or bidentate ligands.[11]

Theoretical models of temperature sensitivity in transition-metal NMR decades ago proposed that $\Delta\delta/\Delta T$ stems from expansions of M–L bonds (*Figure 3.1*).[12–17]

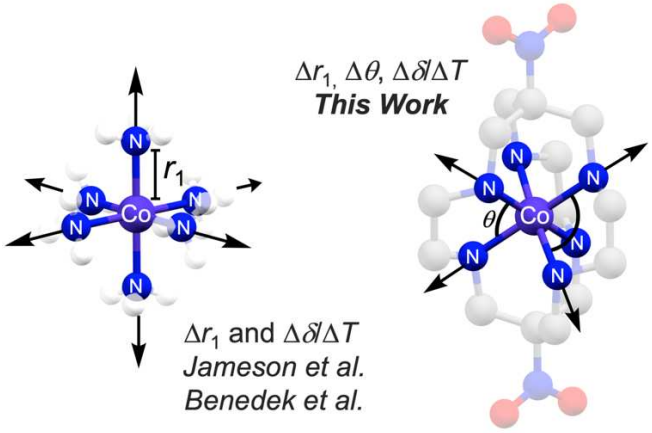

Figure 3.1. Initial modes by Jameson et al.[12,13] and Benedek et al.[14] rationalize ^{59}Co $\Delta\delta/\Delta T$ on the basis of coordination-geometry expansion (Δr_1, *above*). In this paper we use EXAFS spectroscopy to test the contribution(s) of bond expansion to $\Delta\delta/\Delta T$. Faded blue, red, grey, and white spheres represent N, O, C, and H atoms in the ligand backbones for the shown molecules.

In this light, the observed enhancement of $\Delta\delta/\Delta T$ for a macrocyclic ligand[11] over mono or bidentate ligands is counterintuitive, as the rigid structure is envisioned to resist M–L expansion. However, temperature-dependent changes in bond distance for a macrocycle should also induce changes to M–L bond angles. Hence, relatively complex structural changes, including changes to N–Co–N bond angles, could be adjusting the $\delta(^{59}Co)$ as a function of temperature in addition to simple bond expansion. Yet, to the best of

our knowledge, no studies to directly correlate variable-temperature structure to $\Delta\delta/\Delta T$ (^{59}Co) have ever been performed.

Herein, we report a variable-temperature structural study of five Co^{3+} complexes via extended X-ray absorption fine-structure (EXAFS) spectroscopic measurements of $[Co(NH_3)_6]Cl_3$ (**1**),[18] $[Co(en)_3]Cl_3$ (**2**, en = ethylenediamine),[19] $[Co(tn)_3]Cl_3$ (**3**, tn = trimethylenediamine),[20] $[Co(tame)_2]Cl_3$ (**4**, tame = triaminomethylethane),[21] and $[Co(diNOsar)]Cl_3$ (**5**, diNOsar = dinitrosarcophagine).[22] EXAFS spectroscopy is a widely employed technique for elucidating the coordination spheres of metal ions in solution-phase samples.[23–27] Here, we apply this spectroscopic technique for the first time in studying the actual structural changes that govern $\Delta\delta/\Delta T$. The studied complexes were selected to provide a structural progression of increasing connectivity between the donor atoms and to best compare structural changes with previously determined values of $\Delta\delta/\Delta T$.[11] Herein, we find that the magnitude of change in Co–N bond distance (Δr_1) does not directly correlate to $\Delta\delta/\Delta T$. Instead, computational analyses guided by the EXAFS results indicate structurally unique distortions occur, enabled by chelating and macrocyclic ligands.

3.3. Experimental Section

3.3.1. General Considerations

Studied compounds in this chapter were either purchased from commercial chemical vendors or synthesized according to previously reported literature preparations. Potassium hexacyanocobaltate(III) ($K_3[Co(CN)_6]$) and hexamminecobalt(III) chloride ($[Co(NH_3)_6]Cl_3$, **1**) were purchased from commercial vendors and used as received. ^{1}H-NMR, ^{13}C-NMR, and ^{59}Co-NMR spectra were collected on a 400 MHz Bruker spectrometer. UV-vis spectra were collected on an Agilent 8453 Spectrophotometer, and IR spectra were collected via ATR on a Bruker Tensor II FTIR.

3.3.2. Preparation of Compounds

Synthesis of compounds **1–5** studied within this chapter were prepared according to the methods reported in the Experimental Section of Chapter 2.

3.3.3. EXAFS Measurements

XAFS measurements made on compounds **1–5** were collected from samples of each compound which were prepared as described below. Compound **1** was purchased from a chemical vendor and compounds **2–5** were synthesized as reported above. All hydrate-forming compounds were thoroughly dried of water in a high-vac oven over 24 hrs. Sample amounts of each compound were then accurately weighed out and prepared as 15 mM solutions in Millipore purified deionized water. Fluorescence mode XAFS measurements require dilute atomic concentrations of the absorbing atom in order to minimize self-absorption artefacts. Seeking an atomic concentration below 5% for our studies, a 15 mM concentration was chosen for these experiments as calculated for an atomic concentration of 2.5–2.7% for the absorbing cobalt atom.

Variable-temperature X-ray absorption fine structure (XAFS) measurements were conducted at Beamline 9-BM of the Advanced Photon Source (APS) at Argonne National Laboratory. 4 mL aliquots of the 15 mM solutions of **1–5** were transferred into a polyetheretherketone (PEEK) cuvette and capped with an insertable thermocouple. Energy calibration was achieved by alignment to the Co *K*-absorption edge of 7708.78 eV using a cobalt foil standard. The beryllium windowed four-element silicon-drift fluorescence detector was positioned at the center of the PEEK cuvette. Subsequent Co *K*-edge X-ray absorption measurements were recorded from fluorescence detection of the Co-*K*α emission. Individual scans occurred in steps of 0.05 $Å^{-1}$ with 0.5 s integration times over *k*-range 0–15 $Å^{-1}$. The integration time was progressively increased as energy increased through the EXAFS region of the scan. Each experiment consisted of 8–12 collected scans per sample measurement at each temperature. Temperature-specific XAFS measurements were made at 13, 35, and 57 °C. Thermal regulation of the contained sample occurred by fitting the cuvette to a water-jacketed cuvette holder equipped with a temperature-controllable water recirculator. Thermal equilibration of samples was monitored by thermocouple readouts of the solution before preforming XAFS experiments. Sample temperatures were closely monitored throughout the experiment and did not deviate more than ±1.0 °C.

3.3.4. EXAFS Fitting and Data Analysis

Extended X-ray absorption fine structure (EXAFS) spectra were acquired from the variable-temperature XAS data in which the EXAFS regions were analyzed. Scans for each compound were averaged before rebinning the k^2-weighted EXAFS data. All data reduction and fits were made using the Demeter: XAS Data Processing and Analysis software using IFEFFIT.[28] In the completed investigation of dynamic structural change between differing ligand compositions, the Fourier transform (FT) data of all solution-phase EXAFS spectra were fit against their respective crystal structures as each has been previously reported.[18–22] Calculated scattering paths from these experimental solid-stated models were then used to construct fits elucidating the relative changes in bond lengths and degrees of atomic displacements between each solution-phase compound. The calculated scattering paths from the crystal-structure models were used to construct a complete fit for all spectra over *k*-range of 2–12 $Å^{-1}$ (*Figures A2.2–A2.16*). The magnitudes and real parts of the Fourier transforms of $k^2\chi(k)$ along with the resulting fits are shown. All *R*-space fits were taken with *k*, k^2, k^3-weighting from which S_0^2, E_0, ΔR, and σ^2 parameters were evaluated from the fitting software Artemis.[28] Atomic distances *R* were determined from ΔR of the fit, where $\Delta R = R - R_{\text{eff}}$ and R_{eff} is the atomic distance for a specified set of atoms in the reference model structure, and was determined with the ATOMS[29] function in Artemis, using the provided crystal structure data.[18–22] In the fitting process, ΔR was evaluated using a proportionality coefficient α (a solvable parameter) where $\Delta R = \alpha \times R_{\text{eff.}}$ Ultimately, absolute atomic distances were evaluated from $R = R_{\text{eff}}(\alpha + 1)$.

The chosen experimental models provide acceptable fits across all solution-phase compounds of the primary and secondary coordination shells within 1–3 Å of the FT data presented in *R*-space as radial structure functions, not radial distributions. All fits were made with single scattering paths to known atomic ligand shells and were complemented with smaller-angle double scattering type pathways. The inclusion of these secondary scattering paths inherently increases the necessary fitting range and are greater for larger molecules e.g., **4** and **5**. As a result, **1** was only fit only to single scattering paths (i.e., Co–N) over an *R*-range of 1.1–2 Å without double scattering pathways. Owing to solvent effects, challenges in fitting of **1**

beyond the first coordination shell were expected and are reflected in the fit parameters.[23,30–32] For all complexes, we assumed that all Co–N bond distances were equivalent, owing to the homoleptic nature of the complexes and the lack of any expected Jahn-Teller activity for the Co^{3+} ion.

Uncertainty in the values of Co–N bond distances r_1 (*Table A2.2*) were determined from the error in the proportionality coefficient α yielded from the fits. In Artemis, the statistically determined uncertainty in the fit parameters are multiplied by $\sqrt{\chi_\nu^2}$ to account for systematic errors. These systematic errors result largely from imperfect background subtraction used to extract the EXAFS from the X-ray absorption and error and imperfect calculations of the photoelectron phase shifts and scattering amplitudes used to fit the data. Here, the same background subtraction procedure was used for all data sets and fits of the three EXAFS temperature measurement (13, 35, and 57 °C) were made in tandem to the same respective crystal structure model. Thus, these systematic errors will be the same for fits to a given compound at all temperatures, and they will cancel in a relative comparison. In this case, noise in the data and the stability in the energy axis *E* (eV) over the course of the experiments determine the accuracy of the relative bond-length measurements. In VT EXAFS studies, accuracies within ±0.0001 Å have been observed.[33–36] Due to the inherent stability of the X-ray energy estimated to be within 0.05 eV, the accuracies of relative bond distance changes are within ±0.0005 Å in the absence of noise and systematic errors.[37] To account for noise in the data, we have divided the uncertainty in α calculated by Artemis by $\sqrt{\chi_\nu^2}$, and used that value for calculation of the uncertainty in Δ*R*. Based on the assumption that systematic errors are greatly reduced in a relative comparison of the bond lengths, we have added the estimated uncertainties due to energy stability and noise to obtain the total uncertainty reported for relative differences in Co–N bond lengths for a given molecule.

3.3.5. Structure Optimizations and SHAPE Analysis

Structural optimizations of complexes **1–5** were made at the low (13 °C) and high temperature (57 °C) bond lengths elucidated from solution-phase EXAFS bond distance determination of r_1. Optimizations

of each structure were made with Gaussian 16 electronic structure package[38] using the ωB97XD density functional[39] and 6-311+g* basis set (*Tables A2.24–A2.33*).[40] Changes in the N–Co–N angles of bidentate ligands (the "bite" angles) of **2**, **3, 4**, and **5** were determined from the optimized structures (*Tables A2.19 – A2.21 and Figure A2.17*). The change in coordination geometries between the minimized structures at 13 and 57 °C were then analyzed via SHAPE[41–43] to determine relative changes between idealized octahedral and trigonal prismatic symmetries (*Tables A2.22–A2.23*).

3.4. Results and Discussion

Fluorescence detection was used to measure the Co *K*-edge EXAFS spectra of **1–5**. The EXAFS results from photoelectrons scattered between the central absorbing cobalt ion and nearby atoms and can therefore be used to elucidate interatomic distances within the molecules. For each complex, Fourier transform (FT) analysis of EXAFS spectra yielded an intense primary feature at apparent *R* values of 1.5–2.0 Å and many less-intense features at greater *R* values. The highest intensity peaks stem from single scattering paths from the immediate coordination shell of the cobalt ion (r_1 of nitrogen on **5**). Additional single scattering paths occur at longer distances from the cobalt ion, such as from ligand-based carbon atoms (e.g., r_2 and r_3 of ethylene carbons on **5**) and show up between *R* values of 2.2–3.3 Å. Finally, proximate counterions (e.g., Cl^-) or other molecules in the solvent cage produce variable features at the highest *R* values. The EXAFS spectra were fit to extract Co–N bond distances using the reported crystal structures of **1–5**. The resulting determined distances largely agree with reported bond lengths from the experimental literature structure models. For example, the EXAFS-reported Co–N bond length of **5** at 13 °C is r_1 = 1.9701(5) Å, which is within ±0.012 Å to the reported structure of **5** at 1.982 Å (*Figure 3.2*).[22]

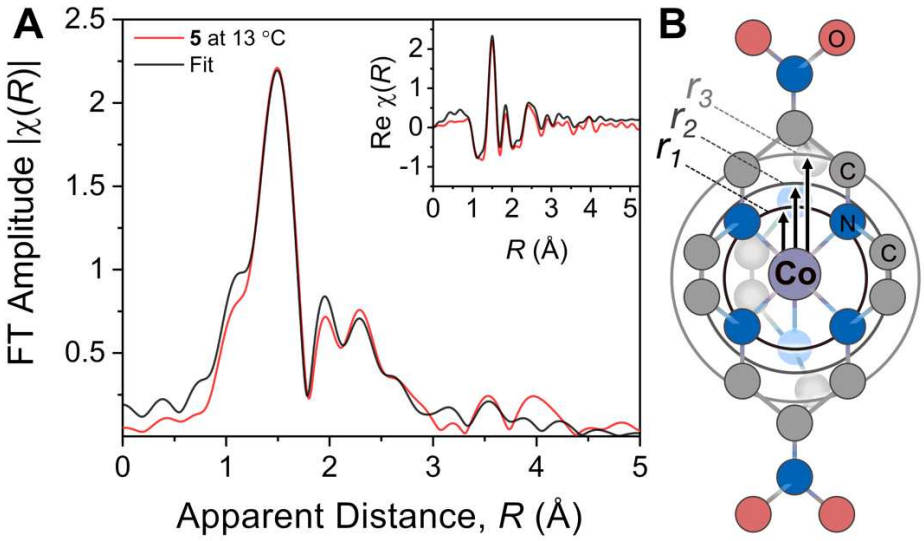

Figure 3.2. a. Radial structure function plot shown as Fourier Transform EXAFS data (*red trace*) of **5** at 13 °C and fit (*black trace*) with k^2-weighting over *k*-range of 2–12 Å^{-1}. *Inset:* Fit of real part of the FT EXAFS data. ***b.*** Highlighted intramolecular atomic single scattering distances of **5** from the primary Co–N_6 shell r_1, followed by second and third shells of methylene carbon atoms r_2 and r_3, respectively.

The correlation between EXAFS and diffraction data also holds for **1–4**, where r_1 values are in agreement with reported Co–N bond lengths (1.96-1.99 Å).[18–21] Distances to secondary and tertiary atomic shells of **5** at 13 °C are r_2 = 2.7984(5) Å and r_3 = 2.9777(5) Å. These values are also in approximate agreement with the Co···C_{ligand} distances of the crystal structure at 2.815 and 2.994 Å. Note that even though r_1, r_2, and r_3 are close to the crystal structure values, slight differences are to be expected given that these data were recorded in solution. Finally, the data are in agreement with prior single-temperature-only EXAFS (and X-ray absorption near-edge structure) investigations.[44–46]

Variable-temperature EXAFS studies were performed to study the temperature dependence of the determined Co–N distances and other structural features in **1–5**. These measurements were conducted in MilliQ deionized water over a ~50 °C temperature window at three temperatures, 13, 35, and 57 °C. Structural analyses (e.g., those for **5**) were made at each temperature measurement, providing a determination of relative Co–N bond distance as a function of temperature. Fitting these spectra using the reported crystal structures as starting points enabled us to probe the temperature dependence of the first coordination shells in **1–5**.

The fits show a complex set of increasing scattering path distances with temperature over the 13–57 °C range (*Figures A2.2–A2.16*). Importantly, an analysis of temperature-driven bond distance shows an increase in r_1 (the Co–N_6 primary coordination sphere) with increasing temperature. For **5**, we determined an increase in the Co–N bond distance from 1.9701(5) Å at 13 °C, to 1.9751(6) Å at 35 °C, and finally to 1.9776(6) at 57 °C. Similar temperature-sensitive behavior of the primary coordination sphere is seen in **1–4** (*Table A2.1*). At the lowest temperature, 13 °C measurement, Co–N_6 coordination distances are r_1 = 1.9588(5) Å for **1**, 1.9694(5) Å for **2**, 1.9825(5) Å for **3**, and 1.9700(5) Å for **4**. In the highest-temperature, 57 °C measurement, the Co–N_6 distances are expanded: r_1 = 1.9836(5) Å for **1**, 1.9714(5) Å for **2**, 1.9910(5) Å for **3**, and 1.9707(5) Å for **4**. The total changes in the Co–N atomic distances over the ~50 °C range are therefore Δr_1 = +0.0248(6), +0.0020(5), +0.0085(5), +0.0007(5), and +0.0075(6) Å for **1–5**, respectively (*Figure 3.3*).

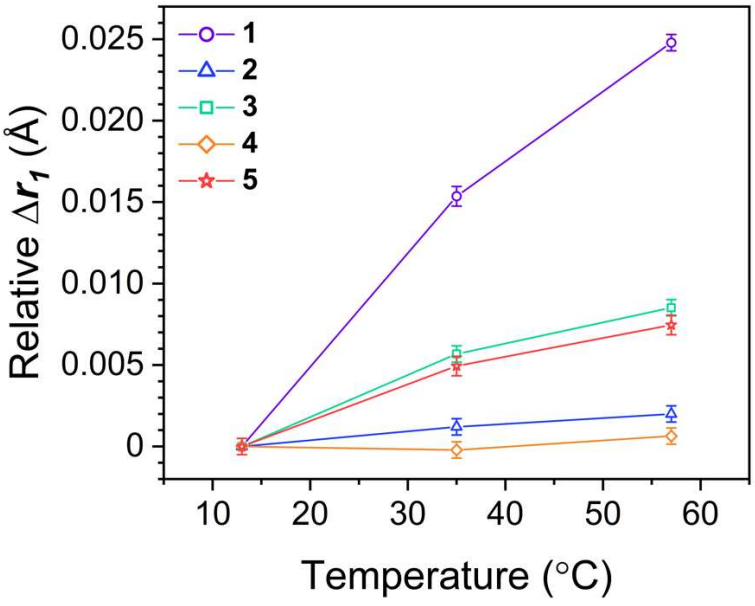

Figure 3.3. Relative changes in Co–N_6 bond length r_1 (Δr_1, Å) for solution-phase samples of **1**–**5** across a 13–57 °C temperature range with error bars at each measurement.

These data indicate the highest change in Co–N bond distances for **1**, in which all N-donor atoms are monodentate NH_3 ligands. Significantly less bond distance variation is observed for **2–5**, which contain chelating or macrocyclic ligands. These variations may seem minute from an absolute comparison to crystal

structure models where precision of atomic distances is commonly difficult to resolve below ~0.001 Å. Yet, *relative* changes in atomic distances are highly accurate when determined by EXAFS with the appropriate fitting methods (*Table A2.3*). We report relative uncertainties as low as ±0.0005 Å as deduced from the EXAFS fits parameters, including noise and energy instability.[32–35,37]

Similar to the Co–N scattering paths, which expand for all compounds **1–5**, the scattering paths from carbon atoms in chelating ligand backbones (e.g., r_2 and r_3 for **5**) also increase with temperature (*Tables A2.4–A2.18*). For **2**, the distances of carbon ligand atoms increase over a range of +0.0029(6) Å. For **3**, there are two unique carbon-atom single scattering paths which arise from the carbons adjacent to the N-donor atoms (r_2), and the bridging methylene carbon atoms (r_3), between them. With increasing temperature, both paths increase by Δr_2 = +0.0130(6) Å and Δr_3 = +0.0145(6) Å, respectively. For **4**, there are individual single scattering paths to three different shells of ligand carbon atoms. At increasing distances, these paths originate from the methylene carbon atoms bound to the N-donor atoms (r_2), the apical quaternary carbons of each tame ligand (r_3), and finally the axial methyl carbons (r_4). For these carbon atoms, all paths increase by +0.0010(5) Å for Δr_2 and Δr_3 and +0.0015(5) Å for Δr_4. Finally, for **5**, there are three independent single scattering paths arising from the carbon atoms of the ethylenediamine fragments (r_2), the apical methylene carbons (r_3), and the NO_2-functionalized quaternary carbons (r_4). Similar to changes in atomic ligand displacements of other complexes, these distances all increase with increasing temperature. For **5**, the differences between the high and low temperature measurements are a positive increase of +0.0110(6) Å for Δr_2, Δr_3 and Δr_4**.**

The EXAFS data provide some support the individual models of Jameson et al. and Benedek et al. while simultaneously suggesting a richer picture of structural dynamics responsible for $\Delta\delta/\Delta T$.[12–14] For example, the Δr_1 values determined for **1–5** vary within 0.0006 to 0.0256 Å over 13–57 °C. Most importantly, however, the observed variation in structure is inconsistent with the previous analyses of $\Delta\delta/\Delta T$. For **1–5**, the $\Delta\delta/\Delta T$ varies as 1.44(2), 1.38(1), 1.30(2), 1.71(1), and 2.04(2) ppm/°C, respectively.[11] This trend in $\Delta\delta/\Delta T$ is **3** < **2** < **1** < **4** < **5**, with the macrocyclic sarcophagine ligand engendering the highest

temperature dependence of $\delta(^{59}\text{Co})$. The trend in $\Delta\delta/\Delta T$ does not correspond to Δr_1 over the same temperature window, which varies as **4** < **2** < **5** < **3** < **1**.

A straightforward method to reconcile the disagreement between $\Delta\delta/\Delta T$ and $\Delta r_1/\Delta T$ is to conclude that the change in Co–N bond distance is not the sole design criterion for enhancing $\Delta\delta/\Delta T$ for a transition-metal nuclear spin. Note that the chemical shift of octahedral ^{59}Co nuclei stems directly the ligand-field splitting Δ_o.[47–50] Hence, *any* potential temperature-dependent structural changes that affect metal-ligand overlap (and hence modulate Δ_o) could impact $\delta(^{59}\text{Co})$. As represented in this work, the lacking correspondence between Δr_1 and $\Delta\delta/\Delta T$ could signal complex structural dynamics beyond simple Co–N expansion, e.g., changes in N–Co–N bond angles.

Computational analyses of the structural variations in **1–5** were performed to gain deeper insight into the motions that accompany lengthening of the Co–N bonds. We used the ωB97XD functional[39] with the 6-311+g* basis set[40] to compute the optimized geometries of **1–5** at the lowest and highest temperatures of EXAFS measurement while restraining the Co–N distances to those determined from r_1 (see experimental section). All other structural distances and angles were then allowed to freely refine during optimization. These computations reflect complex structural dynamics as a function of temperature for the macrocyclic and chelated complexed **2–5** (*Figure 3.4*).

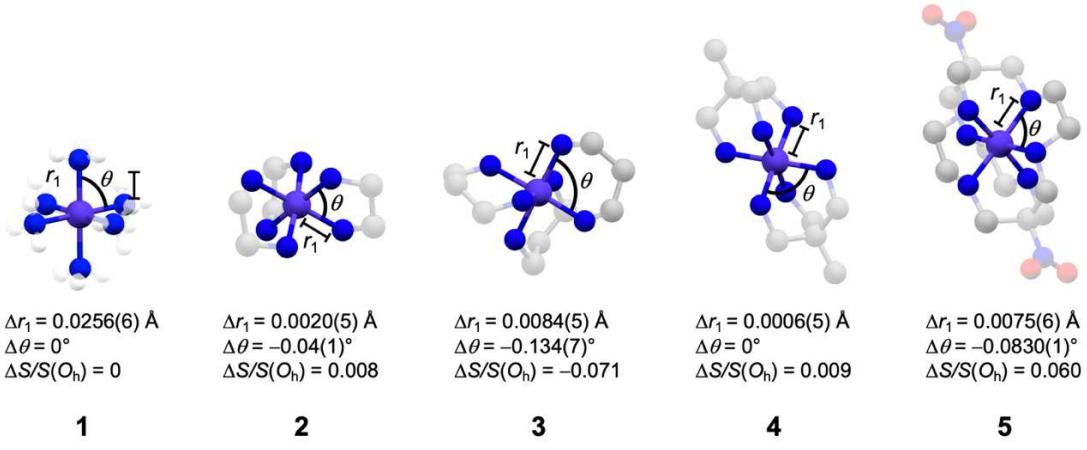

Figure 3.4. Comparative geometric distortions of **1**–**5** from 13–57 °C represented by the change in Co – N bond length Δr_1, average chelate bite angle $\Delta\theta$, and relative deviations from O_h geometry $\Delta S/S(O_h)$ (relative to the 13 °C $S(O_h)$ value). Purple and blue atoms represent Co and N atoms in the first coordination shell, respectively. Faded blue, red, grey, and white spheres represent N, O, C, and H atoms in the ligand backbones for the shown molecules. Hydrogens on structure **2**–**5** are omitted or clarity.

For example, in **2** and **3** the ligand bite angles decrease with increasing Co–N bond length, by –0.04(1)° for **2** and –0.134(7)° for **3** (*Tables A2.19–A2.20*). This change is also seen for the ethylene-bridged amines in **5**, which change by –0.0830(1)° for **5** (*Table A2.21*). Complexes **2** and **5** share ethylene-bridged donor atoms, yet the bite angles change more significantly in **5** which may stem from the additional interconnectivity of the macrocyclic ligand. The least amount of *average* change in chelate bite angle (over the whole molecule) is exhibited by the tridentate ligand of **4** despite individual N–Co–N bite angles changing by 0.018° (*Figure A2.17*). In contrast, **1**, wherein no inter-ligand connectivity is present, exhibits a simple expansion of Co–N distances with increasing temperature.

Changes in the optimized coordination geometries as a function of temperature were also investigated via SHAPE analysis.[41,42] SHAPE is a continuous symmetry measurement tool that enables comparisons of geometric distortions between two idealized geometries.[43] We chose octahedral and trigonal-prismatic idealized structures as the two points of comparison, given the possible enantiomeric and diastereomeric configurations of **2–5**.[51–54] SHAPE analyses are used to evaluate how close a particular structure is to idealized symmetry to octahedral or trigonal prismatic geometries. A shape measure, S, of 0 for a given geometry indicates a perfect match, whereas a large S highlights strong disagreement in the structural assignment.

The analyses revealed two key structural features in **1–5**. First, the immediate coordination environments of **1–5** are better described as O_h symmetry than D_{3h} trigonal-prismatic symmetry, since $S(O_h)$ is < 0.3 for **1–5** in contrast to $S(D_{3h})$, which is greater than 10 for **1–5** (*Tables A2.22–A2.23*). Second, the variable-temperature analyses show small but unique structural deviations in **1–5** with increasing temperatures. For the temperature-specific optimized structures of **1**, for example, SHAPE analysis reveals no deviation from O_h symmetry with increasing temperature. This lack of change is represented by zero change in the shape measure for the O_h geometry relative to the $S(O_h)$ at 13 °C, $\Delta S(O_h)/S(O_h)$. In contrast, **2–5** exhibit more noticeable distortions in coordination geometry. Complex **3** approaches O_h symmetry with increasing temperature, represented by $\Delta S/S(O_h) = –0.071$. Complex **4** shows a comparable scale of change

to **2**, distorting away from O_h symmetry ($\Delta S/S(O_h) = 0.009$) with warming, while **5** shows the greatest deviation away from O_h symmetry ($\Delta S/S(O_h) = 0.060$). With increasing temperature, **5** also shows the strongest shift towards trigonal-prismatic D_{3h} symmetry in the series of studied complexes ($\Delta S/S(D_{3h}) = -0.005$) (*Tables A2.22–A2.23*).

These results highlight two important points for future NMR thermometer development. First, the observed distortions show that relatively small structural changes have significant impacts on ^{59}Co-NMR chemical shifts. Hence, the data provide important experimental corroboration of the initial theoretical arguments by Benedek and Jameson.[12–14] Second, the changes highlight that $\Delta\delta/\Delta T$ in macrocyclic and chelated ligand systems cannot be accounted for by unidirectional M–L bond displacements alone.

A new molecular design strategy is potentially underlined in this latter point. If changes in M–L bond distances are not the essential molecular feature dictating $\Delta\delta/\Delta T$, then the changes in L–M–L angles seem like the next-best feature to tune. Here, one could envision harnessing structural strain in chelating and macrocyclic ligands to spring-load changes in bond distances *and* angles as a function of temperature. Studies evidencing significant strain in chelate and macrocyclic ligands are abundant in the literature,[55–58] underlining the promise of potentially harnessing this feature in metal complexes with significant chemical stability *in vivo*.

3.5. Conclusion

The foregoing study is the first systematic structural examination of ^{59}Co $\Delta\delta/\Delta T$ through variable-temperature EXAFS measurements. Importantly, we find that temperature-dependent changes in Co–N bond distances Δr_1 for **1–5** do not directly follow $\Delta\delta/\Delta T$ in these complexes. Indeed, following computational analyses, the foregoing data reveal a new picture of $\delta(^{59}\text{Co})$ thermometry that involves changes in both M–L bond distances and angles between donor atoms. Importantly, the results suggest future strategies to harness molecular strain to engender higher $\Delta\delta/\Delta T$. In the long run, this concept will be employed in hybrid synthetic/theoretical studies to design macrocyclic complexes with high $\Delta\delta/\Delta T$.

References

(1) Rieke, V.; Pauly, K. B. MR Thermometry. *J. Magn. Reson. Imaging* **2008**, *27* (2), 376–390.

(2) Denis de Senneville, B.; Quesson, B.; Moonen, C. T. W. Magnetic Resonance Temperature Imaging. *Int. J. Hyperthermia* **2005**, *21* (6), 515–531.

(3) Odéen, H.; Parker, D. L. Magnetic Resonance Thermometry and Its Biological Applications – Physical Principles and Practical Considerations. *Prog. Nucl. Magn. Reson. Spectrosc.* **2019**, *110*, 34–61.

(4) Yuan, J.; Mei, C.-S.; Panych, L. P.; McDannold, N. J.; Madore, B. Towards Fast and Accurate Temperature Mapping with Proton Resonance Frequency-Based MR Thermometry. *Quant. Imaging Med. Surg.* **2012**, *2* (1), 21-32–32.

(5) Tseng, H.; Lin, S.-E.; Chang, Y.-L.; Chen, M.-H.; Hung, S.-H. Determining the Critical Effective Temperature and Heat Dispersal Pattern in Monopolar Radiofrequency Ablation Using Temperature-Time Integration. *Exp. Ther. Med.* **2016**, *11* (3), 763–768.

(6) Proctor, W. G.; Yu, F. C. On the Nuclear Magnetic Moments of Several Stable Isotopes. *Phys. Rev.* **1951**, *81* (1), 20–30.

(7) Freeman, R.; Murray, G. R.; Richards, R. E. Cobalt Nuclear Resonance Spectra. *Proc. R. Soc. London. Ser. A* **1957**, *242* (1231), 455–466.

(8) Chan, J. C. C.; Au-Yeung, S. C. F. Cobalt-59 NMR Spectroscopy. In *Annual Reports on NMR Spectroscopy*; Academic Press, 2000; Vol. 41, pp 1–54.

(9) Levy, G. C.; Terry Bailey, J.; Wright, D. A. A Sensitive NMR Thermometer for Multinuclei FT NMR. *J. Magn. Reson.* **1980**, *37* (2), 353–356.

(10) Leyssens, L.; Vinck, B.; Van Der Straeten, C.; Wuyts, F.; Maes, L. Cobalt Toxicity in Humans – A Review of the Potential Sources and Systemic Health Effects. *Toxicology* **2017**, *387*, 43–56.

(11) Ozvat, T. M.; Peña, M. E.; Zadrozny, J. M. Influence of Ligand Encapsulation on Cobalt-59 Chemical-Shift Thermometry. *Chem. Sci.* **2019**, *10* (27), 6727–6734.

(12) Jameson, C. J.; Rehder, D.; Hoch, M. Isotope and Temperature Dependence of Transition-Metal Shielding in Complexes of the Type $M(XY)_6$. *J. Am. Chem. Soc.* **1987**, *109* (9), 2589–2594.

(13) Jameson, C. J. Vibrational Analysis and Mean Bond Displacements in $M(XY)_6$ Complexes. *J. Am. Chem. Soc.* **1987**, *109* (9), 2586–2588.

(14) Benedek, G. B.; Englman, R.; Armstrong, J. A. Temperature and Pressure Dependence of the Co^{59} Nuclear Resonance Chemical Shift. *J. Chem. Phys.* **1963**, *39* (12), 3349–3363.

(15) Gillies, D. G.; Sutcliffe, L. H.; Williams, A. J. Variable-Temperature High-Pressure Investigation of the Cobalt-59 NMR Spectroscopy of Aqueous $K_3[Co(CN)_6]$. *Magn. Reson. Chem.* **2002**, *40* (1), 57–64.

(16) Bendall, M. R.; Doddrell, D. M. Proton-Deuterium Isotope Shifts in ^{59}Co N.M.R. *Aust. J. Chem.* **1978**, *31* (5), 1141–1143.

(17) Osten, H. -Jörg; Jameson, C. J. Rovibrational Effects on Nuclear Shielding of Apex Nuclei in Bent Molecules. *J. Chem. Phys.* **1985**, *82* (10), 4595–4606.

(18) Kruger, G. J.; Reynhardt, E. C. Hexaamminecobalt(III) Chloride. *Acta Crystallogr., Sect. B* **1978**, *34* (3), 915–917.

(19) Nakatsu, K.; Saito, Y.; Kuroya, H. Studies on Crystals of Metallic Tris-ethylenediamine-complexes. I. The Crystal Structure of Δλ-Tris-ethylenediamine-cobalt(III) Chloride Trihydrate, [Co en$_3$]Cl$_3$·3H$_2$O. *Bull. Chem. Soc. Jpn.* **1956**, *29* (3), 428–434.

(20) Nagao, R.; Marumo, F.; Saito, Y. The Crystal Structure of (−)$_{589}$-Tris(1,3-diaminopropane)cobalt(III) Chloride Monohydrate, (−)$_{589}$-[Co(tn)$_3$]Cl$_3$·H$_2$O. *Acta Crystallogr., Sect. B* **1973**, *29* (11), 2438–2443.

(21) Geue, R. J.; Snow, M. R. Structure, Conformational Analysis and Optical Activity of a Bis(tridentate)cobalt(III) Complex. (+)$_{589}$-ΔλλBis[1,1,1-Tris(aminomethyl)ethane]cobalt(III) Chloride (+)$_{589}$-(*R*,*R*)-Tartrate Hydrate. *Inorg. Chem.* **1977**, *16* (2), 231–241.

(22) Clark, I.; Geue, R.; Engelhardt, L.; Harrowfield, J.; Sargeson, A.; White, A. Structural Characterization of Encapsulation Reactions Based on the Tris(ethane-1,2-diamine)cobalt(III) Ion. *Aust. J. Chem.* **1993**, *46* (10), 1485.

(23) Seward, T. M.; Henderson, C. M. B.; Charnock, J. M.; Dobson, B. R. An X-Ray Absorption (EXAFS) Spectroscopic Study of Aquated Ag^+ in Hydrothermal Solutions to 350°C. *Geochim. Cosmochim. Acta* **1996**, *60* (13), 2273–2282.

(24) Frank, P.; Benfatto, M.; Qayyam, M.; Hedman, B.; Hodgson, K. O. A High-Resolution XAS Study of Aqueous Cu(II) in Liquid and Frozen Solutions: Pyramidal, Polymorphic, and Non-Centrosymmetric. *J. Chem. Phys.* **2015**, *142* (8).

(25) Garino, C.; Borfecchia, E.; Gobetto, R.; van Bokhoven, J. A.; Lamberti, C. Determination of the Electronic and Structural Configuration of Coordination Compounds by Synchrotron-Radiation Techniques. *Coord. Chem. Rev.* **2014**, *277–278*, 130–186.

(26) Bowron, D. T.; Diaz Moreno, S. Using Synchrotron X-Ray and Neutron Methods to Investigate Structural Aspects of Metal Ion Solvation and Solution Structure: An Approach Using Empirical Potential Structure Refinement. *Coord. Chem. Rev.* **2014**, *277–278*, 2–14.

(27) Penner-Hahn, J. E. X-Ray Absorption Spectroscopy. In *Encyclopedia of Life Sciences*; John Wiley & Sons, Ltd, Ed.; John Wiley & Sons, Ltd: Chichester, UK, 2005.

(28) Ravel, B.; Newville, M. ATHENA, ARTEMIS, HEPHAESTUS: Data Analysis for X-Ray Absorption Spectroscopy Using IFEFFIT. *J. Synchrotron Rad.* **2005**, *12* (4), 537–541.

(29) Ravel, B. ATOMS: Crystallography for the X-Ray Absorption Spectroscopist. *J. Synchrotron Rad.* **2001**, *8* (2), 314–316.

(30) Bencini, A.; Bianchi, A.; Garcia-España, E.; Micheloni, M.; Ramirez, J. A. Proton Coordination by Polyamine Compounds in Aqueous Solution. *Coord. Chem. Rev.* **1999**, *188* (1), 97–156.

(31) Mizuno, Y.; Yokote, A.; Iida, M. Solvent Effects on ^{59}Co Chemical Shifts for Tripositive Cobalt(III) Complex Ions. *Bull. Chem. Soc. Jpn.* **1997**, *70* (10), 2437–2442.

(32) Sharma, R. P.; Bala, R.; Sharma, R.; Perez, J.; Miguel, D. Second-Sphere Coordination Complexes via Hydrogen Bonding: Synthesis, Characterization of $[Co(NH_3)_6](XO_3)_3 \cdot nH_2O$ (X = Br, I) and Single Crystal X-Ray Structure Determination of $[Co(NH_3)_6](BrO_3)_3 \cdot 0.5H_2O$. *J. Mol. Struct.* **2006**, *788* (1), 49–54.

(33) Purans, J.; Timoshenko, J.; Kuzmin, A.; Dalba, G.; Fornasini, P.; Grisenti, R.; Afify, N. D.; Rocca, F.; Panfilis, S. D.; Ozhogin, I.; Tiutiunnikov, S. I. Femtometer Accuracy EXAFS Measurements: Isotopic Effect in the First, Second and Third Coordination Shells of Germanium. *J. Phys.: Conf. Ser.* **2009**, *190*, 012063.

(34) Purans, J.; Afify, N. D.; Dalba, G.; Grisenti, R.; De Panfilis, S.; Kuzmin, A.; Ozhogin, V. I.; Rocca, F.; Sanson, A.; Tiutiunnikov, S. I.; Fornasini, P. Isotopic Effect in Extended X-Ray-Absorption Fine Structure of Germanium. *Phys. Rev. Lett.* **2008**, *100* (5), 055901.

(35) Purans, J.; Dalba, G.; Fornasini, P.; Kuzmin, A.; De Panfilis, S.; Rocca, F. EXAFS and XRD Studies with Subpicometer Accuracy: The Case of ReO_3. In *AIP Conference Proceedings*; AIP: Stanford, California (USA), 2007; Vol. 882, pp 422–424.

(36) Dalba, G.; Fornasini, P.; Grisenti, R.; Purans, J. Sensitivity of Extended X-Ray-Absorption Fine Structure to Thermal Expansion. *Phys. Rev. Lett.* **1999**, *82* (21), 4240–4243.

(37) Abd el All, N.; Dalba, G.; Diop, D.; Fornasini, P.; Grisenti, R.; Mathon, O.; Rocca, F.; Thiodjio Sendja, B.; Vaccari, M. Negative Thermal Expansion in Crystals with the Zincblende Structure: An EXAFS Study of CdTe. *J. Phys.: Condens. Matter* **2012**, *24* (11), 115403.

(38) Frisch, M. J.; Trucks, G. W.; Schlegel, H. B.; Scuseria, G. E.; Robb, M. A.; Cheeseman, J. R.; Scalmani, G.; Barone, V.; Petersson, G. A.; Nakatsuji, H.; Li, X.; Caricato, M.; Marenich, A. V.; Bloino, J.; Janesko, B. G.; Gomperts, R.; Mennucci, B.; Hratchian, H. P.; Ortiz, J. V.; Izmaylov, A. F.; Sonnenberg, J. L.; Williams; Ding, F.; Lipparini, F.; Egidi, F.; Goings, J.; Peng, B.; Petrone, A.; Henderson, T.; Ranasinghe, D.; Zakrzewski, V. G.; Gao, J.; Rega, N.; Zheng, G.; Liang, W.; Hada, M.; Ehara, M.; Toyota, K.; Fukuda, R.; Hasegawa, J.; Ishida, M.; Nakajima, T.; Honda, Y.; Kitao, O.; Nakai, H.; Vreven, T.; Throssell, K.; Montgomery Jr., J. A.; Peralta, J. E.; Ogliaro, F.; Bearpark, M. J.; Heyd, J. J.; Brothers, E. N.; Kudin, K. N.; Staroverov, V. N.; Keith, T. A.; Kobayashi, R.; Normand, J.; Raghavachari, K.; Rendell, A. P.; Burant, J. C.; Iyengar, S. S.; Tomasi, J.; Cossi, M.; Millam, J. M.; Klene, M.; Adamo, C.; Cammi, R.; Ochterski, J. W.; Martin, R. L.; Morokuma, K.; Farkas, O.; Foresman, J. B.; Fox, D. J. *Gaussian 16 Rev. C.01*; Wallingford, CT, 2016.

(39) Neese, F. A Spectroscopy Oriented Configuration Interaction Procedure. *J. Chem. Phys.* **2003**, *119* (18), 9428–9443.

(40) Krishnan, R.; Binkley, J. S.; Seeger, R.; Pople, J. A. Self-Consistent Molecular Orbital Methods. XX. A Basis Set for Correlated Wave Functions. *J. Chem. Phys.* **1980**, *72* (1), 650–654.

(41) Alvarez, S.; Avnir, D.; Llunell, M.; Pinsky, M. Continuous Symmetry Maps and Shape Classification. The Case of Six-Coordinated Metal Compounds. *New J. Chem.* **2002**, *26* (8), 996–1009.

(42) Alvarez, S.; Alemany, P.; Casanova, D.; Cirera, J.; Llunell, M.; Avnir, D. Shape Maps and Polyhedral Interconversion Paths in Transition Metal Chemistry. *Coord. Chem. Rev.* **2005**, *249* (17–18), 1693–1708.

(43) Pinsky, M.; Avnir, D. Continuous Symmetry Measures. 5. The Classical Polyhedra. *Inorg. Chem.* **1998**, *37* (21), 5575–5582.

(44) Chen, W.-K.; Chen, J.; Rentzepis, P. M. Electron Transfer Mechanism in Organometallic Molecules Studied by Subpicosecond Extended X-Ray Absorption Fine Structure Spectroscopy. *J. Phys. Chem. B* **2013**, *117* (16), 4332–4339.

(45) Akai, T.; Okuda, M.; Horiuchi, K.; Matsuura, J.; Koike, Y.; Yimagawa, M.; Fujikawa, T. Structural Studies on New Co Polyamine Complexes by X-Ray Absorption Fine Structure Spectroscopy. *Jpn. J. Appl. Phys.* **1994**, *33* (Part 1, No. 11), 6360–6367.

(46) Bonnitcha, P. D.; Hall, M. D.; Underwood, C. K.; Foran, G. J.; Zhang, M.; Beale, P. J.; Hambley, T. W. XANES Investigation of the Co Oxidation State in Solution and in Cancer Cells Treated with Co(III) Complexes. *J. Inorg. Biochem.* **2006**, *100* (5–6), 963–971.

(47) Griffith, J. S.; Orgel, L. E. The Residual Paramagnetism and Nuclear Magnetic Resonance Spectra of Cobaltic Complexes. *Trans. Faraday Soc.* **1957**, *53*, 601.

(48) Bramley, R.; Brorson, M.; Sargeson, A. M.; Schaeffer, C. E. Cobalt-59 NMR Chemical Shifts of Cobalt(III) Complexes; Correlations with Parameters Calculated from Ligand-Field Spectra. *J. Am. Chem. Soc.* **1985**, *107* (9), 2780–2787.

(49) Juranić, N. Significance of Nephelauxetic Effect in the Interpretation of Cobalt-59 Nuclear Magnetic Resonance Frequencies of Cobalt(III) Complex Compounds. *Inorg. Chem.* **1980**, *19* (4), 1093–1095.

(50) Juranić, N. A ^{59}Co NMR Study of the Magnetic Shielding of the Cobalt Nucleus in Cobalt(III) Complexes. *J. Chem. Phys.* **1981**, *74* (7), 3690–3693.

(51) Geue, R. J.; Hendry, A. J.; Sargeson, A. M. Configurational and Conformational Effects on Electron Transfer Rates. *J. Chem. Soc., Chem. Commun.* **1989**, No. 21, 1646–1647.

(52) Spees, S. T.; Durham, L. J.; Sargeson, A. M. Nuclear Magnetic Resonance Study of Some Cobalt(III) Complexes with Known Chelate Ring Conformations. *Inorg. Chem.* **1966**, *5* (12), 2103–2105.

(53) Comba, P.; Creaser, I. I.; Gahan, L. R.; Harrowfield, J. M.; Lawrance, G. A.; Martin, L. L.; Mau, A. W. H.; Sargeson, A. M.; Sasse, W. H. F.; Snow, M. R. Macrobicyclic Chromium(III) Hexaamine Complexes. *Inorg. Chem.* **1986**, *25* (3), 384–389.

(54) Comba, P.; Sargeson, A. M.; Engelhardt, L. M.; Harrowfield, J. MacB.; White, A. H.; Horn, E.; Snow, M. R. Analysis of Trigonal-Prismatic and Octahedral Preferences in Hexaamine Cage Complexes. *Inorg. Chem.* **1985**, *24* (15), 2325–2327.

(55) Comba, P. Coordination Geometries of Hexaamine Cage Complexes. *Inorg. Chem.* **1989**, *28* (3), 426–431.

(56) Harrowfield, J. Labile Interactions and Inert Entities in Supramolecular Chemistry – The Identification of Recognition Mechanisms for Macrobicyclic Amine Complexes. *Supramol. Chem.* **2006**, *18* (2), 125–136.

(57) Endicott, J. F.; Brubaker, G. R.; Ramasami, T.; Kumar, K.; Dwarakanath, K.; Cassel, J.; Johnson, D. Electron-Transfer Reactivity in Some Simple Cobalt(III)-Cobalt(II) Couples. Franck-Condon vs. Electronic Contributions. *Inorg. Chem.* **1983**, *22* (25), 3754–3762.

(58) Bond, A. M.; Hambley, T. W.; Snow, M. R. A Force Field for Molecular Mechanics Modeling of Cobalt(II) Amine Complexes and a New Model of Electron Transfer for Cobalt(III)-Cobalt(II) Redox Couples. *Inorg. Chem.* **1985**, *24* (12), 1920–1928.

CHAPTER 4 – Cobalt-59 Nuclear Spin Relaxation Thermometry

4.1. Overview

Studying the correlation between temperature-driven molecular structure and nuclear spin dynamics is essential to understanding fundamental design principles for thermometric nuclear magnetic resonance spin-based probes. Herein, we study the impact of progressively encapsulating ligands on temperature-dependent ^{59}Co T_1 (spin-lattice) and T_2 (spin-spin) relaxation times in a set of Co^{3+} complexes: $K_3[Co(CN)_6]$ (**1**), $[Co(NH_3)_6]Cl_3$ (**2**), $[Co(en)_3]Cl_3$ (**3**, en = ethylenediamine), $[Co(tn)_3]Cl_3$ (**4**, tn = trimethylenediamine), $[Co(tame)_2]Cl_3$ (**5**, tame = triaminomethylethane), and [Co(diNOsar)]Cl_3 (**6**, diNOsar = dinitrosarcophagine). Measurements indicate that ^{59}Co T_1 and T_2 increase with temperature for **1–6** between 10 and 60 °C, with the greatest $\Delta T_1/\Delta T$ and $\Delta T_2/\Delta T$ temperature sensitivities found for **4** and **3**, 5.3(3) $\%T_1$/°C and 6(1) $\%T_2$/°C, respectively. Temperature-dependent T_2* (dephasing time) analyses were also made, revealing the highest $\Delta T_2^*/\Delta T$ sensitivities in structures of greatest encapsulation, as high as 4.64 $\%T_2^*$/°C for **6**. Calculations of the temperature-dependent quadrupolar coupling parameter, $\Delta e^2qQ/\Delta T$, enable insight into the origins of the relative $\Delta T_1/\Delta T$ values. These results suggest tunable quadrupolar coupling interactions as novel design principles for enhancing temperature sensitivity in nuclear spin-based probes.

4.2. Introduction

The control of nuclear-spin properties by molecular design is an important capability for many applications, spanning from diagnostic bioimaging[1–3] to encoding and processing quantum informationn.[4–7] A more focused application is designing temperature dependence into nuclear spin properties toward molecular-level thermometry, an essential technique for next-generation treatments of cancer.[8–11] Here, ^{59}Co nuclear spins are an extremely promising platform for detecting changes in temperature, owing to the extreme sensitivity of the metal-ion chemical shift.[12] We note that chemical shift is not the only temperature-dependent property of nuclear spins. Indeed, the influence of temperature on nuclear spin relaxation

dynamics may provide a practical additional mechanism for thermometry. Importantly, the quadrupolar coupling of the ^{59}Co ($I = {}^{7}/_{2}$) nucleus is exquisitely sensitive to subtle changes in the structure of the coordination shell. Thus, slight temperature-dependent structural changes are expected to drive nuclear-spin behaviors by manipulating the quadrupolar coupling interaction, inducing temperature dependence in the ^{59}Co spin-lattice and spin-spin relaxation times, T_1 and T_2, respectively. We note that other, more common nuclear spin-based probes, e.g., ^{1}H, ^{13}C, ^{19}F, and ^{31}P, are all $I = {}^{1}/_{2}$, are not quadrupolar nuclei and do not sense changes in temperature by a tunable temperature-driven structure.[13–15]

Owing to the foregoing advantages, we target design strategies to control the temperature sensitivity of ^{59}Co nuclear-spin dynamics in encapsulating ligands, which can prevent chemical decomposition *in vivo*, avoiding the release of toxic metal-ions.[16–18] Recent work by us demonstrated that the interconnected structures of encapsulating scaffolds amplify temperature sensitivity for contained ^{59}Co nuclei.[19] Importantly, these studies probed only temperature-driven changes in chemical shift. In contrast, it is unknown to what extent, if any, encapsulation affects the temperature dependence of ^{59}Co nuclear spin relaxation processes.

Herein, we provide the first test of the effect of encapsulation on the thermometric capabilities of the ^{59}Co nuclear spin dynamics in Co^{3+} complexes. To do so, we performed variable-temperature ^{59}Co-NMR relaxation time experiments, specifically T_1, T_2, and linewidth analysis (T_2*) with a series of six octahedral and pseudo-octahedral Co^{3+} complexes (*Figure 4.1*).

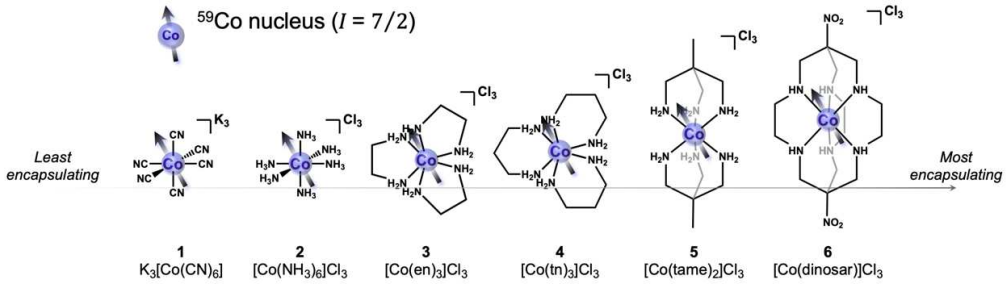

Figure 4.1. Chemical structure series of low-spin octahedral Co^{3+} complexes. Complexes **2**–**6** make up the series of progressively encapsulated ^{59}Co nuclei by greater degrees of chelation. Arrows represent the nuclear spin of the ^{59}Co ($I = {}^{7}/_{2}$) nuclei in each complex. Hydrogens bound to carbons are omitted for clarity.

These compounds are $K_3[Co(CN)_6]$ (**1**), $[Co(NH_3)_6]Cl_3$ (**2**), $[Co(en)_3]Cl_3$ (**3**, en = ethylenediamine), $[Co(tn)_3]Cl_3$ (**4**, tn = trimethylenediamine), $[Co(tame)_2]Cl_3$ (**5**, tame = triaminomethylethane), and [Co(diNOsar)]Cl_3 (**6**, diNOsar = dinitrosarcophagine). This series enables comparison of the temperature-dependent relaxation dynamics of these complexes with *i*) molecular symmetry (e.g., from the O_h complexes **1** and **2** to the nearly D_3 complexes **3–6**), and *ii*) relative degree of encapsulation (from **2–6**). We further computed quadrupolar coupling parameters from computational structures to rationalize the relative temperature dependence of the relaxation dynamics. We find no precise correlation between relaxation and encapsulation. Instead, we propose that $\Delta T_1/\Delta T$ of the ^{59}Co nucleus is driven by changes in the quadrupolar coupling parameters, (Δe^2qQ), from thermally driven structures. These evaluations highlight important structural conditions of chelation among the series, which are shown to yield various trends in temperature-dependent values of T_1, T_2, and T_2*.

4.3. Experimental Section

4.3.1. General Considerations

Compounds utilized in this study were either purchased from commercial chemical vendors and used as received (**1** and **2**) or synthesized according to previously reported literature preparations (**3–6**).[20–24] Characterization of **1–6** is detailed previously by us[19] where NMR spectra were collected on an Agilent Unity INOVA 500 MHz (^{1}H) spectrometer. UV-vis spectra were collected on aqueous solutions of with an Agilent 8453 UV-visible spectrophotometer. IR spectra were collected on solid powders with a Bruker TENSOR II FTIR spectrometer. Combustion analyses were performed by Robertson Microlit Laboratories.

4.3.2 Preparation of Compounds

Synthesis of compounds **2–6** studied within this chapter were prepared according to the methods reported in the Experimental Section of Chapter 2.

4.3.3. Variable Temperature ^{59}Co-NMR Spectroscopy

Samples of all measured compounds were made as 0.7 mL volumes of 30 mM concentrations in protiated distilled water. Spectroscopic measurements were made at 118 MHz (^{59}Co) using an Agilent Unity INOVA 500 MHz (^{1}H) spectrometer at a field strength of 11.74 T with a 5 mm broadband NMR probe. Before any data collection, standard shims, deuterium locking, and probe tuning were made on 1 M sample of $K_3[Co(CN)_6]$ in D_2O, the ^{59}Co-NMR reference standard. During ^{59}Co-NMR experiments, data were collected in the absence of shimming and locking due to field stability of the instrument. Each sample was measured across a temperature range of 10–60 °C in 10 °C intervals. For each regulated temperature interval, samples were allowed to thermally equilibrate for 15 min before the probe was tuned for each pulse experiment.

4.3.4. Variable Temperature ^{59}Co Inversion Recovery and CPMG Experiments

Inversion recovery experiments were made on each sample across a temperature range of 10–60 °C in 10 °C intervals upon thermal equilibration. Inversion recovery data were acquired from 180°–τ–90° pulse sequence experiments with 180° and 90° pulse lengths set at 22.4 and 11.2 μs, respectively. Pulse delay lengths τ were set by exponentially incremented time intervals relative to previously reported room temperature T_1 values of each compound.[19] Similarly, CPMG (Carr-Purcell-Meiboom-Gill) pulse sequence experiments were made on each sample across a temperature range of 10–60 °C in 10 °C increments.[25,26] CPMG data were acquired from 90°–(τ–180°–τ)$_n$ spin echo pulse sequence experiments with 180° and 90° pulse lengths identical to the corresponding inversion-recovery parameters.

Fitting of all inversion recovery and CPMG experimental relaxation data was completed in OriginPro. A three-parameter exponential function (Eq. 1) was used to fit both sets of relaxation arrays in order to extract pertinent T_1 and T_2 relaxation values.

$$y = \mathrm{A}e^{\left(\frac{-x}{t_1}\right)} + y_0 \qquad \text{Eq. 1}$$

Where t_1 was solved for and taken directly as the experimental spin-lattice relaxation time, T_1 (s) from inversion recovery relaxation arrays (*Figures A3.1–A3.6*), and spin-spin relaxation time, T_2 (s) from CPMG experiments (*Figures A3.8–A3.11*). Values of T_2* were extracted the inverse relation of T_2* to the full-width half-maximum (FWHM) of 1D ^{59}Co-NMR spectra (Eq. 2).

$$T_2^* = 1/(2\pi\Delta\upsilon) \qquad \text{Eq. 2}$$

Where $\Delta\upsilon$ (Hz) is the width of the FWHM extracted using a custom script written in MATLAB based on the "findpeaks()" method found in MATLAB's Signal Processing Toolbox. All peak locations and widths were verified graphically before being used to calculate T_2*.[27] The specific script utilized herein is available upon reasonable request.

4.3.5. Predicting ^{59}Co Quadrupolar Coupling Constants and Correlation Times

Computational analyses were completed for the Co–N_6 encapsulation series (**2–6**) by structural optimizations over a range of temperatures. Temperature-specific optimizations were assisted by previous extended X-ray absorption fine-structure (EXAFS) characterization by fixing Co–N distances according to experimentally determined metal-ligand bond lengths to the three temperatures utilized in the EXAFS study, i.e., 13, 35, and 57 °C.[28] The remainder of the structure was allowed to optimize freely about the fixed Co–N_6 coordination sphere using Gaussian 16 electronic structure package.[29] Electronic properties calculations were then performed using Orca 4.11 to predict the quadrupolar coupling constant parameter (e^2qQ) of the temperature-specific optimized structures.[30]

In addition to e^2qQ, the asymmetry parameter, η was predicted from each temperature-specific structure. Together, these values were used to determine correlation times, τ_c from the canonical equation for T_1 (Eq. 3).[31,32]

$$\frac{1}{T_1^Q} = \frac{3(2I+3)}{400I^2(2I-1)}\left(\frac{e^2Qq}{\hbar}\right)^2\left(1+\frac{\eta^2}{3}\right)\left(\frac{2}{1+\omega_x^2\tau_c^2}+\frac{8}{1+4\omega_x^2\tau_c^2}\right)\tau_c \qquad \text{Eq.3}$$

The asymmetry parameters and quadrupole coupling constant vary for each complex and temperature. From these computational values, an equation of a single distinct coefficient was generated

for each compound. The coefficients were plotted against the experimental temperatures and fit using a second-degree polynomial under the assumption that the coefficients varied continuously across the temperature range of 10–60°C. Each compound thus has a second-degree polynomial as a function of temperature which outputs a single coefficient which is then used to generate coefficients for each temperature (10, 20, 30, 40, 50, and 60°C). Finally, the equation of T_1 as a function of rotational correlation time was solved by inserting the experimentally derived T_1 spin-lattice relaxation times and solving for τ_c. This process was accomplished via custom MATLAB script with the assistance of the curve-fitting and symbolic mathematics toolboxes.[33,34]

4.4. Results and Discussion

The first temperature-dependent ^{59}Co nuclear spin property we investigated was the spin-lattice, or T_1, relaxation time. Variable-temperature inversion recovery experiments were performed for **1–6** over a 10–60 °C temperature range. At each temperature, an initially inverted ^{59}Co-NMR peak was observed, and intensity was recovered as a function of increasing delay time. The resulting recovery curves of **4** are obtained from these pulsed experiments at different temperatures (*Figure 4.2*).

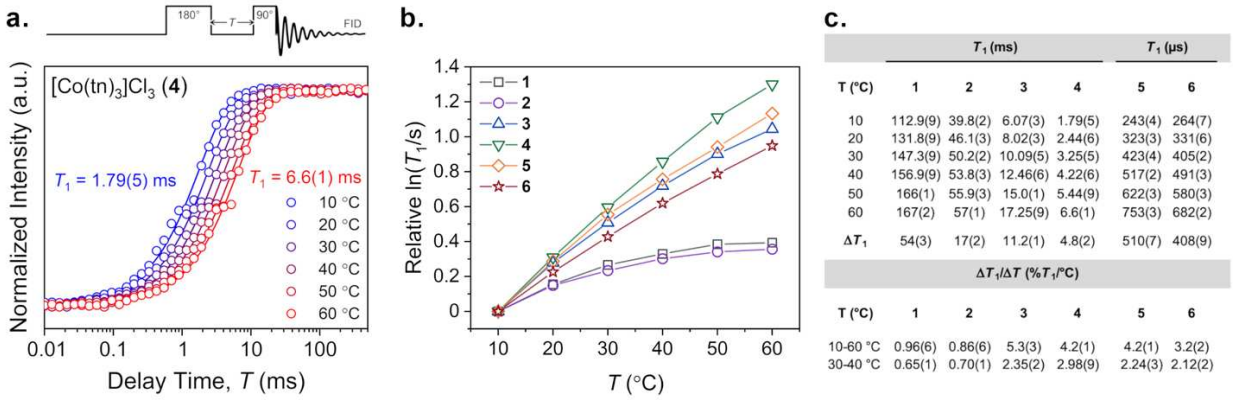

Figure 4.2. a. Experimental variable-temperature (10–60 °C) inversion recovery measurements (*circles*) with exponential decay fits (*traces*) for $[Co(tn)_3]Cl_3$ (**4**) on logarithmic scale. Temperature-specific T_1 values were extracted from exponential decay fits. The general pulse sequence for the inversion recovery experiment is depicted. ***b.*** Variable-temperature T_1 plots of **1**–**6** on logarithmic scale showing relative changes. Error bars are within the width of the data points. Traces are guides for the eye. ***c.*** Temperature-specific T_1 spin-lattice relaxation times with error for **1**–**6** from 10–60 °C with absolute values of ΔT_1 and relative values of $\Delta T_1/\Delta T$ temperature sensitivities.

Additional inversion recovery curves are available in the *Figure A4.1–A4.6*. The fitted inversion recovery data for **1**–**6** reveal lengthening of T_1 with increasing temperature. The observed ranges of T_1 span from 112.9(9) to 167(2) ms for **1**, 39.8(2) to 57(1) ms for **2**, 6.07(3) to 17.25(9) ms for **3**, 1.79(5) to 6.6(1) ms for **4**, 243(4) to 753(3) μs for **5**, and 264(7) to 682(2) μs for **6**. The largest absolute change in T_1 over this temperature range is exhibited by **1** (ΔT_1 = 54(3) ms), while the smallest difference occurs for **6** (ΔT_1 = 408(9) μs). Between the minimum and maximum values of **1** and **6**, absolute changes in ΔT_1 for **2–5** are 17(1) ms, 11.2(1) ms, 4.8(2) ms, and 511(7) μs, respectively. The general magnitudes of these values are consistent with previous ^{59}Co relaxation data on structurally similar cobalt systems.[35–38]

For the purpose of comparison, it is useful to define *relative* changes in T_1 for each complex since absolute differences ΔT_1, as above, heavily weight molecules with long T_1 times. As a result, the use of logarithmic scales of T_1 with temperature are necessary to show a clear comparison of ΔT_1 between **1–6** (*Figure A3.7*). In the following discussion we express a comparative degree of change in T_1 between 10 to 60 °C as a percentage difference divided by the 50 °C window. For example, the ΔT_1 of **1** over 10 to 60 °C is approximately 54 ms. This value corresponds to a 48.2% increase in T_1 from 112.9 ms (10 °C) over the 50 °C window, thus quantitated by 0.96(6) $\%T_1$/°C. Similarly, the other relative $\Delta T_1/\Delta T$ sensitivities are 0.86(6), 3.68(6), 5.3(3), 4.2(1), and 3.2(2) $\%T_1$/°C for **2–6**, respectively. Figure 4.2.a (*above*) depicts the relative magnitudes of these values for all complexes over the 10–60 °C temperature window on a logarithmic scale. Owing to the potential utility of relaxation in modern biomedical imaging techniques, we highlight the aforementioned values of $\Delta T_1/\Delta T$ within the biologically relevant domain of 30–40 °C at 0.65(1), 0.70(1), 2.35(2), 2.98(9), 2.24(3), and 2.12(2) $\%T_1$/°C for **1–6**, respectively. These values follow the same general trend as with the 10–60 °C window, though the change in magnitudes differ slightly.

Notably, **4** shows the greatest change for both temperature windows, and **1** and **2** show the smallest relative increase in T_1. However, the relation between T_1 and T show varying degrees of temperature linearity across the series. T_1 is expected to show a linear temperature dependence if the quadrupolar mechanism is operative. A high degree of linearity is shown by the D_3-symmetric molecules of the series,

3–6. For these complexes, quadrupolar relaxation is expected, due to the interaction between the electric quadrupolar moment and the lower-symmetry electric field gradient at the ^{59}Co nucleus (relative to O_h **1** and **2**). However, the non-linear relaxation behaviors of **1** and **2** suggest different operative relaxation processes of the central ^{59}Co nucleus.[35,39] For these complexes, curvature in the plots of ln(T_1/s) vs. T (°C) in Figure 4.2.b (*above*) show a gradual decline with increasing temperature, indicative of another contributing relaxation mechanism. The spin-rotation relaxation mechanism is known to contribute to relaxation in similar O_h ^{59}Co complexes,[35,36] thus is the likely origin of the non-linear temperature dependence in **1** and **2**.

The second temperature-dependent nuclear spin property we investigated was T_2. Variable-temperature CPMG experiments were performed over a 10–60 °C temperature range for on **1–3**, and a 30–60 °C range for **4** to collect T_2 values. At each temperature measurement, a ^{59}Co-NMR peak was observed with an intensity that decayed as a function of increasing number of π pulses. T_2 times were determined from exponential fits of the decay of all studied complexes (*Figure A3.8–A3.11*). Similar to the temperature-dependent T_1 behaviors, T_2 increases with increasing temperature for **1–4**. The relaxation trends for **1–4** are shown over the 50 °C window (*Figure 4.3*).

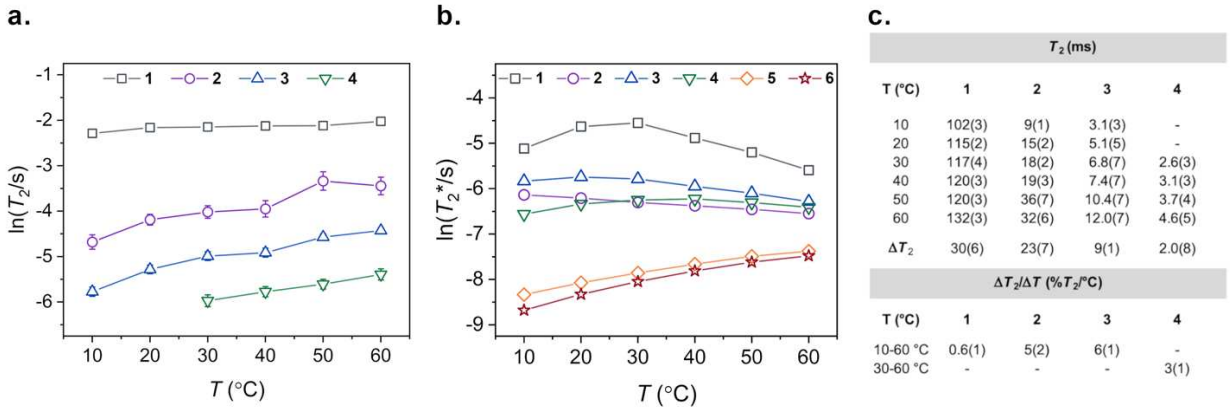

T_2 (ms)				
T (°C)	1	2	3	4
10	102(3)	9(1)	3.1(3)	-
20	115(2)	15(2)	5.1(5)	-
30	117(4)	18(2)	6.8(7)	2.6(3)
40	120(3)	19(3)	7.4(7)	3.1(3)
50	120(3)	36(7)	10.4(7)	3.7(4)
60	132(3)	32(6)	12.0(7)	4.6(5)
ΔT_2	30(6)	23(7)	9(1)	2.0(8)

$\Delta T_2/\Delta T$ (%T_2/°C)				
T (°C)	1	2	3	4
10-60 °C	0.6(1)	5(2)	6(1)	-
30-60 °C	-	-	-	3(1)

Figure 4.3. a. Variable-temperature T_2 plots of **1–4** on logarithmic scale showing relative changes in T_2 spin-spin relaxation times. Error bars for $K_3[Co(CN)_6]$ (**1**) are within the widths of the data points. Traces are meant to guide the eye. ***b.*** Variable temperature T_2* trends from linewidth analyses of **1–6** from 1D ^{59}Co-NMR spectra. ***c.*** Temperature-specific T_2 spin-spin relaxation times with error for **1–4** with absolute values of ΔT_2 and relative values of $\Delta T_2/\Delta T$ temperature sensitivities.

Unfortunately, due to instrumental limitations, we were not able to collect T_2 values for **4** at 10 and 20 °C, nor for **5** and **6** at any temperature between 10–60 °C. Pulse delay times for CPMG experiments on complexes with relatively low T_2 values approached the same timescales as the pulse durations (on the order of 10–20 μs). Thus, CPMG data could not be collected for **5** and **6**, which are likely to have even shorter T_2 times than **4** at 30 °C (the shortest experimentally determined T_2 value). For **1–4**, the observed range of T_2 times span from 102(3) to 132(3) ms for **1**, 9(1) to 32(6) ms for **2**, and 3.1(3) to 12.0(7) ms for **3** shown in Figure 4.3.c (*above*). The largest absolute change in T_2 over a 10–60 °C temperature range is exhibited by **1** (ΔT_2 = 30(6) ms), followed by decreasing values of ΔT_2 at 23(7) ms for **2**, and 9(1) ms for **3**. Between 30–60 °C, T_2 for **4** was measured from 2.6(3) to 4.6(5) ms with an absolute ΔT_2 of 2.0(8) ms. The increases in T_2 over the studied range are expressed as $\Delta T_2/\Delta T$ by 0.6(1), 5(2), and 6(1) $\%T_2$/°C over 10–60 °C for **1–3**, respectively, while an increase of 3(1) $\%T_2$/°C is shown for **4** over 30–60 °C.

As an additional method of comparing the variation in ^{59}Co nuclear spin properties of **1–6**, we investigated the dephasing time, or T_2*, a relaxation time analogous to T_2 above. T_2* can be extracted from the temperature-dependent NMR linewidths through the relationship $T_2^* = 1/(2\pi\Delta\upsilon)$ where $\Delta\upsilon$ (Hz) is the full width at half the maximum height (FWHM) of the ^{59}Co-NMR peak. This method enables a complete comparison of **1–6**, in contrast to the CPMG experiments. Figure 4.3.b (*above*) shows the temperature-dependent trends in T_2* for all complexes over the 10–60 °C range. Complexes **1**, **3**, and **4** all show increasing T_2* with increasing temperature up to a maximum, then begin to decrease with further increasing temperature. The maximum occurs near 30, 20, and 40 °C for **1**, **3**, and **4**, respectively. In contrast, complex **2** shows a continual decline in T_2* over the studied temperature range, while **5** and **6** both exhibit linear increases in T_2*. The absolute changes in ΔT_2* over 10–60 °C are –2.27, –0.73, –1.06, 0.24, 0.39, and 0.40 ms for **1–6**, respectively (*Table A3.1*). This trend is reflected in the smaller, biologically relevant 30–40 °C window, where absolute ΔT_2* values are –2.99, –0.13, –0.46, 0.05, 0.08, and 0.08 ms. As with ΔT_1 and ΔT_2, the absolute difference in timescales heavily weights complexes with already long T_2* values. The relative changes according to $\Delta T_2^*/\Delta T$, which here describe essentially the temperature dependence of the spectral linewidth, are –0.76, –0.67, –0.72, 0.33, 3.21, and 4.64 $\%T_2$*/°C for **1–6**, respectively. The largest

increase in T_2* is shown by **6**, with **5** showing the second largest increase. This trend is reflected in the narrowing linewidths observed in the ^{59}Co-NMR spectra as a function of increasing temperature.

To assist in understanding the relaxation time data, we computed values of the quadrupolar coupling constant parameter (e^2qQ) for the Co–N_6 encapsulation series (**2–6**) at different temperatures within the 10–60 °C window. Predictions of e^2qQ were completed from partially optimized, variable-temperature structures following analyses from extended X-ray absorption fine-structure (EXAFS) spectroscopy.[28] Values of e^2qQ computed for these structures range from –1.861 to –1.910 MHz for **2**, 2.441 to 2.392 for **3**, 1.088 to 0.893 MHz for **4**, 8.165 to 8.156 MHz for **5**, and 6.879 to 6.834 MHz for **6** (*Figure 4.4*).

a.

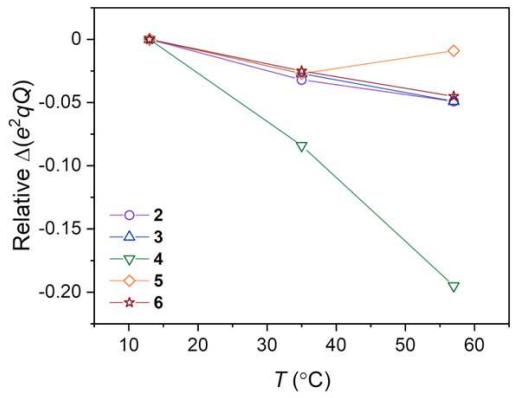

b.

	e^2qQ (MHz)			$\Delta(e^2qQ)$
Complex	**13 °C**	**35 °C**	**57 °C**	
2	-1.861	-1.893	-1.910	-0.049
3	2.441	2.414	2.392	-0.049
4	1.088	1.004	0.893	-0.195
5	8.165	8.138	8.156	-0.009
6	6.879	6.854	6.834	-0.045

Figure 4.4. a. Trends in predicted quadrupolar coupling parameters e^2qQ from variable temperature predicted structures of **2**–**6**. ***b.*** Temperature-specific quadrupolar coupling parameters at each temperature-specific structure and Δe^2qQ over the ~50 °C range.

The smallest values of e^2qQ are found for the smaller complexes (**2–4**) reflecting higher symmetries in molecular structure, relative to the larger, more encapsulating D_3 structures (**5** and **6**) showing the largest values of e^2qQ in the series.

The differences in e^2qQ by temperature-driven structure vary in scale, but all decrease with increasing temperature. Values of Δe^2qQ for **2–6** are found to be –0.049, –0.049, –0.195, –0.009, and –0.045 MHz, respectively. Of these predicted values, the greatest change is found for **4** followed by **2** and **3**, then **6** and **5**. Importantly, the largest Δe^2qQ is exhibited by **4** which also shows the largest $\Delta T_1/\Delta T$ value.

Conversely, the encapsulated D_3 structures of **5** and **6** possess the highest magnitudes of e^2qQ between 8.156 to 8.165 MHz and 6.834 to 6.879 MHz, respectively, but show the least change by Δe^2qQ.

Spin-lattice relaxation of the ^{59}Co nucleus is primarily attributed to the electric quadrupolar coupling interaction,[35–37] which is dictated by the symmetry and structure of a given ligand shell. Evaluation of T_1 *via* Arrhenius analyses of **1–6** elucidate the extent to which this is true. In principle, a higher linearity of ln(T_1) vs. 1/T (10^3 K^{-1}) indicates the contribution of a single relaxation process in governing T_1 (*Figure 4.5*).

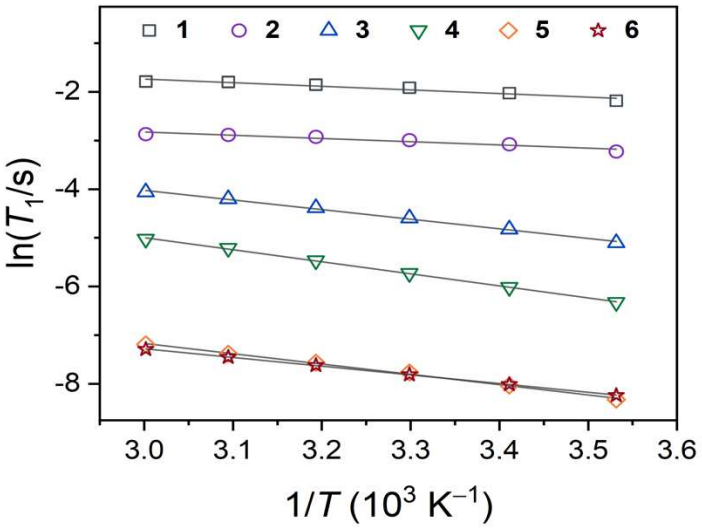

Figure 4.5. Arrhenius plots of variable-temperature T_1 relaxation for **1**–**6**. Solid grey traces indicate linear regressions. Values of R^2 from reach fit are used to determine temperature linearity for each complex.

A slightly curved temperature dependence is observed for O_h **1** and **2**, as evidenced by the lower R^2 values (0.91) to linear regression. Conversely, highly linear trends are observed for the more D_3-symmetry **3–6**, with R^2 values of 0.99. For this latter series of four complexes, an activation energy, E_a can be extracted from these linear fits to the Arrhenius equation, $1/T_1 = A \exp(-E_a/RT)$, where A is a preexponential factor, R is the ideal gas constant, and T is absolute temperature (*Table A3.2*). Here, E_a describes the activation energy to molecular tumbling and a lower E_a suggests more facile motion in solution.[35,40,41] Activation energies for **3–6** are found to be 16.4(5), 20.6(3), 17.6(5), and 14.9(1) kJ/mol respectively (1.37(4), 1.72(3), 1.47(4), and 1.24(1) × 10^3 cm^{-1}, respectively). Values of E_a increase from **6** < **3** < **5** < **4**, reflecting the same

trend in $\Delta T_1/\Delta T$. Notably, the moderately encapsulated complex **4** shows the highest barrier to rotation and also the highest $\Delta T_1/\Delta T$. If the spin-lattice relaxation is expected to be driven by motional changes dependent on molecular mass, then the observed trend in $\Delta T_1/\Delta T$ cannot be strictly reasoned by changes in a temperature-dependent correlation time (*Figure A3.12 and Table A3.3*). If the former were true, larger complexes, i.e., **5** and **6**, would be expected to have higher activation energies than that shown for **4**, reflected by longer τ_c in solution. In fact, they show faster τ_c values, despite having larger ligand scaffolds. Thus, we conclude that the standard mechanisms for describing temperature-dependent relaxation, which principally stem from changes in correlation time, do not solely account for the observed changes here.

We propose that these changes in motion synergize with changes in the local symmetry of the ^{59}Co nucleus to produce the observed trends in $\Delta T_1/\Delta T$, especially in the series of D_3-structures. Previous studies of **3–6** revealed ~0.007 Å changes in Co–N bond distances per °C within the 50 °C temperature range of our investigations.[28] These changes in bond distances were also accompanied by changes in symmetry of the coordination geometry through changes in N–Co–N angles. As a result of these changes in symmetry, we find in our calculations here that the quadrupolar coupling constants decrease with increasing temperature with a magnitude that trends as **4** > **3** > **6** > **5**. The trend in Δe^2qQ does not completely correlate to the trend in relaxation across the series, hence our suggestion that motion is also important. However, complex **4** shows *both* the greatest value of Δe^2qQ at –0.194 MHz, and the highest $\Delta T_1/\Delta T$ at 5.3(3) %$T_1/\Delta T$ over the 50 °C window.

The nearly equivalent values of T_1 and T_2 suggest that T_2 is limited by T_1, and, as such, T_2 is also expected to be impacted by the quadrupolar coupling. However, the temperature dependence of T_2 does not follow T_1. Owing to the large temperature dependence of the ^{59}Co chemical shift, we attribute this discrepancy to slight differences in resonance frequency by small temperature fluctuations which do not affect T_1 as strongly as T_2.[42] We further highlight that the fast time scales of T_2 for **5** and **6** are beyond the limits of the instrumentation. Hence, it would be challenging to utilize T_2 as a thermometric parameter for these species. In that light, the temperature dependence of the ^{59}Co linewidth appears more favorable for thermometry in complexes of greater encapsulation (and thus most chemically stable) owing to the linearity

of $\Delta T_2^*/\Delta T$ in the tridentate and encapsulated species **5** and **6**. Finally, we note that the values of T_2^* obtained here are likely lower bounds for this parameter, as temperature inhomogeneities in the instrument cavity (by even a fraction of 1 °C) will broaden the signal independent of T_2^*.

The above analyses suggest three important points for the development of ^{59}Co spin-based probes for quadrupolar-driven relaxation thermometry. Firstly, we note the importance of chelating or macrocyclic ligands, as **3**–**6** exhibited mostly quadrupolar relaxation, which is likely driven by the D_3-directing nature of these ligands. Secondly, we see that enabling a higher $\Delta T_1/\Delta T$ is largely dependent on whether the species possesses a strong temperature dependence of the quadrupolar coupling constant, not necessarily the magnitude of constant itself. Complex **4** exemplifies this point. Finally, third, the range of computed e^2qQ and Δe^2qQ imply a tunable quadrupolar coupling interaction through temperature-driven structures. It is worth noting that this is, to the best of our knowledge, the first argument for this effect in governing thermometry by relaxation. Moreover, in this context that the most encapsulated structures, **5** and **6**, both show the lowest Δe^2qQ values, compared to the structures of **3** and **4** with lesser denticity. This effect may be rationalized by a hindered variation in the *symmetry* of the structure due to the relative interconnectivity of the individual N donor atoms. Indeed, EXAFS analyses suggest that **4** exhibits the greatest transition *towards* O_h symmetry with increasing temperature when **3**, **5**, and **6** all deviate toward D_3 symmetry.[28] This subtle difference in temperature-dependent structure is likely an important point toward designing future ^{59}Co-NMR thermometers.

4.5. Conclusion

We report a collection of temperature-dependent relaxation dynamic studies on a series of progressively encapsulated Co^{3+} complexes. The foregoing temperature-dependent data underline the fact that structure plays a vital role in controlling relaxation thermometry for the ^{59}Co nucleus, but the coarse design principle of "*encapsulation*" does not solely govern the temperature dependence of T_1 nor T_2^*. Relaxation times are found to be largely determined by the quadrupolar coupling interaction for the D_3 complexes and a combination of quadrupolar and spin-rotation mechanisms for the O_h species (**1** and **2**).

The chelated complex **4** has the largest relative increase in T_1 as a function of its decrease in quadrupolar coupling, as mediated by a temperature-driven structure. We also found that encapsulated $Co–N_6$ species, demonstrated by **5** and **6**, are potentially promising thermometric structures by linear T_2* temperature dependencies. These factors thus provide a foundation for future studies of tuning temperature-dependent nuclear spin relaxation processes in Co^{3+} complexes.

References

(1) Sotoma, S.; Epperla, C. P.; Chang, H.-C. Diamond Nanothermometry. *ChemNanoMat* **2018**, *4* (1), 15–27.

(2) Toyli, D. M.; Casas, C. F. de las; Christle, D. J.; Dobrovitski, V. V.; Awschalom, D. D. Fluorescence Thermometry Enhanced by the Quantum Coherence of Single Spins in Diamond. *Proc. Natl. Acad. Sci. U.S.A.* **2013**, *110* (21), 8417–8421.

(3) Hui, Y. Y.; Chen, O. Y.; Azuma, T.; Chang, B.-M.; Hsieh, F.-J.; Chang, H.-C. All-Optical Thermometry with Nitrogen-Vacancy Centers in Nanodiamond-Embedded Polymer Films. *J. Phys. Chem. C* **2019**, *123* (24), 15366–15374.

(4) Thiele, S.; Balestro, F.; Ballou, R.; Klyatskaya, S.; Ruben, M.; Wernsdorfer, W. Electrically Driven Nuclear Spin Resonance in Single-Molecule Magnets. *Science* **2014**, *344* (6188), 1135–1138.

(5) Gershenfeld, N. A.; Chuang, I. L. Bulk Spin-Resonance Quantum Computation. *Science* **1997**, *275* (5298), 350–356.

(6) Havel, T. F.; Cory, D. G.; Lloyd, S.; Boulant, N.; Fortunato, E. M.; Pravia, M. A.; Teklemariam, G.; Weinstein, Y. S.; Bhattacharyya, A.; Hou, J. Quantum Information Processing by Nuclear Magnetic Resonance Spectroscopy. *Am. J. Phys.* **2002**, *70* (3), 345–362.

(7) Vandersypen, L. M.; Steffen, M.; Breyta, G.; Yannoni, C. S.; Sherwood, M. H.; Chuang, I. L. Experimental Realization of Shor's Quantum Factoring Algorithm Using Nuclear Magnetic Resonance. *Nature* **2001**, *414* (6866), 883–887.

(8) Brace, C. Thermal Tumor Ablation in Clinical Use. *IEEE Pulse* **2011**, *2* (5), 28–38.

(9) Tseng, H.; Lin, S.-E.; Chang, Y.-L.; Chen, M.-H.; Hung, S.-H. Determining the Critical Effective Temperature and Heat Dispersal Pattern in Monopolar Radiofrequency Ablation Using Temperature-Time Integration. *Exp. Ther. Med.* **2016**, *11* (3), 763–768.

(10) Yuan, J.; Mei, C.-S.; Panych, L. P.; McDannold, N. J.; Madore, B. Towards Fast and Accurate Temperature Mapping with Proton Resonance Frequency-Based MR Thermometry. *Quant. Imaging Med. Surg.* **2012**, *2* (1), 21-32–32.

(11) van Rhoon, G. C.; Wust, P. Introduction: Non-Invasive Thermometry for Thermotherapy. *Int. J. Hyperthermia* **2005**, *21* (6), 489–495.

(12) Levy, G. C.; Terry Bailey, J.; Wright, D. A. A Sensitive NMR Thermometer for Multinuclei FT NMR. *J. Magn. Reson.* **1980**, *37* (2), 353–356.

(13) Bornais, J.; Brownstein, S. A Low-Temperature Thermometer for 1H, 19F, and 13C. *J. Magn. Reson. (1969-1992)* **1978**, *29* (2), 207–211.

(14) Quast, H.; Heubes, M.; Dunger, A.; Limbach, H.-H. A High-Precision Carbon-13 Shift Thermometer for the Temperature Range 100–300 K. *J. Magn. Reson.* **1998**, *134* (2), 236–244.

(15) Zuo, C. S.; Bowers, J. L.; Metz, K. R.; Nosaka, T.; Sherry, A. D.; Clouse, M. E. TmDOTP5−: A Substance for NMR Temperature Measurements in Vivo. *Magn. Reson. Med.* **1996**, *36* (6), 955–959.

(16) Sargeson, A. M. Developments in the Synthesis and Reactivity of Encapsulated Metal Ions. *Pure Appl. Chem.* **1986**, *58* (11), 1511–1522.

(17) Liu, S.; Li, D.; Huang, C.-W.; Yap, L.-P.; Park, R.; Shan, H.; Li, Z.; Conti, P. S. The Efficient Synthesis and Biological Evaluation of Novel Bi-Functionalized Sarcophagine for ^{64}Cu Radiopharmaceuticals. *Theranostics* **2012**, *2* (6), 589–596.

(18) Liu, S.; Li, Z.; Conti, P. S. Development of Multi-Functional Chelators Based on Sarcophagine Cages. *Molecules* **2014**, *19* (4), 4246–4255.

(19) Ozvat, T. M.; Peña, M. E.; Zadrozny, J. M. Influence of Ligand Encapsulation on Cobalt-59 Chemical-Shift Thermometry. *Chem. Sci.* **2019**, *10* (27), 6727–6734.

(20) Krause, R.; Megargel, E. Student Synthesis of Tris(ethylenediamine)cobalt(III) Chloride. *J. Chem. Educ.* **1976**, *53* (10), 667.

(21) Bailar, J. C.; Work, J. B. Some Coördination Compounds of Cobalt Containing Trimethylenediamine and Neopentanediamine. *J. Am. Chem. Soc.* **1946**, *68* (2), 232–235.

(22) Geue, R. J.; Snow, M. R. Structure, Conformational Analysis and Optical Activity of a Bis(tridentate)cobalt(III) Complex. $(+)_{589}$-Δλλ-Bis[1,1,1-Tris(aminomethyl)ethane]cobalt(III) Chloride $(+)_{589}$-(*R*,*R*)-Tartrate Hydrate. *Inorg. Chem.* **1977**, *16* (2), 231–241.

(23) Qin, C.-J.; James, L.; Chartres, J. D.; Alcock, L. J.; Davis, K. J.; Willis, A. C.; Sargeson, A. M.; Bernhardt, P. V.; Ralph, S. F. An Unusually Flexible Expanded Hexaamine Cage and Its Cu^{II} Complexes: Variable Coordination Modes and Incomplete Encapsulation. *Inorg. Chem.* **2011**, *50* (18), 9131–9140.

(24) Bottomley, G.; Clark, I.; Creaser, I.; Engelhardt, L.; Geue, R.; Hagen, K.; Harrowfield, J.; Lawrance, G.; Lay, P.; Sargeson, A.; See, A.; Skelton, B.; White, A.; Wilner, F. The Synthesis and Structure of Encapsulating Ligands: Properties of Bicyclic Hexamines. *Aust. J. Chem.* **1994**, *47* (1), 143–179.

(25) Carr, H. Y.; Purcell, E. M. Effects of Diffusion on Free Precession in Nuclear Magnetic Resonance Experiments. *Phys. Rev.* **1954**, *94* (3), 630–638.

(26) Meiboom, S.; Gill, D. Modified Spin-Echo Method for Measuring Nuclear Relaxation Times. *Rev. Sci. Instrum.* **1958**, *29* (8), 688–691.

(27) The MathWorks Inc. *Signal Processing Toolbox References*; Natick, MA, 2020.

(28) Ozvat, T. M.; Sterbinsky, G. E.; Campanella, A. J.; Rappé, A. K.; Zadrozny, J. M. EXAFS Investigations of Temperature-Dependent Structure in Cobalt-59 Molecular NMR Thermometers. *Dalton Trans.* **2020**, *49* (45), 16380–16385.

(29) Frisch, M. J.; Trucks, G. W.; Schlegel, H. B.; Scuseria, G. E.; Robb, M. A.; Cheeseman, J. R.; Scalmani, G.; Barone, V.; Petersson, G. A.; Nakatsuji, H.; Li, X.; Caricato, M.; Marenich, A. V.; Bloino, J.; Janesko, B. G.; Gomperts, R.; Mennucci, B.; Hratchian, H. P.; Ortiz, J. V.; Izmaylov, A. F.; Sonnenberg, J. L.; Williams; Ding, F.; Lipparini, F.; Egidi, F.; Goings, J.; Peng, B.; Petrone, A.; Henderson, T.; Ranasinghe, D.; Zakrzewski, V. G.; Gao, J.; Rega, N.; Zheng, G.; Liang, W.; Hada, M.; Ehara, M.; Toyota, K.; Fukuda, R.; Hasegawa, J.; Ishida, M.; Nakajima, T.; Honda, Y.; Kitao, O.;

Nakai, H.; Vreven, T.; Throssell, K.; Montgomery Jr., J. A.; Peralta, J. E.; Ogliaro, F.; Bearpark, M. J.; Heyd, J. J.; Brothers, E. N.; Kudin, K. N.; Staroverov, V. N.; Keith, T. A.; Kobayashi, R.; Normand, J.; Raghavachari, K.; Rendell, A. P.; Burant, J. C.; Iyengar, S. S.; Tomasi, J.; Cossi, M.; Millam, J. M.; Klene, M.; Adamo, C.; Cammi, R.; Ochterski, J. W.; Martin, R. L.; Morokuma, K.; Farkas, O.; Foresman, J. B.; Fox, D. J. *Gaussian 16 Rev. C.01*; Wallingford, CT, 2016.

(30) Neese, F. The ORCA Program System. *WIREs Computational Molecular Science* **2012**, *2* (1), 73–78.

(31) Sudmeier, J. L.; Anderson, S. E.; Frye, J. S. Calculation of Nuclear Spin Relaxation Times. *Concepts Magn. Reson.* **1990**, *2* (4), 197–212.

(32) Farrar, T.; Becker, E. *Pulse Fourier Transform NMR*; Academic Press: New York, 1971.

(33) The MathWorks Inc. *Curve Fitting Toolbox User's Guide R*; Natick, MA, 2020.

(34) The MathWorks Inc. *Symbolic Math Toolbox*; Natick, MA, 2020.

(35) Kirby, C. W.; Puranda, C. M.; Power, W. P. Cobalt-59 Nuclear Magnetic Relaxation Studies of Aqueous Octahedral Cobalt(III) Complexes. *J. Phys. Chem.* **1996**, *100* (35), 14618–14624.

(36) Ader, R.; Loewenstein, A. Nuclear Magnetic Relaxation Studies in Solutions of Symmetric Cobalt(III) Complexes. *J. Magn. Reson.* **1971**, *5* (2), 248–261.

(37) Chacko, V. P.; Bryant, R. G. Electric Field Gradient Modulation and Nuclear Magnetic Relaxation in Hexacyanocobaltate Ion. *J. Magn. Reson.* **1984**, *57* (1), 79–84.

(38) Doddrell, D. M.; Bendall, M. R.; Healy, P. C.; Smith, G.; Kennard, C. H. L.; Raston, C. L.; White, A. H. ^{59}Co and ^{13}C Nuclear Spin Relaxation Studies in Solutions of Symmetric, Bidentate Cobalt(III) Complexes. On the Mechanism of ^{59}Co Spin Relaxation. Crystal Structure Determination of Tris(tropolonato)cobalt(III). *Aust. J. Chem.* **1979**, *32* (6), 1219–1230.

(39) Boeré, R. T.; Kidd, R. G. Rotational Correlation Times in Nuclear Magnetic Relaxation. In *Annual Reports on NMR Spectroscopy*; Elsevier, 1983; Vol. 13, pp 319–385.

(40) Foster, R. J.; Damion, R. A.; Ries, M. E.; Smye, S. W.; McGonagle, D. G.; Binks, D. A.; Radjenovic, A. Imaging of Nuclear Magnetic Resonance Spin-Lattice Relaxation Activation Energy in Cartilage. *R. Soc. Open Sci.* **2018**, *5* (7), 180221.

(41) Rieke, V.; Pauly, K. B. MR Thermometry. *J. Magn. Reson. Imaging* **2008**, *27* (2), 376–390.

(42) Anet, F. A. L.; O'leary, D. J. The Shielding Tensor Part II: Understanding Its Strange Effects on Relaxation. *Concepts Magn. Reson.* **1992**, *4* (1), 35–52.

CHAPTER 5 – Vibrational Elucidation of Temperature Sensitivity in ^{59}Co-NMR Thermometers

5.1. Overview

Understanding the mechanisms governing temperature-dependent magnetic resonance properties is essential for enabling thermometry via magnetic resonance imaging. Herein we harness a new molecular design strategy for thermometry – that of effective mass engineering via deuteration in the first coordination shell – to reveal the mechanistic origin of ^{59}Co chemical shift thermometry. Exposure of $[Co(en)_3]^{3+}$ (**1**, en = ethylenediamine) and $[Co(diNOsar)]^{3+}$ (**2**, diNOsar = dinitrosarcophagine) to mixtures of H_2O and D_2O produces distributions of d_n-$[Co(en)_3]^{3+}$ (n = 0 to 12) and d_n-$[Co(diNOsar)]^{3+}$ (n = 0 to 6) isotopomers all resolvable by ^{59}Co NMR. Variable-temperature ^{59}Co-NMR analyses reveal a temperature dependence of the ^{59}Co chemical shift, $\Delta\delta/\Delta T$, on deuteration of the N donor atoms. For **1**, deuteration amplifies $\Delta\delta/\Delta T$ by 0.07 ppm/°C. Increasing degrees of deuteration yields an opposing influence on **2**, diminishing $\Delta\delta/\Delta T$ by –0.07 ppm/°C. Solution-phase Raman spectroscopy in the low-frequency 200–600 cm^{-1} regime reveals a redshift of Raman-active Co–N_6 vibrational modes by deuteration. Analysis of the normal vibrational modes showed that Raman modes produce the largest variation in $\delta(^{59}Co)$. Finally, partition function analysis of the Raman-active modes showed that increased populations of Raman-modes predict greater $\Delta\delta/\Delta T$, representing new insight into the thermometry mechanism.

5.2. Introduction

Environmentally sensitive nuclear spins offer a route to novel MRI agents or quantum sensing molecular platforms.[1,2] One such environmental stimulus of interest is temperature, as non-invasive thermometry could enable guided thermal therapies and imaging.[3–6] Cobalt-59 nuclear spins are highly promising for this application because of the strong temperature dependence of the chemical shift, δ.[7–11] The current record for the sensitivity of the chemical shift to temperature ($\Delta\delta/\Delta T$) from a ^{59}Co nucleus is 3.15 ppm/°C in $Co(acac)_3$.[12] Higher sensitivities are ultimately necessary for utility, yet the precise molecular factors (specifically, ligand identity) that control $\Delta\delta/\Delta T$ are unknown.

Theoretical studies decades ago[13–15] proposed strict bond-distance expansion as the mechanistic origin of $\Delta\delta/\Delta T$. In this picture, temperature-dependent changes in physical structure modulate the ligand field splitting (Δ_o) and thus determine $\delta(^{59}\text{Co})$ by changing the energies of the $^1A_{1g}$ and $^1T_{1g}$ states of a Co^{3+} complex, a change that affects the ^{59}Co paramagnetic shift as described by Ramsey's equation.[7] The effect is analogous to the origin of temperature-independent paramagnetism in Co^{3+} complexes.[16] More "flexible" ligands could be envisioned to produce species with greater temperature-dependent inner-coordination spheres, thereby producing higher $\Delta\delta/\Delta T$. However, recent studies by us[17–19] and others[20,21] suggest that bond distance expansion alone is not the dominant feature. In a prior work, we posited a model wherein structural rigidity imparted by the ligand shell engenders long-lived vibrations caused by collisions of a given ^{59}Co-NMR thermometer with surrounding solvent and thus, temperature-driven structures and $\Delta\delta/\Delta T$ (*Figure 5.1*).[17]

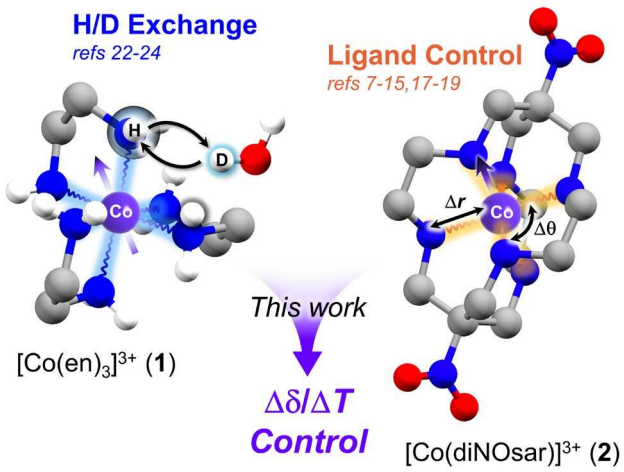

Figure 5.1. Overview of ligand-based influence on metal-ion nuclear spin studies. Our work demonstrates finite yet controllable modulation of ^{59}Co nuclear spin ($I = {}^7/_2$) via chemical shift thermometry $\Delta\delta/\Delta T$ in structures $[Co(en)_3]Cl_3$ (**1**) and $[Co(diNOsar)]Cl_3$ (**2**). Select hydrogens are omitted for clarity.

If this model is correct, then we posited that changes to donor-atom mass would affect $\Delta\delta/\Delta T$, as changes in mass would be expected to alter vibrational lifetimes, amplitudes, equilibrium Co–L distances and ultimately electronic structure.

A controlled test of varying donor-atom mass on $\Delta\delta/\Delta T$ via typical coordination chemistry strategies is, however, intrinsically challenging. For example, a simple swap of N-donor atoms for heavier

O or P-donor atoms will simultaneously affect the ligand mass and the ligand field strength. Separately, isotopically enriched donor-atom ligands are frequently exorbitant and limited in availability. We hypothesized that a facile route to controlled variable-mass studies of the mechanistic origins of $\Delta\delta/\Delta T$ was to use H/D exchange on protonated N-donor atoms. We envisioned the resulting N-donors would retain nearly constant ligand fields whilst mimicking heavier-atom behavior (*Figure 5.2*).

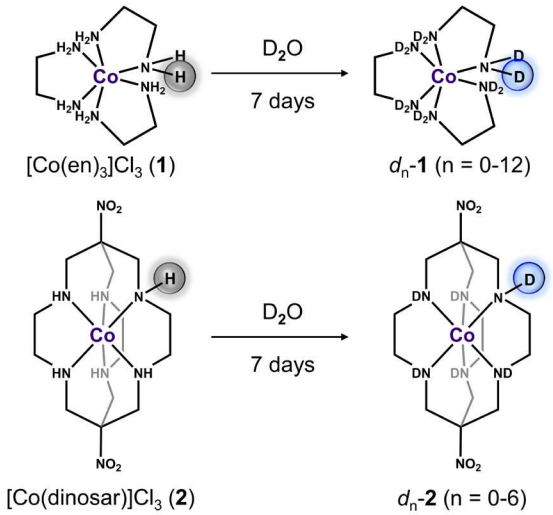

Figure 5.2. Depiction of deuteration process for **1** and **2** to prepare d_n-**1** (n = 0 to 12) and d_n-**2** (n = 0 to 6). Each complex has an overall 3+ charge complete as chloride salts (omitted for clarity).

Herein, we show that H/D exchange on ligand N-donor atoms offers a new strategy to adjust $\Delta\delta/\Delta T$. We do so via studies of deuterated isotopomers of molecules $[Co(en)_3]^{3+}$ (**1**, en = ethylenediamine) and $[Co(diNOsar)]^{3+}$ (**2**, diNOsar = dinitrosarcophagine). These species contain $–NH_2$ (primary) and –NH– (secondary) amine donor atoms that can be deuterated when treated with D_2O.[22–24] We show that this deuteration produces a spectroscopically resolvable distribution of H/D isotopomers in solution by ^{59}Co NMR. Comparative analyses of the temperature dependence of the ^{59}Co chemical shifts of these isotopomers demonstrate that the ligand mass plays a modest role in governing temperature-dependent ^{59}Co-NMR signals. Investigation of vibrational modes via Raman spectroscopy suggests a new model for thermometry based not on vibration lifetime, but on the number and energy of low frequency Raman-active vibrations.

5.3. Experimental Section

5.3.1. General Considerations

Compounds trisethylenediaminecobalt(III) chloride (**1**, $[Co(en)_3]Cl_3$) and (1,8-dinitro-3,6,10,13,16,19-hexaazabicyclo[6.6.6]iscosane)cobalt(III) chloride (**2**, $[Co(diNOsar)]Cl_3$) were synthesized according to previous literature preparations.[25,26] Properties and characterization of these complexes were as described previously by us.[17] Samples that contained D_2O were allowed to complete H/D equilibration over the course of seven days before any spectroscopic investigation. Periodic analysis of the ^{59}Co-NMR signal during those days established when equilibration was finalized, generally within the seven-day window. Those samples containing portions of D_2O were prepared in plastic scintillation vials after thorough drying of **1** and **2** via high-vac removal of residual water.

5.3.2. UV-vis Spectrophotometry

UV-vis spectra were collected on an Agilent 8435 UV-visible spectrophotometer as 5 mM aqueous solutions at room-temperature. Fully protiated and fully deuterated complexes were measured in their respective H_2O and 99.9% D_2O solutions. UV-vis spectrophotometric data were fit (Gaussian) to determine peak values. Quantitation of ligand fields Δ_o were permitted using a d^6 Tanabe-Sugano diagram in correspondence to the *d-d* transitions of the central Co^{3+} octahedral ions in **1** and **2**.

5.3.3. Variable-Temperature ^{59}Co NMR

Cobalt-59 NMR spectra were collected on an Agilent Unity INOVA 500 MHz (^{1}H) spectrometer using 15 mM samples in varying degrees (0%, 25%, 50%, 75%, 99.9%) of D_2O in H_2O solution mixtures. The spectrometer magnet was locked to a sample of D_2O and tuned to the ^{59}Co standard of 1 M $K_3[Co(CN)_6]$ before collection of the highly chemical-shifted samples **1** and **2** absent of locking, shimming, and spinning. It should be noted that any error introduced to the spectra by the unlocked magnet be converted to changes in linewidths of the ^{59}Co spectra of 0.1 Hz/hour. Such deviations are negligible considering the 1–6 kHz

(10–50 ppm) scale of the collected peaks. Variable temperature measurements were made on each sample over 10–60 °C in 5 °C intervals. Temperature was controlled using an FTS Systems TC-84 Kinetics AirJet Temperature Controller to stream temperature-specific nitrogen directly to the probe and probe chamber. Probe temperature was monitored via thermocouple output. Temperature equilibration of the sample was allowed to occur over 15 min before the tuning and use of a 5 mm broadband probe for spectral collection. Variable temperature inversion recovery experiments were performed with the same spectrometer and probe. Deconvolution of all peaks in ^{59}Co-NMR spectra were evaluated from fits (Lorentzian) (*Tables A4.2–A4.3*). Evaluation of $\Delta\delta/\Delta T$ for each isotopomer proceeded by determining the Lorentzian peak positions of each isotopomer as a function of temperature. Evaluating the complete set of isotopomers for **2** (from d_0-**2** to d_6-**2**) was achievable using a single sample with 50% D_2O in H_2O. However, for **1**, three separate samples in varied amounts of D_2O in H_2O had to be used (i.e., 25%, 50%, and 75% D_2O). Minute inconsistencies in the magnet (e.g., field and temperature inhomogeneities, dephasing) require alignment of peaks between sample spectra. Alignments to peak positions were made with respects to the 50% D_2O in H_2O spectra. Similarly, $\Delta\delta/\Delta T$ could be accurately compared between the three samples by simply evaluating the change in $\Delta\delta/\Delta T$ determined at 0.006 ppm/°C (*Figure A4.8*). Furthermore, while the increase in $\Delta\delta/\Delta T$ with increasing deuteration is minute between isotopomers that differ by one deuteron, the difference between fully protiated and deuterated complexes is significant relative to the error. Furthermore, the change in $\Delta\delta/\Delta T$ for **1** is shown to be reliably consistent over three separate sample measurements.

5.3.4. Raman Spectroscopy

Raman spectra of compounds **1** and **2** were collected in their fully deuterated and fully protiated forms in H_2O (deionized) and D_2O (99.9%), respectively. Sample preparation of the solution phase samples included complete equilibration of isotopomer distribution over seven days prior to measurement. All samples were prepared in 4 mL volume vials to 30 mM concentrations and measured using a Horiba Scientific ONDAX IHR 550 Spectrometer equipped with a 785 nm NIR laser. The collected spectral range was made over 200–600 cm^{-1} and background subtracted from each sample's respective H_2O or D_2O blank.

Acquisitions were made for 600 seconds at room temperature. The collected spectra were baselined and fit to identify peak values. Peaks were modeled to pseudo-Voigt functions to yield peak maxima (frequencies, υ) and full-width half maxima (linewidths, Γ). Values from fits are tabulated in *Tables A4.8-A4.9*.

5.3.5. Frequency and ^{59}Co-NMR Calculations

Frequency calculations of vibrational modes were acquired from optimized structures of complexes **1** and **2** (*Tables A4.10–A4.11*). Optimization and frequency calculations were both made with Gaussian 16 electronic software structure package[27] using the ωB97XD[28,29] density functional and 6-311+g(2d,p) basis set.[30] Harmonic approximations via this computational method yielded Raman spectra agreeable with the experimental spectra for all computed structures. Such agreement allowed the assignment and depiction of experimental vibrational modes, and as a result, a scaling factor was not applied. ^{59}Co-NMR properties calculations of vibrationally displaced structures of **1** and **2** were analyzed along the fullest extent of the distortional pathway (Q = +1 to Q = –1) of experimentally observed vibrational modes (*Table A4.8*). These predictions were performed with ORCA 4.11 electronic software package at the GIAO-B3LYP level[31]with def2-TZVPP and def2/JK basis sets.[32] In all predictions, the ^{59}Co nucleus was individually assigned a def2-QZVPP basis set.[32] In both complexes **1** and **2**, the analysis of isotropic shielding was used to determine the range of $\Delta\delta$ (^{59}Co) and is dominated by the paramagnetic term. Evaluation of $\Delta\delta$ was done only for the lowest energy vibrational modes of the 200–600 cm^{-1} energy regime owing to their higher predicted population of states. Thus, vibrationally-driven changes to δ(^{59}Co) are expected to be governed namely by low energy, high population vibrational modes of the Co–N_6 core in this low energy regime.

5.4. Results and Discussion

Initial evaluations of **1** and **2** by ^{59}Co NMR (11.74 T, 118 MHz) in separate solutions of H_2O and 99.9% D_2O showed the mass-dependent effect of the N–H and N–D donor atom on the δ(^{59}Co). At 10 °C, the δ(^{59}Co) of the fully protiated species d_0-[Co(en)$_3$]$^{3+}$ (d_0-**1**) in H_2O is 7,123 ppm while the peak of the fully deuterated species d_{12}-[Co(en)$_3$]$^{3+}$ (d_{12}-**1**) in D_2O is 7,061 ppm (*Figure A4.1*). Similarly, the fully

protiated d_0-[Co(diNOsar)]$^{3+}$ (d_0-**2**) in H_2O showed a broad peak at 6,857 ppm while the fully deuterated d_6-[Co(diNOsar)]$^{3+}$ (d_6-**2**) peak in D_2O is 6,817 ppm (*Figure A4.2*). The mass-driven chemical shift moves $\delta(^{59}Co)$ upfield by 62 ppm for **1** and 40 ppm for **2**. The effect of deuteration on $\delta(^{59}Co)$ is the same up to 60 °C yet produces sharper NMR signals (*Figures A4.3–A4.4*).

Further ^{59}Co-NMR analysis in 1:1 mixtures of H_2O and D_2O reveal distributions of ^{59}Co peaks spaced out by approximately 5.0(1) ppm and 6.7(1) ppm in **1** and **2**, respectively (*Figure 5.3*).

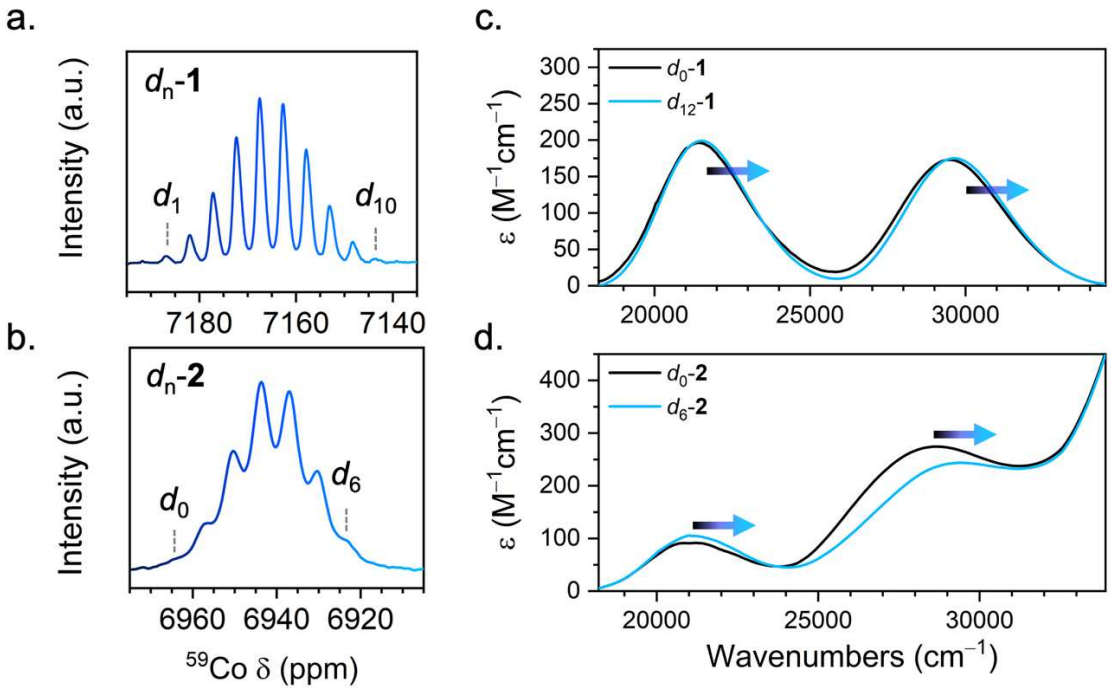

Figure 5.3. a. Solution-phase ^{59}Co-NMR spectrum (11.74 T) depicting an ensemble of isotopomer peaks for d_n-**1** (n = **1**–**9**) at 60 °C after equilibration in a one-to-one D_2O/H_2O mixture. b. Isotopomer peaks for d_n-**2** (n = **0**–**6**) at 60 °C after equilibration in 50% D_2O in H_2O. ***c.*** Solution-phase UV-vis spectra of **1** fully protiated (d_0-**1** in H_2O, *black trace*) and fully deuterated (d_{12}-**1** in D_2O, *blue trace*) at 5 mM. ***d.*** UV-vis spectra of **2** fully protiated (d_0-**2** in H_2O, *black trace*) and fully deuterated (d_6-**2** in D_2O, *blue trace*) at 2.14 mM. Both complexes show blue-shifted transitions after complete H/D exchange.

We note the remarkable similarity of these spectra to the isotopic distributions sometimes observed in mass spectrometry data. Each of the different peaks in these spectra represent a unique isotopomer of **1** and **2**, for which there are a total of 13 for d_n-**1** (n = 0 to 12) and 7 for d_n-**2** (n = 0 to 6). In this case, the number of observed peaks depends on the number of exchangeable protons to the N donor atoms.

Room-temperature UV-vis spectroscopy data demonstrate the relatively small, but measurable, ligand-field consequences of the H/D exchanges. The UV-vis spectrum of d_0-**1** in H_2O showed two peaks at 21,614(9) and 29,572(16) cm^{-1}. Upon dissolution and equilibration in D_2O, d_{12}-**1** showed the same two peaks, but blue-shifted to 21,668(8) and 29,731(14) cm^{-1}. For d_0-**2**, two peaks at 21,008(8) and 27,762(10) cm^{-1} are observed in pure H_2O, and these also shift to higher energy, 21,138(5) and 28,327(8) cm^{-1}, when dissolved in D_2O. For O_h Co^{3+} ions, these two peaks correspond to the $^1A_{1g} \rightarrow {}^1T_{1g}$ and $^1A_{1g} \rightarrow {}^1T_{2g}$ transitions within a low spin d^6 system.[7,33] Tanabe-Sugano analyses (*Table A4.1*) of the changes in the UV-vis spectra suggest a difference in Δ_o of 77 cm^{-1} for **1** upon deuteration, increasing from 23,462 cm^{-1} (d_0-**1**) to 23,539 cm^{-1} (d_{12}-**1**). A larger, 223 cm^{-1} change of Δ_o is observed for d_0-**2** (22,595 cm^{-1}) versus d_6-**2** (22,818 cm^{-1}).

The difference in Δ_o observed between protiated and deuterated species permits the evaluation of ligand field strength changes per deuteration step. For **1**, the total 77 cm^{-1} increase in Δ_o corresponds to a ca. 6.7 cm^{-1} increase per deuteron. For **2**, a greater sensitivity in Δ_o of ca. 37.2 cm^{-1} per deuteron is observed. Extensive prior analysis of multiple families of O_h N-donor Co^{3+} complexes revealed a nearly linear relationship between the $\delta(^{59}Co)$ and Δ_o (6.5 ppm/cm^{-1}).[8,10] The stepwise 5.0 ppm shift in $\delta(^{59}Co)$ peak location and 6.7 cm^{-1} shift in Δ_o per deuteron for **1** is thus consistent with those prior studies. Complex **2**, in contrast, exhibits a much larger effect with half as many deuterons.

The observed change in chemical shift is due to the extraordinary sensitivity of the ^{59}Co nuclear spin to the electronic structure of the Co^{3+} ion. The deuterated ligands are slightly heavier (by ~13% mass for N–D_2 v. N–H_2 and ~7% for N–D v. N–H) and due to that heavier mass, are likely to remain at *slightly* different equilibrium distances from the Co^{3+} ion in solution. This changing distance, which is likely too small to measure by normal structural methods, enables a change to Co–N orbital overlap and thus, Δ_o. In principle, the more closely bound N atom will cause the antibonding e_g* orbitals to rise in energy, increasing Δ_o. The increase in Δ_o then weakens the ^{59}Co paramagnetic shift and causes the $\delta(^{59}Co)$ to move upfield, which is observed for both complexes. In a way, the effect demonstrates that the ^{59}Co nucleus serves as an extraordinarily sensitive detector of a minute structural differences. Finally, we note the spectroscopic

resolution of the different isotopomers in the ^{59}Co-NMR spectra crucially permits their individual interrogation to test how deuteration affects $\Delta\delta/\Delta T$.

The mass effect of H/D exchange on $\Delta\delta/\Delta T$ was tested by investigating the variable temperature ^{59}Co-NMR spectra of **1** and **2** from 10 to 60 °C. These studies were performed in multiple different mixtures of D_2O and H_2O to ensure that the behaviors of all isotopomers were captured (*Figure A4.5–A4.6*). With increasing temperature from 10 °C, all ^{59}Co-NMR peaks shift downfield for **1** and **2** (*Figure 5.4*).

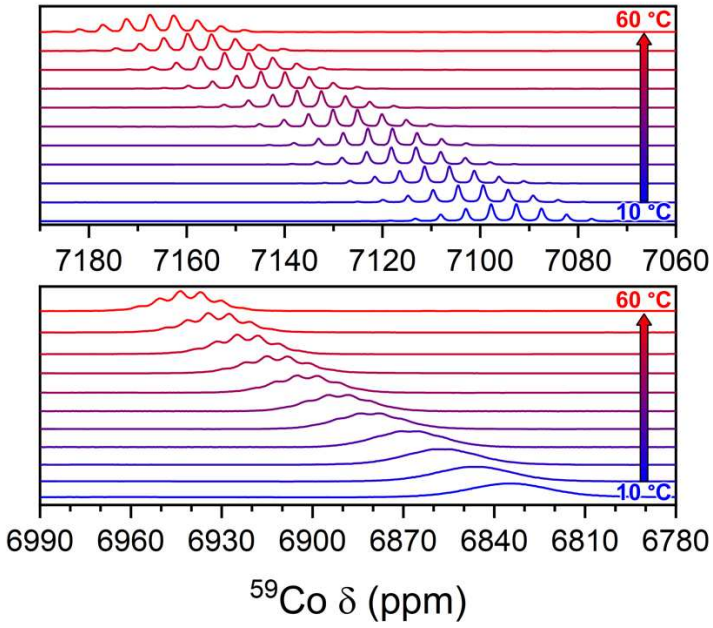

Figure 5.4. Stacked variable temperature ^{59}Co-NMR spectra of isotopomer ensembles of **1** (*top*) and **2** (*bottom*) from 10–60 °C. Measurements were made on equilibrated samples of 50% D_2O/H_2O.

For **1**, all peaks remain resolvable over the temperature range and shift over an approximate 70 ppm window. For **2**, however, the peaks appear to broaden and coalesce with decreasing temperature (relative to the 60 °C spectrum) and the peak itself moves by approximately 100 ppm over the studied temperature range. All peaks were identified from deconvolution of spectra where possible (10–60 °C for **1**, 35–60 °C for **2**). The relative magnitudes of the temperature-driven chemical shifts are consistent with prior analyses of the fully protiated versions of **1** and **2**.[17] The relative intensities appear to be consistent as a function of temperature, indicating negligible redistribution of isotopomer populations during the measurements.

Analysis of the $\delta(^{59}\text{Co})$ peak positions as a function of temperature T (°C) for individual isotopomers provides the key test of the role of deuteration on $\Delta\delta/\Delta T$ (*Figure 5.5*).

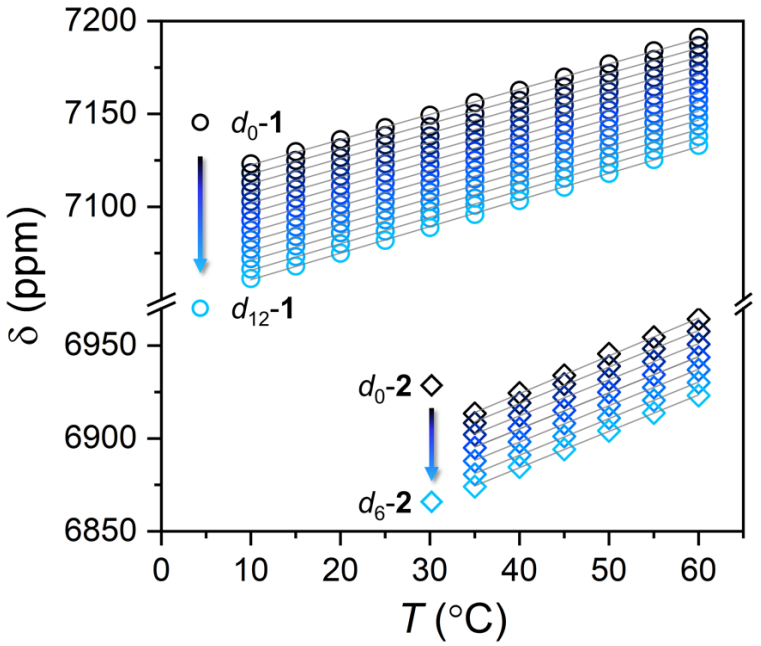

Figure 5.5. Peak positions of all isotopomers by temperature for **1** (*circles*, 10–60 °C) and **2** (*diamonds*, 35–60 °C). Solid lines are linear regressions for each isotopomer to assign each value of $\Delta\delta/\Delta T$.

For **1**, the well-resolved peaks enable the isolation of $\Delta\delta/\Delta T$ values for all possible H/D isotopomers. In the case of **2**, the discernability of each isotopomer signal is obscured below 35 °C, and analyses were applied only above this temperature (*Figure A4.7*). In both complexes (and across all samples), comparison of $\Delta\delta/\Delta T$ values for the different isotopomers show a mild but consistent change in temperature sensitivity with increasing deuteration (*Table A4.2–A4.3*). For **1**, the trend across all isotopomers showed a steady *increase* in $\Delta\delta/\Delta T$ (*Figure A4.8*) with deuteration, from 1.35(1) ppm/°C to 1.42(1) ppm/°C from d_0-**1** to d_{12}-**1**, respectively. Over the 35–60 °C temperature range, **2**, in contrast, showed a *decrease* in $\Delta\delta/\Delta T$ with increasing deuteration, from 2.03(3) ppm/°C to 1.96(2) ppm/°C from d_0-**2** to d_6-**2**, respectively.

We also tested the temperature dependence of the dynamic magnetic properties, specifically spin-lattice, T_1, and spin-spin dephasing, T_2*, relaxation of the ^{59}Co nuclei for the different isotopomers (*Figures A4.9–A4.17 and Tables A4.4–A4.7*) but did not see any appreciable difference between isotopomers. We note the expectation of a trend to be perhaps overambitious, as there may be many different H/D

substitutions for the same d_n isotopomer. Each of these isomers could have differing symmetries (e.g., d_2-**1** possessing two deuterons could be distributed on the same N-donor-atom across different ligands), and thus different T_1 and T_2* values, since ^{59}Co T_1 is typically governed by quadrupolar relaxation. This relaxation mechanism is intimately tied to ligand structure and the longer relaxation times in **1** likely stem from a closer-to-O_h symmetry structure compared to **2**.[19,34]

The foregoing data demonstrate that deuteration produced opposing effects on the change in ^{59}Co $\Delta\delta/\Delta T$. Previous studies of ours suggested a correlation between longer lifetimes for low-energy vibrations (hypothesized to be predominantly Co–N in character)[35,36] and higher $\Delta\delta/\Delta T$.[17] Here, we collected solution-phase Raman spectroscopy on **1**, d_{12}-**1**, **2**, and d_6-**2** from 200 to 600 cm^{-1} to test that hypothesis. Experimental data for **1** revealed four significant active modes at 279(1), 376(1), 445(1), and 529(1) cm^{-1}. Upon deuteration, all four peaks showed a modest redshift to 273(1), 353(1), 419(1), and 497(1) cm^{-1}, respectively (*Figure 5.6*).

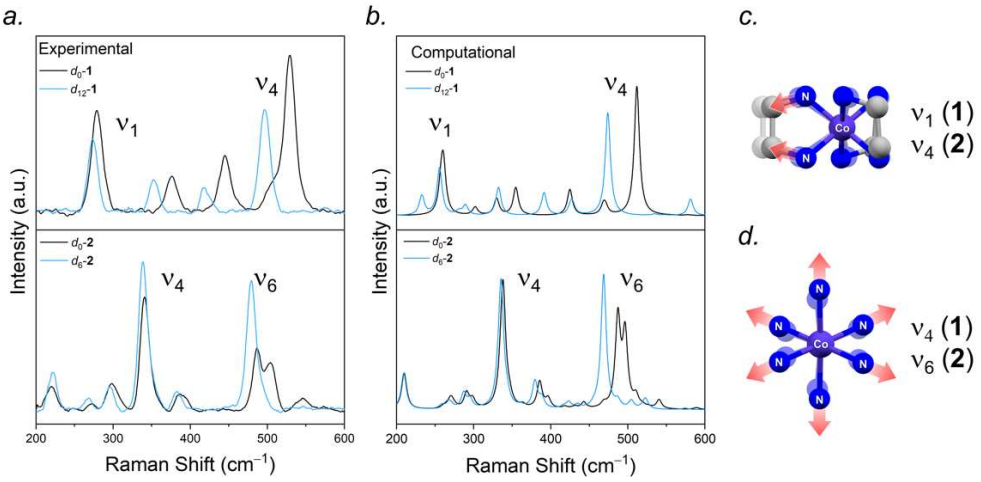

Figure 5.6. a. Experimental Raman spectra of protiated (*black traces*) and deuterated (*blue traces*) isotopomers for **1** (*top*) and **2** (*bottom*) at 30 mM over 200–600 cm^{-1}. ***b.*** Precited Raman spectra of **1** (*top*) and **2** (*bottom*). ***c.*** Depiction of the pincer modes *ca.* 260–340 cm^{-1} (υ_1 for **1** and υ_4 for **2**). ***d.*** Depiction of the breathing modes *ca.* 450–510 cm^{-1} (υ_4 for **1** and υ_6 for **2**).

The redshifted frequencies of the Raman peaks are attributed to the higher mass of the N–D$_2$. For d_0-**2**, eight significant modes were present, ranging from 219(1) to 546(1) cm^{-1} (*Table A4.8*). Upon deuteration, d_6-**2** showed a similar redshift in the vibrational modes, but smaller in magnitude relative to **1**. The largest

change, both in intensity and energy, was observed for the vibrations at ca. 500 cm^{-1} in both complexes. Lifetimes, defined as $\tau = 1/FWHM$ (FWHM = full width at half maximum) were averaged over all observed Raman peaks (*Table A4.9*). As protiated species, τ_{avg} was 0.61(3) ps for **1** and 0.7(1) ps for **2**. Upon deuteration, both spectra sharpened, and τ_{avg} increased to 0.70(2) and 0.8(1) ps for **1** and **2**, respectively. In both complexes, deuteration yielded longer τ, but $\Delta\delta/\Delta T$ does not increase for both. We therefore interpret these results as disproof of our prior hypothesis that longer vibration lifetimes alone enhance $\Delta\delta/\Delta T$.[17]

Despite this disproof, the very clear spectral differences between **1**, d_{12}-**1**, **2**, and d_6-**2** provide an exciting opportunity to test for possible consequences of deuteration on vibrations and therefore $\delta(^{59}Co)$. We consider a new hypothesis for the governing phenomena of $\Delta\delta/\Delta T$. We propose that the population of molecular vibrational states (Raman and IR-active modes) within the inner coordination shell guide the structural distortions that dictate $\Delta\delta/\Delta T$. If true, then changes in populations, energies, and types of specific vibrations, not lifetimes, should correlate to $\Delta\delta/\Delta T$ and provide the true design strategies for controlled ^{59}Co temperature sensitivities.

We sought to test this picture against our experimental observations with two separate analyses that estimated the relative populations of the different vibrational states and the individual impacts on $\delta(^{59}Co)$. We considered **1**, d_{12}-**1**, **2**, and d_6-**2** and the record-holding $Co(acac)_3$, which displayed a $\Delta\delta/\Delta T$ of 3.15 ppm/°C in $CDCl_3$.[12] Frequency calculations were first performed to obtain a complete picture of the vibrational activity. Computed Raman spectra nicely agree with the experimental spectra and reproduced the experimentally redshifted Raman-mode peaks upon deuteration.

The performed frequency calculations enabled qualitative assignment of the observed vibrations. Within the low-energy regime below 600 cm^{-1}, many of the vibrations were complex, incorporating bond stretches, scissoring, and bending motions of the $Co–N_6$ coordination sphere (*Tables A4.10–A4.11*). The most intense modes (experimentally and computationally) were found to possess strong symmetric Co–N stretching character. These were at 261 and 512 cm^{-1} for **1**, and 338 and 487 cm^{-1} for **2**. These predicted frequencies agree with the experimentally collected solution-phase Raman spectra and are supported by literature values.[37,38] Of these two stretching modes, the lower energy vibration (261 cm^{-1} for **1**, 338 cm^{-1}

for **2**) is described by a N–Co–N pincer-like mode of the ethylenediamine ligands in **1** and ethylenediamine-like sidearms in **2**. The higher-energy mode (512 cm^{-1} for **1**, 487 cm^{-1} for **2**) arises due to symmetric stretching of the six N-donor atoms along their bonds to the metal center. This higher-energy vibration, which showed the greatest redshift after deuteration in both structures, is best-described as the A_{1g} *breathing mode* of the octahedral $Co–N_6$ core.

Analysis of the *populations of vibrational states* revealed what we believe is the mechanism governing $\Delta\delta/\Delta T$. We compare $\Delta\delta/\Delta T$ to the total vibrational partition functions, q_{Total}, of **1**, d_{12}-**1**, **2**, and d_6-**2** using the computed vibrations from the frequency calculations including Raman and IR-active modes (*Figure A4.18*). We also computed q_{Total} of additional Co^{3+} complexes with reported $\Delta\delta/\Delta T$ in literature including $[Co(acac)_3]$, $[Co(NO_2)_6]^{3-}$, $[Co(CN)_6]^{3-}$, $[Co(NH_3)_6]^{3+}$, $[Co(tn)_3]^{3+}$, and $[Co(tame)_2]^{3+}$.[12,15,17] Harmonic frequency calculations were first made to predict the normal modes (3N–6) of each structure. Total vibrational partition functions, q_{Total}, are calculated from the product of each normal mode by $q = 1 / (1 - e^{-E/k_BT})$, where E is the normal mode energy (cm^{-1}), k_B is Boltzmann's constant, and T is temperature (Kelvin). These partition functions depend on the number of vibrational normal modes, their respective frequencies, and the temperature. At 25 °C, the value of q_{Total} for **1** (5.4×10^3) is surpassed by **2** (2.0×10^7) by 4 orders of magnitude, and the value of $Co(acac)_3$ (2.2×10^{11}) is even larger. Higher values of q_{Total} reflect a higher population of vibrational states for a given molecule, enabled by greater numbers of low-energy vibrations. Out of all computed normal vibrational modes of **1**, 23% are below 600 cm^{-1}. Similarly, 25% of the modes in **2**, and 32% of the modes in $Co(acac)_3$ are below 600 cm^{-1}. The number of low-energy modes in each complex roughly reflects the 25 °C value of q_{Total}.

Owing to this result, we posit that higher values of $\Delta\delta/\Delta T$ are attributed to generally higher populations of low-energy modes at a given temperature. This insight is unique from all prior proposed models of the origin of the temperature dependence of $\delta(^{59}Co)$.[14,15,17,39] The result also establishes a key design principle for $\Delta\delta/\Delta T$, wherein synthetic strategies to change q_{Total} may guide enhancement of $\Delta\delta/\Delta T$. However, the analysis of q_{Total} alone did not account for the differing effects of deuteration on $\Delta\delta/\Delta T$ between **1** and **2**. Above, we proposed that the *individual* vibrations and their respective impacts on $\delta(^{59}Co)$

must be active, and subsequent calculations were performed to test the relevance of this concept to ^{59}Co $\Delta\delta/\Delta T$.

In principle, one might expect all 3N–6 vibrations for a complex to be important for $\delta(^{59}\text{Co})$, as all modes may contribute to a varying structure. However, different vibrations will affect the $^1A_{1g}$ and $^1T_{1g}$ energies to different extents depending on how they affect the e_g* orbital energies. We hypothesized that only Raman-active vibrations, such as the Co–N_6 breathing mode, would be the most influential on $\delta(^{59}\text{Co})$, as symmetric distortions should produce large-amplitude changes in metal-ligand overlap (and thus e_g* and Δ_o). To test this idea, we computed the $\delta(^{59}\text{Co})$ as a function of atomic displacement along the coordinate pathway, Q for vibrations between 200–600 cm^{-1}. The vibrational coordinate Q describes displacement away from the optimized structure (Q = 0) following the progression of a given vibration. $\Delta\delta/\Delta Q$ curves were then constructed from computed ^{59}Co chemical-shift calculations at individual points along Q (*Figure 5.7*).

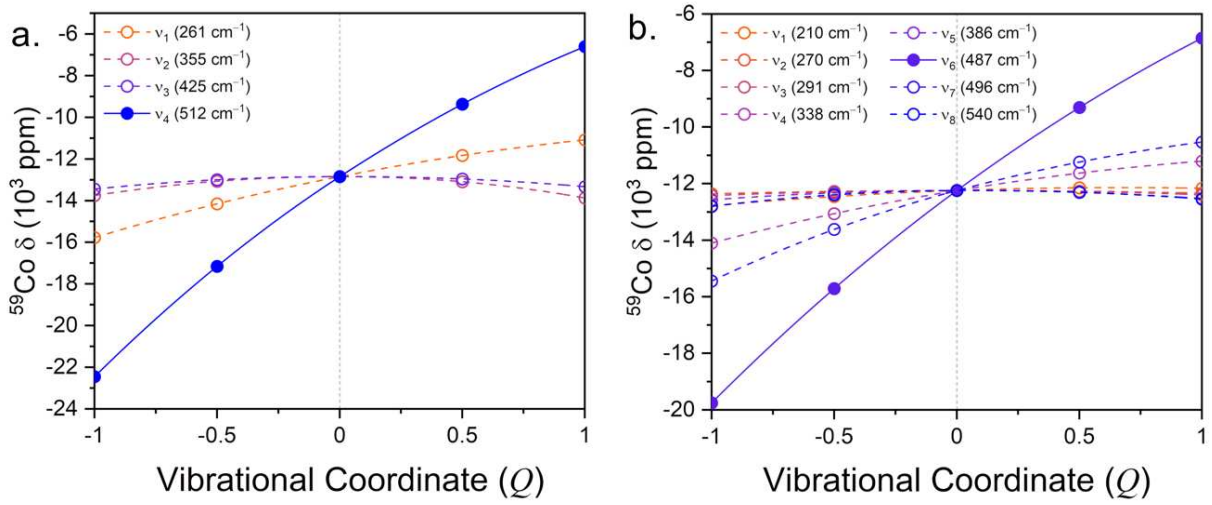

Figure 5.7. a. ^{59}Co δ as a function of vibrational coordinate Q, for experimentally determined Raman modes in **1** between 200–600 cm^{-1}. ***b.*** ^{59}Co δ as a function of Q for Raman modes in **2** between 200–600 cm^{-1}. The Co–N_6 symmetric A_{1g} breathing mode is indicated by filled circles with solid traces.

We found that in all cases, $\delta(^{59}\text{Co})$ values vary over 1000s of ppm and often non-linearly between the extremes of Q (–1 and +1). For a given vibration, we can describe the change in $\delta(^{59}\text{Co})$ relative to Q via $\Delta\delta/\Delta Q$ at Q = 0, which represents a coupling strength between the vibration and $\delta(^{59}\text{Co})$. The symmetric Co–N_6 breathing modes yielded the largest values of $\Delta\delta/\Delta Q$: 7922 ppm/Q for **1**, 6436 ppm/Q for **2**, and

6113 ppm/Q for $Co(acac)_3$ (*Figure A4.19*). The pincer modes showed the second highest $\Delta\delta/\Delta Q$ values, of 2338 ppm/Q and 1445 ppm/Q, for **1** and **2** respectively. In contrast, $\Delta\delta/\Delta Q$ for IR-active modes were all substantially smaller (3–17 ppm/Q), reflected by the parabolic functions centered at $Q = 0$ (*Figure A4.20*). These results collectively suggest that Raman-active modes (not IR) are key vibrational influences of $\delta(^{59}Co)$, with the breathing mode exhibiting the highest effect. It is likely that these modes are most impactful because they shift the e_g* orbitals by the highest amount. This change then induces the largest difference in the paramagnetic shift via changes to the low-lying excited state energies.

The revealed importance of Raman modes inspired us to evaluate their role in $\Delta\delta/\Delta T$ with regards to the partition function of just these modes, q_{Raman}. Comparison of $\Delta\delta/\Delta T$ to q_{Raman} improves upon the original trend with q_{Total}, further suggesting that *Raman*-active modes are the fundamental vibrational components driving $\Delta\delta/\Delta T$ (*Figure 5.8*).

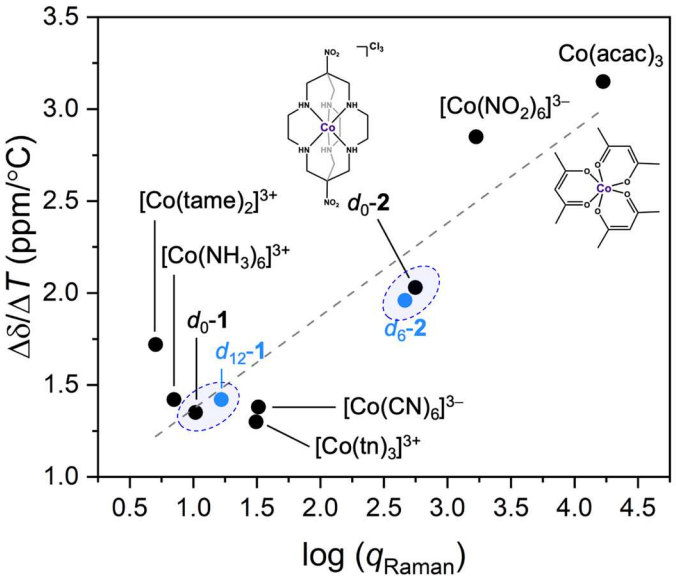

Figure 5.8. Relationship between ^{59}Co $\Delta\delta/\Delta T$ and vibrational partition function of Raman modes, q_{Raman} for **1**, d_{12}-**1**, **2**, d_6-**2**, and other Co^{3+} complexes with known $\Delta\delta/\Delta T$ sensitivities.[12,15,17] R^2 is 0.82 and error is within 0.03 ppm/°C. Shaded areas highlight protiated (*black*) and deuterated (*blue*) pairs of **1** and **2**.

The key finding of this analysis also follows the opposing trends in $\Delta\delta/\Delta T$ between **1** and **2**: q_{Raman} *increases* from 10.4 to 16.6 at 25 °C for **1** to d_{12}-**1** and *decreases* from 559.4 to 463.3 at 25 °C for **2** to d_6-**2**. The values of q_{Raman} follows the changes in $\Delta\delta/\Delta T$ upon deuteration. For both IR and Raman-active modes, deuteration was expected to lower vibrational energies, yet based on the $\Delta\delta/\Delta Q$ values, we propose that

changes in the energies of Raman-active vibrations, thus changing to the populations of these states, will significantly contribute to $\Delta\delta/\Delta T$. For **1**, deuteration lowered the energies of the Raman vibrations to foster higher $\Delta\delta/\Delta T$ via higher q_{Raman}. For **2**, deuteration also lowered the Raman vibration frequencies, but q_{Raman} decreased. In **2**, the IR vibrations also dropped in energy such that they consequently leach population from Raman to IR vibrational states, thus reason for producing a lower $\Delta\delta/\Delta T$ upon deuteration.

The foregoing data inform potential synthetic design strategies aimed at complexes with higher ^{59}Co thermometric sensitivities. (*i*) Higher numbers of vibrations at low energy are advantageous, meaning that potentially higher-coordination numbers, or more complex coordination geometries than the O_h, six-coordinate molecules here may produce higher $\Delta\delta/\Delta T$. (*ii*) Larger mass for donor atoms can be used for potentially enhancing $\Delta\delta/\Delta T$, though this effect appears to be ligand-specific. (*iii*) Raman vibrations appear to be the most important for $\Delta\delta/\Delta T$, and thus low-symmetry coordination shells are desirable, as these should feature more Raman-active vibrations. Tests of these ideas will be reported in due course.

5.5. Conclusion

The foregoing data establish a rationale for how ligand identity enhances ^{59}Co $\Delta\delta/\Delta T$, namely, by increasing the number and populations of Raman-active vibrations that include the first coordination shell of the Co^{3+} ion, as these modes produce the largest-amplitude changes in $\delta(^{59}\text{Co})$. As a result of this discovery, we generate a new figure of merit to target in molecular design of high $\Delta\delta/\Delta T$: q_{Raman}. This parameter describes not only existing trends in $\Delta\delta/\Delta T$ identified in a family of Co^{3+} complexes, but also describes the observed opposing impacts of deuteration, where $\Delta\delta/\Delta T$ increases with deuteration for **1** but decreases for **2**. We note q_{Raman} can be computed independent of molecular isolation. Thus, the pursuit of highly temperature sensitive ^{59}Co-based spin probes is no longer limited to strict synthetic exploration but can potentially proceed in silico. More broadly, the approach here may be useful in estimating or predicting the temperature response of other metal-complex physical properties that involve vibrations, such as reactivity,[40] or magnetic relaxation.[41,42]

References

(1) Liu, Y.-Y.; Chang, B.-M.; Chang, H.-C. Nanodiamond-Enabled Biomedical Imaging. *Nanomedicine* **2020**, *15* (16), 1599–1616.

(2) Yu, C.-J.; von Kugelgen, S.; Laorenza, D. W.; Freedman, D. E. A Molecular Approach to Quantum Sensing. *ACS Cent. Sci.* **2021**, *7* (5), 712–723.

(3) Bogachev, Y. V.; Nikitina, A. V.; Frolov, V. V.; Chizhik, V. I. MRI-Guided Therapy. *Tech. Phys.* **2020**, *65* (9), 1427–1435.

(4) Kokuryo, D.; Kumamoto, E.; Kuroda, K. Recent Technological Advancements in Thermometry. *Adv. Drug Delivery Rev.* **2020**, *163–164*, 19–39.

(5) Winter, L.; Oberacker, E.; Paul, K.; Ji, Y.; Oezerdem, C.; Ghadjar, P.; Thieme, A.; Budach, V.; Wust, P.; Niendorf, T. Magnetic Resonance Thermometry: Methodology, Pitfalls and Practical Solutions. *Int. J. Hyperthermia* **2016**, *32* (1), 63–75.

(6) Rieke, V.; Pauly, K. B. MR Thermometry. *J. Magn. Reson. Imaging* **2008**, *27* (2), 376–390.

(7) Bramley, R.; Brorson, M.; Sargeson, A. M.; Schaeffer, C. E. Cobalt-59 NMR Chemical Shifts of Cobalt(III) Complexes; Correlations with Parameters Calculated from Ligand-Field Spectra. *J. Am. Chem. Soc.* **1985**, *107* (9), 2780–2787.

(8) Griffith, J. S.; Orgel, L. E. The Residual Paramagnetism and Nuclear Magnetic Resonance Spectra of Cobaltic Complexes. *Trans. Faraday Soc.* **1957**, *53*, 601.

(9) Proctor, W. G.; Yu, F. C. On the Nuclear Magnetic Moments of Several Stable Isotopes. *Phys. Rev.* **1951**, *81* (1), 20–30.

(10) Freeman, R.; Murray, G. R.; Richards, R. E. Cobalt Nuclear Resonance Spectra. *Proc. R. Soc. London. Ser. A* **1957**, *242* (1231), 455–466.

(11) Dharmatti, S. S.; Kanekar, C. R. Chemical Shifts in the Nuclear Magnetic Resonance of Co^{59} and the Ligand Field Theory. *J. Chem. Phys.* **1959**, *31* (5), 1436–1437.

(12) Levy, G. C.; Terry Bailey, J.; Wright, D. A. A Sensitive NMR Thermometer for Multinuclei FT NMR. *J. Magn. Reson.* **1980**, *37* (2), 353–356.

(13) Koplitz, L. V.; Kim, K.; McClure, D. S. Temperature Dependence of 10*Dq* for Aqueous Hexaaquomanganese(II). *Inorg. Chem.* **1994**, *33* (4), 702–704.

(14) Jameson, C. J.; Rehder, D.; Hoch, M. Isotope and Temperature Dependence of Transition-Metal Shielding in Complexes of the Type $M(XY)_6$. *J. Am. Chem. Soc.* **1987**, *109* (9), 2589–2594.

(15) Benedek, G. B.; Englman, R.; Armstrong, J. A. Temperature and Pressure Dependence of the Co^{59} Nuclear Resonance Chemical Shift. *J. Chem. Phys.* **1963**, *39* (12), 3349–3363.

(16) Kahn, O. *Molecular Magnetism*; Wiley-VCH, 2001.

(17) Ozvat, T. M.; Peña, M. E.; Zadrozny, J. M. Influence of Ligand Encapsulation on Cobalt-59 Chemical-Shift Thermometry. *Chem. Sci.* **2019**, *10* (27), 6727–6734.

(18) Ozvat, T. M.; Sterbinsky, G. E.; Campanella, A. J.; Rappé, A. K.; Zadrozny, J. M. EXAFS Investigations of Temperature-Dependent Structure in Cobalt-59 Molecular NMR Thermometers. *Dalton Trans.* **2020**, *49* (45), 16380–16385.

(19) Ozvat, T. M.; Johnson, S. H.; Rappé, A. K.; Zadrozny, J. M. Ligand Control of 59Co Nuclear Spin Relaxation Thermometry. *Magnetochemistry* **2020**, *6* (4), 58.

(20) Pham, C. T.; Barnard, I.; Nguyen, H. H.; Abram, U.; Koch, K. R. Cobalt(III) Metallacryptates and Their Guest Cation-Exchange in Solution Monitored by ^{59}Co NMR. *Inorg. Chem.* **2020**, *59* (2), 1183–1192.

(21) Davis, J. C.; Bühl, M.; Koch, K. R. Probing Isotope Shifts in ^{103}Rh and ^{195}Pt NMR Spectra with Density Functional Theory. *J. Phys. Chem. A* **2013**, *117* (33), 8054–8064.

(22) Asaro, F.; Liguori, L.; Pellizer, G. Exceptional Deshielding of ^{59}Co Caused by Deuteration of the Hydrogen Bonds in Cobaloximes. *Angew. Chem., Int. Ed.* **2000**, *39* (11), 1932–1934.

(23) Harris, R. K.; Morrow, R. J. Cobalt-59 Nuclear Magnetic Resonance Studies of the Kinetics and Mechanism of Deuteration for Tris(ethylenediamine)cobalt Chloride. *J. Chem. Soc., Faraday Trans. 1* **1984**, *80* (11), 3071–3094.

(24) Bendall, M. R.; Doddrell, D. M. Proton-Deuterium Isotope Shifts in ^{59}Co NMR. *Aust. J. Chem.* **1978**, *31* (5), 1141–1143.

(25) Krause, R.; Megargel, E. Student Synthesis of Tris(ethylenediamine)cobalt(III) Chloride. *J. Chem. Educ.* **1976**, *53* (10), 667.

(26) Bottomley, G.; Clark, I.; Creaser, I.; Engelhardt, L.; Geue, R.; Hagen, K.; Harrowfield, J.; Lawrance, G.; Lay, P.; Sargeson, A.; See, A.; Skelton, B.; White, A.; Wilner, F. The Synthesis and Structure of Encapsulating Ligands: Properties of Bicyclic Hexamines. *Aust. J. Chem.* **1994**, *47* (1), 143–179.

(27) Frisch, M. J.; Trucks, G. W.; Schlegel, H. B.; Scuseria, G. E.; Robb, M. A.; Cheeseman, J. R.; Scalmani, G.; Barone, V.; Petersson, G. A.; Nakatsuji, H.; Li, X.; Caricato, M.; Marenich, A. V.; Bloino, J.; Janesko, B. G.; Gomperts, R.; Mennucci, B.; Hratchian, H. P.; Ortiz, J. V.; Izmaylov, A. F.; Sonnenberg, J. L.; Williams; Ding, F.; Lipparini, F.; Egidi, F.; Goings, J.; Peng, B.; Petrone, A.; Henderson, T.; Ranasinghe, D.; Zakrzewski, V. G.; Gao, J.; Rega, N.; Zheng, G.; Liang, W.; Hada, M.; Ehara, M.; Toyota, K.; Fukuda, R.; Hasegawa, J.; Ishida, M.; Nakajima, T.; Honda, Y.; Kitao, O.; Nakai, H.; Vreven, T.; Throssell, K.; Montgomery Jr., J. A.; Peralta, J. E.; Ogliaro, F.; Bearpark, M. J.; Heyd, J. J.; Brothers, E. N.; Kudin, K. N.; Staroverov, V. N.; Keith, T. A.; Kobayashi, R.; Normand, J.; Raghavachari, K.; Rendell, A. P.; Burant, J. C.; Iyengar, S. S.; Tomasi, J.; Cossi, M.; Millam, J. M.; Klene, M.; Adamo, C.; Cammi, R.; Ochterski, J. W.; Martin, R. L.; Morokuma, K.; Farkas, O.; Foresman, J. B.; Fox, D. J. *Gaussian 16 Rev. C.01*; Wallingford, CT, 2016.

(28) Neese, F. A Spectroscopy Oriented Configuration Interaction Procedure. *J. Chem. Phys.* **2003**, *119* (18), 9428–9443.

(29) Grimme, S.; Antony, J.; Ehrlich, S.; Krieg, H. A Consistent and Accurate Ab Initio Parametrization of Density Functional Dispersion Correction (DFT-D) for the 94 Elements H–Pu. *J. Chem. Phys.* **2010**, *132* (15), 154104.

(30) Krishnan, R.; Binkley, J. S.; Seeger, R.; Pople, J. A. Self-Consistent Molecular Orbital Methods. XX. A Basis Set for Correlated Wave Functions. *J. Chem. Phys.* **1980**, *72* (1), 650–654.

(31) Ditchfield, R. Self-Consistent Perturbation Theory of Diamagnetism. *Mol. Phys.* **1974**, *27* (4), 789–807.

(32) Weigend, F.; Ahlrichs, R. Balanced Basis Sets of Split Valence, Triple Zeta Valence and Quadruple Zeta Valence Quality for H to Rn: Design and Assessment of Accuracy. *Phys. Chem. Chem. Phys.* **2005**, *7* (18), 3297.

(33) Geue, R. J.; Hambley, T. W.; Harrowfield, J. M.; Sargeson, A. M.; Snow, M. R. Metal Ion Encapsulation: Cobalt Cages Derived from Polyamines, Formaldehyde, and Nitromethane. *J. Am. Chem. Soc.* **1984**, *106* (19), 5478–5488.

(34) Kirby, C. W.; Puranda, C. M.; Power, W. P. Cobalt-59 Nuclear Magnetic Relaxation Studies of Aqueous Octahedral Cobalt(III) Complexes. *J. Phys. Chem.* **1996**, *100* (35), 14618–14624.

(35) Chen, Y.; Christensen, D. H.; Sørensen, G. O.; Nielsen, O. F.; Pedersen, E. The Skeletal Vibrational Spectra and Metal–Ligand Force Constants of Cobalt(III) Ammine Complexes. *J. Mol. Struct.* **1993**, *299*, 61–72.

(36) Stein, P.; Miskowski, V.; Woodruff, W. H.; Griffin, J. P.; Werner, K. G.; Gaber, B. P.; Spiro, T. G. Raman Antiresonance: De-enhancement of Raman Intensity by Forbidden Electronic Transitions. *J. Chem. Phys.* **1976**, *64* (5), 2159–2167.

(37) Saito, Y.; Takemoto, J.; Hutchinson, B.; Nakamoto, K. Infrared Studies of Coordination Compounds Containing Low-Oxidation-State Metals. I. Tris(2,2'-Bipyridine) and Tris(1,10-Phenanthroline) Complexes. *Inorg. Chem.* **1972**, *11* (9), 2003–2011.

(38) Flint, C. D.; Matthews, A. P. Totally Symmetric Metal-Nitrogen Stretching Vibrations of Ethylenediamine Chelate Complexes. *Inorg. Chem.* **1975**, *14* (5), 1219–1220.

(39) Jameson, C. J. Vibrational Analysis and Mean Bond Displacements in $M(XY)_6$ Complexes. *J. Am. Chem. Soc.* **1987**, *109* (9), 2586–2588.

(40) Guo, H.; Liu, K. Control of Chemical Reactivity by Transition-State and Beyond. *Chem. Sci.* **2016**, *7* (7), 3992–4003.

(41) Mirzoyan, R.; Kazmierczak, N. P.; Hadt, R. G. Deconvolving Contributions to Decoherence in Molecular Electron Spin Qubits: A Dynamic Ligand Field Approach. *Chem. – Eur. J.* **2021**, *27* (37), 9482–9494.

(42) Kazmierczak, N. P.; Mirzoyan, R.; Hadt, R. G. The Impact of Ligand Field Symmetry on Molecular Qubit Coherence. *J. Am. Chem. Soc.* **2021**, *143* (42), 17305–17315.

CHAPTER 6 – Summary

6.1. Molecular Structure and ^{59}Co-NMR Thermometry Design

This dissertation outlines a variety of stand-alone studies that begin bridging the knowledge gap on designing NMR thermometers which are meant to address the fundamental question: *What molecular features affect the temperature-dependent nuclear magnetic properties of ^{59}Co?* The results discussed in each chapter reveal four key points about the synthetic control of temperature dependence in cobalt complexes: *(i)* ligand encapsulation enhances $\Delta\delta/\Delta T$, *(ii)* temperature-dependent structure drives $\Delta\delta/\Delta T$ through symmetric distortions over Co–N_6 bond extension, *(iii)* temperature-dependent spin relaxation is highly dependent on molecular structure symmetry, *(iv)* changes in ligand-mass enables finite control of $\Delta\delta/\Delta T$ and is highly structure-dependent. Overall, these points composite the first toolbox of synthetic strategies that guide the discovery of highly temperature-sensitive nuclear spin-based probes in ^{59}Co-contatining complexes.

The initial studies detail the first demonstration of relating $\delta(^{59}\text{Co})$ to molecular structure in a series of progressively encapsulated and structurally similar Co–N_6 complexes. For these complexes it is established that encapsulation of the metal-ion via higher denticity ligands enhances $\Delta\delta/\Delta T$. This feature informs on the synthetic design and usage of ligand rigidity v. flexibility as a method to enhance $\Delta\delta/\Delta T$, where ligand dynamics are restricted. In this instance, synthetic control is enabled by designing these restrictions via interconnected ligands through chelation structures or by exploring π-bonded olefinic structure over purely π-bonded alkyl ligands. As the utility of these systems is motivated by enabling magnetic resonance thermometry imaging, the enhancement of $\Delta\delta/\Delta T$ via encapsulation lends itself well to the need for strongly chelating ligand scaffolds for metal-containing medicines. As such, continuing the evolution of this molecular structure feature in other cobalt complexes is warranted.

For these same series of progressively encapsulated complexes, a detailed investigation of the temperature-responsive molecular structure has also been established via EXAFS spectroscopy. This technique has allowed the precise evaluation of temperature-driven bond distance changes to the Co–N_6 primary coordination sphere and is the first demonstration of this technique to understand $\Delta\delta/\Delta T$. Importantly, changes in the bond lengths of the Co–N_6 primary coordination sphere do not account for

$\Delta\delta/\Delta T$, but more significantly due to changes in the distortion of the coordination geometry of the octahedrally coordinated complexes. A unique feature of this study includes the use of the experimentally guided solution-phase EXAFS data to guide computational prediction of molecular structure at various temperatures. The implication of this work shows that ligand design involves the use of distortion to favorably control temperature-driven coordination geometry of the metal-ion as a route towards designing $\Delta\delta/\Delta T$. Additionally, it is surmised that larger responses in $\Delta\delta/\Delta T$ are likely achieved through "strained" ligand systems in which the interplay of electronic structure and molecular structure force the complex into pseudo-octahedral or slightly trigonal prismatic geometries (i.e., sarcophagine structure). It is through the study of these systems that inspires the investigation of a variety of other dynamic coordination complexes.

Aside from the impact of temperature on chemical shift are the temperature-driven relaxation dynamics in the series of progressively encapsulating $Co–N_6$ complexes. A correlation in molecular structure and relaxation thermometry reaffirms the exceptional role of ligand encapsulation on the ^{59}Co nucleus where greater degrees of chelation produced faster T_1 and T_2 values. The case of molecular symmetry is established as a design strategy by ascertaining the relationship between O_h or D_{3h} symmetries to relaxation times of ^{59}Co. This dependence is ultimately a consequence of the quadrupolar nucleus showing exceptional detection of the local coordination environment as directed by its ligand design. It is the quadrupolar nucleus that also reveals the impacts of temperature in these complexes where $\Delta T_1/\Delta T$ reflected the thermal dependence of the quadrupolar coupling as opposed to the absolute value of the coupling. Through the control of the ligand, it is possible to utilize the quadrupolar coupling as a tunable interaction with a dynamic molecular structure. Regarding the physical potential for ^{59}Co-based biomedical diagnosis, these studies establish the first evaluations of ligand encapsulations on the necessary T_1 and T_2 for modern imaging technique.

Lastly, and perhaps most importantly, quantitatively controlled chemical shift thermometry may be explored via mass-dependent ligand design. Up to this point, previous evaluations of thermometry show qualitative relationships between structure and $\Delta\delta/\Delta T$, yet it has been shown that finite and step-wise control of temperature sensitivity is possible. Decisively, the use of H/D exchange via mixtures of H_2O and D_2O

allows the control of identifiable molecular analogues of Co–N_6 complexes via ^{59}Co NMR. For a single molecular structure, an ensemble of unique structures may be generated depending on the available number of exchangeable H atoms. Not only has each structure been shown to exhibit a characteristic value of $\Delta\delta/\Delta T$ relative to the mass of the molecule, but the sign of the change in $\Delta\delta/\Delta T$ has been informed on via molecular structure response. Unique to the molecule structure, the finite impact on $\Delta\delta/\Delta T$ was elucidated via vibrational means which ultimately lead to the first illustration of the dependence of $\Delta\delta/\Delta T$ on vibrational structure. The design strategies enabled by these studies suggest the use of isotopomer-specific structures to elucidate mechanisms of temperature sensitivity via vibrational consequence. These strategies include the utilization of ligand structures that possess a large abundance of low-energy vibrational modes through heavier donor atoms. Specifically, molecular Raman vibrations are crucial to the change in molecular structure which are ultimately used to tie thermally dependent vibrational modes to changes in ΔE in Ramsey's equations. These studied broadly establish a pathway for understanding thermometry in other NMR-active metal-ion systems.

APPENDIX 1: Supporting Information for Chapter 2

Appendix Table 1.1. Experimental values of *B* and Δ_o for compounds **1**–**5** over a temperature range of 25–60 °C. Values were calculated by a d^6 Tanabe-Sugano diagram using the maximum absorption energies collected from UV-vis spectroscopy measurements.

	1		**2**		**3**		**4**		**5**	
T (°C)	B (cm^{-1})	Δ_o (10^3 cm^{-1})	B (cm^{-1})	Δ_o (10^3 cm^{-1})	B (cm^{-1})	Δ_o (10^3 cm^{-1})	B (cm^{-1})	Δ_o (10^3 cm^{-1})	B (cm^{-1})	Δ_o (10^3 cm^{-1})
25	631.09	22.86	596.45	23.11	593.23	22.27	609.96	23.12	578.02	22.65
30	631.92	22.86	596.38	23.10	592.37	22.27	610.26	23.11	576.37	22.63
35	631.67	22.85	598.20	23.09	594.96	22.26	607.19	23.10	579.92	22.61
40	632.97	22.83	597.57	23.09	595.42	22.26	612.07	23.11	582.28	22.61
45	633.83	22.82	596.99	23.08	596.79	22.25	608.56	23.11	580.44	22.60
50	634.15	22.82	598.97	23.08	599.16	22.23	610.32	23.09	583.21	22.59
55	635.47	22.80	602.01	23.07	596.97	22.24	612.90	23.09	585.29	22.59
60	635.71	22.80	598.71	23.07	598.40	22.24	613.99	23.09	584.78	22.58

Appendix Table 1.2. Variable-temperature ^{59}Co chemical shifts and UV-vis peak positions. [a]

	1			**2**			**3**		
T (°C)	**^{59}Co δ(ppm)**	**ν_1 (10^3 cm^{-1})**	**ν_2 (10^3 cm^{-1})**	**^{59}Co δ(ppm)**	**ν_1 (10^3 cm^{-1})**	**ν_2 (10^3 cm^{-1})**	**^{59}Co δ(ppm)**	**ν_1 (10^3 cm^{-1})**	**ν_2 (10^3 cm^{-1})**
10	8222	-	-	7125	-	-	8318	-	-
15	8157	-	-	7131	-	-	8328	-	-
20	8164	-	-	7138	-	-	8334	-	-
25	8171	20.97	29.13	7145	21.40	29.29	8340	20.47	28.24
30	8178	20.94	29.11	7151	21.39	29.33	8346	20.45	28.25
35	8185	20.93	29.08	7158	21.35	29.28	8352	20.44	28.24
40	8192	20.92	29.08	7165	21.36	29.31	8358	20.41	28.25
45	8200	20.91	29.07	7173	21.35	29.32	8365	20.40	28.27
50	8207	20.92	29.06	7179	21.34	29.28	8372	20.38	28.24
55	8215	20.89	29.05	7187	21.33	29.29	8379	20.35	28.21
60	8222	20.87	29.03	7194	21.35	29.29	8386	20.34	28.22

	4			**5**		
T (°C)	**^{59}Co δ(ppm)**	**ν_1 (10^3 cm^{-1})**	**ν_2 (10^3 cm^{-1})**	**^{59}Co δ(ppm)**	**ν_1 (10^3 cm^{-1})**	**ν_2 (10^3 cm^{-1})**
10	7384	-	-	6864	-	-
15	7393	-	-	6872	-	-
20	7401	-	-	6883	-	-
25	7409	21.29	29.24	6894	20.93	28.83
30	7418	21.30	29.26	6904	20.91	28.78
35	7427	21.27	29.22	6914	20.92	28.76
40	7435	21.26	29.21	6924	20.89	28.74
45	7443	21.23	29.22	6934	20.89	28.73
50	7452	21.20	29.21	6944	20.85	28.74
55	7461	21.17	29.19	6953	20.83	28.70
60	7470	21.16	29.21	6963	20.81	28.67

[a] ν_1 and ν_2 represent the lowest and second-lowest observed transitions in the UV-Vis spectrum, respectively

Appendix Table 1.3. Data for comparison of temperature sensitivity of the chemical shift versus ^{59}Co chemical shift. [a]

Compound	$\Delta\delta/\Delta T$ (ppm/°C)	^{59}Co δ (ppm)	$\lambda_{max(1)}$ (nm)	$\lambda_{max(2)}$ (nm)	ν_1 (10^3 cm^{-1})	ν_2 (10^3 cm^{-1})
$K_3[Co(CN)_6]$	1.44(1)	0	312	-	32.05	-
1	1.44(2)	8171	477	343	20.97	29.13
2	1.38(1)	7145	467	341	21.40	29.29
3	1.30(2)	8340	489	354	20.47	28.24
4	1.71(1)	7409	470	342	21.29	29.24
5	2.04(2)	6894	478	347	20.93	28.83

[a]Spectral data and ^{59}Co chemical shifts are reported for 25 °C

Appendix Table 1.4. Summary of Raman linewidth data (υ, peak position, and Γ, linewidth, both in cm^{-1}, τ, lifetime = 1/πΓ, in picosecond units, *g* unitless) from deconvolution.

Compound **1**				Compound **2**				Compound **3**				Compound **4**				Compound **5**			
ν	Γ	τ	g	ν	Γ	τ	g	ν	Γ	τ	g	ν	Γ	τ	g	ν	Γ	τ	g
105	33	0.32	0.00	119	20	0.53	0.76	124	25	0.43	0.00	124	41	0.26	1.00	104	12	0.87	0.89
278	52	0.21	0.00	136	33	0.32	1.00	221	31	0.35	1.00	208	8	1.35	0.58	139	10	1.11	0.17
306	42	0.25	1.00	189	22	0.47	1.00	259	70	0.15	0.86	219	53	0.20	0.85	148	11	1.01	0.53
331	45	0.23	1.00	205	20	0.54	0.70	265	21	0.51	0.97	284	56	0.19	0.66	178	15	0.70	0.72
444	25	0.42	0.75	278	26	0.40	0.88	282	20	0.53	0.89	319	22	0.49	1.00	198	21	0.50	0.54
461	15	0.70	1.00	307	26	0.40	1.00	303	10	1.04	1.00	392	10	1.08	0.76	212	9	1.18	1.00
484	17	0.64	0.38	336	21	0.50	0.48	314	49	0.22	1.00	402	10	1.02	0.00	265	10	1.04	0.88
501	16	0.66	0.71	369	9	1.12	0.64	341	18	0.60	1.00	429	9	1.13	1.00	276	7	1.58	0.00
				440	13	0.80	0.83	361	34	0.31	0.75	469	20	0.54	0.83	295	7	1.57	0.00
				500	13	0.82	1.00	435	46	0.23	1.00	488	19	0.55	0.90	300	6	1.92	0.00
				524	9	1.18	0.27	450	20	0.53	1.00	510	15	0.70	0.75	333	7	1.53	0.80
				580	10	1.09	1.00	462	53	0.20	1.00	601	7	1.63	0.00	345	8	1.30	0.34
								493	22	0.49	1.00					360	6	1.67	0.00
								533	27	0.40	0.56					380	5	2.12	0.01
								620	31	0.34	0.89					390	7	1.45	0.75
																416	9	1.16	0.97
																458	11	0.96	0.09
																483	7	1.44	0.00
																503	6	1.75	0.00
																536	11	0.96	0.11
																622	22	0.49	0.82

Appendix Table 1.5. Data for comparison of temperature sensitivity of ^{59}Co δ for $[Co(en)_3]Cl_3$ in various solvents.

	^{59}Co δ (ppm) of **2**				
T (°C)	H_2O	DMSO	d_6-DMSO	DMF	HMPA
20	7138	7014	-	6996	-
25	7145	7020	7019	-	-
30	7151	7026	7026	7007	6962
35	7158	7032	7032	-	-
40	7165	7039	7038	7019	6974
45	7173	7045	7045	-	-
50	7179	7051	7051	7031	6986
55	7187	7058	7057	-	-
60	7194	7065	7064	7044	6999

Solvent	Δδ/ΔT (ppm/°C)	π*[a]	AN[a]	DN[a]	β[a]
H_2O	1.38(1)	1.09	54.8	18	0.18
DMSO	1.27(1)	1.00	19.3	29.8	0.76
DMF	1.19(2)	0.88	16	26.6	0.69
HMPA	1.23(1)	0.87	10.6	38.8	1.05

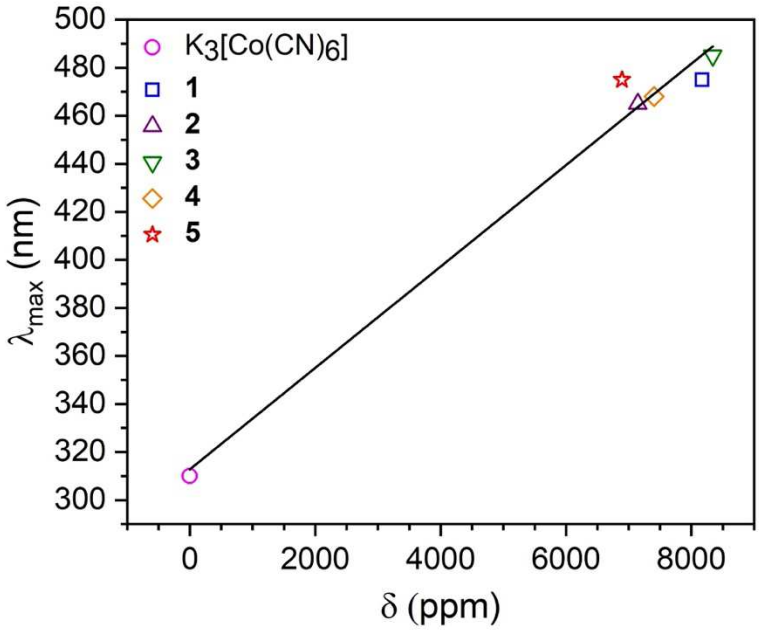

Appendix Figure 1.1. Correlation between maximum wavelength of absorption (λ_{max}) and chemical shift (δ) for $K_3[Co(CN)_6]$ and compounds **1**–**5**. UV-vis data were collected in water at a concentration of 10 mM for each sample. NMR data were collected in water at a concentration of 100 mM.

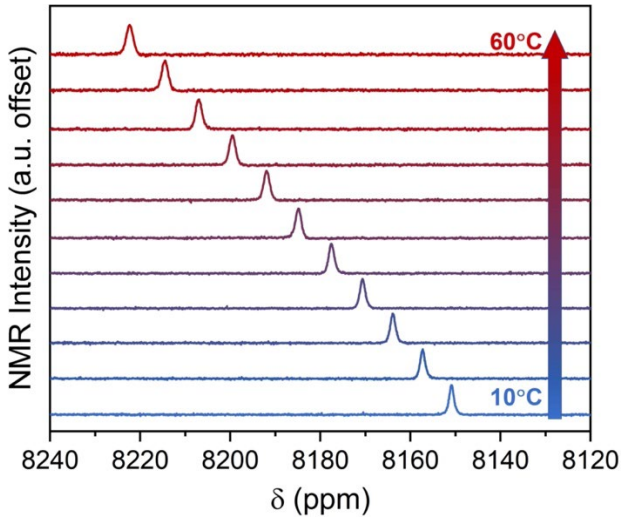

Appendix Figure 1.2. Chemical shift data of compound **1** from 10–60 °C. NMR measurements were taken in a solution of H_2O at a concentration of 100 mM.

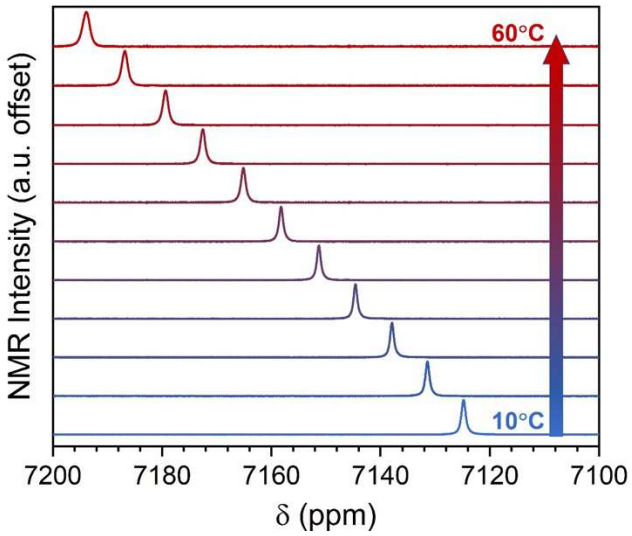

Appendix Figure 1.3. Chemical shift data of compound **2** from 10–60 °C. NMR measurements were taken in a solution of H_2O at a concentration of 100 mM.

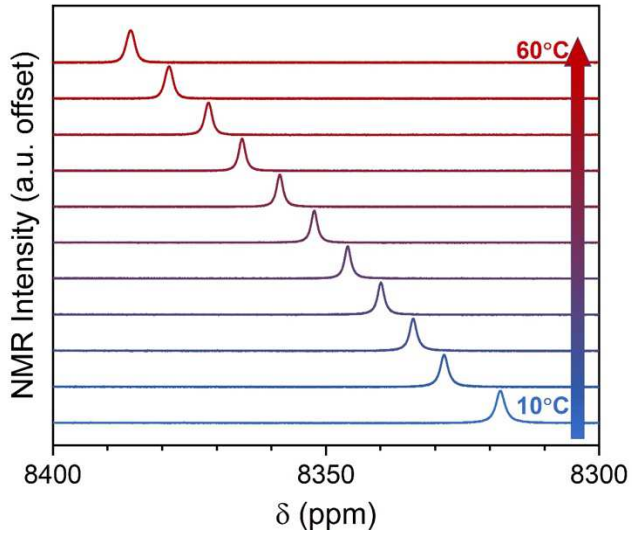

Appendix Figure 1.4. Chemical shift data of compound **3** from 10–60 °C. NMR measurements were taken in a solution of H_2O at a concentration of 100 mM.

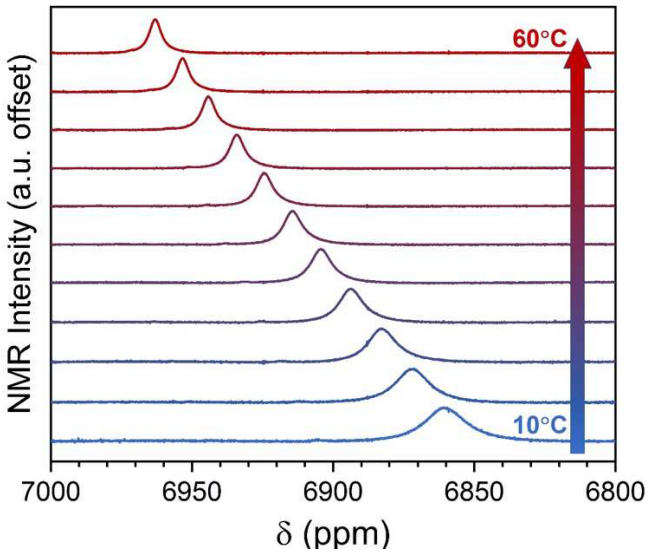

Appendix Figure 1.5. Chemical shift data of compound **5** from 10–60 °C. NMR measurements were taken in a solution of H_2O at a concentration of 33.3 mM.

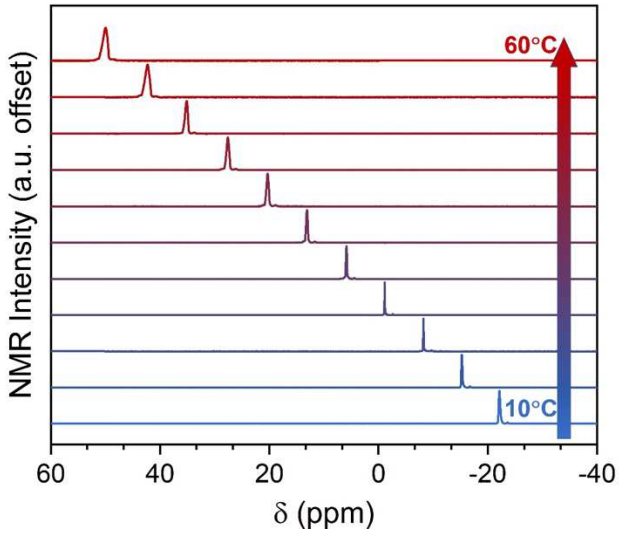

Appendix Figure 1.6. Chemical shift data of $K_3[Co(CN)_6]$ from 10–60 °C. NMR measurements were taken in a solution of H_2O at a concentration of 100 mM.

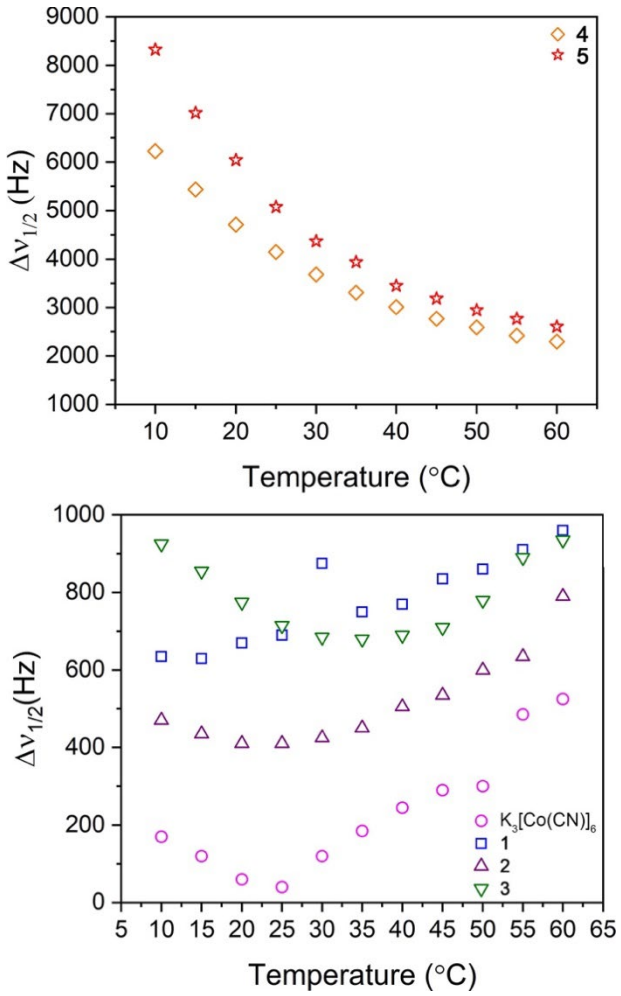

Appendix Figure 1.7. Temperature dependence of the ^{59}Co NMR linewidths for $K_3[Co(CN)_6]$ and **1**–**3** (*top*) and **4**–**5** (*bottom*). Data were extracted from the full-width half maxima of the located peaks in the spectra.

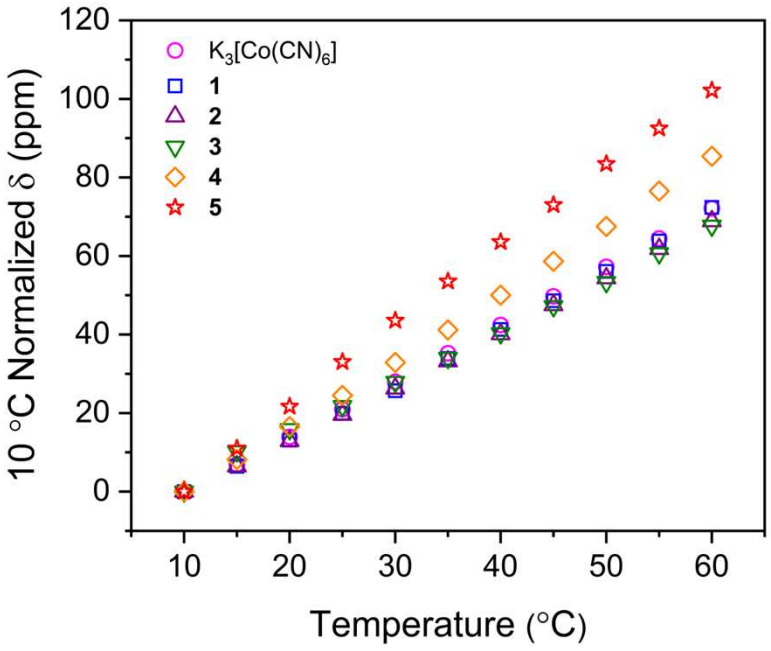

Appendix Figure 1.8. Variable-temperature chemical shift data from 10–60 °C, normalized to 10 °C. NMR measurements were taken in a solution of H_2O at concentrations of 100 mM.

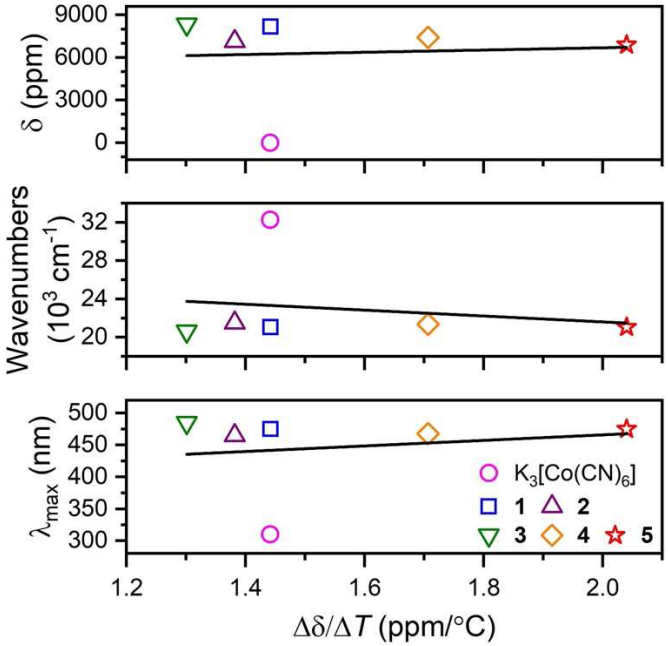

Appendix Figure 1.9. Plots of chemical shift (δ, *top*) and UV-vis data (in cm^{-1}, *middle*, and λ_{max}, *bottom*) as a function of $\Delta\delta/\Delta T$. UV-vis data were collected in H_2O at a concentration of 10 mM for each sample. NMR data were collected in water at a concentration of 100 mM.

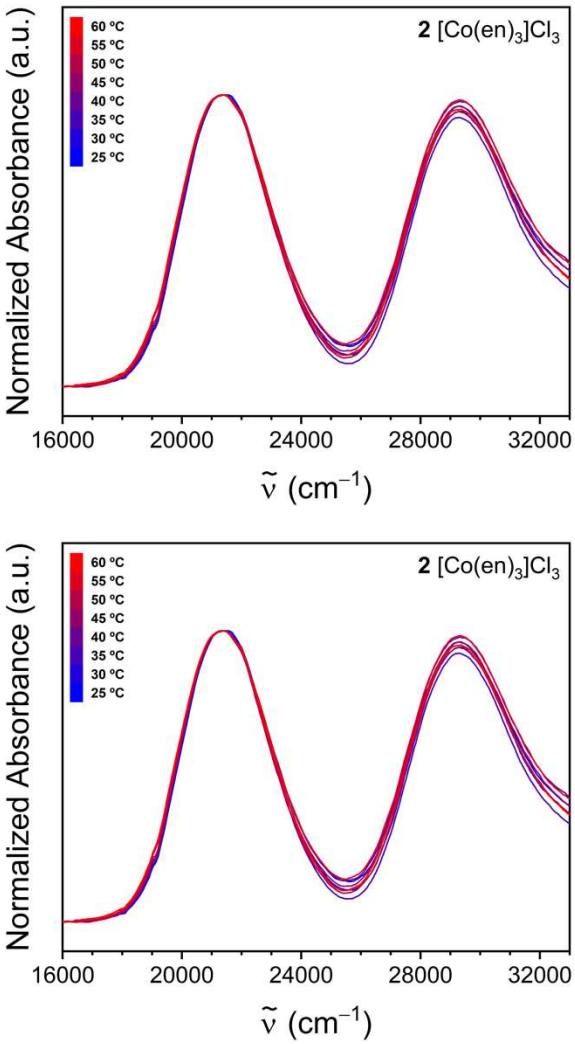

Appendix Figure 1.10. Variable-temperature UV-vis data for **1** (*top*) and **2** (*bottom*) in H_2O. Spectra were collected at concentrations of 9.5 mM (**1**) and 6.7 mM (**2**). Intensities were normalized for ease of view.

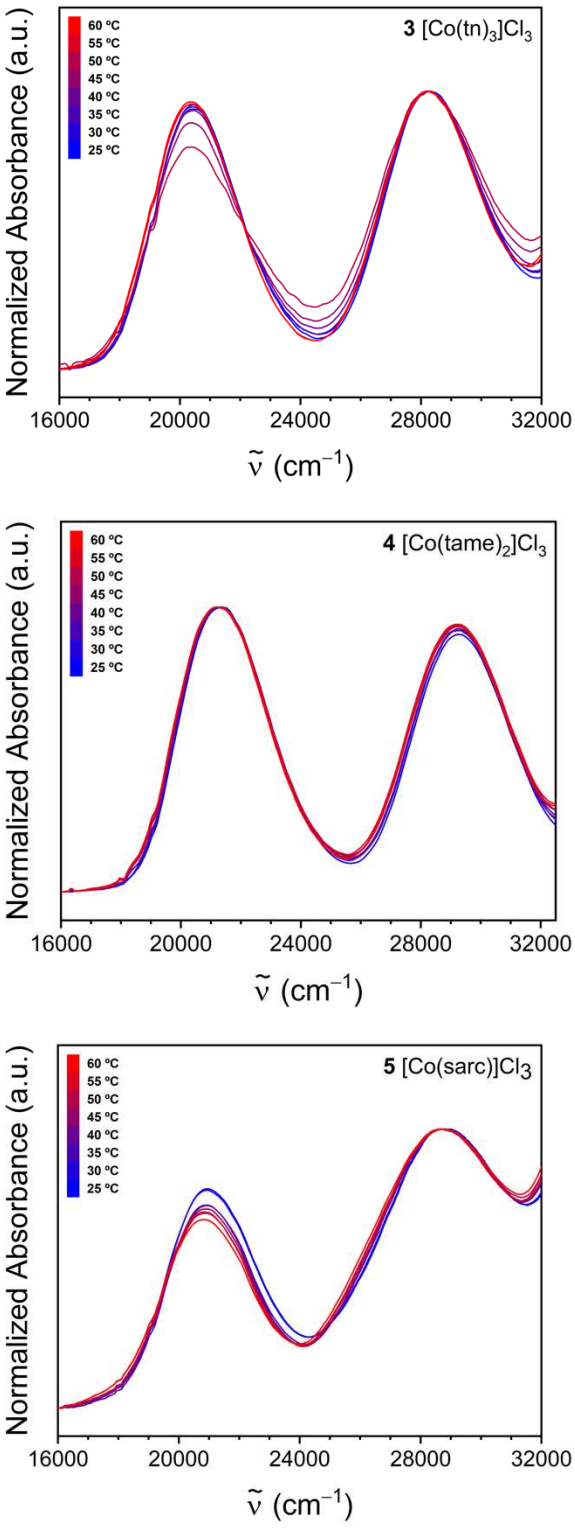

Appendix Figure 1.11. Variable-temperature UV-vis data for **3** (*top*), **4** (*middle*), and **5** (*bottom*) in H_2O. Spectra were collected at concentrations of 5.9 mM (**3**), 6.5 mM (**4**), and 4.5 mM (**5**). Intensities were normalized for ease of view.

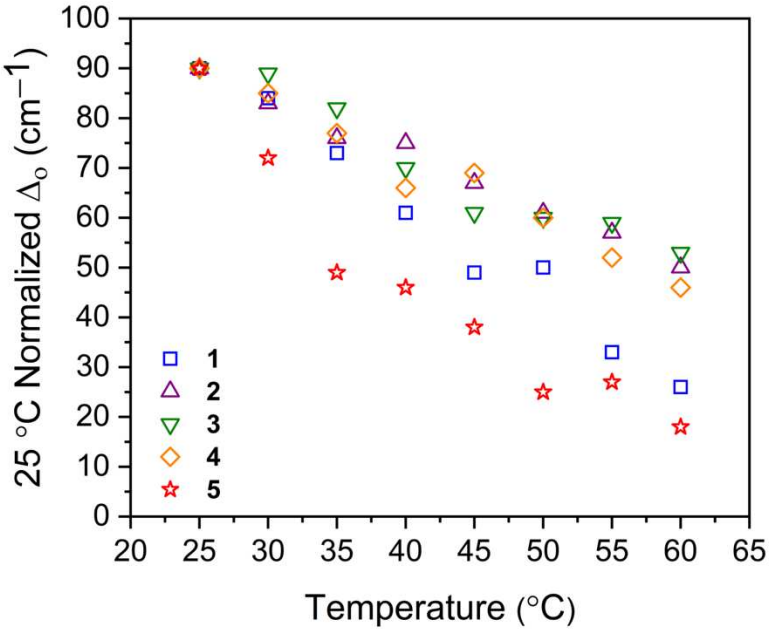

Appendix Figure 1.12. Variable-temperature Δ_o normalized to 25 °C.

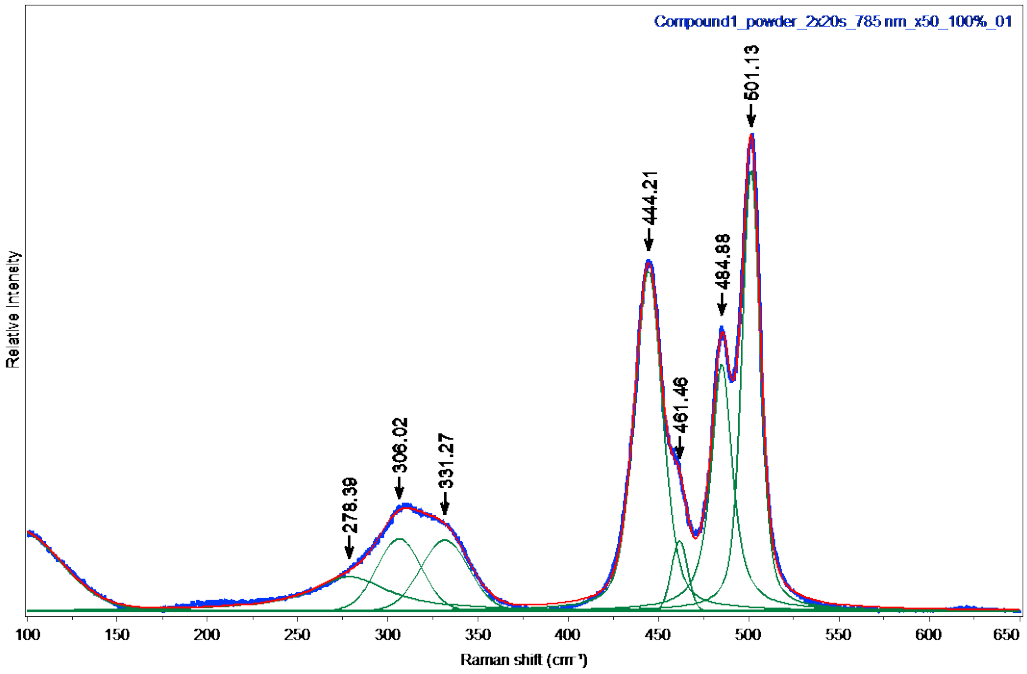

Appendix Figure 1.13. Raman spectrum for a pure powder of **1** at room temperature. The data are presented in blue, the deconvoluted peaks are in green and the sum of the determined peaks is red, which overlays the experimental data.

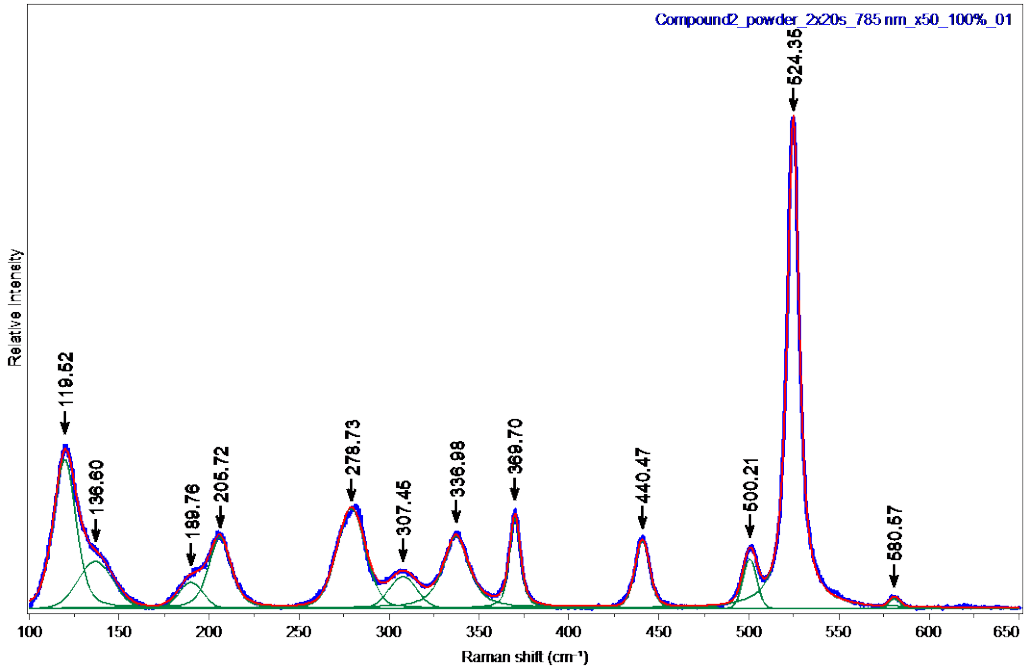

Appendix Figure 1.14. Raman spectrum for a pure powder of **2** at room temperature. The data are presented in blue, the deconvoluted peaks are in green and the sum of the determined peaks is red, which overlays the experimental data.

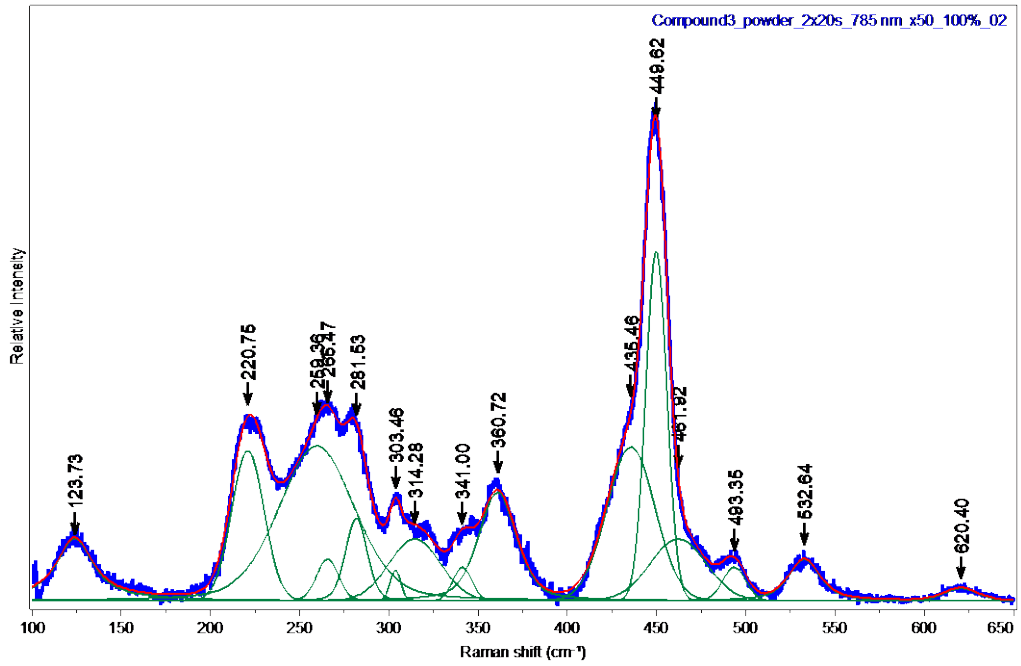

Appendix Figure 1.15. Raman spectrum for a pure powder of **3** at room temperature. The data are presented in blue, the deconvoluted peaks are in green and the sum of the determined peaks is red, which overlays the experimental data.

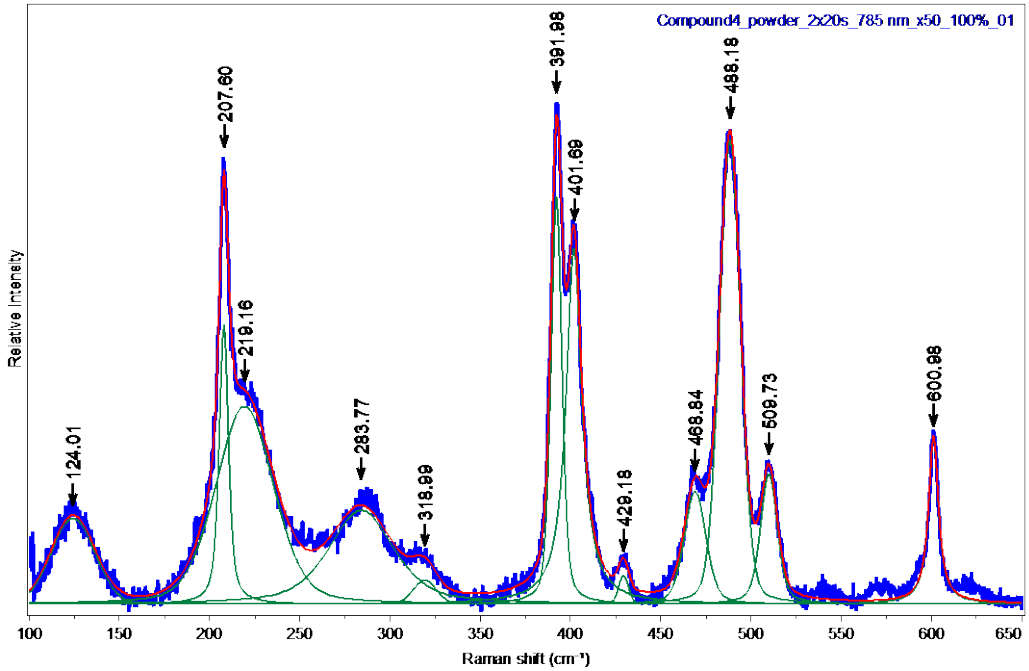

Appendix Figure 1.16. Raman spectrum for a pure powder of **4** at room temperature. The data are presented in blue, the deconvoluted peaks are in green and the sum of the determined peaks is red, which overlays the experimental data.

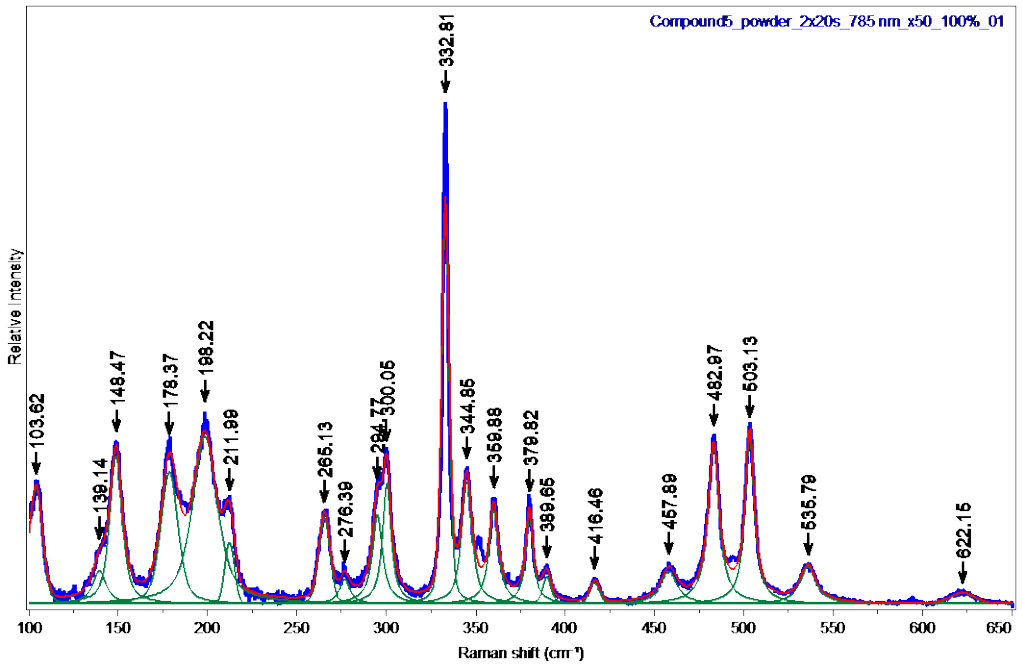

Appendix Figure 1.17. Raman spectrum for a pure powder of **5** at room temperature. The data are presented in blue, the deconvoluted peaks are in green and the sum of the determined peaks is red, which overlays the experimental data.

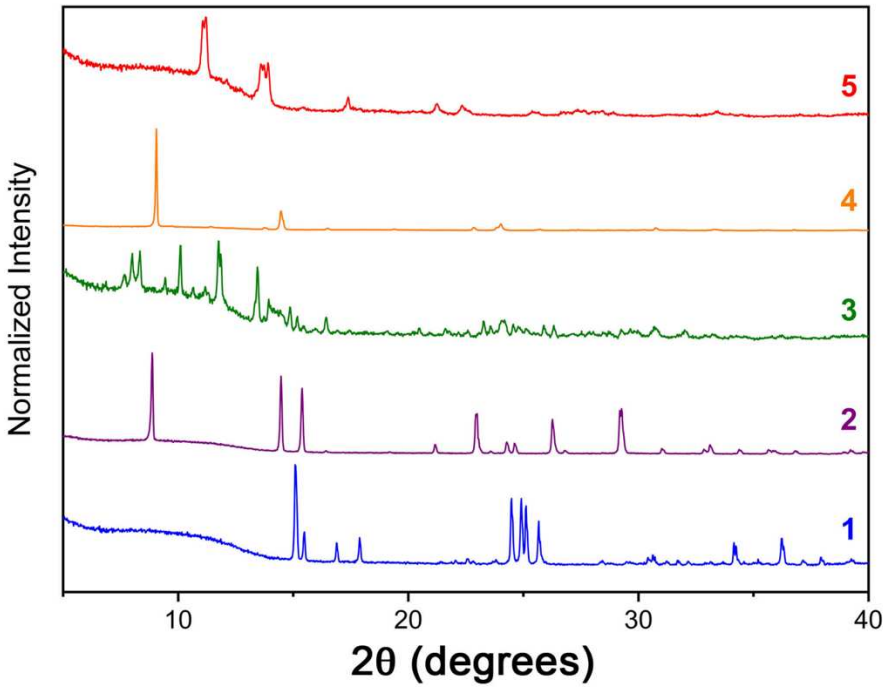

Appendix Figure 1.18. X-ray powder diffraction data for **1**–**5**. Diffraction patterns were normalized to be the highest intensity peak and offset prior to depiction. The low-angle humps are from the Vaseline used to restrict sample motion in the instrument.

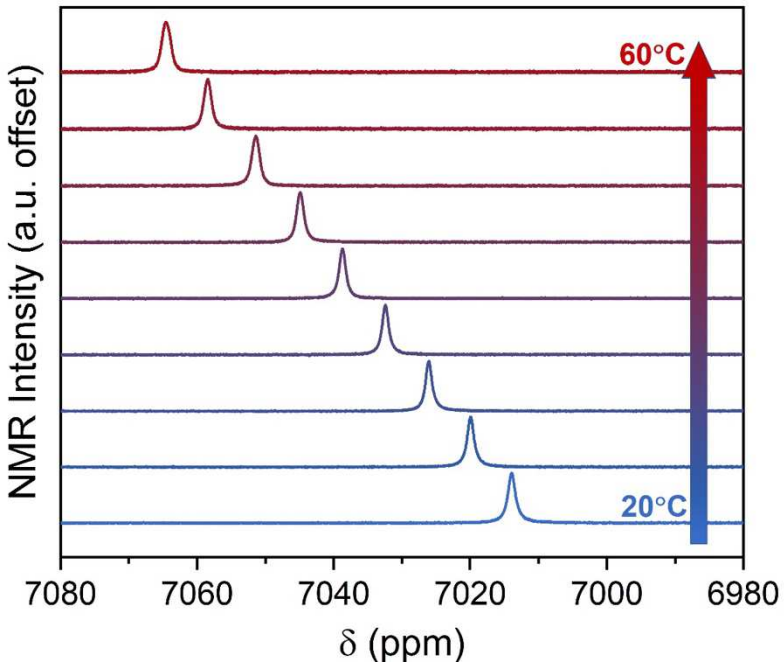

Appendix Figure 1.19. Chemical shift data of compound **2** from 20–60 °C. NMR measurements were taken in a solution of DMSO at a concentration of ~20 mM.

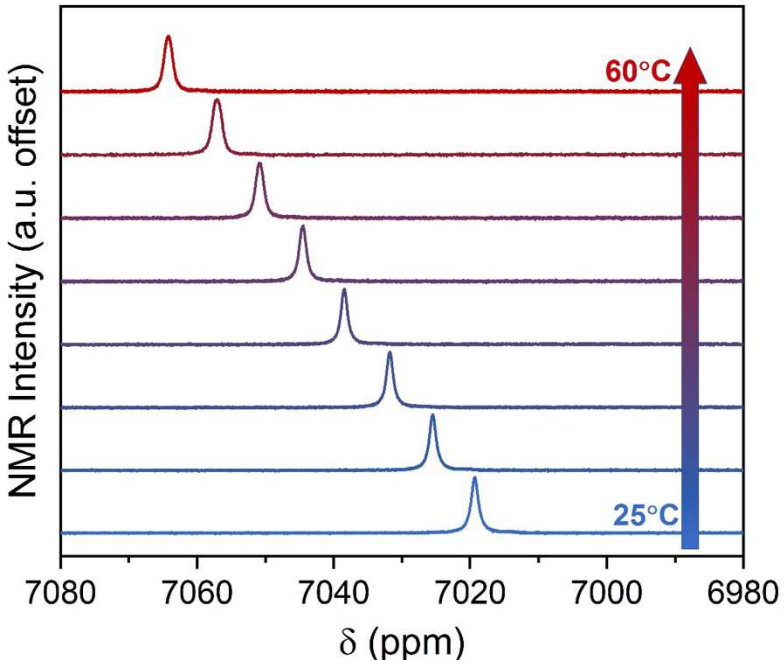

Appendix Figure 1.20. Chemical shift data of compound **2** from 25–60 °C. NMR measurements were taken in a solution of d_6-DMSO at a concentration of ~20 mM.

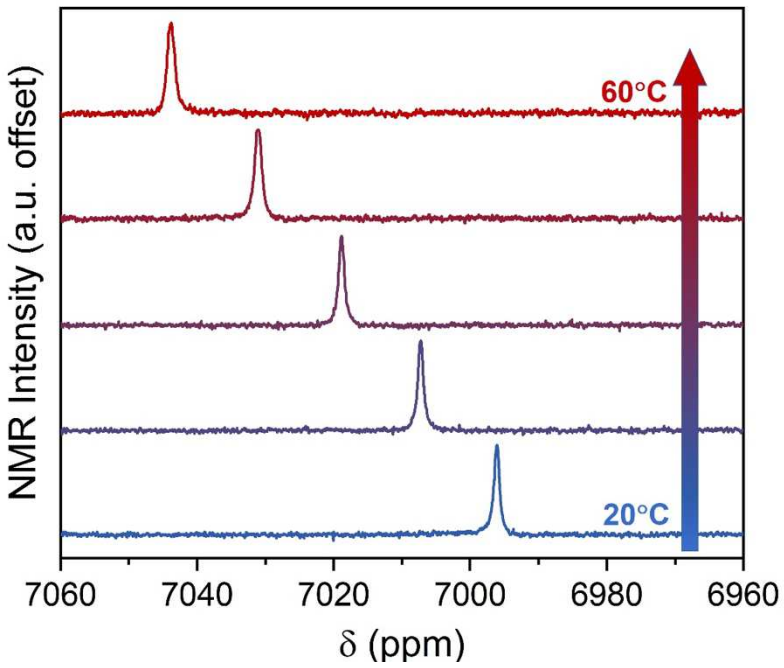

Appendix Figure 1.21. Chemical shift data of compound **2** from 20–60 °C. NMR measurements were taken in a solution of DMF at a concentration of ~15 mM.

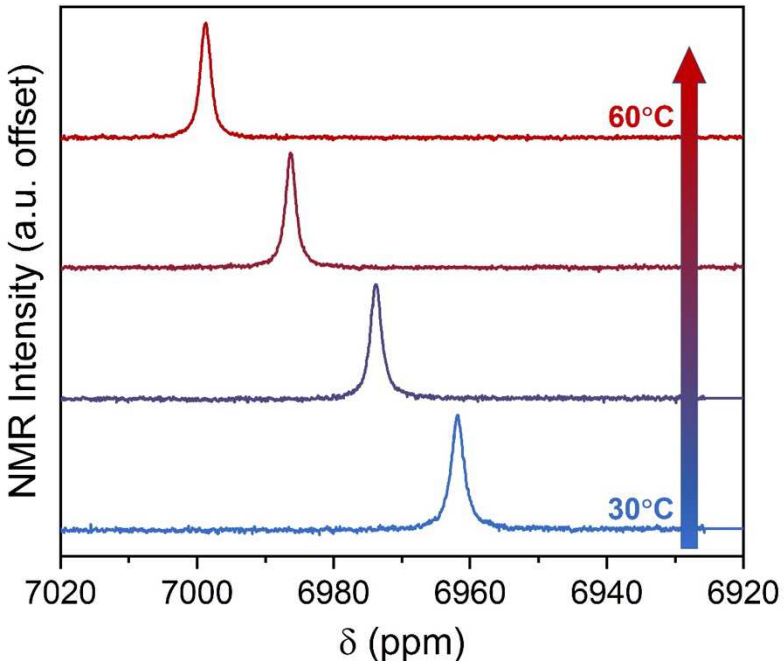

Appendix Figure 1.22. Chemical shift data of compound **2** from 30–60 °C. NMR measurements were taken in a solution of HMPA at a concentration of ~10 mM.

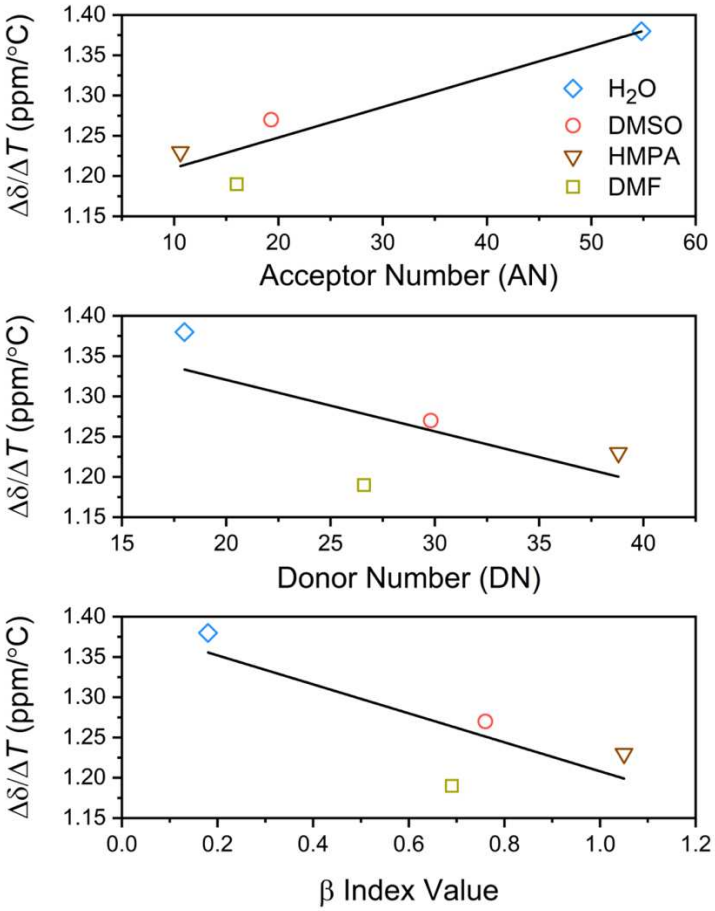

Appendix Figure 1.23. Plots of ^{59}Co chemical shift sensitivity as a function of solvent donor number for **2**. Donor numbers for the utilized solvents were taken from ref 20 from Chapter 1. The solid line is the result of linear regression ($R^2 = 0.251$).

APPENDIX 2: Supporting Information for Chapter 3

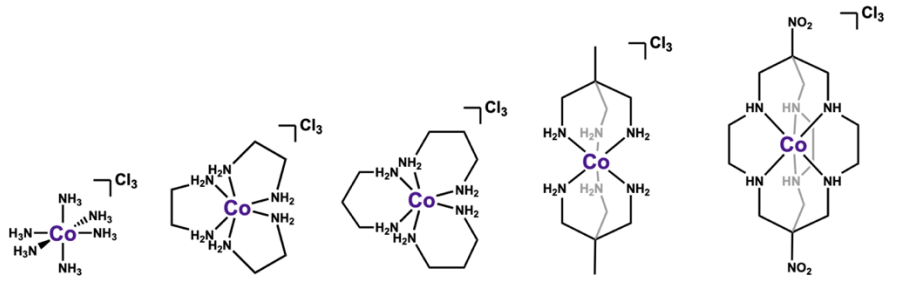

Appendix Figure 2.1. Bond-line chemical structure representations of the five Co^{3+} studied complexes in Chapter 3. All complexes are studied as 15 mM solutions in water as chloride salts. Hydrogens bound to carbons are omitted for clarity.

Appendix Table 2.1. Variable-temperature EXAFS measurements of complexes **1**–**5** of the $Co–N_6$ bond lengths from single scattering distances of the primary coordination sphere. Measurements were made over ~50 °C temperature window between 13, 35, and 57 °C. Values of r_1 (Å) were elucidated from fits of the EXAFS data. Determination of uncertainties in r_1 are detailed in above. Values of r_1 are the same as reported in *Table A2.2*. Reported Δr_1 values are between the 13 and 57 °C data.

		Co–N_6 Radial Distance, r_1 (Å)			
	Structure	13 °C	35 °C	57 °C	Δr_1
1	$[Co(NH_3)_6]Cl_3$	1.9588(5)	1.9742(6)	1.9836(5)	0.0248(6)
2	$[Co(en)_3]Cl_3$	1.9694(5)	1.9706(5)	1.9714(5)	0.0020(5)
3	$[Co(tn)_3]Cl_3$	1.9825(5)	1.9881(5)	1.9910(5)	0.0085(5)
4	$[Co(tame)_2]Cl_3$	1.9700(5)	1.9698(5)	1.9707(5)	0.0007(5)
5	$[Co(diNOsar)]Cl_3$	1.9701(5)	1.9751(6)	1.9776(6)	0.0075(6)

Appendix Table 2.2. Variable-temperature EXAFS fit parameters of **1**–**5** made specifically for the Co–N_6 distance of the first shell. All temperature-specific data for a given complex were fit collectively to their respective crystal structure models with a common amplitude reduction factor S_0^2, and E_0 (eV). Values of r_1 are the same as reported in *Table A2.1*. [a]

	Temp (°C)	S_0^2	E_0	α	σ^2 (Co-N_6)	ΔR (Å)	R_{eff} (Å)	r_1 (Å)
1	13	0.475(55)	0.14(1.2)	-0.005(6)	-0.0006(14)	-0.00991	1.9687	1.9588(5)
	35	0.475(55)	0.14(1.2)	0.003(9)	-0.0012(23)	0.00545	1.9687	1.9742(6)
	57	0.475(55)	0.14(1.2)	0.008(6)	0.0076(61)	0.01488	1.9687	1.9836(5)
2	13	0.644(27)	3.30(39)	0.007(2)	0.0004(6)	0.01448	1.9549	1.9694(5)
	35	0.644(27)	3.30(39)	0.008(2)	0.0006(4)	0.01569	1.9549	1.9706(5)
	57	0.644(27)	3.30(39)	0.008(2)	0.0012(4)	0.01648	1.9549	1.9714(5)
3	13	0.761(31)	1.21(46)	-0.008(2)	0.0002(4)	-0.01665	1.9991	1.9825(5)
	35	0.761(31)	1.21(46)	-0.005(2)	0.0019(5)	-0.01097	1.9991	1.9881(5)
	57	0.761(31)	1.21(46)	-0.004(1)	0.0021(4)	-0.00813	1.9991	1.9910(5)
4	13	0.895(27)	2.17(34)	-0.001(1)	0.0012(3)	-0.00259	1.9726	1.9700(5)
	35	0.895(27)	2.17(34)	-0.001(1)	0.0016(4)	-0.0028	1.9726	1.9698(5)
	57	0.895(27)	2.17(34)	-0.001(1)	0.0016(3)	-0.00195	1.9726	1.9707(5)
5	13	0.924(40)	1.17(44)	-0.006(2)	0.0013(5)	-0.01188	1.9820	1.9701(5)
	35	0.924(40)	1.17(44)	-0.004(1)	0.0026(4)	-0.00694	1.9820	1.9751(6)
	57	0.924(40)	1.17(44)	-0.002(2)	0.0024(5)	-0.00442	1.9820	1.9776(6)

[a] Note that ΔR in this table and Δr_1 commonly used in Chapter 3 are distinct values. ΔR (Å) is determined by $\Delta R = r_1 - R_{eff}$, and Δr_1 (Å) is the difference in r_1 between 13 and 57 °C EXAFS measurements (plotted in *Figure 3.3*, Chapter 3).

Appendix Table 2.3. Evaluation of fit parameters χ^2, reduced-χ^2, R-factor, number of independent points N_{ind}, and number of variables N_{var}, over the selected fit ranges for **1**–**5**. These parameters apply to all temperature-specific data for a compound as each set was made in the same fit.

	1	**2**	**3**	**4**	**5**
χ^2	630474.56	558155.64	473168.89	193677.43	193966.20
χ_ν^2	70782.37	12412.08	9438.67	4109.35	4395.25
R-factor	0.038375	0.0241832	0.0189678	0.0126918	0.023611
N_{ind}	19.9	56.0	64.1	64.1	64.1
N_{var}	8	11	14	17	20

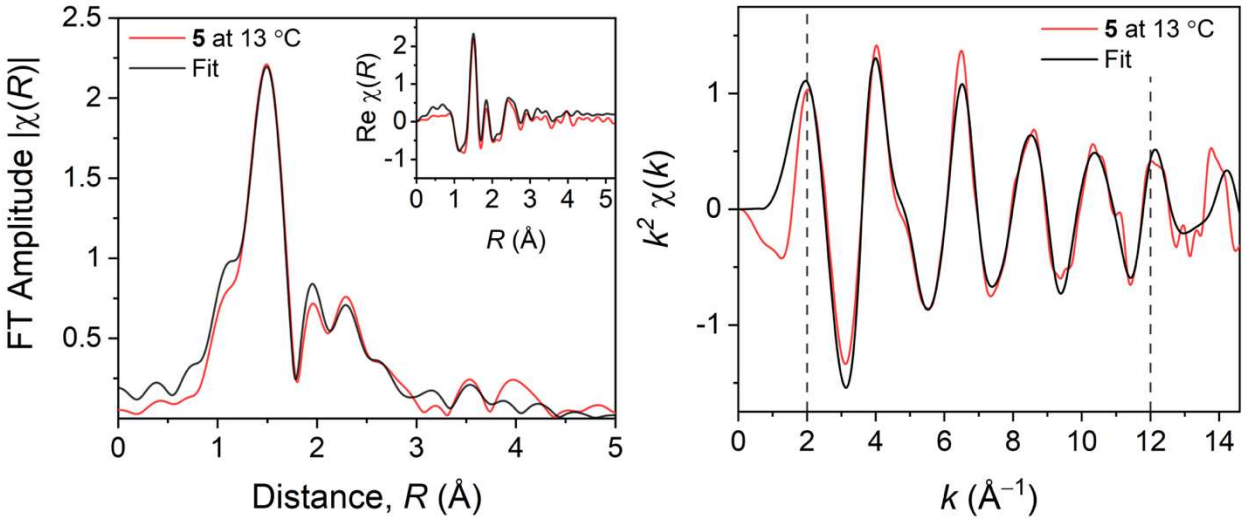

Appendix Figure 2.2. Derived *R*-space (*left*) and *k*-space (*right*) plots of EXAFS fluorescence measured spectra for **5** at 13 °C at the Co *K*-edge (0–15 Å^{-1} at Δk = 0.05 Å^{-1}). EXAFS data (*red*) against simulated fits (*black*) are made with k^2-weighting over *R*-range of 1.1–4.5 Å and *k*-range of 2–12 Å^{-1}. ***Inset:*** Fit of real part of the FT EXAFS data. Fits were made according to reported crystal structure data.

Appendix Table 2.4. EXAFS fit parameters of single scatter pathways for **5** at 13 °C.

Path	Atom Type	N	R_{eff} (Å)	ΔR (Å)	*r* (Å)	σ^2 (Å^2)
r_1	N	6	1.9820	-0.01188	1.97012	0.0013(5)
r_2	C	6	2.8153	-0.01688	2.79842	0.003(2)
r_3	C	6	2.9957	-0.01796	2.97774	0.004(4)
r_4	C	2	3.0221	-0.01812	3.00398	0.04(15)

Common fit parameters for this set include S_0^2 = 0.92(4), E_0 = 1.2(4) eV, and α = –0.006(2)

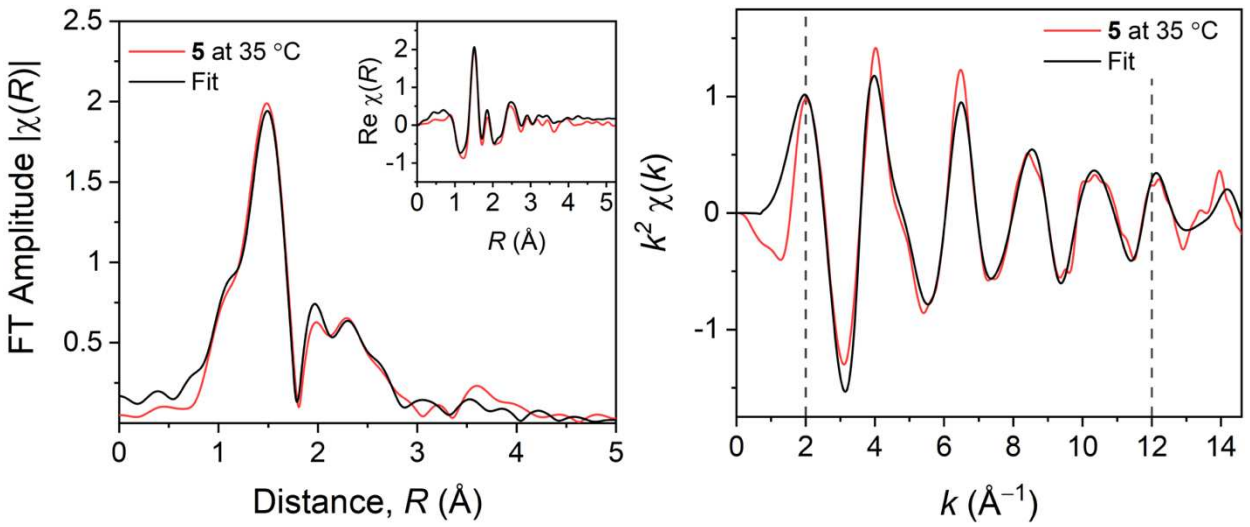

Appendix Figure 2.3. Derived *R*-space (*left*) and *k*-space (*right*) plots of EXAFS fluorescence measured spectra for **5** at 35 °C at the Co *K*-edge (0–15 Å^{-1} at Δk = 0.05 Å^{-1}). EXAFS data (*red*) against simulated fits (*black*) are made with k^2-weighting over *R*-range of 1.1–4.5 Å and *k*-range of 2–12 Å^{-1}. ***Inset:*** Fit of real part of the FT EXAFS data. Fits were made according to reported crystal structure data.

Appendix Table 2.5. EXAFS fit parameters of single scatter pathways for **5** at 35 °C.

Path	Atom Type	N	R_{eff} (Å)	ΔR (Å)	*r* (Å)	σ^2 (Å^2)
r_1	N	6	1.9820	-0.0069	1.97506	0.0026(4)
r_2	C	6	2.8153	-0.00986	2.80544	0.004(1)
r_3	C	6	2.9957	-0.01049	2.98521	0.007(3)
r_4	C	2	3.0221	-0.01059	3.01151	0.03(4)

Common fit parameters for this set include S_0^2 = 0.92(4), E_0 = 1.2(4) eV, and α = –0.004(1)

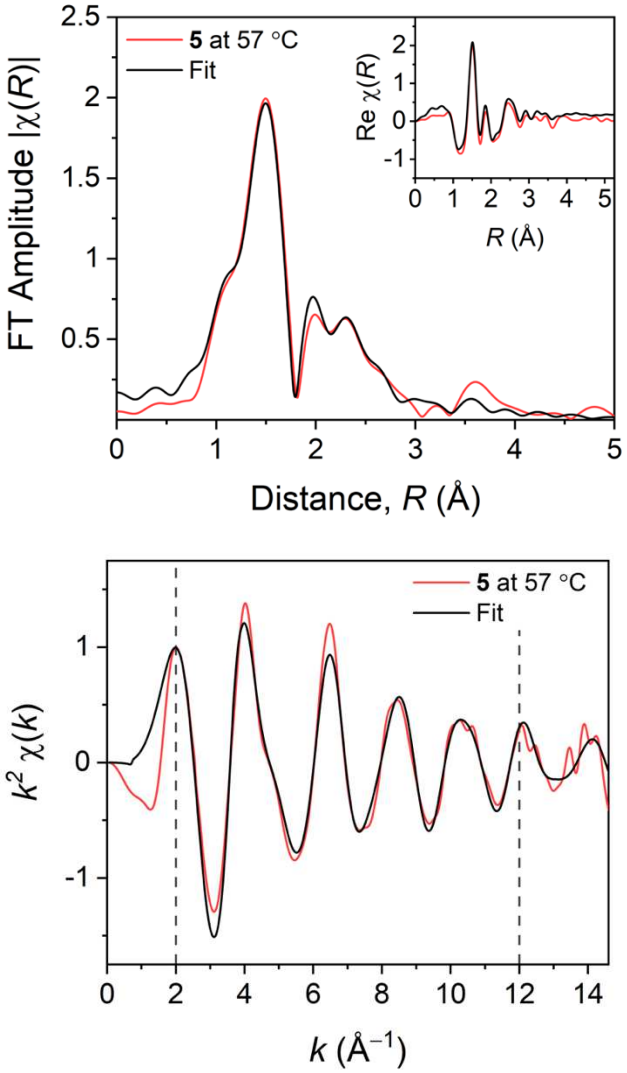

Appendix Figure 2.4. Derived *R*-space (*left*) and *k*-space (*right*) plots of EXAFS fluorescence measured spectra for **5** at 57 °C at the Co *K*-edge (0–15 $Å^{-1}$ at Δk = 0.05 $Å^{-1}$). EXAFS data (*red*) against simulated fits (*black*) are made with k^2-weighting over *R*-range of 1.1–4.5 Å and *k*-range of 2–12 $Å^{-1}$. ***Inset:*** Fit of real part of the FT EXAFS data. Fits were made according to reported crystal structure data.

Appendix Table 2.6. EXAFS fit parameters of single scatter pathways for **5** at 57 °C.

Path	Atom Type	N	R_{eff} (Å)	ΔR (Å)	r (Å)	σ^2 (Å^2)
r_1	N	6	1.982	-0.00442	1.97758	0.0024(5)
r_2	C	6	2.8153	-0.00628	2.80902	0.005(2)
r_3	C	6	2.9957	-0.00669	2.98901	0.01(1)
r_4	C	2	3.0221	-0.00674	3.01536	0.02(6)

Common fit parameters for this set include S_0^2 = 0.92(4), E_0 = 1.2(4) eV, and α = –0.002(2)

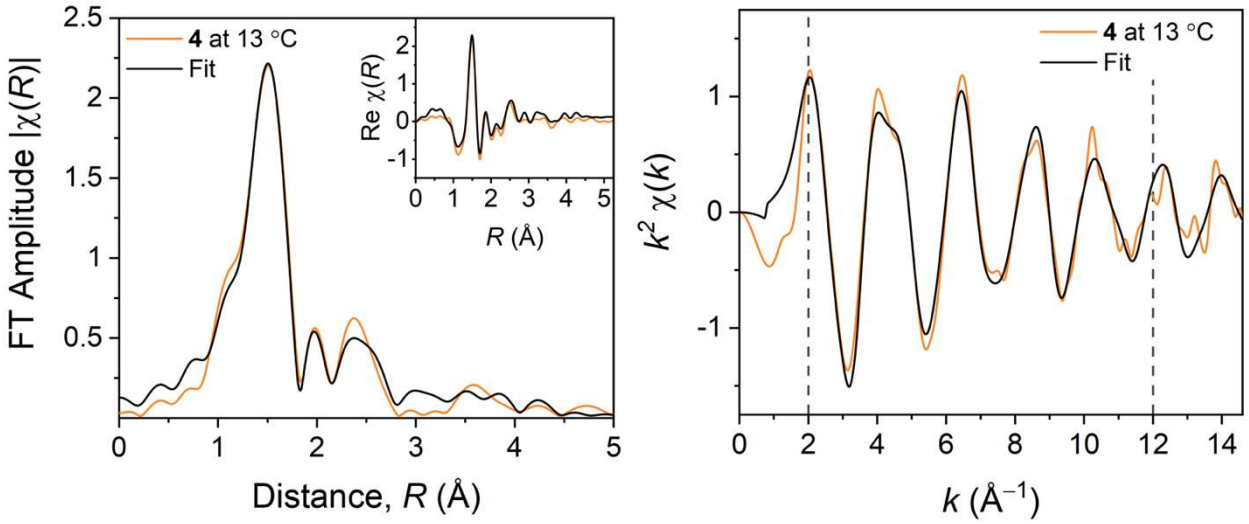

Appendix Figure 2.5. Derived *R*-space (*left*) and k-space (*right*) plots of EXAFS fluorescence measured spectra for **4** at 13 °C at the Co *K*-edge (0–15 Å^{-1} at Δk = 0.05 Å^{-1}). EXAFS data (*brown*) against simulated fits (*black*) are made with k^2-weighting over *R*-range of 1.1–4.5 Å and *k*-range of 2–12 Å^{-1}. ***Inset:*** Fit of real part of the FT EXAFS data. Fits were made according to reported crystal structure data.

Appendix Table 2.7. EXAFS fit parameters of single scatter pathways for **4** at 13 °C.

Path	Atom Type	N	R_{eff} (Å)	ΔR (Å)	*r* (Å)	σ^2 (Å^2)
r_1	N	6	1.9726	-0.00259	1.97001	0.0012(3)
r_2	C	6	2.9727	-0.0039	2.9688	0.003(1)
r_3	C	2	3.0861	-0.00405	3.08205	0.03(3)
r_4	C	2	4.6287	-0.00608	4.62262	0.06(19)

Common fit parameters for this set include S_0^2 = 0.80(3), E_0 = 2.2(3) eV, and α = –0.001(1)

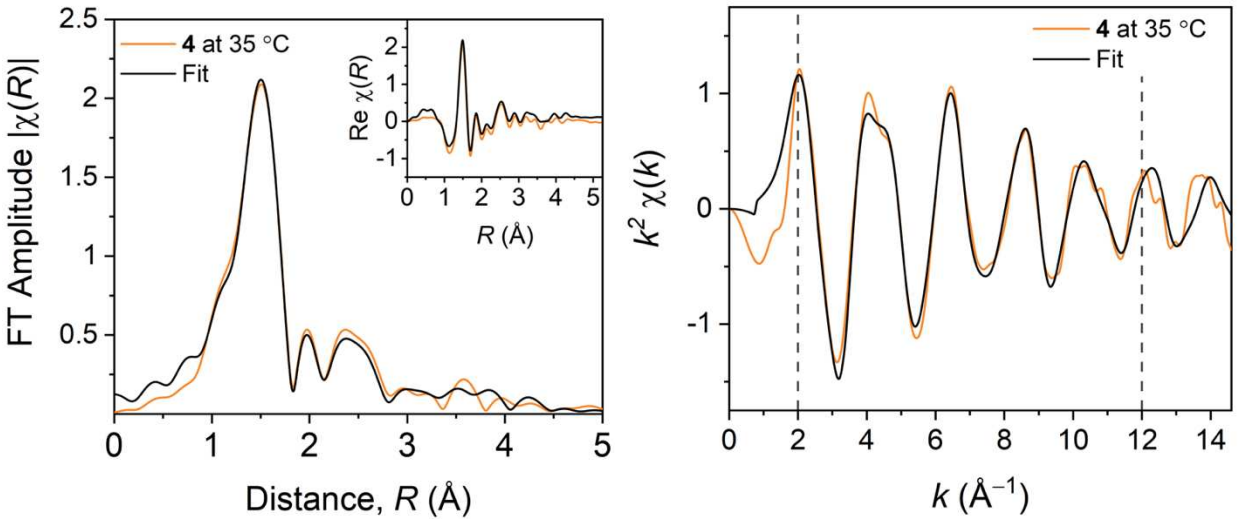

Appendix Figure 2.6. Derived *R*-space (*left*) and k-space (*right*) plots of EXAFS fluorescence measured spectra for **4** at 35 °C at the Co *K*-edge (0–15 Å^{-1} at Δk = 0.05 Å^{-1}). EXAFS data (*brown*) against simulated fits (*black*) are made with k^2-weighting over *R*-range of 1.1–4.5 Å and *k*-range of 2–12 Å^{-1}. ***Inset:*** Fit of real part of the FT EXAFS data. Fits were made according to reported crystal structure data.

Appendix Table 2.8. EXAFS fit parameters of single scatter pathways for **4** at 35 °C.

Path	Atom Type	N	R_{eff} (Å)	ΔR (Å)	*r* (Å)	σ^2 (Å^2)
r_1	N	6	1.9726	-0.0028	1.9698	0.0016(4)
r_2	C	6	2.9727	-0.00422	2.96848	0.003(1)
r_3	C	2	3.0861	-0.00438	3.08172	0.02(2)
r_4	C	2	4.6287	-0.00656	4.62214	0.01(4)

Common fit parameters for this set include S_0^2 = 0.80(3), E_0 = 2.2(3) eV, and α = –0.001(1)

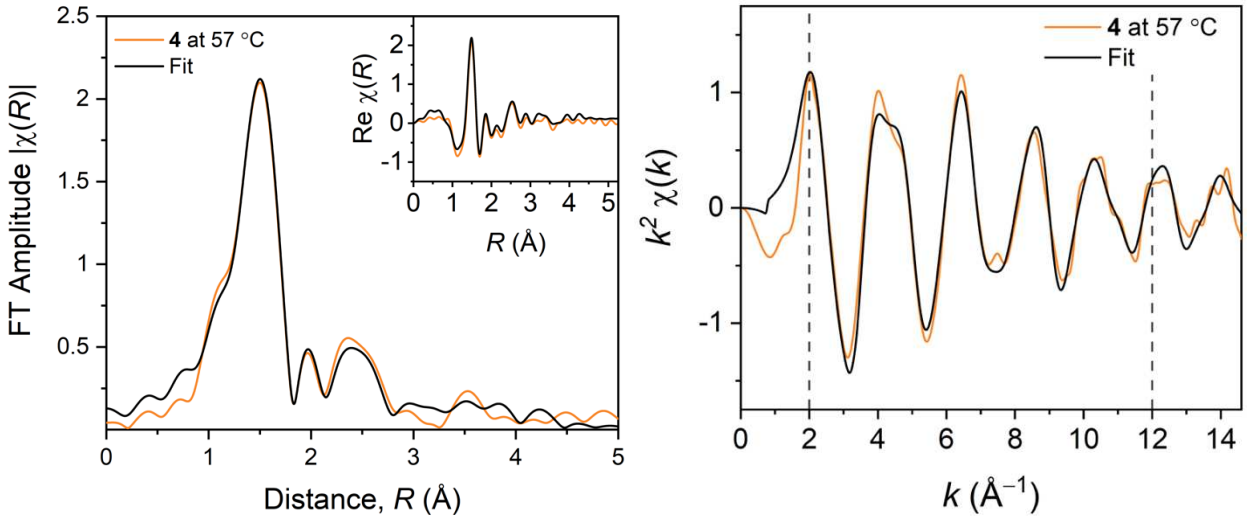

Appendix Figure 2.7. Derived *R*-space (*left*) and k-space (*right*) plots of EXAFS fluorescence measured spectra for **4** at 57 °C at the Co *K*-edge (0–15 Å^{-1} at Δk = 0.05 Å^{-1}). EXAFS data (*brown*) against simulated fits (*black*) are made with k^2-weighting over *R*-range of 1.1–4.5 Å and *k*-range of 2–12 Å^{-1}. ***Inset:*** Fit of real part of the FT EXAFS data. Fits were made according to reported crystal structure data.

Appendix Table 2.9. EXAFS fit parameters of single scatter pathways for **4** at 57 °C.

Path	Atom Type	N	R_{eff} (Å)	ΔR (Å)	*r* (Å)	σ^2 (Å^2)
r_1	N	6	1.9726	-0.00195	1.97065	0.0016(3)
r_2	C	6	2.9727	-0.00294	2.96976	0.003(1)
r_3	C	2	3.0861	-0.00306	3.08304	0.01(1)
r_4	C	2	4.6287	-0.00458	4.62412	0.002(9)

Common fit parameters for this set include S_0^2 = 0.80(3), E_0 = 2.2(3) eV, and α = –0.001(1)

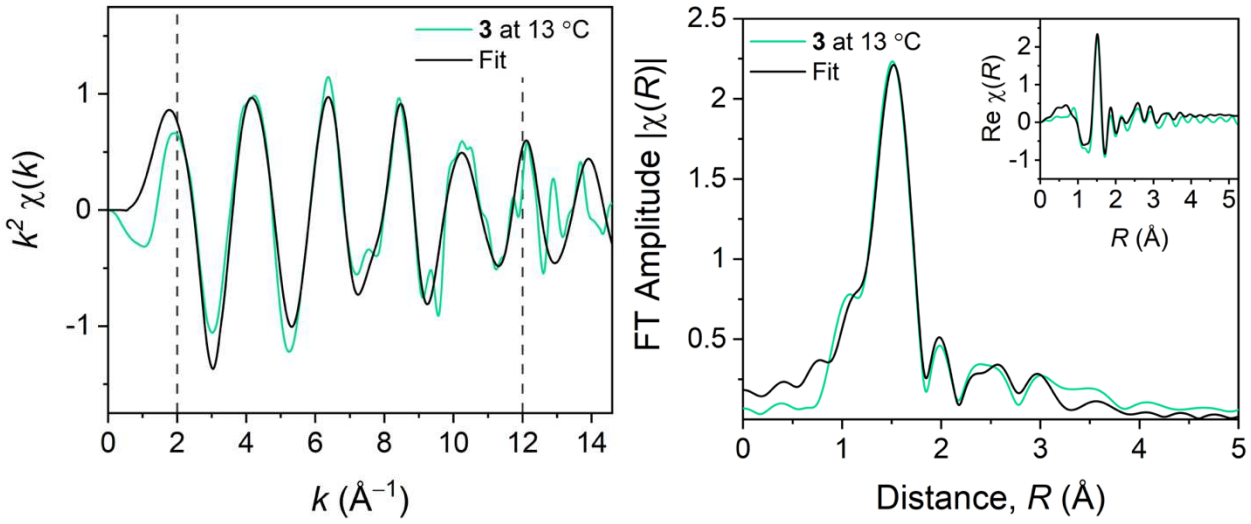

Appendix Figure 2.8. Derived *R*-space (*left*) and *k*-space (*right*) plots of EXAFS fluorescence measured spectra for **3** at 13 °C at the Co *K*-edge (0–15 Å^{-1} at $\Delta k = 0.05$ Å^{-1}). EXAFS data (*green*) against simulated fits (*black*) are made with k^2-weighting over *R*-range of 1.1–4.5 Å and *k*-range of 2–12 Å^{-1}. ***Inset:*** Fit of real part of the FT EXAFS data. Fits were made according to reported crystal structure data.

Appendix Table 2.10. EXAFS fit parameters of single scatter pathways for **3** at 13 °C.

Path	Atom Type	N	R_{eff} (Å)	ΔR (Å)	*r* (Å)	σ^2 (Å^2)
r_1	N	6	1.9991	-0.01665	1.98245	0.0002(4)
r_2	C	6	3.0372	-0.0253	3.0119	0.003(2)
r_3	C	3	3.4031	-0.02835	3.37475	0.05(7)

Common fit parameters for this set include $S_0^2 = 0.76(3)$, $E_0 = 1.2(5)$ eV, and $\alpha = -0.008(2)$

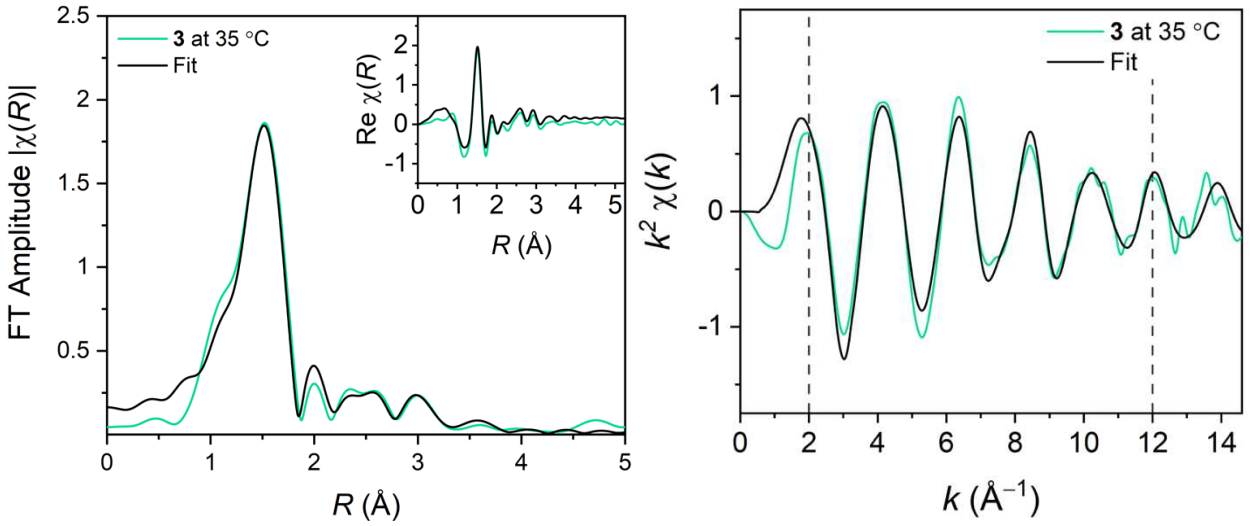

Appendix Figure 2.9. Derived *R*-space (*left*) and *k*-space (*right*) plots of EXAFS fluorescence measured spectra for **3** at 35 °C at the Co *K*-edge (0–15 Å^{-1} at Δk = 0.05 Å^{-1}). EXAFS data (*green*) against simulated fits (*black*) are made with k^2-weighting over *R*-range of 1.1–4.5 Å and *k*-range of 2–12 Å^{-1}. ***Inset:*** Fit of real part of the FT EXAFS data. Fits were made according to reported crystal structure data.

Appendix Table 2.11. EXAFS fit parameters of single scatter pathways for **3** at 35 °C.

Path	Atom Type	N	R_{eff} (Å)	ΔR (Å)	*r* (Å)	σ^2 (Å^2)
r_1	N	6	1.9991	-0.01097	1.98813	0.0019(5)
r_2	C	6	3.0372	-0.01667	3.02053	0.006(3)
r_3	C	3	3.4031	-0.01867	3.38443	0.04(7)

Common fit parameters for this set include S_0^2 = 0.76(3), E_0 = 1.2(5) eV, and α = –0.005(2)

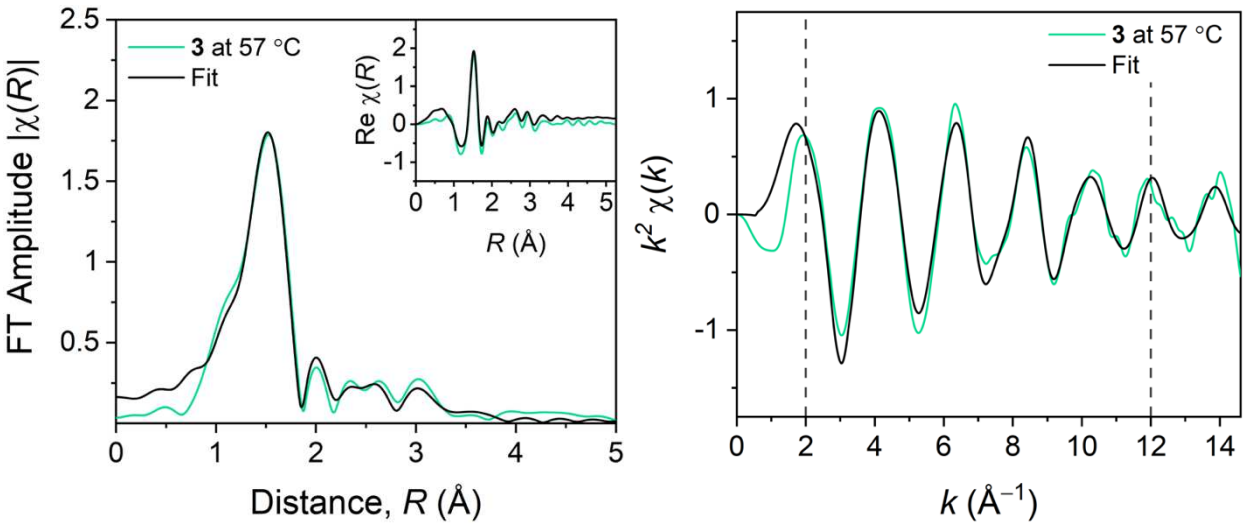

Appendix Figure 2.10. Derived *R*-space (*left*) and *k*-space (*right*) plots of EXAFS fluorescence measured spectra for **3** at 57 °C at the Co *K*-edge (0–15 Å^{-1} at Δk = 0.05 Å^{-1}). EXAFS data (*green*) against simulated fits (*black*) are made with k^2-weighting over *R*-range of 1.1–4.5 Å and *k*-range of 2–12 Å^{-1}. ***Inset:*** Fit of real part of the FT EXAFS data. Fits were made according to reported crystal structure data.

Appendix Table 2.12. EXAFS fit parameters of single scatter pathways for **3** at 57 °C.

Path	Atom Type	N	R_{eff} (Å)	ΔR (Å)	*r* (Å)	σ^2 (Å^2)
r_1	N	6	1.9991	-0.00813	1.99097	0.0021(4)
r_2	C	6	3.0372	-0.01235	3.02485	0.007(2)
r_3	C	3	3.4031	-0.01384	3.38926	0.05(6)

Common fit parameters for this set include S_0^2 = 0.76(3), E_0 = 1.2(5) eV, and α = –0.004(1)

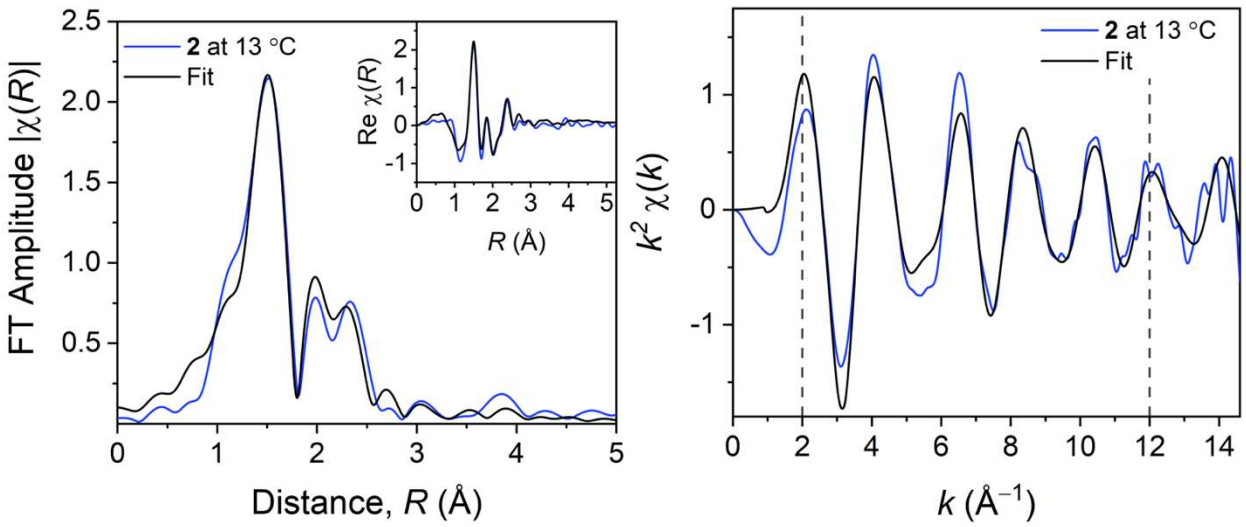

Appendix Figure 2.11. Derived *R*-space (*left*) and *k*-space (*right*) plots of EXAFS fluorescence measured spectra for **2** at 13 °C at the Co *K*-edge (0–15 Å^{-1} at Δk = 0.05 Å^{-1}). EXAFS data (*blue*) against simulated fits (*black*) are made with k^2-weighting over *R*-range of 1.1–4.2 Å and *k*-range of 2–12 Å^{-1}. ***Inset:*** Fit of real part of the FT EXAFS data. Fits were made according to reported crystal structure data.

Appendix Table 2.13. EXAFS fit parameters of single scatter pathways for **2** at 13 °C.

Path	Atom Type	N	R_{eff} (Å)	ΔR (Å)	*r* (Å)	σ^2 (Å^2)
r_1	N	6	1.9549	0.01448	1.96938	0.0004(6)
r_2	C	6	2.8207	0.02089	2.84159	0.002(1)

Common fit parameters for this set include S_0^2 = 0.64(3), E_0 = 3.3(4) eV, and α = 0.007(2)

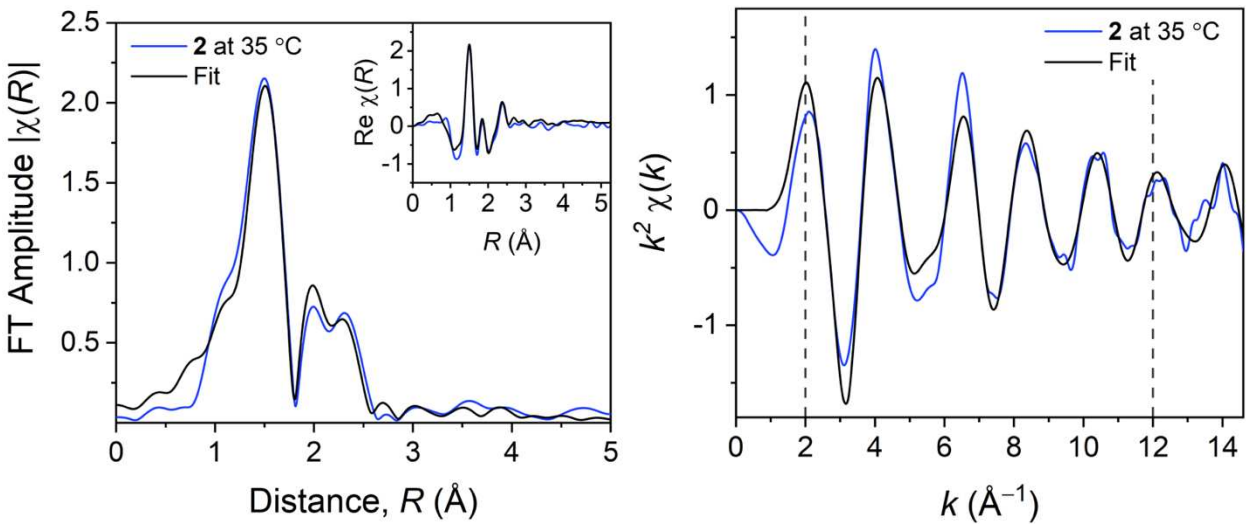

Appendix Figure 2.12. Derived *R*-space (*left*) and *k*-space (*right*) plots of EXAFS fluorescence measured spectra for **2** at 35 °C at the Co *K*-edge (0–15 Å^{-1} at Δk = 0.05 Å^{-1}). EXAFS data (*blue*) against simulated fits (*black*) are made with k^2-weighting over *R*-range of 1.1–4.2 Å and *k*-range of 2–12 Å^{-1}. ***Inset:*** Fit of real part of the FT EXAFS data. Fits were made according to reported crystal structure data.

Appendix Table 2.14. EXAFS fit parameters of single scatter pathways for **2** at 35 °C.

Path	Atom Type	N	R_{eff} (Å)	ΔR (Å)	*r* (Å)	σ^2 (Å^2)
r_1	N	6	1.9549	0.01569	1.97059	0.0006(4)
r_2	C	6	2.8207	0.02264	2.84334	0.001(1)

Common fit parameters for this set include S_0^2 = 0.64(3), E_0 = 3.3(4) eV, and α = 0.008(2)

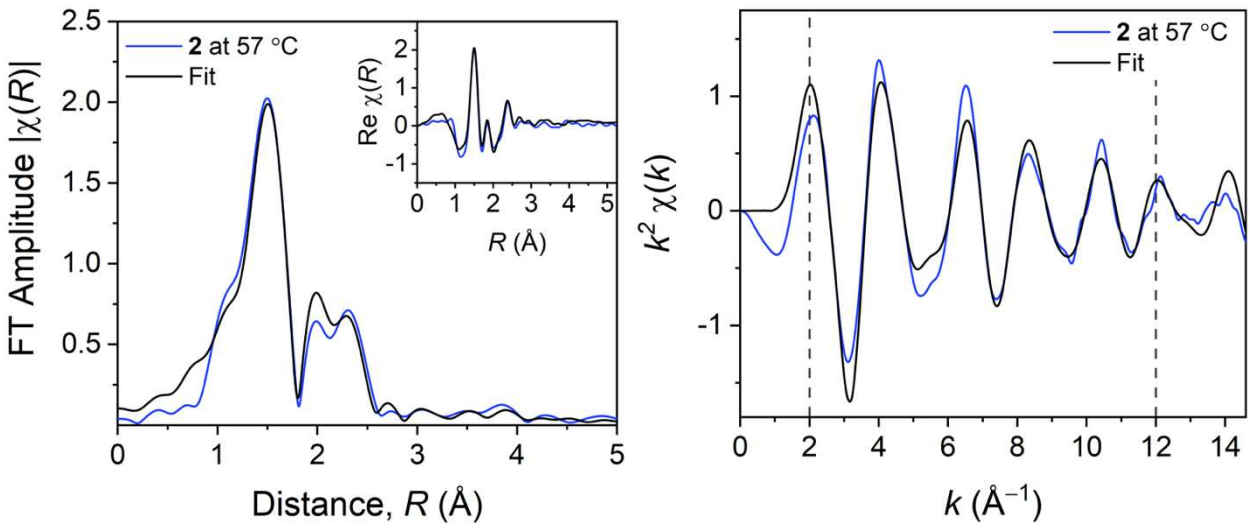

Appendix Figure 2.13. Derived *R*-space (*left*) and *k*-space (*right*) plots of EXAFS fluorescence measured spectra for **2** at 57 °C at the Co *K*-edge (0–15 Å^{-1} at Δk = 0.05 Å^{-1}). EXAFS data (*blue*) against simulated fits (*black*) are made with k^2-weighting over *R*-range of 1.1–4.2 Å and *k*-range of 2–12 Å^{-1}. ***Inset:*** Fit of real part of the FT EXAFS data. Fits were made according to reported crystal structure data.

Appendix Table 2.15. EXAFS fit parameters of single scatter pathways for **2** at 57 °C.

Path	Atom Type	N	R_{eff} (Å)	ΔR (Å)	*r* (Å)	σ^2 (Å^2)
r_1	N	6	1.9549	0.01648	1.97138	0.0012(4)
r_2	C	6	2.8207	0.02378	2.84448	0.001(1)

Common fit parameters for this set include S_0^2 = 0.64(3), E_0 = 3.3(4) eV, and α = 0.008(2)

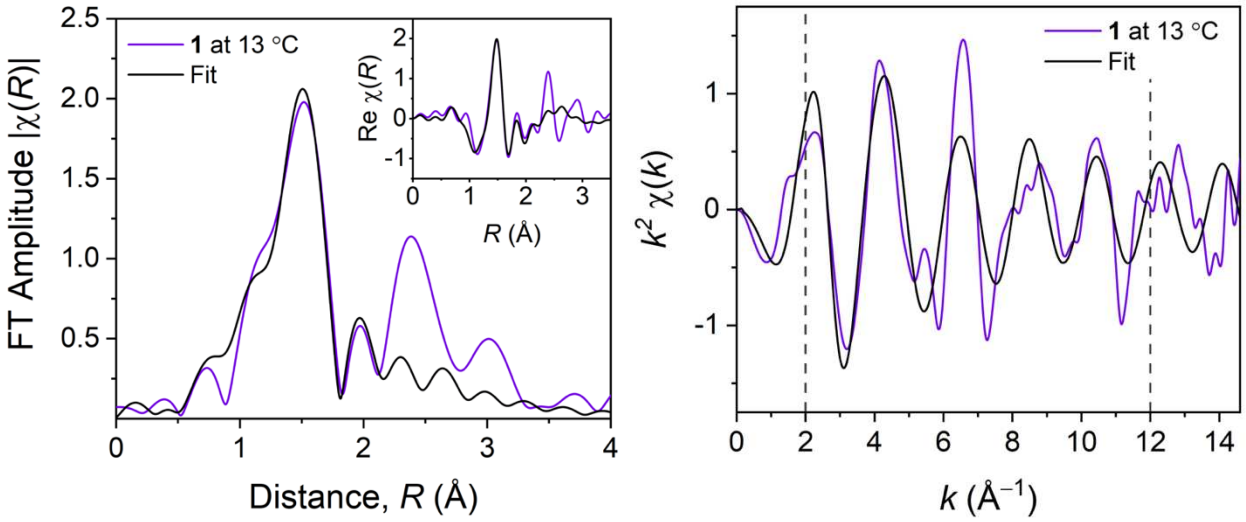

Appendix Figure 2.14. Derived *R*-space (*left*) and *k*-space (*right*) plots of EXAFS fluorescence measured spectra for **1** at 13 °C at the Co *K*-edge (0–15 Å^{-1} at $\Delta k = 0.05$ Å^{-1}). EXAFS data (*purple*) against simulated fits (*black*) are made with k^2-weighting over *R*-range of 1.1–2 Å and k-range of 2–12 Å^{-1}. ***Inset:*** Fit of real part of the FT EXAFS data. Fits were made according to reported crystal structure data.

Appendix Table 2.16. EXAFS fit parameters of single scatter pathways for **1** at 13 °C.

Path	Atom Type	N	R_{eff} (Å)	ΔR (Å)	*r* (Å)	σ^2 (Å^2)
r_1	N	6	1.9687	-0.00991	1.95879	-0.006(1)

Common fit parameters for this set include $S_0^2 = 0.48(5)$, $E_0 = 0.1(1.1)$ eV, and $\alpha = -0.005(6)$

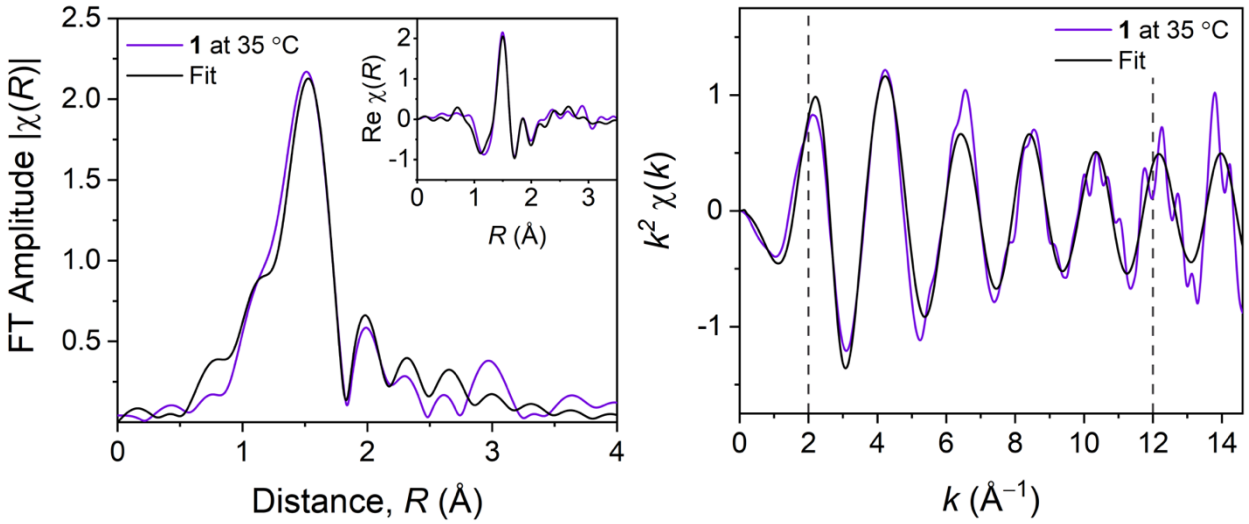

Appendix Figure 2.15. Derived *R*-space (*left*) and *k*-space (*right*) plots of EXAFS fluorescence measured spectra for **1** at 35 °C at the Co *K*-edge (0–15 Å^{-1} at $\Delta k = 0.05$ Å^{-1}). EXAFS data (*purple*) against simulated fits (*black*) are made with k^2-weighting over *R*-range of 1.1–2 Å and k-range of 2–12 Å^{-1}. ***Inset:*** Fit of real part of the FT EXAFS data. Fits were made according to reported crystal structure data.

Appendix Table 2.17. EXAFS fit parameters of single scatter pathways for **1** at 35 °C.

Path	Atom Type	N	R_{eff} (Å)	ΔR (Å)	*r* (Å)	σ^2 (Å^2)
r_1	N	6	1.9687	0.00545	1.97415	-0.001(2)

Common fit parameters for this set include $S_0^2 = 0.48(5)$, $E_0 = 0.1(1.1)$ eV, and $\alpha = 0.003(9)$

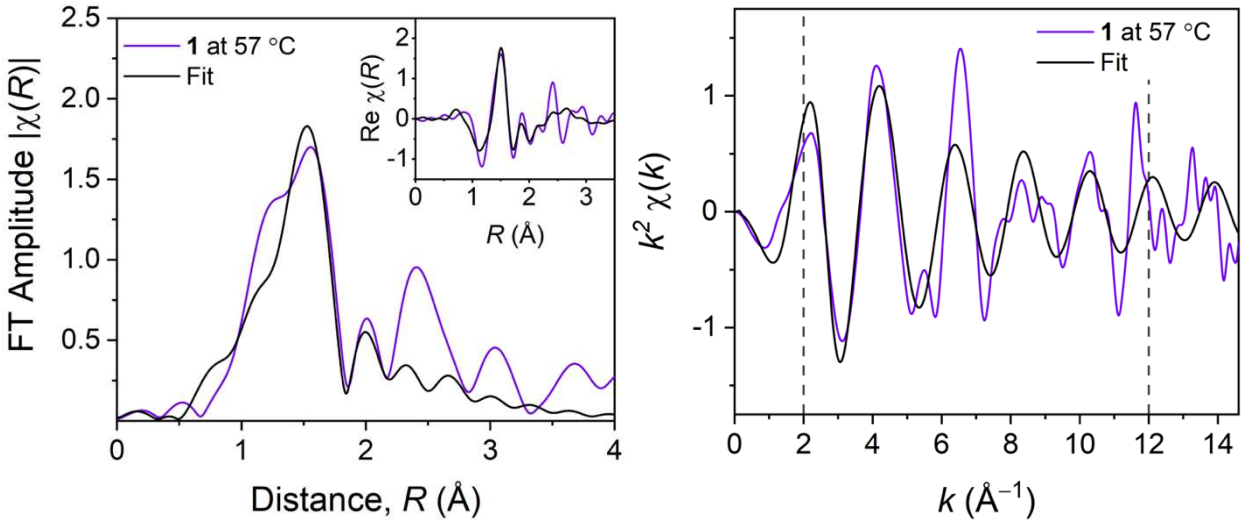

Appendix Figure 2.16. Derived *R*-space (*left*) and *k*-space (*right*) plots of EXAFS fluorescence measured spectra for **1** at 57 °C at the Co *K*-edge (0–15 Å^{-1} at $\Delta k = 0.05$ Å^{-1}). EXAFS data (*purple*) against simulated fits (*black*) are made with k^2-weighting over *R*-range of 1.1–2 Å and k-range of 2–12 Å^{-1}. ***Inset:*** Fit of real part of the FT EXAFS data. Fits were made according to reported crystal structure data.

Appendix Table 2.18. EXAFS fit parameters of single scatter pathways for **1** at 57 °C.

Path	Atom Type	N	R_{eff} (Å)	ΔR (Å)	*r* (Å)	σ^2 (Å^2)
r_1	N	6	1.9687	0.01488	1.98358	0.0004(16)

Common fit parameters for this set include $S_0^2 = 0.48(5)$, $E_0 = 0.1(1.1)$ eV, and $\alpha = 0.008(6)$

Appendix Table 2.19. Ligand bite angles of **2** at 13 and 57 °C. Chelating N–Co–N ligand bond angle of the three separate ethylene bridging units in the temperature-specific optimized structures. The average N–Co–N bond angle of this –0.04(1)° from 13 to 57 °C EXAFS bond measurements.

N–Co–N Ligand Bite Angle		
13 °C	57 °C	Δ (N–Co–N)
84.938	84.919	-0.019
84.956	84.919	-0.038
84.968	84.921	-0.047

Appendix Table 2.20. Ligand bite angles of **3** at 13 and 57 °C. Chelating N–Co–N ligand bond angle of the three separate trismethylene bridging units in the temperature-specific optimized structures. The average N–Co–N bond angle of this –0.134(7)° from 13 to 57 °C EXAFS bond measurements.

N–Co–N Ligand Bite Angle		
13 °C	57 °C	Δ (N–Co–N)
93.596	93.456	-0.140
93.565	93.428	-0.137
93.626	93.500	-0.126

Appendix Table 2.21. Ligand bite angles of **5** at 13 and 57 °C. Chelating N–Co–N ligand bond angle of the three separate ethylene bridging units in the temperature-specific optimized structures. The average N–Co–N bond angle of this –0.0830(1)° from 13 to 57 °C EXAFS bond measurements.

N–Co–N Ligand Bite Angle		
13 °C	57 °C	Δ (N–Co–N)
86.617	86.534	-0.083
86.618	86.535	-0.083
86.603	86.519	-0.083

Appendix Table 2.22. SHAPE analysis of the change in relative geometric distortion from ideal octahedral symmetry (O_h symmetry) for optimized structures of **1**–**5** at 13 and 57 °C temperature-specific bond lengths. In the case of Δ*S*, a positive change indicates a greater distortion, while a negative change indicates an improvement of O_h symmetry. Relative changes in shape factors, Δ*S*/*S*(O_h), are made with respect to *S*(O_h) at 13°C.

Structure	13 °C *S* (O_h)	57 °C *S* (O_h)	Δ*S* (O_h)	Δ*S*/*S* (O_h)
$[Co(NH_3)_6]Cl_3$	0.004	0.004	0.000	0.000
$[Co(en)_3]Cl_3$	0.264	0.266	0.002	0.008
$[Co(tn)_3]Cl_3$	0.112	0.104	-0.008	-0.071
$[Co(tame)_2]Cl_3$	0.111	0.112	0.001	0.009
$[Co(diNOsar)]Cl_3$	0.133	0.141	0.008	0.060

Appendix Table 2.23. SHAPE analysis of the change in relative geometric distortion from ideal trigonal prismatic symmetry (D_{3h} symmetry) for optimized structures of **1**–**5** at 13 and 57 °C temperature-specific bond lengths. In the case of ΔS, a positive change indicates a greater distortion, while a negative change indicates an improvement of D_{3h} symmetry. Relative changes shape factors, Δ*S*/*S*(D_{3h}), are made with respect to *S*(D_{3h}) at 13°C.

Structure	13 °C *S* (D_{3h})	57 °C *S* (D_{3h})	Δ*S* (D_{3h})	Δ*S*/*S* (D_{3h})
$[Co(NH_3)_6]Cl_3$	16.627	16.627	0.000	0.000
$[Co(en)_3]Cl_3$	13.883	13.876	-0.007	-0.001
$[Co(tn)_3]Cl_3$	14.331	14.412	0.081	0.006
$[Co(tame)_2]Cl_3$	14.376	14.37	-0.006	0.000
$[Co(diNOsar)]Cl_3$	14.535	14.464	-0.071	-0.005

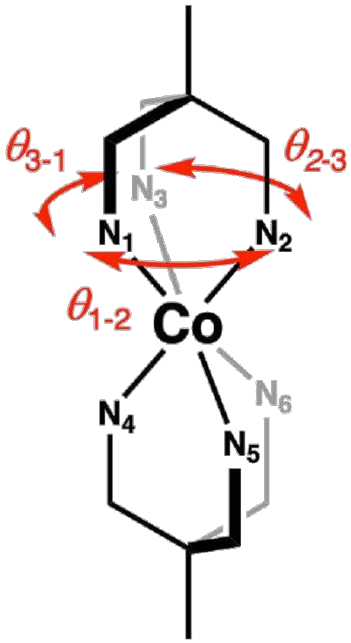

	N–Co–N Ligand Bite Angle		
	θ (13 °C)	θ (57 °C)	$\Delta\theta$
1 to 2	88.499	88.512	0.013
2 to 3	88.483	88.493	0.010
3 to 1	88.474	88.456	-0.018
4 to 5	88.473	88.460	-0.013
5 to 6	88.494	88.507	0.013
6 to 4	88.491	88.493	0.002
		Average	**0.001**
		Deviation	**0.013615**

Appendix Figure 2.17. Depiction of computed changes in bite angles for the tame ligand in **4**. Note that though there are somewhat large changes to individual N–Co–N angles for the tame ligands, the average of the change is relatively minor compared with other bite angle differences (e.g., *Figure 3.4*, Chapter 3).

Appendix Table 2.24. Computed coordinates of $[Co(diNOsar)]^{3+}$ with fixed Co–N bond distances to 13 °C EXAFS (1.9701 Å, see *Tables A2.1 and A2.4*). Total energy: –2671.56817364 Hartrees

Symbol	x	y	z
Co	-0.00001746	0.00003590	-0.00321822
N	4.58123096	-0.00315094	0.00592137
O	5.15200180	1.05047166	0.11788921
O	5.06253958	-1.10616903	-0.08148905
C	3.04267963	0.03606325	-0.00674495
C	2.61657699	-0.63751270	-1.30764245
C	2.60443849	1.49270006	0.06612590
C	2.61975460	-0.76377662	1.22397064
N	1.13429509	-0.85688789	-1.36882594
N	1.11293024	1.62559678	-0.07226585
N	1.13461047	-0.73671173	1.43054973
C	0.77482152	-2.30661580	-1.41702752
C	0.72544921	2.39301258	-1.29451749
C	0.75075595	-0.06414566	2.70851316
H	0.85892026	-0.48975260	-2.27627619
H	0.83975145	2.22096501	0.70554336
H	0.87839211	-1.71227804	1.56114915
N	-4.58129970	0.00339967	0.00593612
O	-5.15213092	-1.05040541	0.11613290
O	-5.06263912	1.10652715	-0.07958190
C	-3.04272238	-0.03590631	-0.00696511
C	-2.60458044	-1.49274200	0.06251794
C	-2.61662149	0.64062632	-1.30628830
C	-2.61973551	0.76106774	1.22562102
N	-1.11297229	-1.62537605	-0.07557432
N	-1.13426371	0.85971998	-1.36714536
N	-1.13462785	0.73356769	1.43221127
C	-0.72508818	-2.39068367	-1.29899977
C	-0.77446665	2.30939262	-1.41296566
C	-0.75087675	0.05795454	2.70858706
H	-0.84016512	-2.22202377	0.70138898
H	-0.85896733	0.49390341	-2.27515013
H	-0.87842394	1.70881076	1.56514626
H	3.13030401	-1.59491812	-1.39880718
H	2.91929234	-0.02399025	-2.15811300
H	3.09294765	2.06898438	-0.71920915
H	2.91634245	1.93259992	1.01323439
H	3.10974968	-0.35924677	2.11179481
H	2.95290640	-1.79614147	1.11652766
H	1.26969482	-2.81416218	-0.58549573
H	1.13791182	-2.76545807	-2.33857887
H	1.21719604	1.93909872	-2.15842199
H	1.07254632	3.42595367	-1.22977388
H	1.22913794	0.91780114	2.74002553
H	1.11331571	-0.62992302	3.56885253
H	-3.09274116	-2.06709921	-0.72446352

H	-2.91685934	-1.93496575	1.00839086
H	-3.13006543	1.59839745	-1.39512349
H	-2.91961483	0.02924136	-2.15821322
H	-3.10975741	0.35444850	2.11246531
H	-2.95290167	1.79369268	1.12056144
H	-1.21671961	-1.93533345	-2.16222529
H	-1.07207745	-3.42377800	-1.23611031
H	-1.26934184	2.81569904	-0.58068310
H	-1.13730146	2.76983871	-2.33382016
H	-1.22925360	-0.92407893	2.73766406
H	-1.11355041	0.62164207	3.57024759

Appendix Table 2.25. Computed coordinates of $[Co(diNOsar)]^{3+}$ with fixed Co–N bond distances to 57 °C EXAFS (1.9776 Å, see *Tables A2.1 and A2.6*). Total energy: –2671.56901712 Hartrees

Symbol	x	y	z
Co	-0.00000394	0.00001705	-0.00309016
N	4.58310477	-0.00331242	0.00579444
O	5.15430137	1.05067177	0.11198244
O	5.06432835	-1.10676566	-0.07619557
C	3.04396908	0.03612525	-0.00686273
C	2.61992135	-0.64370393	-1.30580020
C	2.60781655	1.49426353	0.05932452
C	2.62305883	-0.75871051	1.22847312
N	1.13826676	-0.86234475	-1.37196989
N	1.11684222	1.63114810	-0.07537517
N	1.13863874	-0.73653537	1.43709837
C	0.77520724	-2.31099708	-1.41621649
C	0.72547541	2.39479222	-1.29840122
C	0.75107731	-0.06112315	2.71212084
H	0.86377912	-0.49516418	-2.27963162
H	0.84488031	2.22650152	0.70282627
H	0.88351074	-1.71231837	1.56790199
N	-4.58312654	0.00343664	0.00578447
O	-5.15435512	-1.05062900	0.11105055
O	-5.06432262	1.10695801	-0.07523002
C	-3.04398265	-0.03605229	-0.00692913
C	-2.60788098	-1.49427581	0.05758643
C	-2.61993333	0.64521743	-1.30511220
C	-2.62303782	0.75739030	1.22929026
N	-1.11685815	-1.63103358	-0.07705181
N	-1.13825964	0.86379692	-1.37108781
N	-1.13864254	0.73491282	1.43794780
C	-0.72534955	-2.39354495	-1.30072148
C	-0.77507403	2.31243438	-1.41405256
C	-0.75116900	0.05789192	2.71213940
H	-0.84503040	-2.22708013	0.70067201
H	-0.86377266	0.49733522	-2.27903973
H	-0.88347660	1.71051492	1.57000202

H	3.13321887	-1.60194808	-1.39064537
H	2.92632418	-0.03461202	-2.15817102
H	3.09560995	2.06519062	-0.73040385
H	2.92369718	1.93843926	1.00310301
H	3.11263791	-0.34803645	2.11374525
H	2.95984531	-1.79040456	1.12580813
H	1.26788604	-2.81698887	-0.58240125
H	1.13876502	-2.77354322	-2.33578711
H	1.21496063	1.93824021	-2.16224427
H	1.07293667	3.42791063	-1.23774188
H	1.22716982	0.92203199	2.74115790
H	1.11408902	-0.62327913	3.57470235
H	-3.09554043	-2.06425119	-0.73291341
H	-2.92390153	-1.93958212	1.00077382
H	-3.13314407	1.60360959	-1.38883629
H	-2.92642109	0.03712980	-2.15817380
H	-3.11267998	0.34576658	2.11408182
H	-2.95977599	1.78921810	1.12775094
H	-1.21480643	-1.93620722	-2.16417054
H	-1.07277590	-3.42673410	-1.24104698
H	-1.26774970	2.81773726	-0.57982283
H	-1.13857477	2.77581824	-2.33322696
H	-1.22725878	-0.92530459	2.73988872
H	-1.11426180	0.61894648	3.57540362

Appendix Table 2.26. Computed coordinates of $[Co(tame)_2]^{3+}$ with fixed Co–N bond distances to 13 °C EXAFS (1.9700 Å, see *Tables A2.1 and A2.7*). Total energy: –2109.54797542 Hartrees

Symbol	x	y	z
Co	-0.00000347	0.00026855	0.00013800
N	-1.16688756	-1.36565803	0.80857250
N	-1.16696618	-0.01657170	-1.58695199
N	1.16676891	-1.43273672	-0.68256134
N	-1.16734922	1.38306928	0.77866627
N	1.16708267	1.30778504	-0.89944564
N	1.16729811	0.12585389	1.58209106
C	-4.64680352	-0.00048948	-0.00030824
C	-3.11426948	-0.00032950	-0.00007533
C	-2.60840971	-0.99667970	1.04747613
C	-2.60810793	-0.40917475	-1.38666869
C	-2.60868229	1.40509670	0.33918814
C	2.60826729	-1.08671343	-0.95383579
C	3.11426447	-0.00023486	-0.00017904
C	4.64681594	-0.00052409	-0.00019484
C	2.60847624	-0.28292936	1.41761373
C	2.60857697	1.36906715	-0.46396050
H	-1.17927408	-2.17178325	0.18471381
H	-0.80696977	-0.57782351	-2.35828537
H	0.80665405	-1.89602002	-1.51638867

H	-1.17997696	1.24590158	1.78872434
H	1.17923630	1.08134022	-1.89329024
H	0.80760127	-0.36408281	2.40072487
H	-5.03823579	-0.94835206	-0.37485339
H	-5.03853196	0.14911460	1.00771240
H	5.03838498	0.05747337	-1.01767911
H	-3.20353192	-1.91097901	1.02017900
H	-2.69895608	-1.48658235	-1.53877537
H	-2.70038243	2.07558247	-0.51769056
H	3.20329668	-1.99490842	-0.84440876
H	2.69952799	-1.34231745	1.66583596
H	3.20387882	1.72857178	-1.30491224
H	-0.80689062	-1.75209423	1.68070945
H	-1.17997355	0.92696462	-1.97264836
H	1.17920999	-2.17956753	0.01117579
H	-0.80782756	2.33182585	0.67758156
H	0.80731307	2.26165035	-0.88315728
H	1.18025773	1.10015339	1.88164753
H	-5.03831812	0.79772414	-0.63398939
H	5.03817798	-0.91082842	0.45821381
H	5.03854261	0.85151785	0.55884749
H	-2.70025774	-0.59009094	2.05666919
H	-3.20369694	0.07083907	-2.16494168
H	-3.20413793	1.83859331	1.14439121
H	2.70008237	-0.77266469	-1.99553305
H	3.20416550	0.26513040	2.14947802
H	2.70033074	2.11373663	0.32929369

Appendix Table 2.27. Computed coordinates of $[Co(tame)_2]^{3+}$ with fixed Co–N bond distances to 57 °C EXAFS (1.9707 Å, see *Tables A2.1 and A2.9*). Total energy: –2109.54796698 Hartrees

Symbol	x	y	z
Co	-0.00002601	0.00074305	0.00055857
N	-1.16688893	-1.54889778	0.34769887
N	-1.16733941	0.47520857	-1.51460612
N	1.16675876	-1.15213634	-1.09166143
N	-1.16810024	1.07590680	1.16807191
N	1.16767954	1.52238978	-0.45167702
N	1.16772835	-0.36794571	1.54454054
C	-4.64682460	-0.00154565	-0.00119689
C	-3.11412683	-0.00082791	-0.00051572
C	-2.60842817	-1.27169381	0.68852041
C	-2.60803758	0.03871999	-1.44557743
C	-2.60969110	1.23131967	0.75641952
C	2.60821662	-0.73969065	-1.24293472
C	3.11427754	-0.00076721	-0.00048792
C	4.64695022	-0.00148864	-0.00069595
C	2.60846886	-0.70707874	1.26107404
C	2.60951949	1.44510545	-0.01941544

H	-1.17864676	-2.12277741	-0.49468067
H	-0.80677893	0.18135110	-2.42188505
H	0.80647093	-1.33571692	-2.02762587
H	-1.18032488	0.63333990	2.08627004
H	1.17922811	1.61357971	-1.46689901
H	0.80765614	-1.08528670	2.17329448
H	-5.03765208	-0.78714590	-0.65084548
H	-5.03866420	-0.17150296	1.00355136
H	5.03852600	0.36689361	-0.95091189
H	-3.20353399	-2.13294357	0.38048083
H	-2.69793646	-0.93916962	-1.92286281
H	-2.70185214	2.13368231	0.14862430
H	3.20324055	-1.63726316	-1.41932402
H	2.69853199	-1.79138387	1.16989326
H	3.20474362	2.04584415	-0.70905859
H	-0.80705120	-2.18569275	1.05802044
H	-1.18119961	1.49184356	-1.58780778
H	1.17882710	-2.07632818	-0.66170068
H	-0.80936177	2.00981834	1.36466970
H	0.80878644	2.42471475	-0.14101085
H	1.18162678	0.46749007	2.12848500
H	-5.03858883	0.95345192	-0.35680223
H	5.03791828	-1.00886567	0.15516446
H	5.03882367	0.63688084	0.79356489
H	-2.70034793	-1.19588617	1.77386806
H	-3.20431575	0.73503032	-2.03755347
H	-3.20537625	1.39429482	1.65606938
H	2.69999732	-0.11896823	-2.13648700
H	3.20491356	-0.41235309	2.12607724
H	2.70222954	1.90901407	0.96463377

Appendix Table 2.28. Computed coordinates of $[Co(tn)_3]^{3+}$ with fixed Co–N bond distances to 13 °C EXAFS (1.9825 Å, see *Tables A2.1 and A2.10*). Total energy: –2071.43715806 Hartrees

Symbol	x	y	z
Co	0.00082394	-0.00002603	-0.09780114
C	-1.67282784	-2.17837128	1.24936642
C	-1.77491496	-2.90315556	-0.07575167
C	-0.45650228	-2.95717548	-0.81567793
C	2.72373640	-0.35588755	1.25023271
C	3.40342413	-0.08269594	-0.07456158
C	2.78952128	1.08354880	-0.81730302
C	-1.05366242	2.53618474	1.24881154
C	-1.63271379	2.98669205	-0.07539859
C	-2.33446143	1.87051619	-0.81725600
H	-2.32720288	-0.32451903	0.73126376
H	0.41907415	1.33548225	1.99310469
H	-1.98804116	0.03629590	-1.61380668
H	-0.95854105	1.14261209	-2.12762713

H	-0.85379547	-2.58105273	1.84953281
H	-2.58662465	-2.30451453	1.83258381
H	-2.09174256	-3.92988912	0.11991995
H	-2.56551387	-2.47155450	-0.70155007
H	0.31912715	-3.38878179	-0.17824541
H	-0.52689688	-3.59751468	-1.69644582
H	2.66029410	0.55557102	1.84890315
H	-1.35844103	-0.30601111	1.99696177
H	3.29070317	-1.08209232	1.83525507
H	4.45033630	0.15869951	0.12176674
H	3.42733950	-0.98422107	-0.69877502
H	2.77380214	1.97243504	-0.18182372
H	3.37933387	1.34169038	-1.69833838
H	-1.80950426	2.02467818	1.84901788
H	-0.70867367	3.39119469	1.83278618
H	-2.36652370	3.77124442	0.12169140
H	-0.86559572	3.45953241	-0.70061152
H	-3.09585915	1.41190671	-0.18150223
H	0.96371313	-1.74425618	-1.61006990
H	-2.85369763	2.25109730	-1.69833702
H	-0.50697896	-1.40254490	-2.12753042
H	1.44978775	-1.85200810	0.72960481
H	0.94638533	-1.02549379	1.99625442
H	1.02889230	1.70249829	-1.61480012
H	1.47028817	0.25694854	-2.12763835
H	0.87830325	2.18373158	0.72399074
N	-1.44260765	-0.70684239	1.06281267
N	0.01216135	-1.59799250	-1.27103737
N	1.33570777	-0.89553023	1.06248588
N	1.37871252	0.80669814	-1.27284486
N	0.10896238	1.60574993	1.05973859
N	-1.38802044	0.78814600	-1.27253716

Appendix Table 2.29. Computed coordinates of $[Co(tn)_3]^{3+}$ with fixed Co–N bond distances to 57 °C EXAFS (1.9910 Å, see *Tables A2.1 and A2.12*). Total energy: –2071.43833732 Hartrees

Symbol	x	y	z
Co	-0.00091913	0.00005460	-0.09993031
C	1.72968398	2.13716024	1.25236300
C	1.85144179	2.86009847	-0.07230998
C	0.53644922	2.94992895	-0.81524822
C	-2.71742800	0.42655991	1.25256303
C	-3.40500936	0.16936571	-0.07155763
C	-2.82267295	-1.01201418	-0.81618102
C	0.98951459	-2.56553382	1.25119378
C	1.55848757	-3.03101633	-0.07235868
C	2.28925096	-1.93460636	-0.81601186
H	2.34132165	0.26906883	0.73050887
H	-0.45779294	-1.33147320	1.99363145

H	1.98946628	-0.09600752	-1.62353816
H	0.93088217	-1.17886382	-2.13045624
H	0.91876822	2.55806185	1.85103449
H	2.64498254	2.24285247	1.83737078
H	2.19439061	3.87812225	0.12486583
H	2.63166053	2.40889669	-0.69730107
H	-0.22950832	3.39928041	-0.17841510
H	0.62603808	3.59136791	-1.69351736
H	-2.67443393	-0.48607554	1.85122464
H	1.37320310	0.27046558	1.99824246
H	-3.26757078	1.16536513	1.83795045
H	-4.45726013	-0.04589608	0.12672119
H	-3.40781805	1.07112552	-0.69585205
H	-2.82586075	-1.90074000	-0.18032877
H	-3.42307162	-1.25584902	-1.69418928
H	1.75661485	-2.07054049	1.85094231
H	0.62567150	-3.41220418	1.83595691
H	2.27228444	-3.83342082	0.12643404
H	0.78040694	-3.48546184	-0.69764691
H	3.05985762	-1.49237972	-0.17978890
H	-0.91269171	1.77637865	-1.61836573
H	2.80144699	-2.33157641	-1.69402653
H	0.55100365	1.39630437	-2.13101869
H	-1.40888765	1.89244371	0.72838000
H	-0.92373748	1.05619792	1.99704980
H	-1.08177060	-1.67342844	-1.62486358
H	-1.48821784	-0.21430680	-2.13037627
H	-0.93346219	-2.16888362	0.72203913
N	1.46708930	0.67173276	1.06530006
N	0.03373440	1.60560892	-1.27677211
N	-1.31810450	0.93461726	1.06436240
N	-1.40824592	-0.77055848	-1.27872162
N	-0.15177676	-1.61004144	1.06144599
N	1.37167413	-0.83135239	-1.27836670

Appendix Table 2.30. Computed coordinates of $[Co(en)_3]^{3+}$ with fixed Co–N bond distances to 13 °C EXAFS (1.9694 Å, see *Tables A2.1 and A2.13*). Total energy: –1953.43347520 Hartrees

Symbol	x	y	z
Co	0.00007964	-0.00016764	0.00031164
C	0.89173474	2.61316490	0.74934824
C	1.93710856	-1.96657225	-0.75055951
C	1.81808218	-2.07805438	0.74955723
H	2.33267589	0.03607462	-1.00890472
H	1.34069901	-0.54747408	-2.11808332
H	-0.20836619	-2.32363484	1.00909271
H	0.44794361	-1.37804768	2.11816861
H	-0.01304352	2.95425925	1.25776881
H	1.71480354	3.23941669	1.09739793

H	1.26909287	-2.66591634	-1.25866368
H	2.94996663	-2.17393474	-1.09966290
H	1.94948155	-3.10385570	1.09776376
H	2.56565918	-1.46460195	1.25776887
H	0.96971114	1.07658492	2.11793816
H	2.11693722	0.98039701	1.00921898
N	1.12140551	1.17432481	1.11460698
N	1.51985922	-0.57045710	-1.11481094
N	0.45704447	-1.55820877	1.11482917
N	-0.26612128	1.60160367	-1.11410483
N	-1.57760981	0.38357793	1.11480421
N	-1.25450187	-1.03166537	-1.11346394
C	0.73478814	2.66094359	-0.75065921
H	-0.19787894	1.43513017	-2.11752539
H	-1.19758324	2.00245317	-1.00684595
C	-2.70964608	-0.53377578	0.74943529
H	-1.90632569	1.34313450	1.00988501
H	-1.41701885	0.30042019	2.11807296
C	-2.67226774	-0.69412936	-0.75040950
H	-1.13604536	-2.03871317	-1.00570662
H	-1.14472574	-0.88993256	-2.11700203
H	1.67416681	2.43263471	-1.25948063
H	0.40747357	3.64181683	-1.09929780
H	-2.55401465	-1.48777875	1.25846218
H	-3.66332902	-0.13301734	1.09679191
H	-3.35815306	-1.46795921	-1.09904477
H	-2.94360960	0.23338406	-1.25982596

Appendix Table 2.31. Computed coordinates of $[Co(en)_3]^{3+}$ with fixed Co–N bond distances to 57 °C EXAFS (1.9714 Å, see *Tables A2.1 and A2.15*). Total energy: –1953.43280799 Hartree

Symbol	x	y	z
Co	0.00019508	0.00004906	0.00060861
C	2.75615827	0.19294588	0.74938480
C	-1.06182947	-2.54904138	-0.75088589
C	-1.21193373	-2.48274823	0.74925518
H	0.93861878	-2.13851295	-1.00506315
H	0.01928172	-1.45134510	-2.11780278
H	-2.22332871	-0.70966434	1.00992409
H	-1.09728881	-0.94900061	2.11899024
H	2.71984672	1.15957439	1.25716555
H	3.65296814	-0.32234108	1.09726475
H	-1.96485164	-2.20381558	-1.25968768
H	-0.86092912	-3.56328343	-1.09985472
H	-2.10707252	-3.00122634	1.09666328
H	-0.35720846	-2.93496034	1.25762390
H	1.37091940	-0.47430937	2.11939392
H	1.72702692	-1.56974655	1.01095750
N	1.51975921	-0.57689452	1.11613569

N	0.06469696	-1.62455438	-1.11422003
N	-1.26005644	-1.02695564	1.11567238
N	1.37489372	0.86744891	-1.11481097
N	-0.25994628	1.60522255	1.11509697
N	-1.43824840	0.75621346	-1.11538221
C	2.73877837	0.35477460	-0.75085231
H	1.24780399	0.74021766	-2.11825263
H	1.38301300	1.88137356	-1.00699630
C	-1.54567948	2.28972792	0.74914383
H	0.49539222	2.28187817	1.00844047
H	-0.27296466	1.42592823	2.11854793
C	-1.67751974	2.19355820	-0.75105813
H	-2.32006227	0.25548143	-1.00845364
H	-1.26365264	0.71020521	-2.11868480
H	2.89146450	-0.60028826	-1.25885022
H	3.51666532	1.03568240	-1.10024273
H	-2.36384022	1.77411307	1.25732587
H	-1.54868110	3.32398979	1.09715355
H	-2.65649283	2.52592546	-1.10025295
H	-0.92743153	2.80413543	-1.25910970

Appendix Table 2.32. Computed coordinates of $[Co(NH_3)_6]^{3+}$ with fixed Co–N bond distances to 13 °C EXAFS (1.9588 Å, see *Tables A2.1 and A2.18*). Total energy: –1721.20216299 Hartrees

Symbol	x	y	z
Co	-0.00001889	-0.00000617	0.00000120
N	1.23807732	-0.97098441	1.16669648
H	1.78259482	-0.38630969	1.80596446
H	1.95122903	-1.51101564	0.66940526
H	0.80542103	-1.66177330	1.78498900
N	0.48552315	1.68448014	0.87385107
H	-0.13871341	2.47064657	0.67567895
H	1.41090659	2.04586543	0.62854990
H	0.50636052	1.64558130	1.89636500
N	1.45610061	0.26386165	-1.28333376
H	1.40732521	1.13128276	-1.82367941
H	1.54365264	-0.46044526	-2.00069314
H	2.38872844	0.29887086	-0.86326792
N	-1.45607156	-0.26407391	1.28337085
H	-1.54303461	0.45957597	2.00146542
H	-1.40769501	-1.13206783	1.82283516
H	-2.38881729	-0.29815387	0.86349021
N	-0.48575199	-1.68446668	-0.87379222
H	-1.41128750	-2.04555103	-0.62862450
H	0.13820269	-2.47080410	-0.67541439
H	-0.50639798	-1.64569411	-1.89631437
N	-1.23784637	0.97119472	-1.16679388
H	-1.95280266	1.50897871	-0.66965982
H	-1.78018484	0.38702110	-1.80836607

H	-0.80519576	1.66407819	-1.78274598

Appendix Table 2.33. Computed coordinates of $[Co(NH_3)_6]^{3+}$ with fixed Co–N bond distances to 57 °C EXAFS (1.9836 Å, see *Tables A2.1 and A2.18*). Total energy: –1721.20581740 Hartrees

Symbol	x	y	z
Co	-0.00001858	-0.00000606	0.00000108
N	1.25528531	-0.98001056	1.18253798
H	1.79618280	-0.39028822	1.81965342
H	1.96775020	-1.51763193	0.68243655
H	0.81976929	-1.66965194	1.79950325
N	0.48825966	1.70738106	0.88374524
H	-0.13978910	2.48919903	0.68231310
H	1.41321450	2.06683318	0.63553956
H	0.50797699	1.66530460	1.90578106
N	1.47425987	0.26890645	-1.29952933
H	1.42010076	1.13652956	-1.83834885
H	1.55941632	-0.45768724	-2.01434132
H	2.40475989	0.30520960	-0.87578829
N	-1.47422984	-0.26911947	1.29956613
H	-1.55879797	0.45682296	2.01511003
H	-1.42046935	-1.13731304	1.83750919
H	-2.40484908	-0.30449342	0.87600825
N	-0.48849026	-1.70736782	-0.88368519
H	-1.41360399	-2.06650961	-0.63562506
H	0.13926809	-2.48936149	-0.68203356
H	-0.50799950	-1.66542261	-1.90572992
N	-1.25505345	0.98022185	-1.18263617
H	-1.96931892	1.51559278	-0.68269019
H	-1.79377643	0.39099630	-1.82204745
H	-0.81955193	1.67195456	-1.79726960

APPENDIX 3: Supporting Information for Chapter 4

Appendix Table 3.1. Temperature-specific T_2* dephasing times for **1**–**6** from 10–60 °C. Values were determined from full-width half-max (FWHM) linewidth analysis of 1D ^{59}Co NMR spectra.

	T_2* (ms)				T_2* (μs)	
T (°C)	1	2	3	4	5	6
10	6.00	2.16	2.93	1.41	240	170
20	9.76	2.02	3.21	1.77	312	242
30	10.57	1.83	3.07	1.93	387	320
40	7.58	1.70	2.61	1.98	471	405
50	5.53	1.57	2.25	1.83	560	492
60	3.73	1.43	1.87	1.65	626	566

Appendix Table 3.2. Arrhenius analysis of **1**–**6**. Linearity is determined from evaluations of R^2 values with error in slope and intercept values. Activation energy, E_a (kJ/mol) is calculated from the slope of ln(T_1) vs $1/T$ (10^3 K^{-1}) plots (see *Figure 4.5*, Chapter 4).

	1	2	3	4	5	6
R^2	0.9138	0.9131	0.9953	0.9988	0.9964	0.9997
Slope	-0.7(1)	-0.66(9)	-1.98(6)	-2.4(4)	-2.12(6)	-1.79(1)
Intercept	2.3(2)	2.0(3)	6.0(2)	7.5(1)	6.4(2)	5.37(5)
E_a (kJ/mol)	6.2(8)	5.5(8)	16.4(5)	20.6(3)	17.6(5)	14.9(1)

Appendix Table 3.3. Calculated correlation times of **2**–**6** from 10–60 °C. Values of correlation times, τ_c are determined using Eq. 3 detailed in *Section 4.3.5*, Chapter 4.

	τ_c (10^{-12} s)				
T (°C)	**2**	**3**	**4**	**5**	**6**
10	17.35	68.37	1150	153.25	190.31
20	14.63	52.34	891.31	115.58	152.26
30	13.19	42.03	722.32	88.69	124.83
40	12.15	34.35	610.67	72.49	103.29
50	11.57	28.87	526.34	60.2	87.53
60	11.32	25.21	488.02	49.47	74.61

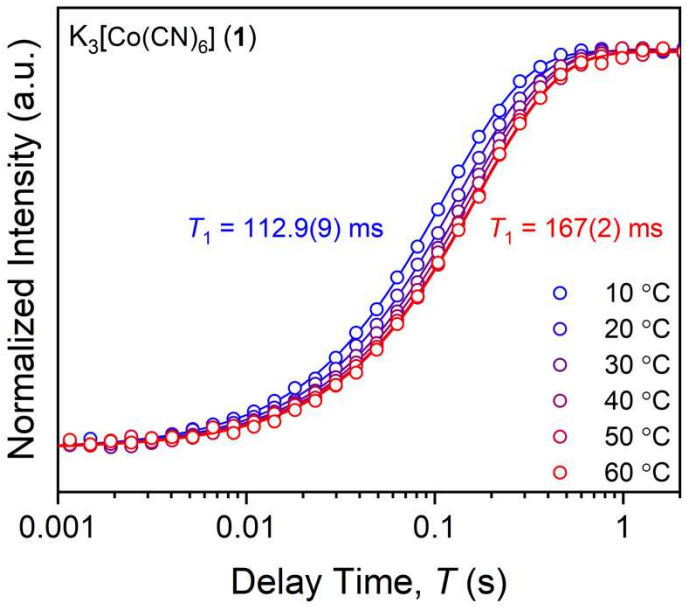

Appendix Figure 3.1. Variable temperature inversion recovery of complex **1** over a 10–60 °C temperature range at 30 mM concentration. Inversion recovery data (*circles*) are fit to relaxation curves (*lines*) to parameterize T_1 over a range of 112.9(9) to 167(2) ms with temperature.

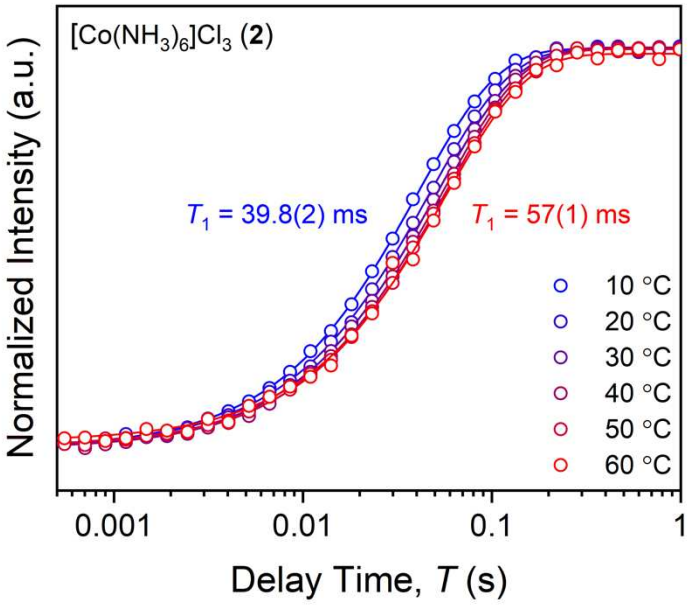

Appendix Figure 3.2. Variable temperature inversion recovery of complex **2** over a 10–60 °C temperature range at 30 mM concentration. Inversion recovery data (*circles*) are fit to relaxation curves (*lines*) to parameterize T_1 over a range of 39.8(2) to 57(1) ms with temperature.

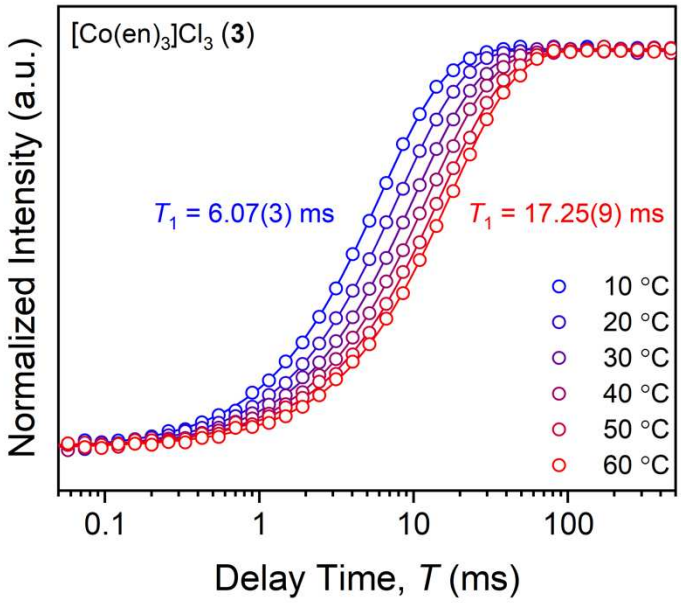

Appendix Figure 3.3. Variable temperature inversion recovery of complex **3** over a 10–60 °C temperature range at 30 mM concentration. Inversion recovery data (*circles*) are fit to relaxation curves (*lines*) to parameterize T_1 over a range of 6.07(3) to 17.25(9) ms with temperature.

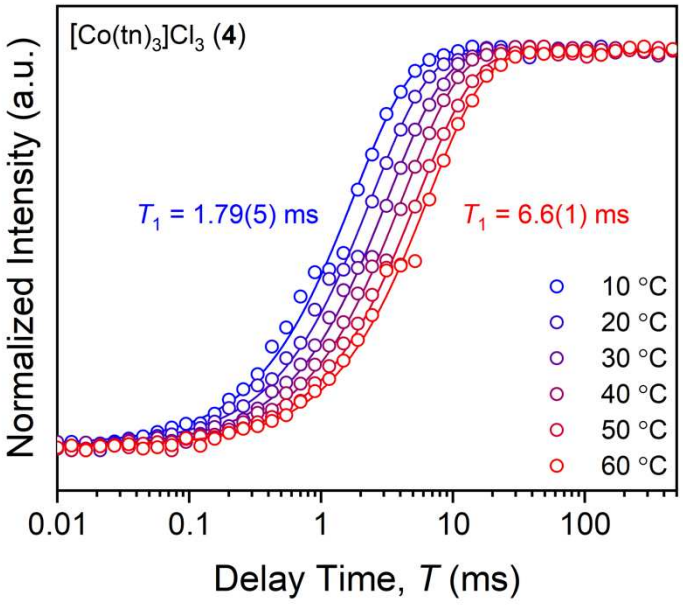

Appendix Figure 3.4. Variable temperature inversion recovery of complex **4** over a 10–60 °C temperature range at 30 mM concentration. Inversion recovery data (*circles*) are fit to relaxation curves (*lines*) to parameterize T_1 over a range of 1.79(5) to 6.6(1) ms with temperature.

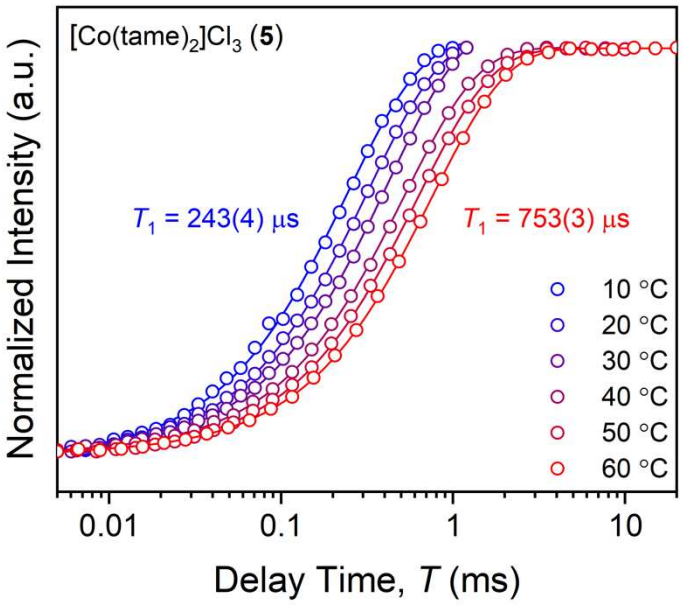

Appendix Figure 3.5. Variable temperature inversion recovery of complex **5** over a 10–60 °C temperature range at 30 mM concentration. Inversion recovery data (*circles*) are fit to relaxation curves (*lines*) to parameterize T_1 over a range of 243(4) to 753(3) µs with temperature.

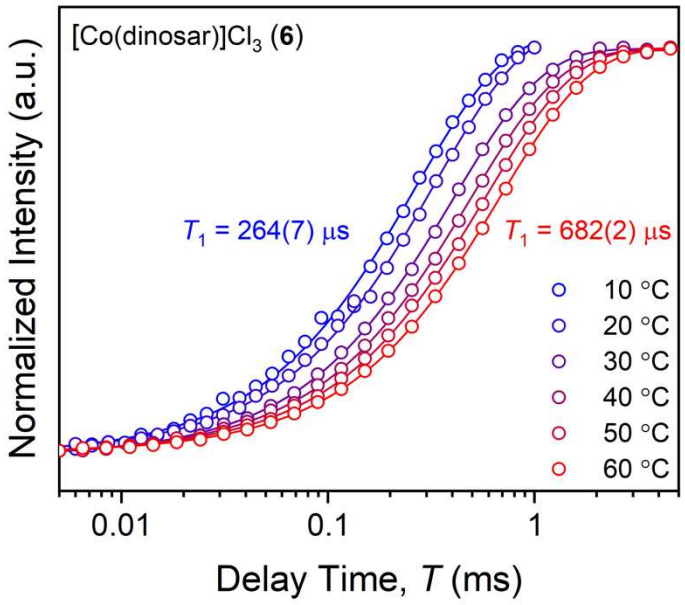

Appendix Figure 3.6. Variable temperature inversion recovery of complex **6** over a 10–60 °C temperature range at 30 mM concentration. Inversion recovery data (*circles*) are fit to relaxation curves (*lines*) to parameterize T_1 over a range of 264(7) to 682(2) μs with temperature.

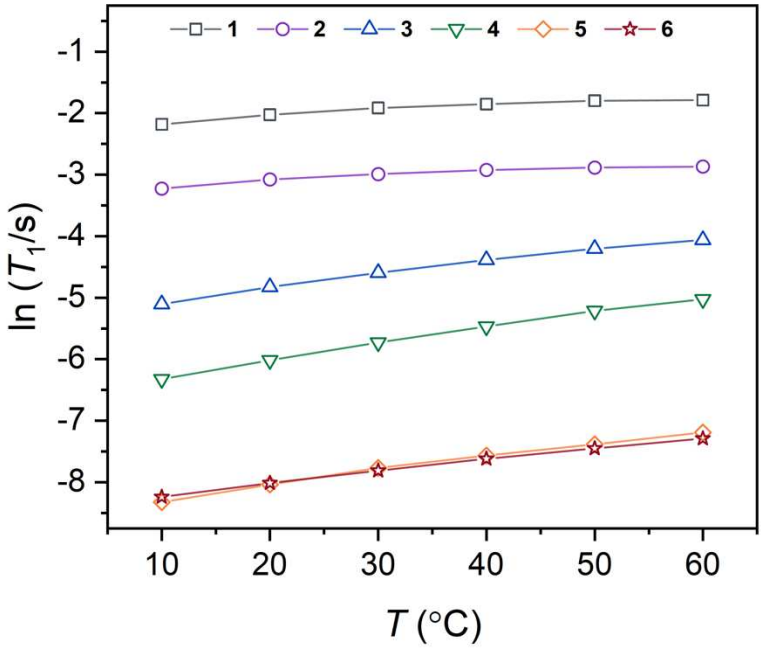

Appendix Figure 3.7. Variable temperature trends of $ln(T_1/s)$ vs. T (°C) from fitted T_1 values. Colored traces are guides for the eye.

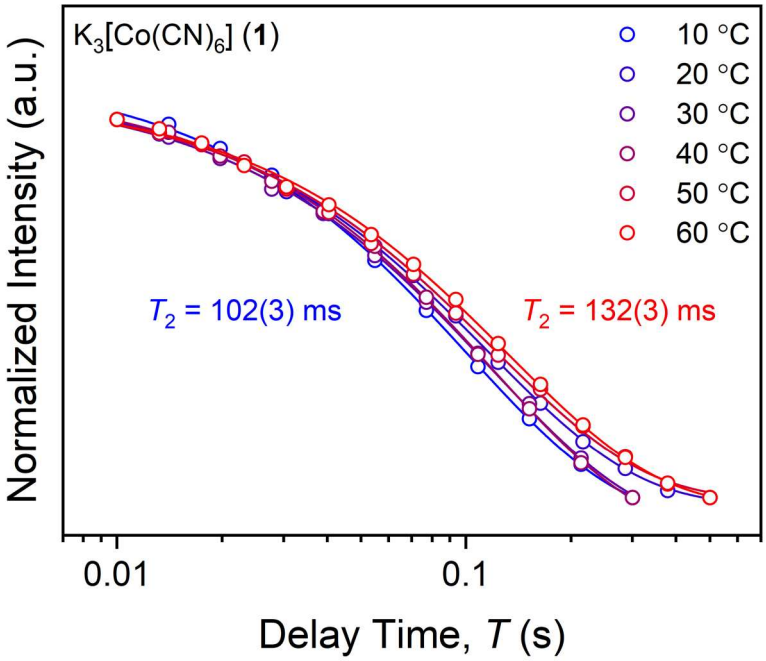

Appendix Figure 3.8. Variable temperature CPMG data of complex **1** over a 10–60 °C temperature range at 30 mM concentration. CPMG data (*circles*) are fit to relaxation curves (*lines*) to parameterize T_2 over a range of 102(3) to 132(3) ms with temperature.

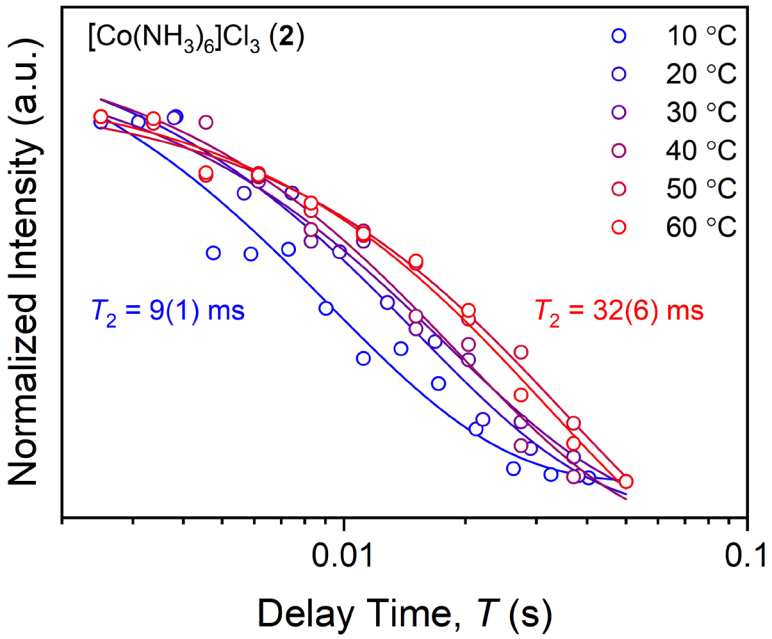

Appendix Figure 3.9. Variable temperature CPMG data of complex **2** over a 10–60 °C temperature range at 30 mM concentration. CPMG data (circles) are fit to relaxation curves (lines) to parameterize T_2 over a range of 9(1) to 32(6) ms with temperature.

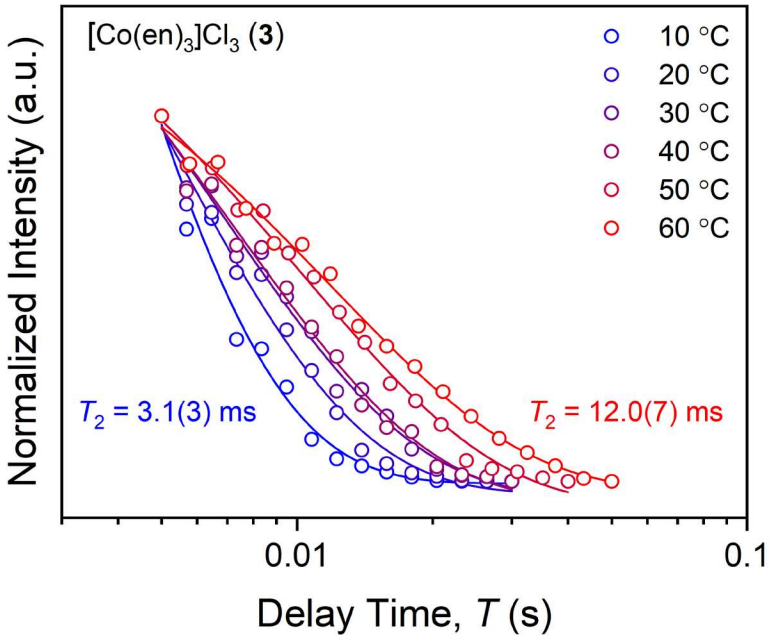

Appendix Figure 3.10. Variable temperature CPMG data of complex **3** over a 10–60 °C temperature range at 30 mM concentration. CPMG data (*circles*) are fit to relaxation curves (*lines*) to parameterize T_2 over a range of 3.1(3) to 12.0(7) ms with temperature.

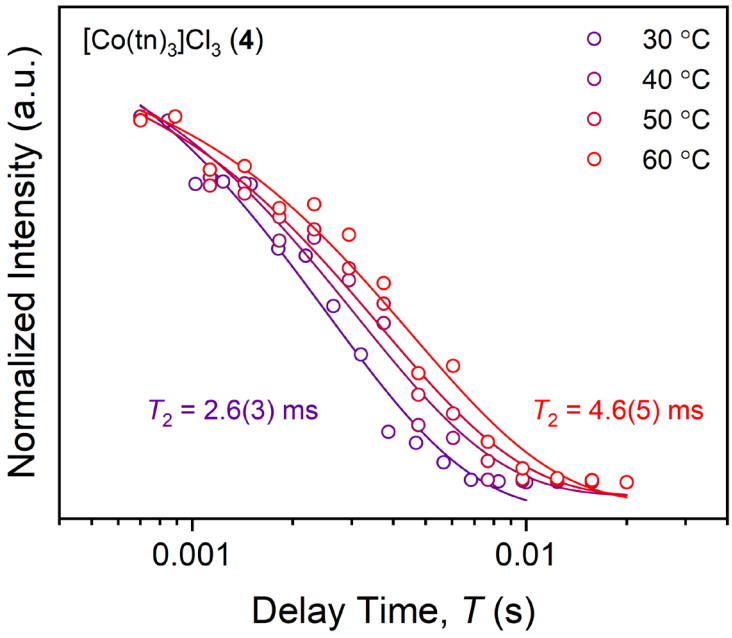

Appendix Figure 3.11. Variable temperature CPMG data of complex **4** over a 30–60 °C temperature range at 30 mM concentration. CPMG data (*circles*) are fit to relaxation curves (*lines*) to parameterize T_2 over a range of 2.6(3) to 4.6(5) ms with temperature.

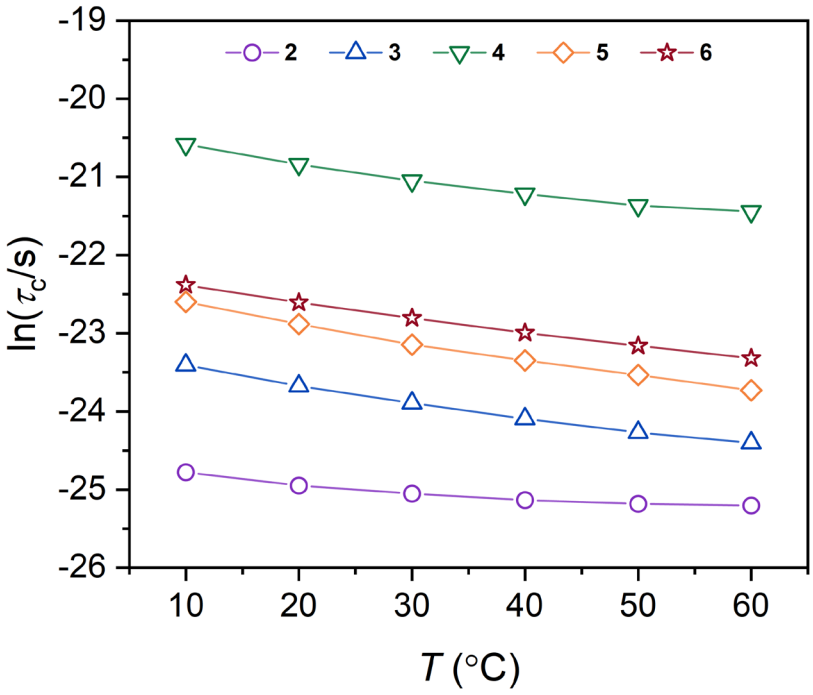

Appendix Figure 3.12. Variable-temperature correlation time, τ_c (s) trends on a logarithmic scale. Traces are guides for the eye. Calculated from values of τ_c are compiled in Table A3.3, determined via Eq. 3 from *Section 4.3.5*, Chapter 4.

Appendix Table 3.4. Computed coordinates of $[Co(en)_3]Cl_3$ (**3**) with fixed Co–N_6 bond distances from previous 13 °C EXAFS data (1.9694(5) Å). Total energy: –1953.43347520 Hartrees

Symbol	x	y	z
Co	0.00007964	-0.00016764	0.00031164
C	0.89173474	2.61316490	0.74934824
C	1.93710856	-1.96657225	-0.75055951
C	1.81808218	-2.07805438	0.74955723
H	2.33267589	0.03607462	-1.00890472
H	1.34069901	-0.54747408	-2.11808332
H	-0.20836619	-2.32363484	1.00909271
H	0.44794361	-1.37804768	2.11816861
H	-0.01304352	2.95425925	1.25776881
H	1.71480354	3.23941669	1.09739793
H	1.26909287	-2.66591634	-1.25866368
H	2.94996663	-2.17393474	-1.09966290
H	1.94948155	-3.10385570	1.09776376
H	2.56565918	-1.46460195	1.25776887
H	0.96971114	1.07658492	2.11793816
H	2.11693722	0.98039701	1.00921898
N	1.12140551	1.17432481	1.11460698
N	1.51985922	-0.57045710	-1.11481094
N	0.45704447	-1.55820877	1.11482917

N	-0.26612128	1.60160367	-1.11410483
N	-1.57760981	0.38357793	1.11480421
N	-1.25450187	-1.03166537	-1.11346394
C	0.73478814	2.66094359	-0.75065921
H	-0.19787894	1.43513017	-2.11752539
H	-1.19758324	2.00245317	-1.00684595
C	-2.70964608	-0.53377578	0.74943529
H	-1.90632569	1.34313450	1.00988501
H	-1.41701885	0.30042019	2.11807296
C	-2.67226774	-0.69412936	-0.75040950
H	-1.13604536	-2.03871317	-1.00570662
H	-1.14472574	-0.88993256	-2.11700203
H	1.67416681	2.43263471	-1.25948063
H	0.40747357	3.64181683	-1.09929780
H	-2.55401465	-1.48777875	1.25846218
H	-3.66332902	-0.13301734	1.09679191
H	-3.35815306	-1.46795921	-1.09904477
H	-2.94360960	0.23338406	-1.25982596

Appendix Table 3.5. Computed coordinates of $[Co(en)_3]Cl_3$ (**3**) with fixed Co–N_6 bond distances from previous 35 °C EXAFS data (1.9706(5) Å). Total energy: –1953.43368251 Hartrees

Symbol	x	y	z
Co	0.00000706	-0.00017152	0.00025222
C	0.17550713	2.75683253	0.74935382
C	2.38563166	-1.39131003	-0.75053436
C	2.29979109	-1.53002972	0.74974107
H	2.24330749	0.64527030	-1.00868895
H	1.43962576	-0.17722466	-2.11855791
H	0.40858394	-2.29819727	1.01004048
H	0.79447600	-1.21395733	2.11887920
H	-0.78716014	2.84885788	1.25759261
H	0.80590603	3.57659474	1.09772468
H	1.92416563	-2.24122598	-1.25861146
H	3.41739483	-1.32578378	-1.09974342
H	2.69488947	-2.48558464	1.09842992
H	2.86051377	-0.74195370	1.25768552
H	0.65418695	1.29511874	2.11840133
H	1.78605569	1.50277484	1.00940050
N	0.77442288	1.42856948	1.11481230
N	1.61749119	-0.15289548	-1.11495421
N	0.84997475	-1.38489635	1.11531141
N	-0.67647665	1.47713777	-1.11473294
N	-1.62412082	-0.04348867	1.11541907
N	-0.94132988	-1.32474338	-1.11449397
C	0.01216318	2.76161311	-0.75089377
H	-0.56689621	1.33505808	-2.11836161
H	-1.68054904	1.62028078	-1.00819176
C	-2.47512458	-1.22617111	0.75002811

H	-2.19400901	0.79568171	1.01036858
H	-1.44811812	-0.08114875	2.11893271
C	-2.39798108	-1.36996842	-0.75022530
H	-0.56360930	-2.26599225	-1.00767669
H	-0.87319502	-1.15919385	-2.11818921
H	0.97882745	2.78674451	-1.25923512
H	-0.56051345	3.62231871	-1.10018432
H	-2.07324124	-2.10590020	1.25805086
H	-3.50017578	-1.09014548	1.09864615
H	-2.85742396	-2.29612616	-1.09938277
H	-2.90288705	-0.54521676	-1.25848813

Appendix Table 3.6. Computed coordinates of $[Co(en)_3]Cl_3$ (**3**) with fixed Co–N_6 bond distances from previous 57 °C EXAFS data (1.9714(5) Å). Total energy: –1953.43280799 Hartrees

Symbol	x	y	z
Co	0.00019508	0.00004906	0.00060861
C	2.75615827	0.19294588	0.74938480
C	-1.06182947	-2.54904138	-0.75088589
C	-1.21193373	-2.48274823	0.74925518
H	0.93861878	-2.13851295	-1.00506315
H	0.01928172	-1.45134510	-2.11780278
H	-2.22332871	-0.70966434	1.00992409
H	-1.09728881	-0.94900061	2.11899024
H	2.71984672	1.15957439	1.25716555
H	3.65296814	-0.32234108	1.09726475
H	-1.96485164	-2.20381558	-1.25968768
H	-0.86092912	-3.56328343	-1.09985472
H	-2.10707252	-3.00122634	1.09666328
H	-0.35720846	-2.93496034	1.25762390
H	1.37091940	-0.47430937	2.11939392
H	1.72702692	-1.56974655	1.01095750
N	1.51975921	-0.57689452	1.11613569
N	0.06469696	-1.62455438	-1.11422003
N	-1.26005644	-1.02695564	1.11567238
N	1.37489372	0.86744891	-1.11481097
N	-0.25994628	1.60522255	1.11509697
N	-1.43824840	0.75621346	-1.11538221
C	2.73877837	0.35477460	-0.75085231
H	1.24780399	0.74021766	-2.11825263
H	1.38301300	1.88137356	-1.00699630
C	-1.54567948	2.28972792	0.74914383
H	0.49539222	2.28187817	1.00844047
H	-0.27296466	1.42592823	2.11854793
C	-1.67751974	2.19355820	-0.75105813
H	-2.32006227	0.25548143	-1.00845364
H	-1.26365264	0.71020521	-2.11868480
H	2.89146450	-0.60028826	-1.25885022
H	3.51666532	1.03568240	-1.10024273
H	-2.36384022	1.77411307	1.25732587

H	-1.54868110	3.32398979	1.09715355
H	-2.65649283	2.52592546	-1.10025295
H	-0.92743153	2.80413543	-1.25910970

Appendix Table 3.7. Computed coordinates of $[Co(tn)_3]Cl_3$ (**4**) with fixed Co–N_6 bond distances from previous 13 °C EXAFS data (1.9825(5) Å). Total energy: –2071.43715806 Hartrees

Symbol	x	y	z
Co	0.00082394	-0.00002603	-0.09780114
C	-1.67282784	-2.17837128	1.24936642
C	-1.77491496	-2.90315556	-0.07575167
C	-0.45650228	-2.95717548	-0.81567793
C	2.72373640	-0.35588755	1.25023271
C	3.40342413	-0.08269594	-0.07456158
C	2.78952128	1.08354880	-0.81730302
C	-1.05366242	2.53618474	1.24881154
C	-1.63271379	2.98669205	-0.07539859
C	-2.33446143	1.87051619	-0.81725600
H	-2.32720288	-0.32451903	0.73126376
H	0.41907415	1.33548225	1.99310469
H	-1.98804116	0.03629590	-1.61380668
H	-0.95854105	1.14261209	-2.12762713
H	-0.85379547	-2.58105273	1.84953281
H	-2.58662465	-2.30451453	1.83258381
H	-2.09174256	-3.92988912	0.11991995
H	-2.56551387	-2.47155450	-0.70155007
H	0.31912715	-3.38878179	-0.17824541
H	-0.52689688	-3.59751468	-1.69644582
H	2.66029410	0.55557102	1.84890315
H	-1.35844103	-0.30601111	1.99696177
H	3.29070317	-1.08209232	1.83525507
H	4.45033630	0.15869951	0.12176674
H	3.42733950	-0.98422107	-0.69877502
H	2.77380214	1.97243504	-0.18182372
H	3.37933387	1.34169038	-1.69833838
H	-1.80950426	2.02467818	1.84901788
H	-0.70867367	3.39119469	1.83278618
H	-2.36652370	3.77124442	0.12169140
H	-0.86559572	3.45953241	-0.70061152
H	-3.09585915	1.41190671	-0.18150223
H	0.96371313	-1.74425618	-1.61006990
H	-2.85369763	2.25109730	-1.69833702
H	-0.50697896	-1.40254490	-2.12753042
H	1.44978775	-1.85200810	0.72960481
H	0.94638533	-1.02549379	1.99625442
H	1.02889230	1.70249829	-1.61480012
H	1.47028817	0.25694854	-2.12763835
H	0.87830325	2.18373158	0.72399074
N	-1.44260765	-0.70684239	1.06281267

N	0.01216135	-1.59799250	-1.27103737
N	1.33570777	-0.89553023	1.06248588
N	1.37871252	0.80669814	-1.27284486
N	0.10896238	1.60574993	1.05973859
N	-1.38802044	0.78814600	-1.27253716

Appendix Table 3.8. Computed coordinates of $[Co(tn)_3]Cl_3$ (**4**) with fixed Co–N_6 bond distances from previous 35 °C EXAFS data (1.9881(5) Å). Total energy: –2071.43959515 Hartrees

Symbol	x	y	z
Co	-0.00047770	0.00001042	-0.09864853
C	1.65713891	2.19355690	1.25071602
C	1.75385978	2.91927955	-0.07445244
C	0.43591109	2.96392578	-0.81621854
C	-2.72902004	0.33678225	1.25098215
C	-3.40625076	0.05731522	-0.07392494
C	-2.78482696	-1.10512844	-0.81670927
C	1.07321152	-2.53103862	1.25032354
C	1.65492809	-2.97724353	-0.07429306
C	2.35008781	-1.85720121	-0.81687628
H	2.32936170	0.34598104	0.73108147
H	-0.40870314	-1.34150001	1.99578641
H	1.99210579	-0.02637329	-1.61780756
H	0.96964749	-1.14077050	-2.12993827
H	0.83344980	2.58814275	1.84990310
H	2.56899456	2.32917067	1.83490344
H	2.06242557	3.94842113	0.12179462
H	2.54843360	2.49421810	-0.69968032
H	-0.34406204	3.38821371	-0.17916260
H	0.50278324	3.60664848	-1.69555684
H	-2.65777072	-0.57387020	1.84999143
H	1.36138157	0.31739414	1.99816940
H	-3.30286161	1.05798436	1.83554743
H	-4.45133673	-0.19154465	0.12282760
H	-3.43704034	0.95823808	-0.69869428
H	-2.76093158	-1.99321373	-0.18037356
H	-3.37494251	-1.36864382	-1.69598996
H	1.82530377	-2.01304023	1.84968466
H	0.73625957	-3.38897494	1.83476756
H	2.39368341	-3.75715564	0.12274859
H	0.89079902	-3.45509497	-0.69936497
H	3.10711245	-1.39222022	-0.18055386
H	-0.97395352	1.74113529	-1.61519611
H	2.87354086	-2.23603489	-1.69624913
H	0.50081316	1.41056284	-2.13018196
H	-1.46708545	1.84374346	0.72970512
H	-0.95704180	1.02171084	1.99752871
H	-1.02098006	-1.71146317	-1.61827077
H	-1.47390793	-0.26836428	-2.12982665

H	-0.86243109	-2.19380974	0.72650076
N	1.44202919	0.72015104	1.06458556
N	-0.02172985	1.60257226	-1.27503540
N	-1.34611266	0.88867714	1.06414130
N	-1.37761739	-0.81858090	-1.27590666
N	-0.09714474	-1.61075224	1.06266165
N	1.39766321	-0.78224721	-1.27585590

Appendix Table 3.9. Computed coordinates of $[Co(tn)_3]Cl_3$ (**4**) with fixed Co–N_6 bond distances from previous 57 °C EXAFS data (1.9910(5) Å). Total energy: –2071.43833732 Hartrees

Symbol	x	y	z
Co	-0.00091913	0.00005460	-0.09993031
C	1.72968398	2.13716024	1.25236300
C	1.85144179	2.86009847	-0.07230998
C	0.53644922	2.94992895	-0.81524822
C	-2.71742800	0.42655991	1.25256303
C	-3.40500936	0.16936571	-0.07155763
C	-2.82267295	-1.01201418	-0.81618102
C	0.98951459	-2.56553382	1.25119378
C	1.55848757	-3.03101633	-0.07235868
C	2.28925096	-1.93460636	-0.81601186
H	2.34132165	0.26906883	0.73050887
H	-0.45779294	-1.33147320	1.99363145
H	1.98946628	-0.09600752	-1.62353816
H	0.93088217	-1.17886382	-2.13045624
H	0.91876822	2.55806185	1.85103449
H	2.64498254	2.24285247	1.83737078
H	2.19439061	3.87812225	0.12486583
H	2.63166053	2.40889669	-0.69730107
H	-0.22950832	3.39928041	-0.17841510
H	0.62603808	3.59136791	-1.69351736
H	-2.67443393	-0.48607554	1.85122464
H	1.37320310	0.27046558	1.99824246
H	-3.26757078	1.16536513	1.83795045
H	-4.45726013	-0.04589608	0.12672119
H	-3.40781805	1.07112552	-0.69585205
H	-2.82586075	-1.90074000	-0.18032877
H	-3.42307162	-1.25584902	-1.69418928
H	1.75661485	-2.07054049	1.85094231
H	0.62567150	-3.41220418	1.83595691
H	2.27228444	-3.83342082	0.12643404
H	0.78040694	-3.48546184	-0.69764691
H	3.05985762	-1.49237972	-0.17978890
H	-0.91269171	1.77637865	-1.61836573
H	2.80144699	-2.33157641	-1.69402653
H	0.55100365	1.39630437	-2.13101869
H	-1.40888765	1.89244371	0.72838000
H	-0.92373748	1.05619792	1.99704980

H	-1.08177060	-1.67342844	-1.62486358
H	-1.48821784	-0.21430680	-2.13037627
H	-0.93346219	-2.16888362	0.72203913
N	1.46708930	0.67173276	1.06530006
N	0.03373440	1.60560892	-1.27677211
N	-1.31810450	0.93461726	1.06436240
N	-1.40824592	-0.77055848	-1.27872162
N	-0.15177676	-1.61004144	1.06144599
N	1.37167413	-0.83135239	-1.27836670

Appendix Table 3.10. Computed coordinates of $[Co(tame)_2]Cl_3$ (**5**) with fixed Co–N_6 bond distances from previous 13 °C EXAFS data (1.9700(5) Å). Total energy: –2109.54797542 Hartrees

Symbol	x	y	z
Co	-0.00000347	0.00026855	0.00013800
N	-1.16688756	-1.36565803	0.80857250
N	-1.16696618	-0.01657170	-1.58695199
N	1.16676891	-1.43273672	-0.68256134
N	-1.16734922	1.38306928	0.77866627
N	1.16708267	1.30778504	-0.89944564
N	1.16729811	0.12585389	1.58209106
C	-4.64680352	-0.00048948	-0.00030824
C	-3.11426948	-0.00032950	-0.00007533
C	-2.60840971	-0.99667970	1.04747613
C	-2.60810793	-0.40917475	-1.38666869
C	-2.60868229	1.40509670	0.33918814
C	2.60826729	-1.08671343	-0.95383579
C	3.11426447	-0.00023486	-0.00017904
C	4.64681594	-0.00052409	-0.00019484
C	2.60847624	-0.28292936	1.41761373
C	2.60857697	1.36906715	-0.46396050
H	-1.17927408	-2.17178325	0.18471381
H	-0.80696977	-0.57782351	-2.35828537
H	0.80665405	-1.89602002	-1.51638867
H	-1.17997696	1.24590158	1.78872434
H	1.17923630	1.08134022	-1.89329024
H	0.80760127	-0.36408281	2.40072487
H	-5.03823579	-0.94835206	-0.37485339
H	-5.03853196	0.14911460	1.00771240
H	5.03838498	0.05747337	-1.01767911
H	-3.20353192	-1.91097901	1.02017900
H	-2.69895608	-1.48658235	-1.53877537
H	-2.70038243	2.07558247	-0.51769056
H	3.20329668	-1.99490842	-0.84440876
H	2.69952799	-1.34231745	1.66583596
H	3.20387882	1.72857178	-1.30491224
H	-0.80689062	-1.75209423	1.68070945
H	-1.17997355	0.92696462	-1.97264836
H	1.17920999	-2.17956753	0.01117579

H	-0.80782756	2.33182585	0.67758156
H	0.80731307	2.26165035	-0.88315728
H	1.18025773	1.10015339	1.88164753
H	-5.03831812	0.79772414	-0.63398939
H	5.03817798	-0.91082842	0.45821381
H	5.03854261	0.85151785	0.55884749
H	-2.70025774	-0.59009094	2.05666919
H	-3.20369694	0.07083907	-2.16494168
H	-3.20413793	1.83859331	1.14439121
H	2.70008237	-0.77266469	-1.99553305
H	3.20416550	0.26513040	2.14947802
H	2.70033074	2.11373663	0.32929369

Appendix Table 3.11. Computed coordinates of $[Co(tame)_2]Cl_3$ (**5**) with fixed Co–N_6 bond distances from previous 35 °C EXAFS data (1.9698(5) Å). Total energy: –2109.54887608 Hartrees

Symbol	x	y	z
Co	0.00000097	0.00072136	0.00018597
N	1.16625438	-1.22688610	-1.00626598
N	1.16706731	-0.25646809	1.56604750
N	-1.16624230	-1.51940555	0.45757358
N	1.16720556	1.48542682	-0.55963163
N	-1.16738390	1.15656640	1.08708403
N	-1.16692513	0.36488948	-1.54441032
C	4.64678658	-0.00140353	-0.00003446
C	3.11409782	-0.00066163	-0.00015564
C	2.60797535	-0.82642351	-1.18663075
C	2.60798268	-0.61506824	1.30837059
C	2.60890918	1.44005620	-0.12221780
C	-2.60776433	-1.21883315	0.77835707
C	-3.11410115	-0.00088924	-0.00010227
C	-4.64675639	-0.00149225	-0.00045140
C	-2.60790341	-0.06516864	-1.44429970
C	-2.60922217	1.28237159	0.66614310
H	1.17854770	-2.11848127	-0.51214917
H	0.80706155	-0.92708393	2.24452801
H	-0.80616597	-2.10404511	1.21135349
H	1.17970409	1.50323728	-1.57882998
H	-1.17949465	0.78235538	2.03525345
H	-0.80684594	0.00634557	-2.42840392
H	5.03775152	-0.99517605	0.22693691
H	5.03862902	0.29865023	-0.97387286
H	-5.03844289	-0.09854110	1.01398610
H	3.20256966	-1.73460406	-1.29832066
H	2.69820354	-1.70313731	1.29520854
H	2.70091450	1.97310264	0.82626181
H	-3.20254208	-2.10025785	0.53312317
H	-2.69827228	-1.07460599	-1.85058157
H	-3.20437046	1.50962570	1.55212015

H	0.80634568	-1.47660876	-1.92699805
H	1.18112734	0.61833775	2.08925675
H	-1.17878072	-2.15234719	-0.34146388
H	0.80831522	2.40808577	-0.31560748
H	-0.80865173	2.10236077	1.21524170
H	-1.18094868	1.37357461	-1.69148136
H	5.03857955	0.69164267	0.74703192
H	-5.03784634	-0.83178717	-0.59171792
H	-5.03856541	0.92541617	-0.42386462
H	2.69987786	-0.27151409	-2.12247784
H	3.20370959	-0.25895001	2.15045728
H	3.20413306	1.99038595	-0.85273026
H	-2.69920955	-1.06551568	1.85554883
H	-3.20355929	0.58743209	-2.08471047
H	-2.70165623	2.13883980	-0.00477191

Appendix Table 3.12. Computed coordinates of $[Co(tame)_2]Cl_3$ (**5**) with fixed Co–N_6 bond distances from previous 57 °C EXAFS data (1.9707(5) Å). Total energy: –2109.54796698 Hartrees

Symbol	x	y	z
Co	-0.00002601	0.00074305	0.00055857
N	-1.16688893	-1.54889778	0.34769887
N	-1.16733941	0.47520857	-1.51460612
N	1.16675876	-1.15213634	-1.09166143
N	-1.16810024	1.07590680	1.16807191
N	1.16767954	1.52238978	-0.45167702
N	1.16772835	-0.36794571	1.54454054
C	-4.64682460	-0.00154565	-0.00119689
C	-3.11412683	-0.00082791	-0.00051572
C	-2.60842817	-1.27169381	0.68852041
C	-2.60803758	0.03871999	-1.44557743
C	-2.60969110	1.23131967	0.75641952
C	2.60821662	-0.73969065	-1.24293472
C	3.11427754	-0.00076721	-0.00048792
C	4.64695022	-0.00148864	-0.00069595
C	2.60846886	-0.70707874	1.26107404
C	2.60951949	1.44510545	-0.01941544
H	-1.17864676	-2.12277741	-0.49468067
H	-0.80677893	0.18135110	-2.42188505
H	0.80647093	-1.33571692	-2.02762587
H	-1.18032488	0.63333990	2.08627004
H	1.17922811	1.61357971	-1.46689901
H	0.80765614	-1.08528670	2.17329448
H	-5.03765208	-0.78714590	-0.65084548
H	-5.03866420	-0.17150296	1.00355136
H	5.03852600	0.36689361	-0.95091189
H	-3.20353399	-2.13294357	0.38048083
H	-2.69793646	-0.93916962	-1.92286281
H	-2.70185214	2.13368231	0.14862430

H	3.20324055	-1.63726316	-1.41932402
H	2.69853199	-1.79138387	1.16989326
H	3.20474362	2.04584415	-0.70905859
H	-0.80705120	-2.18569275	1.05802044
H	-1.18119961	1.49184356	-1.58780778
H	1.17882710	-2.07632818	-0.66170068
H	-0.80936177	2.00981834	1.36466970
H	0.80878644	2.42471475	-0.14101085
H	1.18162678	0.46749007	2.12848500
H	-5.03858883	0.95345192	-0.35680223
H	5.03791828	-1.00886567	0.15516446
H	5.03882367	0.63688084	0.79356489
H	-2.70034793	-1.19588617	1.77386806
H	-3.20431575	0.73503032	-2.03755347
H	-3.20537625	1.39429482	1.65606938
H	2.69999732	-0.11896823	-2.13648700
H	3.20491356	-0.41235309	2.12607724
H	2.70222954	1.90901407	0.96463377

Appendix Table 3.13. Computed coordinates of [Co(dinosar)]Cl_3 (**6**) with fixed Co–N_6 bond distances from previous 13 °C EXAFS data (1.9701(5) Å). Total energy: –2672.10724547 Hartrees

Symbol	x	y	z
Co	-0.00001941	0.00000970	-0.00322799
N	4.58102675	-0.00318521	0.00587450
O	5.15176360	1.05038301	0.11873404
O	5.06236875	-1.10611100	-0.08226495
C	3.04251516	0.03605914	-0.00689277
C	2.61600956	-0.63741035	-1.30755835
C	2.60394321	1.49247291	0.06592851
C	2.61923168	-0.76362026	1.22367696
N	1.13357426	-0.85695034	-1.36773535
N	1.11224491	1.62460936	-0.07279474
N	1.13396349	-0.73572627	1.42997503
C	0.77475115	-2.30690051	-1.41543190
C	0.72523630	2.39193991	-1.29530838
C	0.75075218	-0.06252143	2.70786313
H	0.85800159	-0.49049625	-2.27538880
H	0.83910099	2.22031936	0.70475221
H	0.87764424	-1.71114226	1.56135256
N	-4.58106245	0.00335145	0.00593089
O	-5.15184120	-1.05032380	0.11758247
O	-5.06235369	1.10637325	-0.08114332
C	-3.04255293	-0.03595083	-0.00692876
C	-2.60405438	-1.49245668	0.06446588
C	-2.61608262	0.63872278	-1.30696591
C	-2.61921188	0.76260036	1.22436671
N	-1.11230278	-1.62452641	-0.07396472
N	-1.13360093	0.85797148	-1.36711581

N	-1.13394933	0.73450172	1.43065482
C	-0.72501411	-2.39122907	-1.29677797
C	-0.77452698	2.30787173	-1.41412714
C	-0.75075621	0.06009318	2.70791408
H	-0.83938982	-2.22060767	0.70337613
H	-0.85816006	0.49184086	-2.27493629
H	-0.87760420	1.70978598	1.56296904
H	3.12974394	-1.59476045	-1.39912544
H	2.91804656	-0.02375893	-2.15818104
H	3.09225982	2.06895109	-0.71938459
H	2.91540283	1.93254080	1.01308290
H	3.10925013	-0.35931875	2.11157093
H	2.95184601	-1.79616951	1.11625211
H	1.27006684	-2.81407177	-0.58394624
H	1.13770794	-2.76576089	-2.33701263
H	1.21733521	1.93796794	-2.15898697
H	1.07222130	3.42490158	-1.23045304
H	1.22948061	0.91927334	2.73888248
H	1.11334167	-0.62816299	3.56826248
H	-3.09215671	-2.06805631	-0.72162218
H	-2.91581822	-1.93354921	1.01104246
H	-3.12959527	1.59628838	-1.39748835
H	-2.91839577	0.02602063	-2.15817554
H	-3.10924638	0.35753316	2.11190417
H	-2.95178978	1.79525529	1.11783923
H	-1.21706751	-1.93689273	-2.16029664
H	-1.07187985	-3.42426512	-1.23247883
H	-1.26979689	2.81470069	-0.58239980
H	-1.13737397	2.76723954	-2.33549783
H	-1.22950315	-0.92172175	2.73802265
H	-1.11334582	0.62493688	3.56883774

Appendix Table 3.14. Computed coordinates of [Co(dinosar)]Cl_3 (**6**) with fixed Co–N_6 bond distances from previous 35 °C EXAFS data (1.9751(6) Å). Total energy: –2627.10776777 Hartrees

Symbol	x	y	z
Co	-0.00000612	0.00000743	-0.00319053
N	4.58211821	-0.00326077	0.00598911
O	5.15304418	1.05052806	0.11583316
O	5.06331305	-1.10648798	-0.07918376
C	3.04333872	0.03611602	-0.00691795
C	2.61839494	-0.64133181	-1.30653270
C	2.60626551	1.49363499	0.06180545
C	2.62152785	-0.76058757	1.22665161
N	1.13649010	-0.86067920	-1.37016453
N	1.11506477	1.62865567	-0.07491884
N	1.13684280	-0.73584421	1.43455772
C	0.77509870	-2.30985870	-1.41536941
C	0.72545590	2.39331978	-1.29802657

C	0.75099071	-0.06083911	2.71046686
H	0.86140310	-0.49415796	-2.27796724
H	0.84245268	2.22450934	0.70274097
H	0.88106090	-1.71141438	1.56605993
N	-4.58218430	0.00337833	0.00588206
O	-5.15317880	-1.05044671	0.11499076
O	-5.06339996	1.10667860	-0.07817561
C	-3.04337780	-0.03602482	-0.00701109
C	-2.60634379	-1.49360059	0.06076777
C	-2.61841027	0.64220504	-1.30620935
C	-2.62152625	0.75994577	1.22702928
N	-1.11509634	-1.62859625	-0.07562657
N	-1.13646107	0.86127552	-1.36983260
N	-1.13684693	0.73508376	1.43496070
C	-0.72521615	-2.39296436	-1.29883163
C	-0.77485213	2.31040716	-1.41472823
C	-0.75103082	0.05932112	2.71048118
H	-0.84269916	-2.22461432	0.70198013
H	-0.86147082	0.49485943	-2.27770459
H	-0.88105282	1.71057068	1.56706267
H	3.13220560	-1.59905387	-1.39409634
H	2.92286240	-0.03030540	-2.15820039
H	3.09462481	2.06676982	-0.72597525
H	2.92015970	1.93608966	1.00704590
H	3.11161604	-0.35254731	2.11284753
H	2.95650523	-1.79267337	1.12199629
H	1.26864745	-2.81614702	-0.58226712
H	1.13849478	-2.77130135	-2.33553722
H	1.21582557	1.93742587	-2.16170709
H	1.07282412	3.42638233	-1.23618597
H	1.22793556	0.92189163	2.73990308
H	1.11394474	-0.62392368	3.57244233
H	-3.09448797	-2.06612334	-0.72758787
H	-2.92053892	-1.93675984	1.00557874
H	-3.13201112	1.60009967	-1.39306733
H	-2.92310317	0.03183171	-2.15826712
H	-3.11163359	0.35141729	2.11299035
H	-2.95648316	1.79209579	1.12294827
H	-1.21552182	-1.93691298	-2.16247064
H	-1.07249171	-3.42607502	-1.23727954
H	-1.26838768	2.81656198	-0.58153228
H	-1.13813172	2.77209770	-2.33481670
H	-1.22799087	-0.92342021	2.73933618
H	-1.11400193	0.62190321	3.57277774

Appendix Table 3.15. Computed coordinates of [Co(dinosar)]Cl_3 (**6**) with fixed Co–N_6 bond distances from previous 57 °C EXAFS data (1.9776(6) Å). Total energy: –2672.10799293 Hartrees

Symbol	x	y	z
Co	-0.00001838	0.00000776	-0.00312521
N	4.58288555	-0.00331392	0.00594435
O	5.15406833	1.05055231	0.11366243
O	5.06419398	-1.10664168	-0.07729689
C	3.04383231	0.03613041	-0.00692978
C	2.61957848	-0.64336284	-1.30593766
C	2.60745161	1.49416036	0.05961782
C	2.62268804	-0.75896305	1.22815269
N	1.13790406	-0.86234714	-1.37147456
N	1.11646168	1.63068351	-0.07573622
N	1.13827720	-0.73607695	1.43679351
C	0.77520038	-2.31111593	-1.41552823
C	0.72550021	2.39409203	-1.29905635
C	0.75111186	-0.06026516	2.71174534
H	0.86318016	-0.49563355	-2.27926306
H	0.84428040	2.22646413	0.70207707
H	0.88289926	-1.71172194	1.56820770
N	-4.58289886	0.00341114	0.00593909
O	-5.15407668	-1.05052886	0.11288972
O	-5.06414609	1.10681847	-0.07650532
C	-3.04386031	-0.03605605	-0.00695980
C	-2.60753431	-1.49413878	0.05868101
C	-2.61962982	0.64419598	-1.30557160
C	-2.62269317	0.75833118	1.22857381
N	-1.11651126	-1.63062741	-0.07644661
N	-1.13792386	0.86296786	-1.37110707
N	-1.13828492	0.73532148	1.43721033
C	-0.72534746	-2.39368070	-1.29992163
C	-0.77504427	2.31170076	-1.41478088
C	-0.75113095	0.05877089	2.71177473
H	-0.84449304	-2.22660888	0.70126776
H	-0.86329537	0.49642190	-2.27899006
H	-0.88289302	1.71088573	1.56920077
H	3.13308072	-1.60144857	-1.39130119
H	2.92541075	-0.03387411	-2.15822644
H	3.09545543	2.06549461	-0.72969440
H	2.92275182	1.93803468	1.00371822
H	3.11251021	-0.34882001	2.11353614
H	2.95895309	-1.79079113	1.12508690
H	1.26794634	-2.81698353	-0.58168449
H	1.13881397	-2.77364955	-2.33507673
H	1.21505773	1.93730196	-2.16273541
H	1.07307525	3.42717518	-1.23851548
H	1.22721987	0.92289793	2.74043814
H	1.11428471	-0.62223964	3.57436861
H	-3.09538774	-2.06489746	-0.73114050

H	-2.92306484	-1.93866817	1.00239653
H	-3.13297595	1.60242379	-1.39026430
H	-2.92565354	0.03531197	-2.15822566
H	-3.11252240	0.34770797	2.11373132
H	-2.95894588	1.79021942	1.12607005
H	-1.21486828	-1.93668319	-2.16351652
H	-1.07284311	-3.42680919	-1.23970482
H	-1.26776388	2.81738185	-0.58080478
H	-1.13857850	2.77452152	-2.33421533
H	-1.22725231	-0.92440271	2.73990617
H	-1.11430463	0.62025296	3.57471845

APPENDIX 4: Supporting Information for Chapter 5

Appendix Table 4.1. UV-vis transition energies υ (cm^{-1}) of **1** and **2** in pure water (d_0-**1**, d_0-**2**) and 99.9% D_2O (d_{12}-**1**, d_6-**2**). Values of Δ_o (cm^{-1}) are calculated from the ratios of the energy transitions by a d_6 Tanabe-Sugano diagram for each complex to determine the difference in ligand field strength $\Delta\Delta_o$ (cm^{-1}). Values of λ_{max} from each transition were taken from the peak maxima of fit Gaussian curves.

Compound	Isotopomer	ν_1 (cm^{-1})	ν_2 (cm^{-1})	Δ_o (cm^{-1})	$\Delta\Delta_o$ (cm^{-1})
1	d_0-**1** (H_2O)	21,614(9)	29,572(16)	23,462	77
	d_{12}-**1** (D_2O)	21,668(8)	29,731(14)	23,539	
2	d_0-**2** (H_2O)	21,008(8)	27,762(10)	22,595	223
	d_6-**2** (D_2O)	21,138(5)	28,327(8)	22,818	

Appendix Table 4.2. Isotopomer chemical shift values for d_n-[Co(en)$_3$]Cl$_3$ (d_n-**1**) with temperature. Chemical shift sensitivities $\Delta\delta/\Delta T$ for each isotopomer species is calculated over 10–60 °C.

	δ (ppm)						
T **(°C)**	d_0-**1**	d_1-**1**	d_2-**1**	d_3-**1**	d_4-**1**	d_5-**1**	d_6-**1**
10	7123	7118	7113	7108	7103	7098	7093
15	7130	7125	7120	7115	7110	7105	7099
20	7136	7132	7127	7122	7116	7111	7106
25	7143	7138	7133	7128	7123	7118	7113
30	7149	7143	7138	7133	7128	7123	7118
35	7156	7150	7145	7140	7135	7130	7125
40	7163	7157	7152	7147	7142	7137	7132
45	7170	7165	7160	7155	7150	7145	7140
50	7177	7172	7167	7162	7157	7152	7147
55	7184	7179	7174	7170	7165	7160	7155
60	7191	7187	7182	7177	7172	7167	7163

		δ (ppm)					
T **(°C)**		d_7-**1**	d_8-**1**	d_9-**1**	d_{10}-**1**	d_{11}-**1**	d_{12}-**1**
10		7087	7082	7077	7072	7066	7061
15		7094	7089	7084	7079	7073	7068
20		7101	7096	7091	7086	7080	7075
25		7108	7103	7098	7093	7087	7082
30		7113	7108	7103	7098	7094	7089
35		7120	7115	7110	7105	7101	7096
40		7128	7123	7118	7113	7108	7103
45		7135	7130	7125	7120	7115	7111
50		7142	7137	7132	7127	7123	7118
55		7150	7145	7140	7135	7130	7125
60		7158	7153	7148	7143	7138	7133

	Δδ/Δ*T* (ppm/°C)						
T **(°C)**	d_0-**1**	d_1-**1**	d_2-**1**	d_3-**1**	d_4-**1**	d_5-**1**	d_6-**1**
10-60 °C	1.35(1)	1.36(2)	1.36(2)	1.37(2)	1.37(2)	1.38(2)	1.39(2)

		Δδ/Δ*T* (ppm/°C)					
T **(°C)**		d_7-**1**	d_8-**1**	d_9-**1**	d_{10}-**1**	d_{11}-**1**	d_{12}-**1**
10-60 °C		1.39(2)	1.40(2)	1.40(2)	1.41(2)	1.41(1)	1.42(1)

Appendix Table 4.3. Isotopomer chemical shift values for d_n-[Co(diNOsar)$_3$]Cl$_3$ (d_n-**2**) with temperature. Chemical shift sensitivities $\Delta\delta/\Delta T$ for each isotopomer species is calculated over 35–60 °C. Isotopomer peaks below 35 °C are unreliable for use in determining $\Delta\delta/\Delta T$ (see *Figure A4.7*).

	δ (ppm)						
T **(°C)**	d_0-**2**	d_1-**2**	d_2-**2**	d_3-**2**	d_4-**2**	d_5-**2**	d_6-**2**
10	6857	6850	6844	6838	6832	6825	6817
15	6869	6862	6856	6849	6843	6836	6829
20	6880	6873	6867	6861	6854	6847	6840
25	6891	6884	6878	6872	6864	6857	6851
30	6903	6897	6892	6885	6878	6871	6864
35	6914	6908	6902	6895	6888	6881	6874
40	6925	6919	6912	6905	6898	6891	6885
45	6934	6929	6922	6915	6908	6901	6894
50	6946	6939	6932	6925	6918	6911	6904
55	6955	6948	6941	6934	6927	6921	6914
60	6964	6958	6951	6944	6937	6930	6923
	Δδ/Δ*T* (ppm/°C)						
T **(°C)**	d_0-**2**	d_1-**2**	d_2-**2**	d_3-**2**	d_4-**2**	d_5-**2**	d_6-**2**
35-60 °C	2.03(3)	1.97(3)	1.94(2)	1.95(2)	1.96(2)	1.97(2)	1.96(2)

Appendix Table 4.4. Spin-lattice relaxation T_1 data of all isotopomers of **1** over 10-60 °C.

	T_1 (ms)						
T **(°C)**	d_0-**1**	d_1-**1**	d_2-**1**	d_3-**1**	d_4-**1**	d_5-**1**	d_6-**1**
10	2.54(12)	5.84(4)	5.84(2)	5.85(2)	5.87(3)	5.92(4)	7.13(16)
20	7.56(18)	7.74(6)	7.72(3)	7.73(3)	7.75(4)	7.77(6)	8.37(20)
30	11.13(45)	9.79(10)	9.84(5)	9.85(4)	9.94(6)	9.99(9)	10.37(23)
40	12.09(37)	12.06(10)	12.04(6)	12.08(6)	12.14(6)	12.30(13)	12.65(38)
50	15.90(93)	14.38(16)	14.29(8)	14.32(7)	14.35(10)	14.37(16)	14.35(35)
60	16.21(86)	16.61(17)	16.43(11)	16.61(11)	16.94(11)	10.68(24)	16.13(38)

	T_1 (ms)					
T **(°C)**	d_7-**1**	d_8-**1**	d_9-**1**	d_{10}-**1**	d_{11}-**1**	d_{12}-**1**
10	5.67(13)	5.49(5)	5.40(4)	5.42(3)	5.46(4)	5.97(14)
20	7.40(14)	7.24(5)	7.16(3)	7.16(3)	7.21(7)	7.26(12)
30	9.36(16)	5.72(15)	9.12(5)	9.16(4)	9.27(5)	9.71(17)
40	11.58(28)	11.36(10)	11.25(5)	11.30(5)	11.32(7)	11.60(22)
50	13.76(32)	15.42(33)	10.87(13)	13.68(6)	13.71(8)	16.07(27)
60	8.01(33)	15.57(16)	15.58(10)	15.61(8)	15.81(11)	15.62(31)

Appendix Table 4.5. Dephasing time T_2* data of all isotopomers of **1** over 10–60 °C. Values of T_2* are extracted from the linewidths of ^{59}Co peaks where the peak width at half-max, Δυ, could be determined.

	T_2* (ms)						
T **(°C)**	d_0-**1**	d_1-**1**	d_2-**1**	d_3-**1**	d_4-**1**	d_5-**1**	d_6-**1**
10	3.96	3.06	2.47	2.50	2.51	2.52	2.53
20	3.41	2.81	3.00	2.78	2.69	2.65	2.64
30	3.03	2.70	3.00	2.87	2.81	2.77	2.73
40	2.00	2.39	2.21	2.32	2.41	2.47	2.55
50	2.45	2.19	2.59	2.45	2.36	2.28	2.25
60	2.07	1.83	2.39	2.04	1.91	1.86	1.83

	T_2* (ms)					
T **(°C)**	d_7-**1**	d_8-**1**	d_9-**1**	d_{10}-**1**	d_{11}-**1**	d_{12}-**1**
10	2.57	2.62	2.78	2.56	2.60	2.70
20	2.66	2.72	2.87	2.86	2.90	2.93
30	2.69	2.59	2.47	2.80	2.84	2.87
40	2.66	2.96	3.64	2.62	2.62	2.57
50	2.17	2.04	1.93	2.25	2.19	2.03
60	1.87	1.93	2.25	1.79	1.81	1.98

Appendix Table 4.6. Spin-lattice relaxation T_1 data of all isotopomers of **2** over 40–60 °C.

	T_1 (μs)						
T **(°C)**	d_0-**1**	d_1-**1**	d_2-**1**	d_3-**1**	d_4-**1**	d_5-**1**	d_6-**1**
40	620(44)	440(10)	449(5)	456(2)	454(2)	646(29)	419(14)
50	256(18)	549(10)	544(6)	546(3)	548(3)	550(9)	225(14)
60	873(53)	635(12)	332(14)	645(3)	646(4)	651(9)	677(21)

Appendix Table 4.7. Dephasing time T_2* data of all isotopomers of **2** over 40–60 °C. Values of T_2* are extracted from the linewidths of ^{59}Co peaks where the peak width at half-max, Δυ, could be determined.

	T_2* (ms)						
T (°C)	**d_0-1**	**d_1-1**	**d_2-1**	**d_3-1**	**d_4-1**	**d_5-1**	**d_6-1**
40	0.47	0.57	0.39	0.38	0.37	0.41	0.55
50	0.67	0.47	0.43	0.46	0.46	0.47	0.82
60	0.87	0.63	0.52	0.52	0.51	0.53	0.77

Appendix Table 4.8. Frequency assignments of experimental Raman-active vibrational modes over 200–600 cm^{-1} frequency regime. Measurements are made in solution at 30 mM in H_2O (d_0-**1** and d_0-**2**) and D_2O (d_{12}-**1** and d_6-**2**).

Frequency, ν (cm^{-1})			
d_0-1	**d_{12}-1**	**d_0-2**	**d_6-2**
279(1)	273(1)	219(1)	221(1)
376(1)	353(1)	272(1)	267(1)
445(1)	419(1)	298(1)	295(1)
529(1)	497(1)	341(1)	339(1)
		388(1)	383(1)
		486(1)	479(1)
		505(1)	-
		546(1)	-

Appendix Table 4.9. Linewidth (Γ) and lifetime (τ) of experimental Raman-active vibrational modes over 200–600 cm^{-1} frequecy regime (see *Figure 5.6*, Chapter 5). Lifetimes of each peak are calculated from the FWHM linewidths (converted to Hz) of pseudo-Voigt fits via FWHM = $1/\tau\pi$.

Linewidth, Γ (cm^{-1})				Lifetime, τ (ps)			
d_0-**1**	d_{12}-**1**	d_0-**2**	d_6-**2**	d_0-**1**	d_{12}-**1**	d_0-**2**	d_6-**2**
18(1)	15(1)	17(1)	13(1)	0.62(1)	0.70(1)	0.64(5)	0.80(5)
17(1)	14(1)	11(2)	12(2)	0.61(5)	0.74(3)	1.0(4)	0.9(3)
17(1)	15(1)	17(1)	12(1)	0.62(4)	0.72(4)	0.62(4)	0.9(1)
17(1)	17(1)	14(1)	14(1)	0.61(1)	0.64(1)	0.78(1)	0.75(1)
		16(1)	12(1)			0.66(8)	0.9(2)
		15(1)	15(1)			0.72(2)	0.72(2)
		15(1)				0.71(2)	
		20(2)				0.53(5)	

Appendix Table 4.10. Displacement vectors of $Co–N_6$ core and energies of predicted vibrations for experimental Raman-active modes in $[Co(en)_3]^{3+}$ (**1**). Pink-, blue-, and grey-colored spheres correspond to Co, N, and C atoms, respectively. Hydrogens are omitted for clarity.

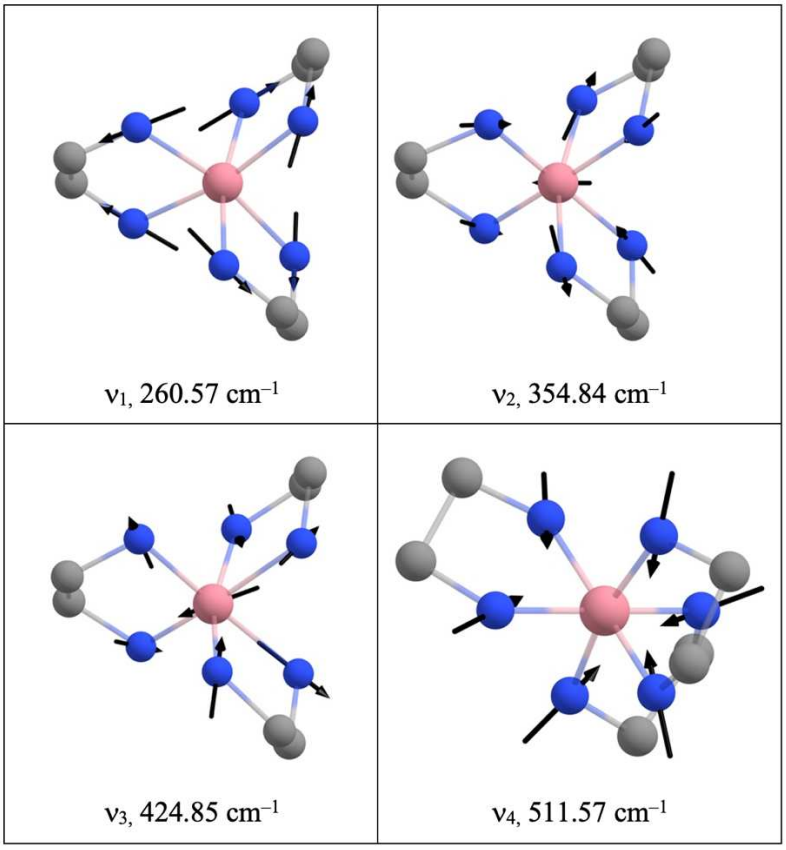

Appendix Table 4.11. Displacement vectors of Co–N_6 core and energies of predicted vibrations for experimental Raman modes in $[Co(diNOsar)]^{3+}$ (**2**). Pink-, blue-, red-, and grey-colored spheres correspond to Co, N, O, and C atoms, respectively. Hydrogens are omitted for clarity.

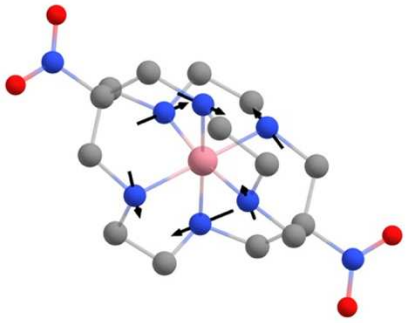 ν_1, 209.78 cm^{-1}	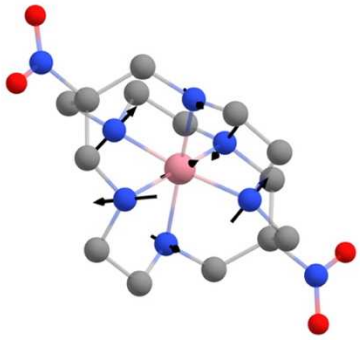 ν_2, 269.77 cm^{-1}	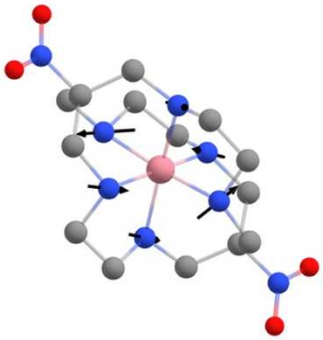 ν_3, 290.76 cm^{-1}
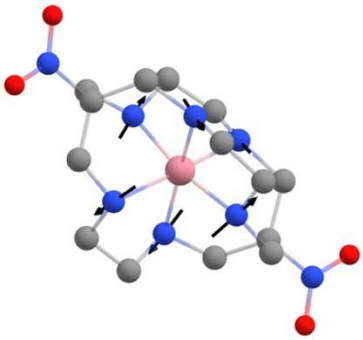 ν_4, 337.94 cm^{-1}	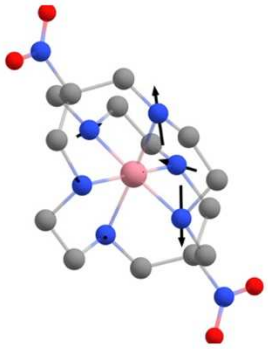 ν_5, 385.57 cm^{-1}	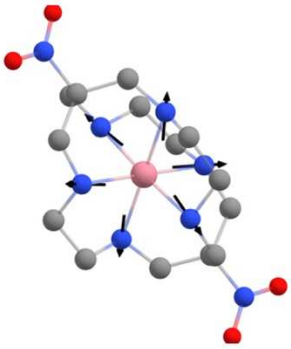 ν_6, 486.98 cm^{-1}
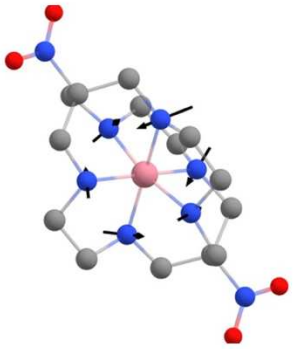 ν_7, 496.34 cm^{-1}	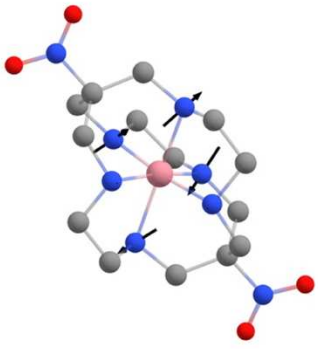 ν_8, 540.47 cm^{-1}	

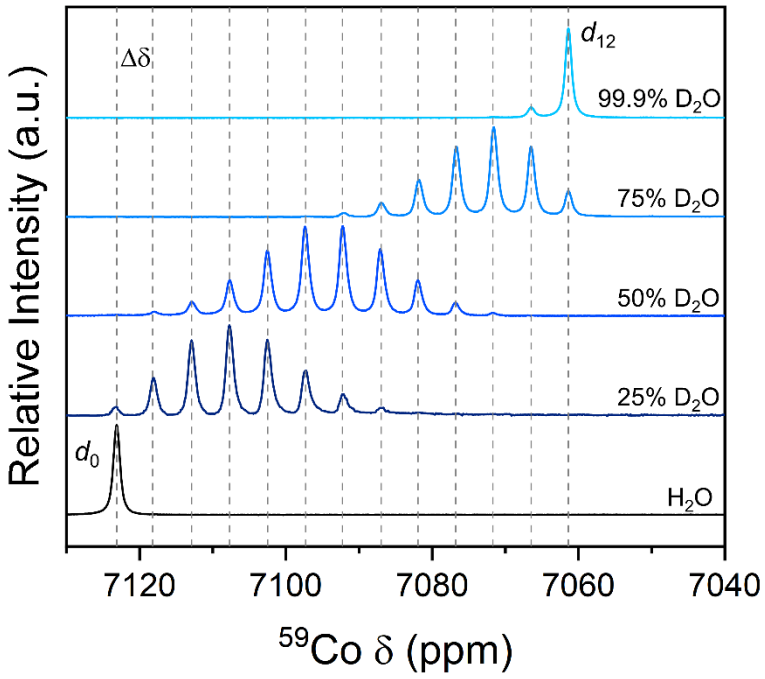

Appendix Figure 4.1. At 10 °C, ^{59}Co NMR of **1** in varying mixtures (0%, 25%, 50%, 75%, and 99.9%) of D_2O in H_2O showing an ensemble of distributed isotopomer peaks. The average difference in chemical shift Δδ is 5.0(1) ppm between each isotopomer.

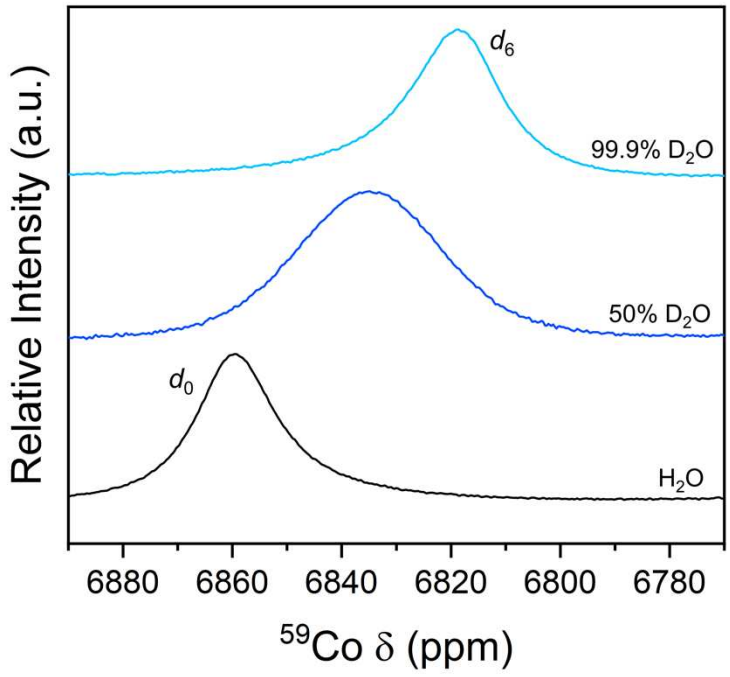

Appendix Figure 4.2. At 10 °C, ^{59}Co NMR of **2** in varying mixtures (0%, 50%, and 99.9%) of D_2O in H_2O showing broad signals.

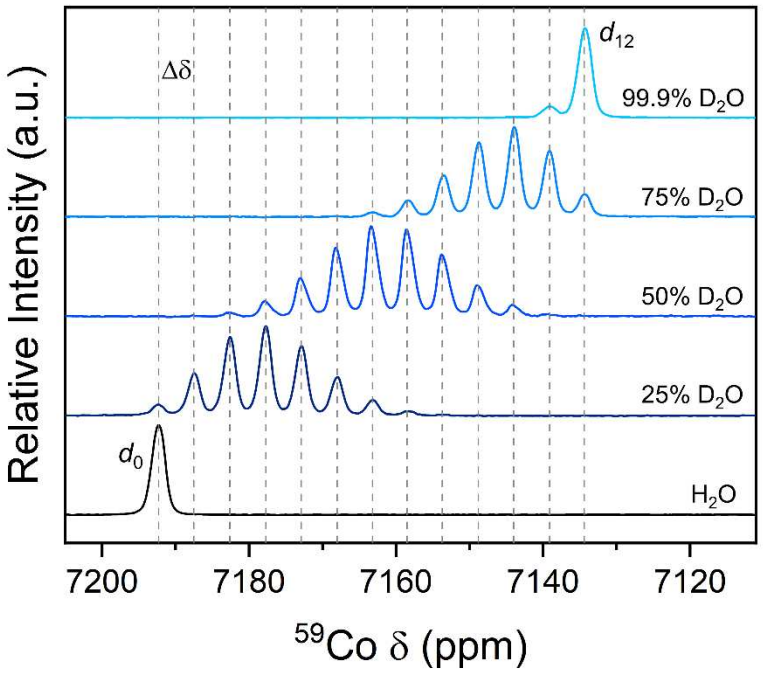

Appendix Figure 4.3. At 60 °C, ^{59}Co NMR of **1** at 60 °C in varying mixtures (0%, 25%, 50%, 75%, and 99.9%) of D_2O in H_2O showing an ensemble of distributed isotopomer peaks. The average difference in chemical shift Δδ is 5.0(1) ppm between each isotopomer.

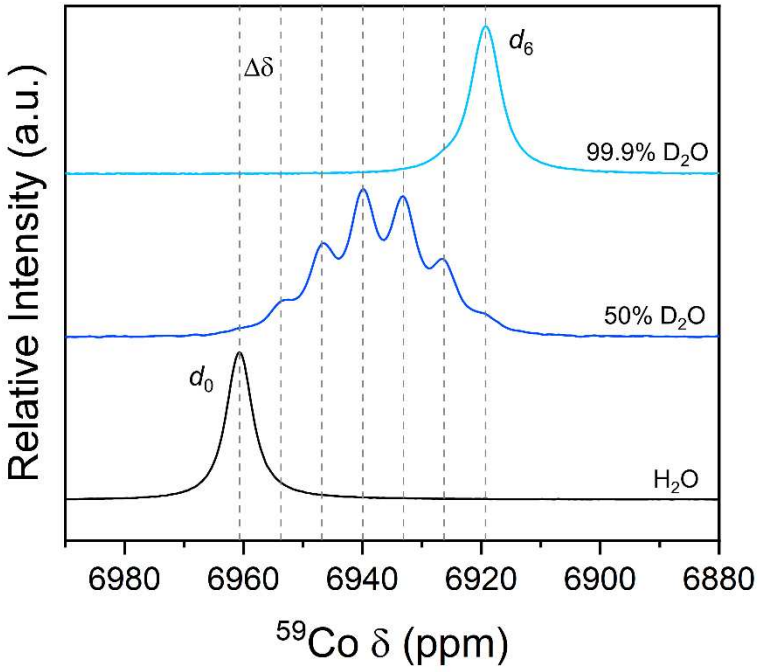

Appendix Figure 4.4. At 60 °C, ^{59}Co NMR of **2** at 60 °C in varying mixtures (0% 50%, and 99.9%) of D_2O in H_2O showing an ensemble of distributed isotopomer peaks. The average difference in chemical shift Δδ is 6.7(1) ppm between each isotopomer.

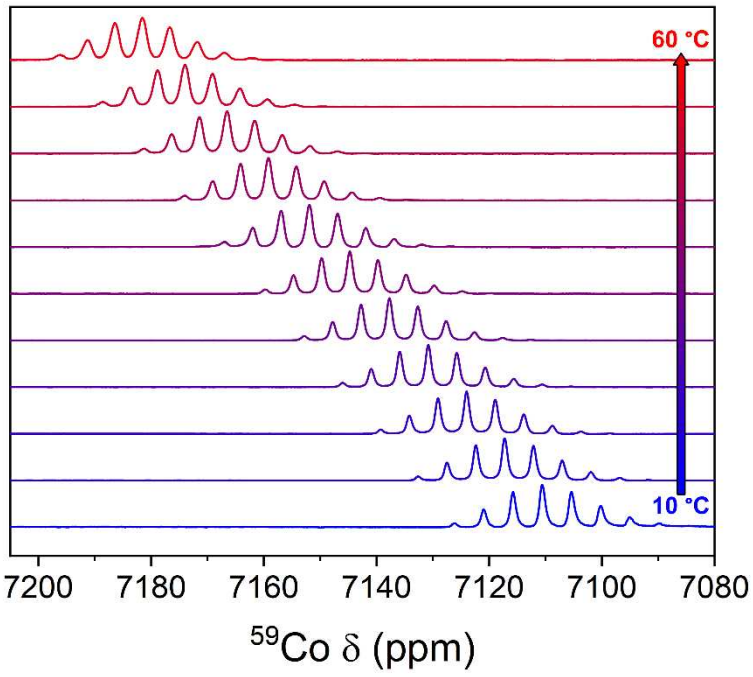

Appendix Figure 4.5. Variable temperature ^{59}Co NMR of **1** in 25% D_2O from 10–60 °C.

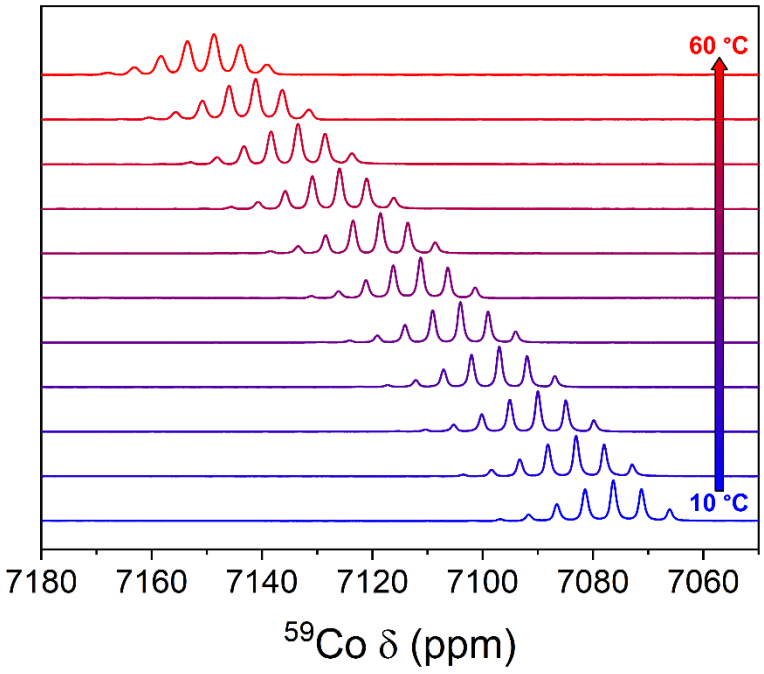

Appendix Figure 4.6. Variable temperature ^{59}Co NMR of **1** in 75% D_2O from 10–60 °C.

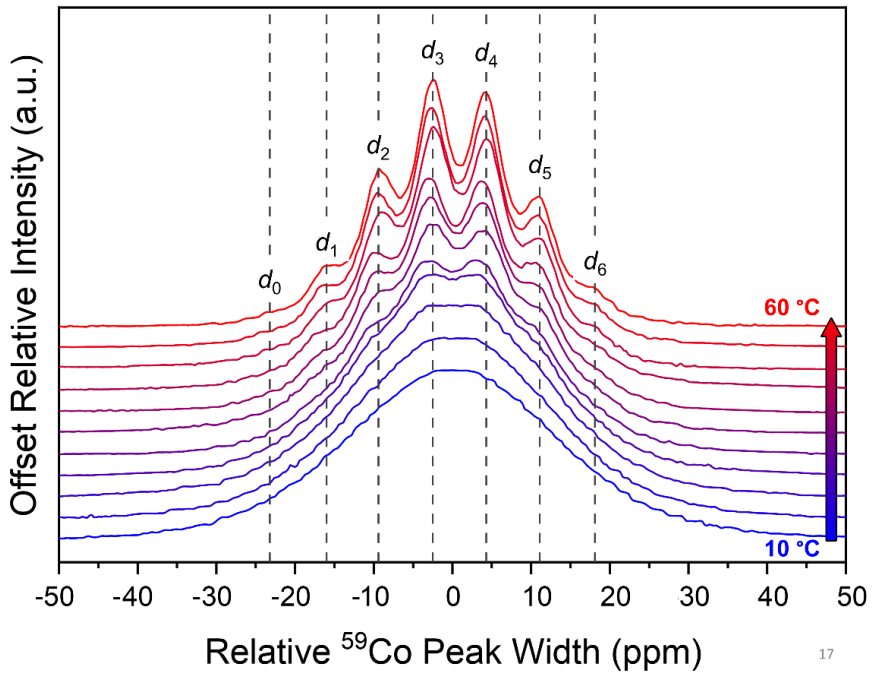

Appendix Figure 4.7. Variable temperature ^{59}Co NMR of **2** in 50% D_2O from 10–60 °C. The spectra are aligned with a relative chemical shift baseline showing the range of signal broadening with temperature.

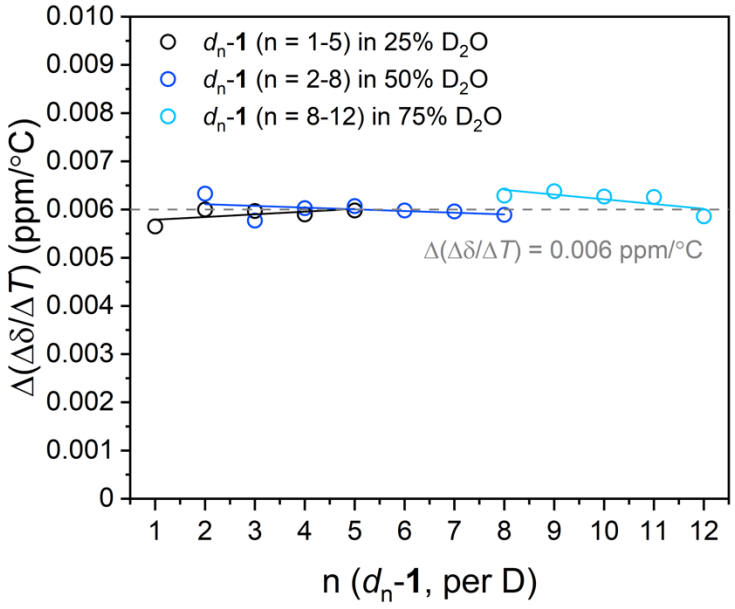

Appendix Figure 4.8. The change in temperature response $\Delta(\Delta\delta/\Delta T)$ (ppm/°C) between isotopomers of d_n-**1** (n = 0–12) is calculated to a consistent change of 0.006 ppm/°C per ^{2}H. Values of $\Delta\delta/\Delta T$ were separately collected from ensembles at 25% (*black*), 50% (*blue*), 75% (*light blue*) D_2O in H_2O. Linear regressions (*solid lines*) revealed the slopes to be within error, indicating a consistent increase in $\Delta\delta/\Delta T$ with higher degrees of deuteration.

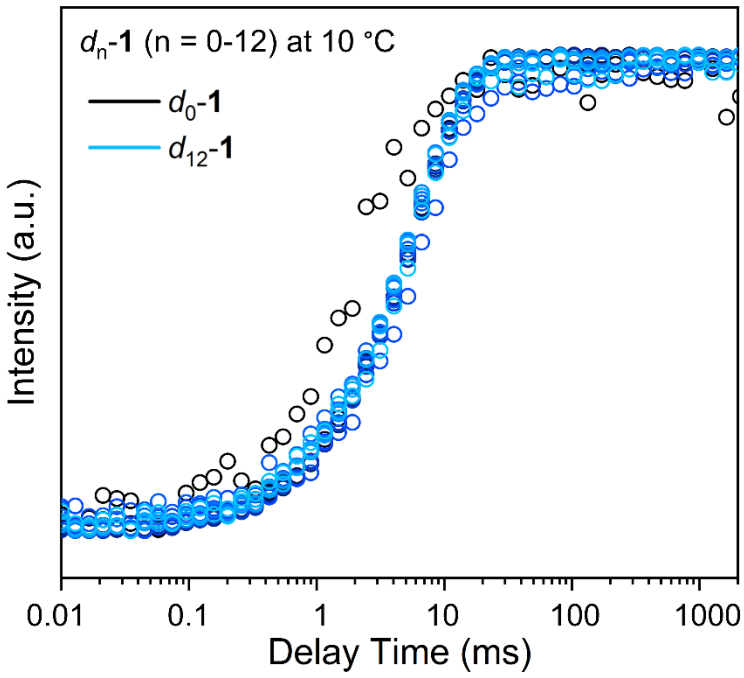

Appendix Figure 4.9. Inversion recovery curves of d_n-**1** at 10 °C. Tabulated values are found in Table A4.4.

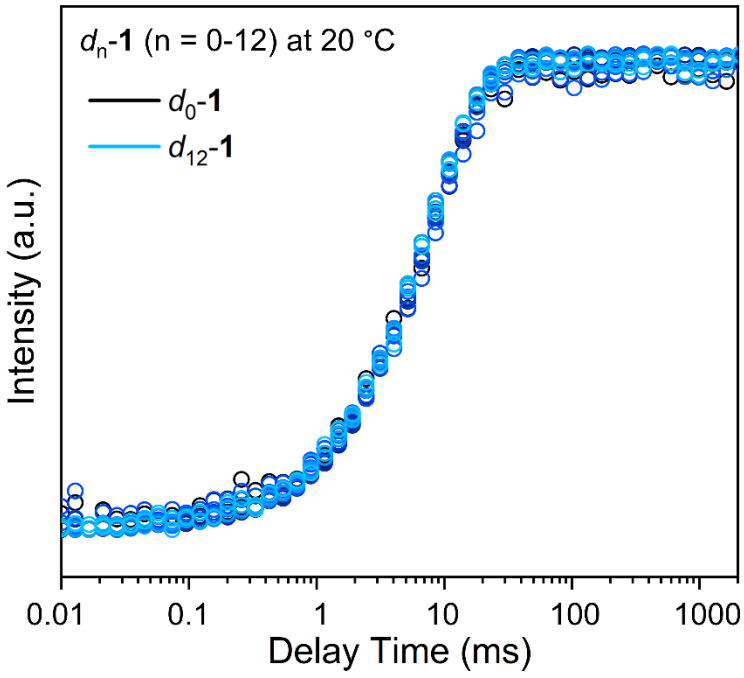

Appendix Figure 4.10. Inversion recovery curves of d_n-**1** at 20 °C. Tabulated values are found in Table A4.4.

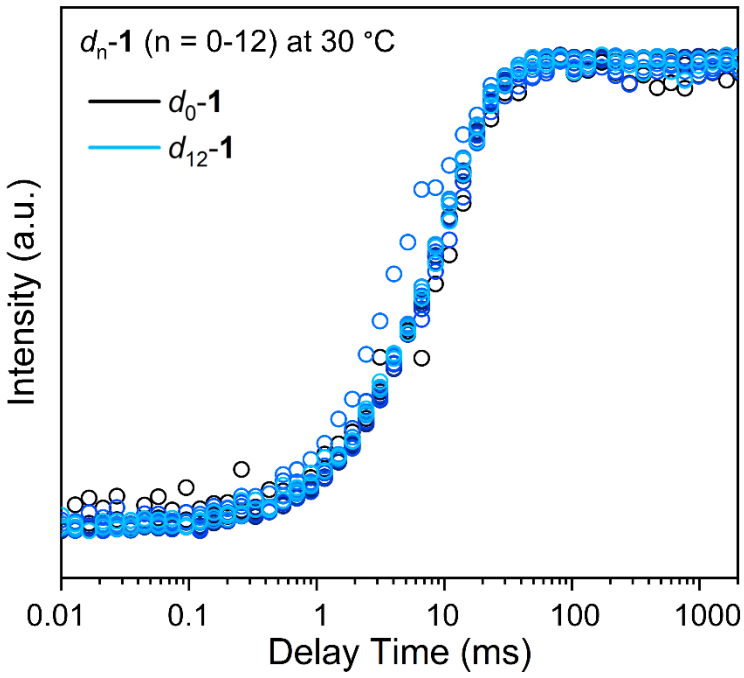

Appendix Figure 4.11. Inversion recovery curves of d_n-**1** at 30 °C. Tabulated values are found in Table A4.4.

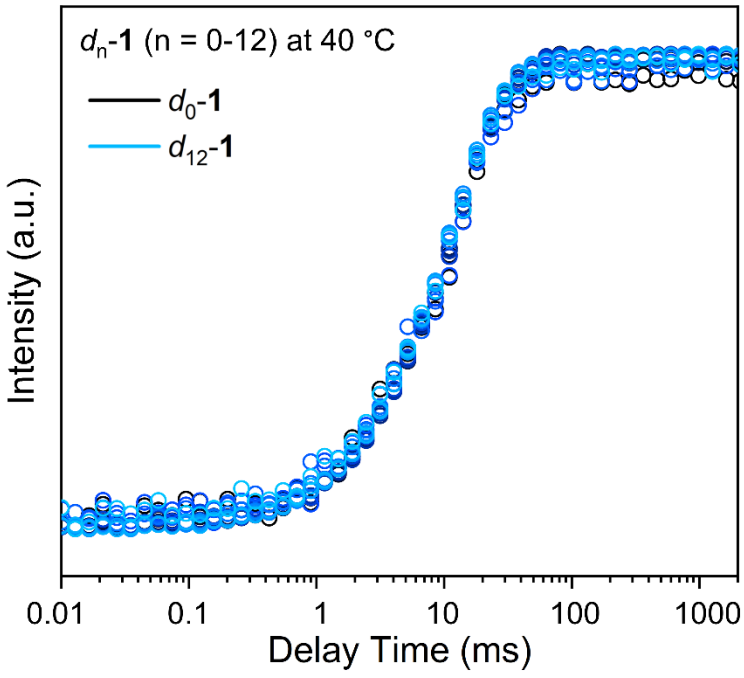

Appendix Figure 4.12. Inversion recovery curves of d_n-**1** at 40 °C. Tabulated values are found in Table A4.4.

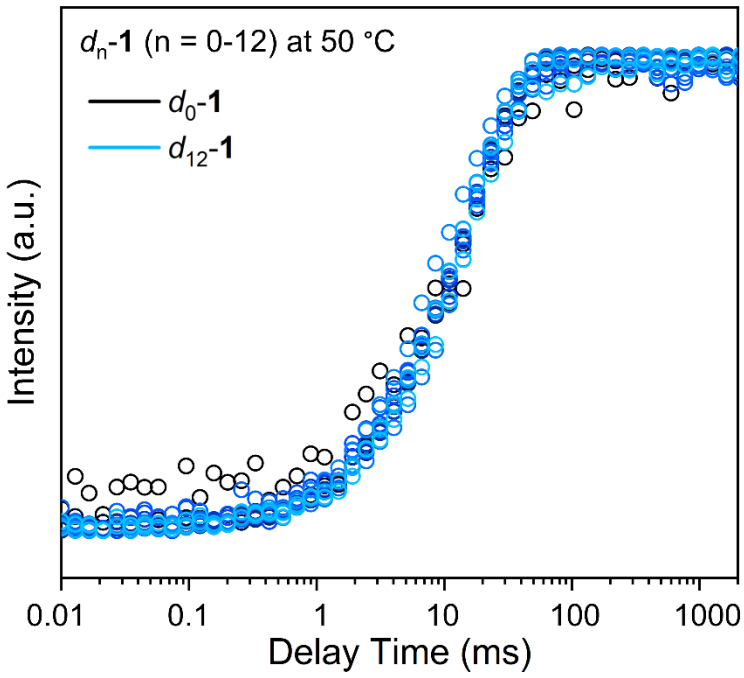

Appendix Figure 4.13. Inversion recovery curves of d_n-**1** at 50 °C. Tabulated values are found in Table A4.4.

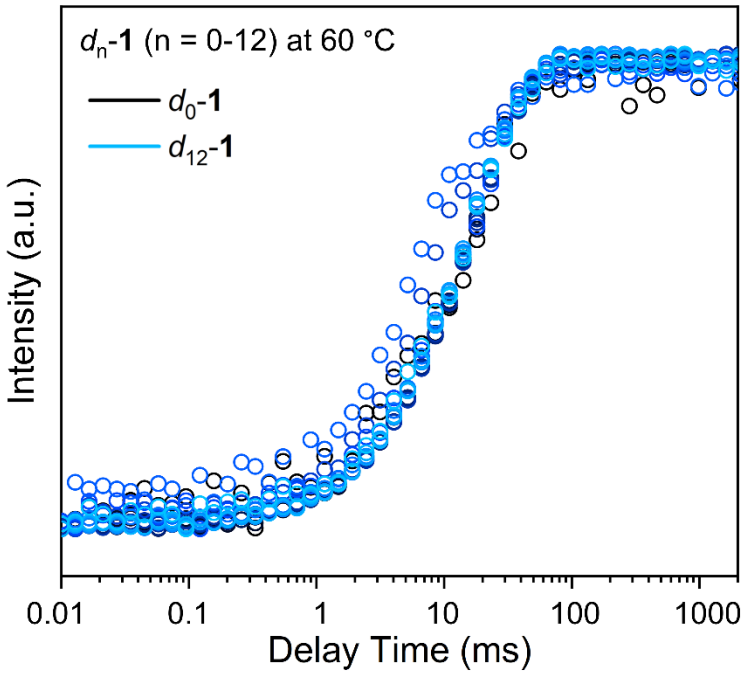

Appendix Figure 4.14. Inversion recovery curves of d_n-**1** at 60 °C. Tabulated values are found in Table A4.4.

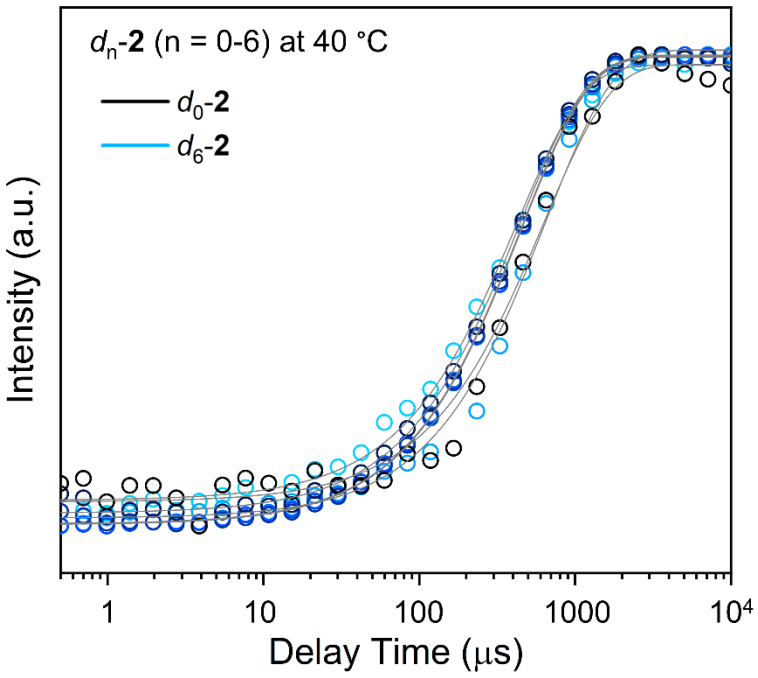

Appendix Figure 4.15. Inversion recovery curves of d_n-**2** at 40 °C. Tabulated values are found in Table A4.6.

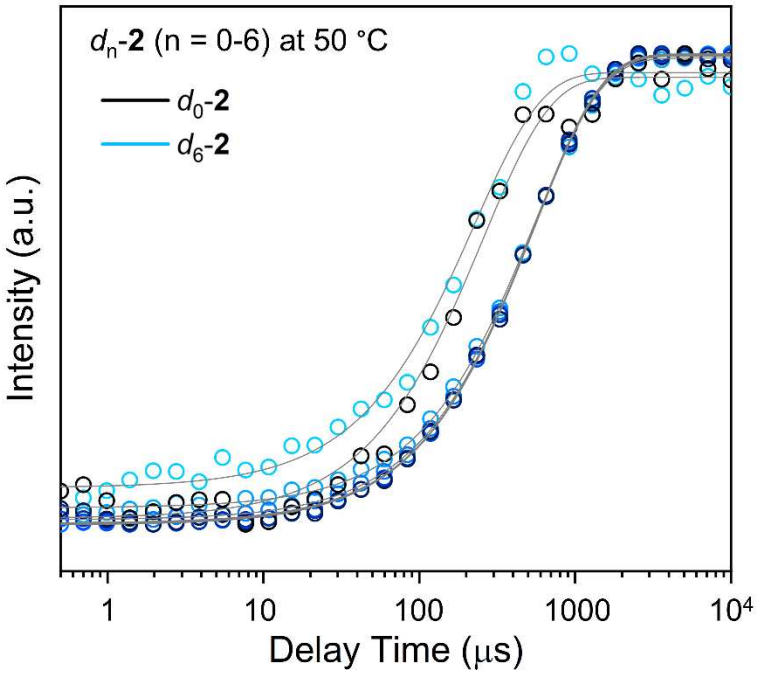

Appendix Figure 4.16. Inversion recovery curves of d_n-**2** at 50 °C. Tabulated values are found in Table A4.6.

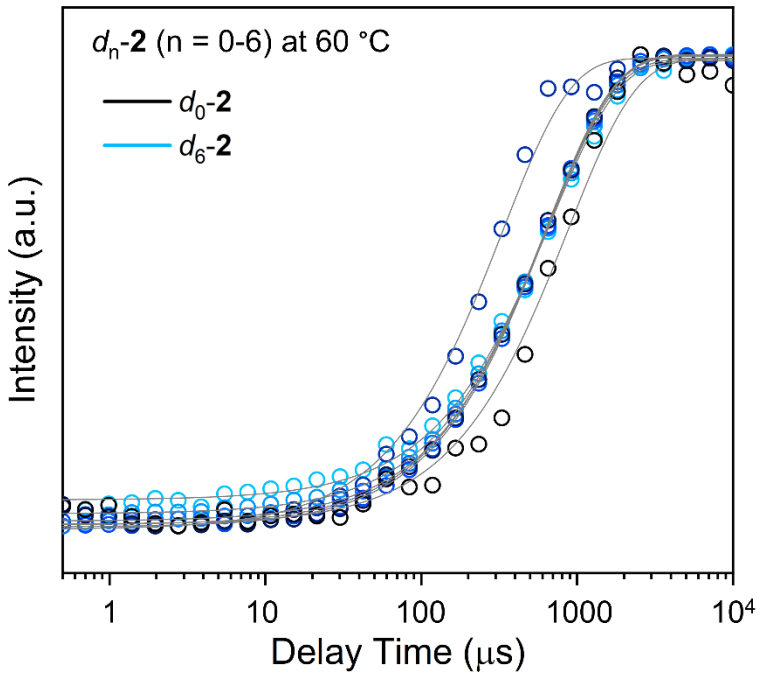

Appendix Figure 4.17. Inversion recovery curves of d_n-**2** at 60 °C. Tabulated values are found in Table A4.6.

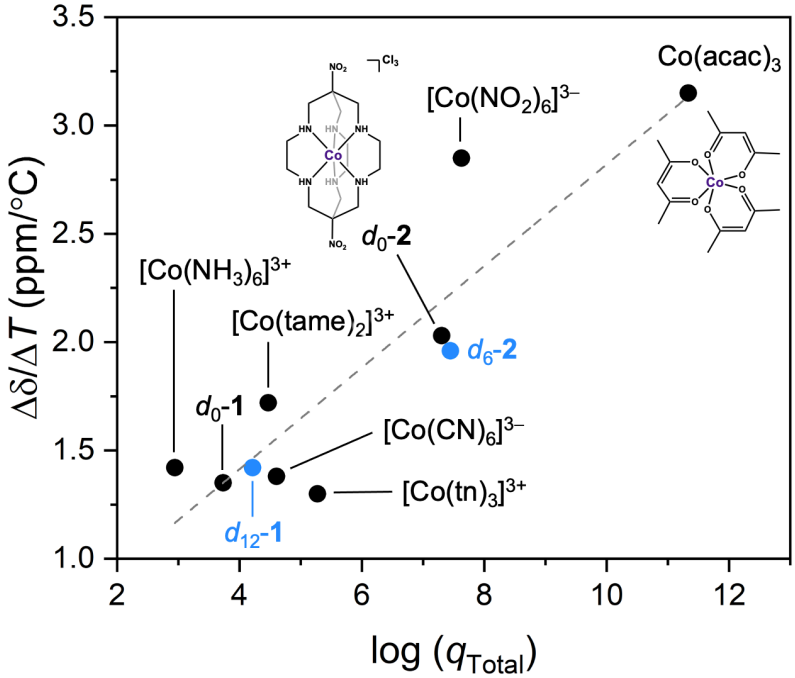

Appendix Figure 4.18. Relation between ^{59}Co $\Delta\delta/\Delta T$ and total (IR and Raman) vibrational partition functions, q_{Total} (logarithmic) of all complexes from *Figure 5.8* in Chapter 5. Linear correlation by R^2 is 0.80. Error in $\Delta\delta/\Delta T$ is within 0.03 ppm/°C.

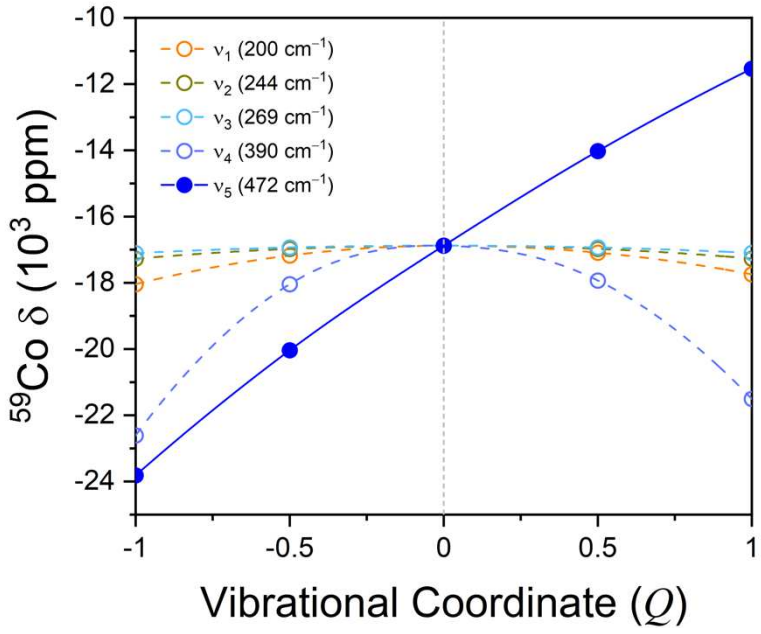

Appendix Figure 4.19. ^{59}Co δ as a function of Q for Raman modes in Co(acac)$_3$ between 200–600 cm^{-1}. The Co–O$_6$ symmetric stretching breathing mode is indicated by filled circles with solid traces, while the other modes are indicated by open circles with dashed traces. Values of $\Delta\delta/\Delta Q$ for modes υ_1 to υ_5 are 136, 2, 1, 463, and 6113 ppm/Q, respectively.

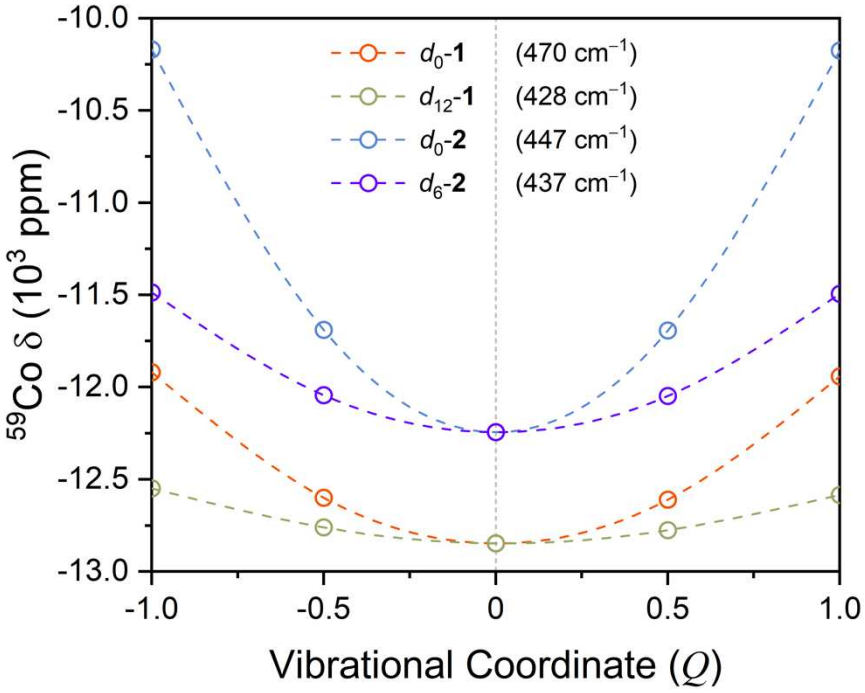

Appendix Figure 4.20. ^{59}Co δ as a function of Q for the asymmetric T_{1u} IR-active modes in d_0-**1**, d_{12}-**1**, d_0-**2,** and d_6-**2** between 200–600 cm^{-1}. Values of $\Delta\delta/\Delta Q$ for T_{1u} distortions are 10, 17, 3, and 8 ppm/Q, respectively.

Appendix Table 4.12. Optimized d_0-**1** (d_0-$[Co(en)_3]^{3+}$). Total energy: –1953.480447 Hartrees

Symbol	x	y	z
Co	-0.00033655	0.00001114	-0.00003260
C	-2.77884227	-0.01751483	-0.75005501
C	1.26821852	-2.47171115	0.75014640
C	1.40550929	-2.39693372	-0.74988528
H	-0.76024239	-2.23251992	1.01472394
H	0.10681953	-1.47350495	2.13025749
H	2.29051725	-0.55644209	-1.01701107
H	1.18415826	-0.88251849	-2.13125569
H	-2.80933563	0.95249623	-1.25028185
H	-3.64070492	-0.58947907	-1.09637144
H	2.14180448	-2.04944784	1.25077137
H	1.16004920	-3.50032112	1.09673618
H	2.33213489	-2.85690725	-1.09578628
H	0.58115024	-2.90876880	-1.25044710
H	-1.35658229	-0.58357502	-2.13099462
H	-1.62818388	-1.70475283	-1.01686846
N	-1.49801714	-0.69918495	-1.12764939
N	0.07084335	-1.65183774	1.12679494
N	1.35475841	-0.94692362	-1.12782381
N	-1.46619690	0.76369572	1.12758050
N	0.14270991	1.64723153	-1.12684140
N	1.39459726	0.88714045	1.12791299
C	-2.77541235	0.13823139	0.75008209
H	-1.32988936	0.64211688	2.13092977
H	-1.55255799	1.77395765	1.01673293
C	1.37461656	2.41419017	-0.75010541
H	-0.66227275	2.26360307	-1.01482240
H	0.17093969	1.46751239	-2.13030520
C	1.50836479	2.33356559	0.74994120
H	2.31251063	0.45634268	1.01722300
H	1.22123502	0.83024705	2.13132437
H	-2.84787302	-0.82955935	1.25029590
H	-3.61164663	0.74700598	1.09647504
H	2.22906028	1.95427853	-1.25063138
H	1.31135448	3.44652708	-1.09672431
H	2.45406873	2.75283804	1.09593426
H	0.70698150	2.88075595	1.25041500

Appendix Table 4.13. Optimized d_0-**2** (d_0-$[Co(diNOsar)]^{3+}$). Total energy: –2672.108975 Hartrees

Symbol	x	y	z
Co	-0.00002201	-0.00000102	-0.00317873
N	4.58918068	-0.00401354	0.00522611
O	5.16171035	1.05087664	0.09295972
O	5.06978137	-1.10885576	-0.05959769

C	3.04822082	0.03622455	-0.00656596
C	2.63059618	-0.66350499	-1.29913564
C	2.61906101	1.49904420	0.03857962
C	2.63427180	-0.74236904	1.24356191
N	1.15092422	-0.87903990	-1.38240190
N	1.13012550	1.64943842	-0.08502485
N	1.15226021	-0.73688336	1.45856989
C	0.77586597	-2.32409391	-1.41602928
C	0.72677670	2.40107267	-1.31046661
C	0.75218069	-0.05331379	2.72429055
H	0.88023933	-0.51056890	-2.29056710
H	0.86163062	2.24480766	0.69423453
H	0.90106425	-1.71357133	1.58935697
N	-4.58921444	0.00401290	0.00525226
O	-5.16177261	-1.05083635	0.09327042
O	-5.06979037	1.10883440	-0.05991198
C	-3.04823666	-0.03626946	-0.00652419
C	-2.61908892	-1.49906568	0.03920439
C	-2.63062349	0.66291210	-1.29941415
C	-2.63424536	0.74283882	1.24324865
N	-1.13011728	-1.64948817	-0.08427122
N	-1.15094307	0.87842210	-1.38272341
N	-1.15222716	0.73756415	1.45818346
C	-0.72674303	-2.40174949	-1.30928971
C	-0.77584739	2.32341984	-1.41711276
C	-0.75206294	0.05481115	2.72431550
H	-0.86163536	-2.24438697	0.69535819
H	-0.88014171	0.50941301	-2.29064359
H	-0.90110227	1.71434900	1.58832331
H	3.14183781	-1.62454158	-1.36319347
H	2.94964847	-0.06883832	-2.15714399
H	3.10503621	2.05288611	-0.76445559
H	2.94743510	1.95593693	0.97195422
H	3.12181682	-0.31127841	2.12035746
H	2.98378518	-1.77131056	1.15675470
H	1.26102705	-2.82621810	-0.57541694
H	1.14113799	-2.79732210	-2.32964806
H	1.20895407	1.93625951	-2.17409212
H	1.07555808	3.43459272	-1.26272034
H	1.22019432	0.93396001	2.74581502
H	1.11686371	-0.60394853	3.59377222
H	-3.10498960	-2.05322179	-0.76365346
H	-2.94747610	-1.95562236	0.97273281
H	-3.14182800	1.62394186	-1.36387794
H	-2.94964352	0.06788075	-2.15717687
H	-3.12170853	0.31205837	2.12023502
H	-2.98386060	1.77172052	1.15607112
H	-1.20895851	-1.93740432	-2.17315151
H	-1.07548394	-3.43526380	-1.26102449
H	-1.26097880	2.82599754	-0.57675535
H	-1.14114589	2.79618432	-2.33096430

H	-1.22007952	-0.93244821	2.74647639
H	-1.11670535	0.60600302	3.59345875

Appendix Table 4.14. Optimized $[Co(CN)_6]^{3-}$.Total energy: –1939.759072 Hartrees

Symbol	x	y	z
Co	0.00000000	0.00000000	0.00000000
C	0.00000000	0.00000000	1.94584009
C	0.00000000	1.94584009	-0.00000000
C	1.94584009	0.00000000	0.00000000
C	0.00000000	-1.94584009	0.00000000
C	-1.94584009	0.00000000	-0.00000000
C	0.00000000	-0.00000000	-1.94584009
N	0.00000000	3.10675969	0.00000000
N	3.10675969	-0.00000000	0.00000000
N	0.00000000	0.00000000	3.10675969
N	-0.00000000	-0.00000000	-3.10675969
N	-0.00000000	-3.10675969	0.00000000
N	-3.10675969	0.00000000	-0.00000000

Appendix Table 4.15. Optimized $[Co(NO_2)_6]^{3-}$. Total energy: –2613.466612 Hartrees

Symbol	x	y	z
Co	0.00000539	0.00000801	-0.00001911
N	-1.51694948	0.34668829	-1.26511379
N	-0.50183827	1.63371713	1.04914281
N	1.21212962	1.11020217	-1.14893796
N	1.51694568	-0.34671045	1.26509622
N	-1.21209991	-1.11015582	1.14892584
O	-1.33937144	1.04152027	-2.26292887
O	-2.62528936	-0.13540591	-1.04354750
O	-1.84936728	-0.58430492	2.05848455
O	-1.31855668	-2.31711545	0.94437191
O	1.46032886	-2.31876511	-0.69990421
O	2.62506568	0.13610088	1.04400363
O	-0.14874157	-1.95121212	-2.04204715
O	1.33957514	-1.04225855	2.26245410
O	1.85028140	0.58422965	-2.05781715
O	1.31771272	2.31734468	-0.94501497
O	0.14883318	1.95127080	2.04196418
N	0.50182502	-1.63375248	-1.04912428
O	-1.46049992	2.31857852	0.70005572

Appendix Table 4.16. Optimized $[Co(NH_3)_6]^{3+}$. Total energy: –1721.208313 Hartrees

Symbol	x	y	z
Co	-0.00023112	-0.00032485	0.00002029
N	-1.39629113	0.72442670	1.25754924
H	-1.77302704	0.03781576	1.91482647
H	-2.22298617	1.09975279	0.78680072
H	-1.07914594	1.49256596	1.85298120
N	-0.14799195	-1.81382050	0.86092263
H	0.61781930	-2.45233946	0.63472504
H	-0.99039835	-2.33346834	0.60468681
H	-0.16572579	-1.79465782	1.88327077
N	-1.46265782	-0.50924933	-1.28857382
H	-1.25349355	-1.32258125	-1.87154467
H	-1.71230739	0.22156608	-1.95855069
H	-2.34833670	-0.74872650	-0.83687114
N	1.46142995	0.50701725	1.28937201
H	1.70377926	-0.22209904	1.96384257
H	1.25513632	1.32417250	1.86799224
H	2.35022032	0.73800690	0.83946064
N	0.14619325	1.81227287	-0.86291553
H	0.99051979	2.33099382	-0.61100273
H	-0.61785549	2.45197323	-0.63395901
H	0.15921511	1.79118116	-1.88529378
N	1.39989622	-0.71982990	-1.25645362
H	2.20180457	-1.14449216	-0.78471198
H	1.81537526	-0.01785378	-1.87286903
H	1.07159714	-1.44875849	-1.89363750

Appendix Table 4.17. optimized $[Co(tn)_3]^{3+}$. Total energy: –2071.440944 Hartrees

Symbol	x	y	z
Co	-0.00022190	0.00066930	-0.09999786
C	0.01950382	-2.75356607	1.25916826
C	0.39010290	-3.40192506	-0.05838970
C	1.46236212	-2.64629008	-0.81340941
C	2.37540322	1.39377241	1.26054912
C	2.75323404	2.03553163	-0.05824109
C	1.56373090	2.58825314	-0.81353823
C	-2.39647138	1.35875282	1.25978509
C	-3.14248725	1.36235303	-0.05816573
C	-3.02270168	0.05658172	-0.81422055
H	-1.64253585	-1.71309568	0.71041345
H	-0.48846608	1.34272891	1.99256877
H	-1.63501952	-1.15986429	-1.66836861
H	-1.50314101	0.36331698	-2.13769978
H	0.91093055	-2.55182089	1.85732400
H	-0.61557357	-3.41683306	1.84929166

H	0.77369287	-4.40241568	0.15340167
H	-0.49786470	-3.55982980	-0.68234244
H	2.33897607	-2.49366297	-0.17899654
H	1.80161105	-3.21557773	-1.68056372
H	1.75552660	2.06717776	1.85669330
H	-0.91787133	-1.09230570	1.99253603
H	3.26646804	1.17502340	1.85186752
H	3.43089878	2.86608528	0.15112883
H	3.33121600	1.34216818	-0.68125963
H	0.99363328	3.27107790	-0.17875579
H	1.88788054	3.16706338	-1.68021437
H	-2.66695811	0.48547256	1.85754274
H	-2.65381702	2.24000065	1.85034405
H	-4.20104398	1.52976304	0.15249233
H	-2.83484668	2.21073437	-0.68135433
H	-3.32696450	-0.77998057	-0.18017806
H	1.82539314	-0.83498052	-1.66391611
H	-3.68611946	0.04686202	-1.68077707
H	0.44071660	-1.48035794	-2.13685364
H	2.30201812	-0.56710673	0.71637449
H	1.40063971	-0.24487921	1.99620459
H	-0.18678187	1.99931900	-1.66493718
H	1.06352392	1.12148366	-2.13772123
H	-0.66583074	2.27901993	0.70961441
N	-0.71981046	-1.46337368	1.06358246
N	0.99430353	-1.30090430	-1.29922101
N	1.62540728	0.10948767	1.06687284
N	0.63154221	1.51141589	-1.30006240
N	-0.90943165	1.35518084	1.06384414
N	-1.62349088	-0.20801192	-1.30146515

Appendix Table 4.18. Optimized $[Co(tame)_2]^{3+}$. Total energy: –2109.550431 Hartrees

Symbol	x	y	z
Co	-0.00002790	0.00002550	0.00009395
N	1.19144318	-1.48547292	-0.61628139
N	1.19163058	0.20876446	1.59482348
N	-1.19150954	-1.34038503	0.88881316
N	1.19140765	1.27692022	-0.97795888
N	-1.19159115	1.43979608	0.71656818
N	-1.19130721	-0.09957855	-1.60510244
C	4.66158933	-0.00015114	-0.00035874
C	3.12824637	-0.00002714	-0.00014806
C	2.62881272	-1.13818786	-0.89686483
C	2.62914322	-0.20744015	1.43402298
C	2.62901369	1.34571582	-0.53735207
C	-2.62905040	-0.94596720	1.09753127
C	-3.12832330	0.00000441	-0.00013501
C	-4.66164798	0.00000114	-0.00025781

C	-2.62882591	-0.47761723	-1.36814244
C	-2.62898538	1.42356937	0.27033323
H	1.19955802	-2.19358106	0.11662157
H	0.83350172	-0.24399366	2.43482829
H	-0.83342744	-1.67739316	1.78157161
H	1.19905742	0.99704746	-1.95788235
H	-1.19976625	1.35119347	1.73180822
H	-0.83297493	-0.70418068	-2.34326244
H	5.05320318	-0.88308466	0.50858158
H	5.05306481	0.00043693	-1.01952788
H	-5.05337364	0.19503114	0.99997468
H	3.23221279	-2.03397885	-0.74020058
H	2.72243264	-1.25277146	1.73523352
H	2.72244053	2.12916033	0.21738273
H	-3.23238892	-1.85523940	1.11464772
H	-2.72187053	-1.56127573	-1.46401644
H	-3.23242146	1.89308807	1.04911404
H	0.83318632	-1.98707221	-1.42800472
H	1.19938485	1.19738759	1.84222383
H	-1.19946941	-2.17558231	0.30486583
H	0.83330144	2.23077381	-1.00560685
H	-0.83337779	2.38149035	0.56259424
H	-1.19924024	0.82374942	-2.03640340
H	5.05339728	0.88206604	0.50967466
H	-5.05324083	-0.96376566	-0.33155249
H	-5.05318084	0.76876339	-0.66932667
H	2.72165823	-0.87620682	-1.95274491
H	3.23255611	0.37644813	2.13119476
H	3.23222638	1.65770792	-1.39168460
H	-2.72214026	-0.48725688	2.08397938
H	-3.23207026	-0.03784502	-2.16424346
H	-2.72183433	2.04848502	-0.62018221

Appendix Table 4.19. Optimized $Co(acac)_3$. Total energy: –2418.451742 Hartrees

Symbol	x	y	z
Co	0.00004343	0.00005489	-0.00009677
C	-2.29360346	1.26077888	-0.99513940
C	0.57112663	-3.58309485	-2.02675060
C	2.23886199	1.35621005	-0.99470990
C	2.61690485	-0.04671025	0.99516801
C	3.06334333	0.82632453	0.00045784
C	2.81796637	2.28597691	-2.02671378
C	3.58473793	-0.55967998	2.02714652
C	-1.26833400	2.28950631	0.99492750
C	-2.24727504	2.23992357	-0.00014452
C	-3.38787153	1.29713900	-2.02766820
C	-1.30864064	3.38344014	2.02766738
C	0.05478264	-2.61666430	-0.99512052

C	-1.34932694	-2.24273649	0.99467534
C	-0.81723525	-3.06560068	-0.00062834
C	-2.27689293	-2.82461130	2.02707976
H	0.20325938	-4.59534125	-1.86634025
H	0.26710249	-3.23815765	-3.01690510
H	1.66239386	-3.58287533	-2.00025758
H	4.10614705	1.10772757	0.00074085
H	3.87745451	2.47704494	-1.86351562
H	2.26915509	3.22928985	-2.00439525
H	2.67574960	1.84727256	-3.01625399
H	4.59633143	-0.19065660	1.86528868
H	3.24012353	-0.25397208	3.01692491
H	3.58599829	-1.65098113	2.00301922
H	-3.01228819	3.00239049	-0.00013383
H	-4.08471553	2.11756505	-1.86342441
H	-2.93645488	1.39608999	-3.01677821
H	-3.92857687	0.34911944	-2.00735258
H	-2.13157899	4.07738305	1.86356992
H	-0.36257490	3.92749108	2.00758204
H	-1.40603825	2.93139284	3.01663877
H	-1.09548707	-4.10924958	-0.00092236
H	-2.46808844	-3.88374211	1.86157537
H	-3.22028965	-2.27584271	2.00831228
H	-1.83600022	-2.68500581	3.01604126
O	1.00490065	1.12878238	-1.13062347
O	1.43592681	-0.47083386	1.13046600
O	-1.12543846	-1.00810600	1.13056595
O	-1.47957096	0.30582801	-1.13056208
O	-0.31053394	1.47884264	1.13027194
O	0.47545855	-1.43446742	-1.13040383